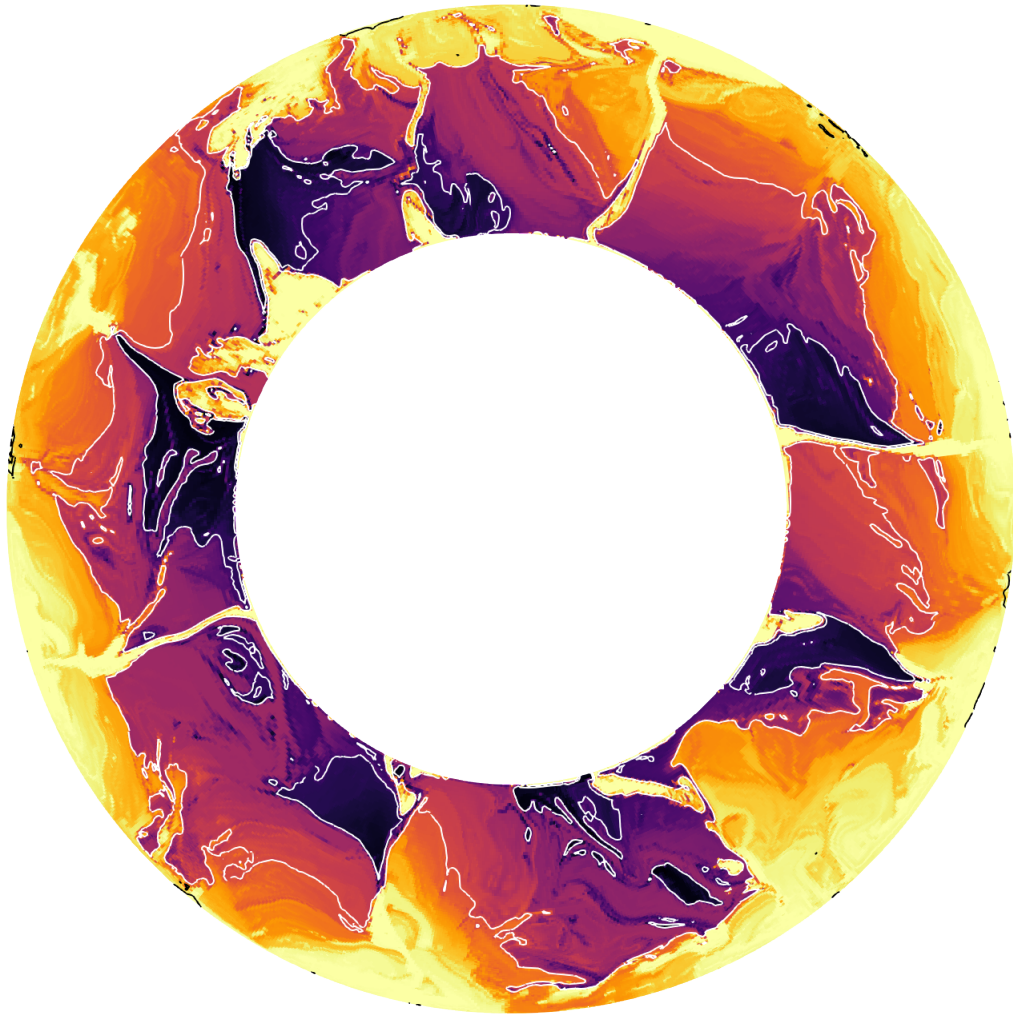# Self-Consistent Generation of Continents and Their Influence on Global Mantle Dynamics

Charitra Jain

Age of the Earth after 2.5 billion years of thermo-chemical evolution shown in 2D spherical annulus geometry. Older material is represented by darker colours with mantle regions having the same age: 1 Ga or 2 Ga (white contours) and Archean continental crust (black countour).

Diss. ETH No. 24953

SELF-CONSISTENT GENERATION OF CONTINENTS AND THEIR INFLUENCE ON GLOBAL MANTLE DYNAMICS

A thesis submitted to attain the degree of

DOCTOR OF SCIENCES of ETH ZURICH

(Dr sc. ETH Zurich)

presented by

CHARITRA JAIN

MSc in Applied Geophysics, TU Delft, ETH Zurich, RWTH Aachen

born on *11.01.1989*

citizen of *India*

accepted on the recommendation of

Prof. Dr. Paul Tackley, ETH Zurich, Switzerland (examiner)

Prof. Dr. Taras Gerya, ETH Zurich, Switzerland (co-examiner)

Dr. Antoine Rozel, ETH Zurich, Switzerland (co-examiner)

Prof. Jeroen van Hunen, Durham University, United Kingdom (co-examiner)

2018

Abstract

A reasonable model for Earth's origins and its internal workings exists on the basis of tested theories, natural data, geophysical and -chemical investigations, modelling and high-pressure experiments. Nonetheless, many fundamental questions driving Earth sciences remain unresolved. Considering that most of the Earth is inaccessible to direct measurements and there is a paucity of natural evidence from its early stages of formation, geodynamic modelling efforts have become essential to further our understanding of planetary evolution. In this thesis, with the help of the mantle convection code StagYY, I have worked on the following two themes: (i) identifying the qualitative and quantitative correlation between continents and elevated temperatures in the mantle, and (ii) creating continental crust in global models in a self-consistent manner.

Continents are the landmasses that cover about a third of the planet's surface and float atop the convecting mantle. It has been suggested that the compositionally evolved continental crust at the top and the melt-depleted cratonic roots underneath it evolved simultaneously during Earth's early history and have survived for billions of years. The existence of dynamic feedback between mantle convection and continents is indisputable and is evident from numerical and analogue modelling done previously. Continents have been shown to affect mantle's convective wavelength, however, whether they insulate the underlying mantle or not remains a matter of debate. In Chapter 3, I provide qualitative observations on the nature of this correlation by conducting a systematic parameter study in 2D global models with mobile (and prescribed) continents. The results of my models show that downwellings bring cold material down into the mantle along continental margins and thermal anomalies are pronounced underneath the continents. Spectral decomposition of temperature and composition fields output by these models gives the dominant degree and amplitude of this correlation. The dominant degree of correlation is shown to evolve with time and continental configuration. Using analytical scaling laws, it is quantitatively shown that correlation decreases with increasing core temperature, number of continents, internal heating, and Rayleigh number. Additionally, the results show for the first time, that melting-induced crustal

production (MCP) events resulting from this correlation tend to break the continents apart, thereby destroying the correlation and acting as a negative feedback.

In Chapter 2, I developed a new melting parameterisation that has the capability to create continental crust self-consistently. It is a two-step differentiation process to generate continental crust. The basaltic magma is extracted from the mantle, it gets hydrated, and then partially melts to form felsic crust. Formation of continental crust in global models with material recycling and secular cooling of the mantle has never been attempted before.

In Chapter 4, I use this newly developed parameterisation to generate primordial continental crust and investigate the global geodynamic regime of early Earth. It is often accepted that subduction zones and intra-plate tectonic settings are the loci of present-day continental crust formation. However, the majority of continental crust from the Archean Eon (4.0-2.5 Ga) was made of Tonalite-Trondhjemite-Granodiorite (TTG) rocks and it was formed in a tectonic regime that still remains an enigma. Parameters such as core temperature, internal friction coefficient, and the ratio of intrusive (plutonism) and eruptive (volcanism) magmatism are varied systematically in global models with radiogenic heat production and core cooling. The results from my simulations and analytical scaling laws show two distinct stages of TTG production: a period of continuous linear growth with time and intense recycling similar to 'plume-lid' tectonics that lasts until 1 billion years, followed by a stage with the TTG growth proportional to cubic root of time and moderate recycling.

Most importantly and surprisingly, my results show that a drop in TTG production can happen without a major shift in the global geodynamic regime. This is in contradiction with previous suggestions that subduction and onset of plate tectonics were required to explain the decline of continental crust growth around 3.5 Ga.

Overall, this work demonstrates the important coupling between continents and mantle dynamics, improves our understanding of early terrestrial planetary evolution, and offers a state-of-the-art melting parameterisation to generate continents.

Kurzfassung

Das derzeitige Modell zur Entstehung und internen Funktionsweise der Erde beruht auf überprüften Theorien, geophysikalischen und -chemischen Messungen, Modellierung und Hochdruckexperimenten. Trotz dieser vielfältigen Informationen sind noch viele fundamentale Fragen der Erdwissenschaften ungelöst. Da der grösste Teil der Erde direkten Messungen unzugänglich ist und es sehr wenige Daten von der frühen Phase der Erdentstehung gibt, hat sich die geodynamische Modellierung als essentielle Methode zum Verständnis der Planetevolution herausgebildet. In dieser Arbeit stelle ich die Ergebnisse meines Doktorats vor, in dem ich mit Hilfe des Mantelkonvektion-Computercodes StagYY an folgenden zwei Themenbereichen gearbeitet habe: (i) Die Identifizierung und quantitative Korrelation zwischen Kontinenten und erhöhten Temperaturen im Mantel, und (ii) die eigenständige Bildung von kontinentaler Kruste in globalen Computermodellen.

Kontinente sind Landmassen die circa ein Drittel der Planetenoberfläche bedecken und auf dem konvektierenden Mantel treiben. Es wurde vorgeschlagen, dass die kontinentale Kruste oberhalb und die schmelzarmen, kratonischen Wurzeln darunter gleichzeitig während der erdgeschichtlich frühen Ergeschichte entstanden sind und seitdem für Milliarden Jahre erhalten blieben. Die Existenz von dynamischen Rück-kopplungsprozessen zwischen Mantel und Kontinenten ist unstrittig und hinreichend durch numerische und analoge Modelle belegt. Darin hat sich gezeigt, dass Konti-nente die konvektive Wellenlänge des Mantels beeinflussen können. Jedoch ist derzeit noch unklar ob Kontinente den darunter liegenden Mantel isolieren oder nicht. In Kapitel 3 stelle ich qualitative Beobachtungen zur Ursache dieser Korrelation mittels einer systematischen Studie in globalen, zweidimensionalen Modellen mit mobilen (und vordefinierten) Kontinenten dar. Die Resultate meiner Modelle zeigen, dass absinkendes, kaltes Material an kontinentalen Rändern nach unten in den Mantel befördert wird und thermale Anomalien unterhalb der Kontinente stärker hervortreten. Eine spektrale Dekomposition der Temperatur und chemischen Zusammensetzung der Modelle liefern den dominanten Grad und die Amplitude der Korrelation zwischen Anomalien und Kontinenten. Der bevorzugte Grad der Korrelation verändert sich mit der Zeit und

kontinentaler Konfiguration. Mittels analytischer Skalierungsgesetze zeige ich quantitativ, dass sich die genannte Korrelation mit ansteigender Kerntemperatur, Anzahl der Kontinente, interner Wärmeentwicklung und Rayleighzahl verringert. Zusätzlich zeigen diese Resultate zum ersten Mal, dass Schmelz-induzierte Krustenentstehung dazu tendiert die Kontinente aufzubrechen und dadurch die Korrelation durch eine negativen Rückkopplung zerstören.

In Kapitel 2 dieser Arbeit entwickle ich eine neue Parametrisierung zur Aufschmelzung von Erdmantelgestein. Diese generiert in eigenständiger Weise kontinentale Kruste durch einen zweistufigen Differenzierungsprozess: Zuerst wird basaltisches Magma vom Erdmantel extrahiert, welches hydriert und unter günstigen Bedingungen erneut partiell schmilzt und dabei bei Abkühlung felsische Kruste formt. Diese Art von Generierung kontinentaler Kruste inklusive Subduktion und potentiell erneutem Aufschmelzen, also einem Recyclingprozess, hat es in globalen Modellierungen bisher noch nicht gegeben.

In Kapitel 4 wende ich die neu entwickelte Parametrisierung an, um primitive kontinentale Kruste zu bilden und ihren EInfluss auf das globale geodynamische Regime der frühen Erde zu untersuchen. Häufig wird angenommen, dass Subduktionszonen und Gebiete innerhalb einer Erdplatte die Orte sind, wo gegenwärtig kontinentale Kruste gebildet wird. Jedoch bestand der Grossteil der kontinentalen Kruste aus dem Archaikum, genauer dem Äon (4.0-2.5 Jahre seit Entstehung der Erde) aus Tonalit-Trondhjemit-Granodiorit, der in einem bisher noch nicht identifizierten tektonischen Regime entstand. Parameter wie die Temperatur des Erdkerns, das Verhältnis von intrusivem (Plutonismus) zu extrusivem (Vulkanismus) Magmatismus und den internen Reibungskoeffizienten variiere ich systematisch. Diese globalen Modelle beinhalten ausserdem eine zeitabhängige radiogene Wärmeproduktion und Abkühlung des Erdkerns. Die Ergebnisse meiner Simulationen und Skalierungsgesetze zeigen zwei eindeutige Phasen der TTG-Produktion. Die Erste ist eine Periode kontinuierlicher, linearer Zunahme von TTG und intensivem Recycling, ähnlich dem 'Plume-lid'-Regime, welche bis zu einer Milliarde nach Erdentstehung andauert. Diese wird von einer zweiten Phase abgelöst, welche von TTG Wachstum, proportional zur dritten Wurzel der Zeit, sowie moderatem Recycling gekennzeichnet ist.

Überraschenderweise zeigen unsere Ergebnisse, dass eine Abnahme der TTG-Produktion nicht unbedingt mit einem Wechsel des geodynamischen Regimes zusammenhängt. Diese Erkenntnis ist besonders wichtig, da vorherige Studien vorgeschlagen hatten, dass Subduktion und der Beginn der Plattentektonik vonnöten waren, um den

Produktionsrückgang kontinentaler Kruste nach ca. 3.5 Milliarden Jahren Erdgeschichte zu erklären.

Zusammengenommen zeigt meine Arbeit, wie wichtig die Kopplung von Kontinenten und Erdmanteldynamik ist, verbessert das Verständnis der frühen Entstehung von terrestrischen Planeten und ermöglicht die Anwendung einer neuartigen, modernen Parametrisierung des Aufschmelzvorgangs im Erdmantel, welche auf eigenständige Weise Kontinente generiert.

Table of contents

List of figures

List of tables

Chapter 1

Introduction

About 4.55 billion years ago, our planet Earth accreted from the solar nebula [*Patterson*, 1956]. It is believed that Earth underwent a magma ocean stage in its early history and later on crystallised to become the rocky planet as we know today [*Abe*, 1993a,b, 1997; *Elkins-Tanton*, 2012]. Its distance from the Sun and the amount of radiant energy it receives from its star allow the liquid water to exist on the planet's surface and deem it habitable [*Huang*, 1959; *Rasool and de Bergh*, 1970; *Kasting et al.*, 1988]. It is the only planet in the solar system that exhibits plate tectonics and sustains life. Even though most of Earth is inaccessible, many disciplines of Earth sciences have shown that the surface expressions such as the continents, the volcanoes, the mountains, the ocean basins are linked with the planet's interior. Therefore, understanding the coupled thermo-chemical evolution of the deep interior and the surface over time is imperative.

In this chapter, the concepts of mantle convection, continental drift, and plate tectonics are introduced. Following that, a literature review of the continents detailing their structure, petrology, formation, destruction, age, etc. is presented. Afterwards, the goals and structure of this thesis are defined.

1.1 Mantle convection and continental drift

The idea of a molten, flowing interior beneath the surface had been floating around for several centuries, even garnering the support of James Hutton (1726-1797), the originator of Uniformitarianism theory. He advocated for internal heat being the driving force behind Earth's evolution and argued that the geological processes operating today were also responsible for shaping the Earth in the past [*Schubert et al.*, 2001]. It took another 150 years for the confluence of significant developments in the fields of Earth

sciences, physics, fluid mechanics, and material sciences to decipher what transpires below the surface.

Henri Bénard in 1900 conducted quantitative experiments on the onset of convection in fluids heated from below and highlighted the role of viscosity [*Bénard*, 1900, 1901]. Later on, Lord Rayleigh developed the theory of convective instability in fluids that were heated from below and cooled from above [*Rayleigh*, 1916]. The idea of a thermally convecting fluid interior existed prior to this [*Prout*, 1834; *Fisher*, 1881; *Brown*, 1957] but it was dismissed as the mantle was already known to be solid in the late 19th century.

Realising that the South American east coast fits exceptionally well with the African west coast (see Fig. 1.1), and bolstered by the evidence coming from geological mapping and studies of ancient climates, several scientists proposed the idea of continental drift but only in terms of small vertical displacements relative to the oceans. F. B. Taylor and Alfred Wegener were the pioneering advocates for continental drift with large horizontal displacements. However their proposed mechanisms, tidal and differential centrifugal forces respectively, were considered insufficient to drive the mantle flow and the resulting continental motion [*Taylor*, 1910; *Wegener*, 1915]. Therefore, a mechanism was required that could operate in the solid, crystalline mantle and at the same time be strong enough to influence the surface observations. It was only when the material scientists established the viscoelastic and creep behaviour of solids, thermal convection was accepted as the driving mechanism behind solid mantle flow and the surface processes such as continental drift, volcanism, and seismicity [*Holmes*, 1931, 1933; *Gordon*, 1965]. Thermal convection is a process in which a fluid layer heated from below and cooled from above creates gravitational instabilities where a warm, lighter fluid rises while a cold, denser fluid sinks. It is powered by the secular cooling of the mantle and heat produced by the radioactive decay of the uranium isotopes ^{238}U and ^{235}U, the thorium isotope ^{232}Th, and the potassium isotope ^{40}K. For the present-day surface heat flow of the Earth, radiogenic heating is considered to be the dominant contributor (up to 80%) [*Schubert et al.*, 2001]. Dissipation of orbital energy as tidal heat in the interior of a planet or a satellite is another power source for thermal convection. Whilst insignificant on Earth, it is maybe relevant for Jupiter's moon Io [*Peale et al.*, 1979].

Further evidence in favour of continental drift came from the studies of paleo-magnetism and seafloor spreading. During crystallisation, rocks with magnetic and paramagnetic minerals acquire a weak remnant magnetism, thereby preserving the record of Earth's magnetic field orientation from that time. Discrepancies between

Fig. 1.1 Alfred Wegener proposed this reconstruction of pre-Atlantic continental blocks in 1915. From *Wegener* [1915].

the magnetic field orientations from old rocks and present-day field pointed towards continental motion and secular variations in global magnetic field. The hypothesis of seafloor spreading was proposed in the late 1960s following the discovery of oceanic ridges, mid-Atlantic ridge being the prominent one [*Dietz*, 1961; *Hess*, 1962, 1965]. It stated that the magma rising from the mantle creates new oceanic crust at the ridge, which spreads laterally away from the ridge in both directions. It was easy to see the correlation between these spreading ridges and areas of continental breakup. This increase in surface area had to be compensated somewhere. *Hess* [1962] and *Vine and Matthews* [1963] proposed that oceanic crust gets destroyed at ocean trenches. This process was later known as subduction. Ultimately, the concepts of continental drift, seafloor spreading and subduction were unified together as plate tectonics, with Earth being the sole planet in our solar system to exhibit them.

1.2   Plate tectonics

Plate tectonics is a theory where the outer surface of the Earth (lithosphere) is fragmented into a number of mobile plates that drift at a speed of few centimetres per year relative to each other, atop a convecting mantle. Mountains, volcanoes and

earthquakes are found at the boundaries of these plates. The plates are continuously
created at mid-ocean ridges (divergent boundaries) as the ascending hot mantle rock
cools down (Fig. 1.2). The plates move apart and some of them descend into the mantle
and get destroyed at subduction zones (convergent boundaries). The solid-state creep
processes are responsible for the fluid behaviour of the hot, solid mantle on geological
time scales [*Schubert et al.*, 2001]. The three different forces driving plate tectonics
in their decreasing order of relative importance are slab-pull, ridge-push, and basal
traction [*Forsyth and Uyeda*, 1975; *Schubert et al.*, 2001]. Slab-pull is a body force due
to the negative buoyancy of the cold, dense oceanic lithosphere subducting at ocean
trenches. Ridge-push is a body force separating the adjacent ridges apart from the
elevated mid-ocean ridges. Basal traction is the dragging of the overlying plate by the
convecting mantle underneath.
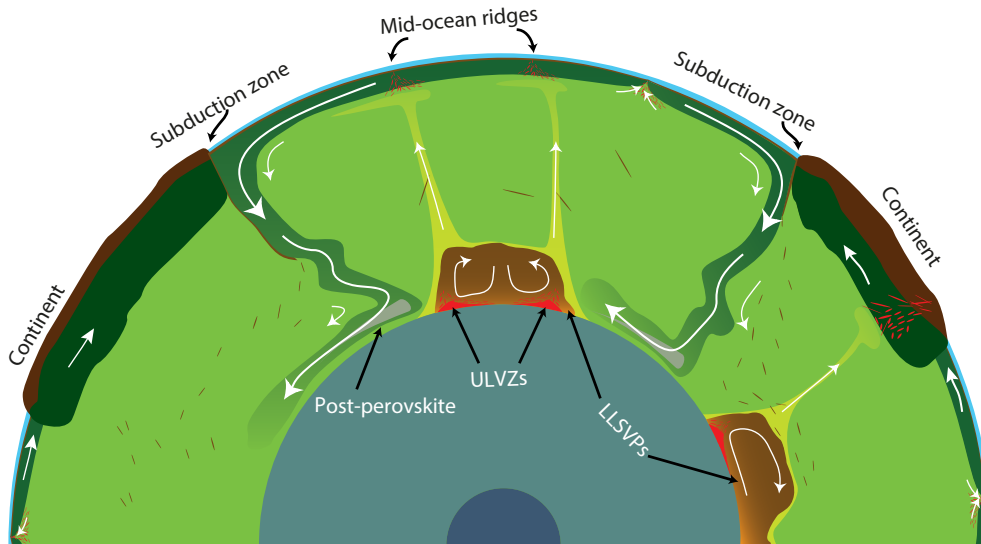
Fig. 1.2 Cartoon model of the mantle with mid-ocean ridges, subduction zones and
continents. Also shown are large low-shear-velocity provinces (LLSVPs) and ultra low
velocity zones (ULVZs) at the core-mantle boundary. Modified from *Labrosse et al.*
[2015].

Plate tectonics is one of the tectonic regimes that can exist on a planetary surface
driven by the thermal convection in its interior. Thanks to the advancements in the
planetary exploration and computing capabilities, we know more about the planets
in the solar system. Several other tectonic regimes have been identified. Stagnant-lid
regime is characterised by little or no surface motion and is active on Mercury, Mars
and the Moon [*Solomatov*, 1995]. Venus experiences episodic resurfacing accompanied
by massive volcanism and is exhibiting an episodic-lid regime [*Moresi and Solomatov*,

1998a; *Rozel*, 2012; *Armann and Tackley*, 2012]. A heat-pipe regime is characterised by extensive surface volcanism with a stagnant lid and is proposed for the surface of Io [*Turcotte*, 1989].

Plate tectonics is considered to play an important role in the evolution of the atmosphere and it may also have implications for origin of life on Earth [*Korenaga*, 2012]. Recent discoveries of Earth-like exoplanets [*Rivera et al.*, 2005; *Borucki et al.*, 2011; *Gillon et al.*, 2017] mean it is relevant that we understand when plate tectonics began on Earth.

1.2.1   When was the onset of plate tectonics?

The debate concerning the inception time of plate tectonics has proven to be quite controversial. Proposed timings range from Neoproterozoic Era (1.0-0.54 Ga) to as far back as the Hadean Eon (4.5-4.0 Ga). Figure 1.3 shows just a sample of a broad spectrum of differing arguments for the onset of plate tectonics. The igneous zircons from Jack Hills, Western Australia that formed > 4 billion years ago make up for a sparse geological record of the early Earth [*Wilde et al.*, 2001]. Based on their geochemical investigations, *Hopkins et al.* [2008, 2010] proposed that these zircons formed in environments that are similar to modern convergent margins. They therefore argued that plate tectonics might have been active during the Hadean Eon (4.5-4.0 Ga). Many authors preferred the Archean Eon (4.0-2.5 Ga) for the onset of plate tectonics as relevant indicators, such as orogens, accretionary prisms, and paired metamorphic belts became more prevalent in the late Archean [e.g., *Komiya et al.*, 1999; *Brown*, 2006; *Cawood et al.*, 2006; *Van Kranendonk et al.*, 2007; *Shirey et al.*, 2008; *Condie and Kröner*, 2008]. Citing the lack of ultrahigh-pressure metamorphism and ophiolites before the Neoproterozoic Era (1.0-0.54 Ga), *Stern* [2005] argued that plate tectonics could not have been operational before 1 Ga. Based on their numerical simulations, *van Hunen and van den Berg* [2008] proposed that the weak lithosphere resulting from hotter Archean conditions [*Jaupart et al.*, 2007; *Herzberg et al.*, 2010] might not allow for subduction, thereby making plate tectonics unviable. This would also the explain the lack of ultrahigh-pressure metamorphism (UHPM) and subsequent exhumation of these rocks.

Dhuime et al. [2017] reported a decline in continental crustal growth since 3 Ga. Interestingly, it has been suggested that Earth might have undergone a major regime transition towards "horizontal tectonics" around the same time, owing to secular cooling and the resulting evolvement of mantle temperature and rheology [e.g., *van Hunen et al.*, 2008; *Sizova et al.*, 2010; *Van Kranendonk*, 2010; *Korenaga*, 2011, 2013; *van*
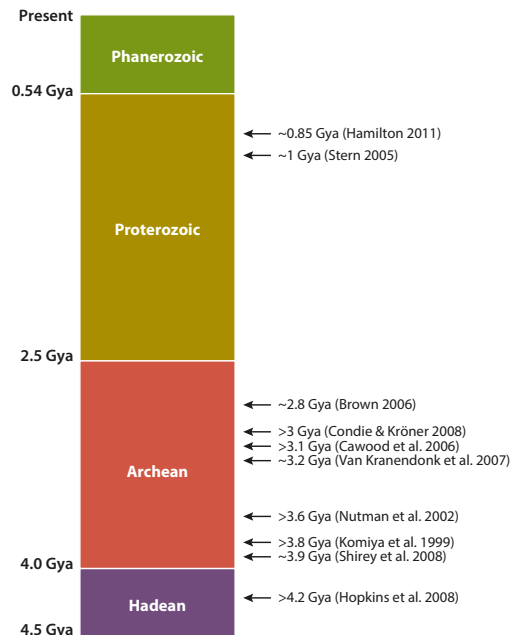
Fig. 1.3 A sample of diverse opinions regarding the onset time of plate tectonics during Earth's evolutionary history. From *Korenaga* [2013].

Hunen and Moyen, 2012; *Debaille et al.*, 2013; *Gerya*, 2014; *Johnson et al.*, 2013a, 2017; *Gerya et al.*, 2015; *Condie et al.*, 2016; *Fischer and Gerya*, 2016; *Van Kranendonk and Kirkland*, 2016; *Rozel et al.*, 2017]. Nevertheless, narrowing down the timing of emergence of plate tectonics on Earth remains an outstanding scientific challenge. More observational constraints need to be obtained and geodynamical modelling should provide further insights.

1.3 Continents

1.3.1 Structure

Floating at the top of the mantle, continents are the landmasses that cover about a third of the Earth's surface area. They have cores of cratonic basements underlying a compositionally evolved continental crust. Continental crust with an average thickness of 40 km [*Rudnick and Gao*, 2003] makes up the upper part of the continental lithosphere ($\sim$ 200-300 km thick) and it is less dense, older, and more silicic in composition compared to the basaltic oceanic crust. Unlike ephemeral oceanic basins, which have a life span of < 200 Myr, continents have survived for billions of years. Their relative stability compared to oceanic basins is attributed to the subcontinental lithospheric mantle's

(SCLM) compositional buoyancy (consists of low-density, melt-depleted peridotite or forsterite-rich olivine), viscous rheology (anhydrous or low-volatile content) and higher yield stress [e.g., *Jordan*, 1978; *Pollack*, 1986; *Jordan*, 1988; *Hirth and Kohlstedt*, 1996; *Lenardic and Moresi*, 1999; *Lenardic et al.*, 2003; *Kelly et al.*, 2003; *Lee*, 2003; *Sleep*, 2003; *Cooper et al.*, 2004, 2006a; *Lee*, 2006; *Arndt et al.*, 2009; *Rolf and Tackley*, 2011]. Being cooler than the underlying asthenosphere, SCLM has a negative thermal buoyancy, and for its survival, a compensation in the form of positive compositional buoyancy is required. The peridotite must have high Mg/Fe ratio and/or low amounts of garnet [*Arndt et al.*, 2009]. It is also argued that SCLM's composition is related to the tectonothermal age of the overlying crust. There is evidence that Phanerozoic (0.5-0 Ga) SCLM is more fertile than Archean (4.0-2.5 Ga) SCLM [*Griffin et al.*, 2009].

1.3.2   Composition of subcontinental lithospheric mantle

Subcontinental lithospheric mantle (SCLM) is primarily made of peridotites, which comprise olivine, orthopyroxene, clinopyroxene, and an aluminous phase (spinel at low pressure, garnet at high pressure). Continental peridotites can be classified into fertile pyrolytic (clinopyroxene) and highly melt-depleted harzburgitic (olivine and orthopyroxene) lithologies [*Boyd*, 1987, 1989]. Progressive melt extraction decreases the Al_2O_3, CaO, and Na_2O and increases the magnesium number Mg# (Mg# = atomic Mg/(Mg + Fe) where Fe represents the total iron content) in the residual peridotite. Higher Mg# in Archean peridotites compared to Proterozoic and Phanerozoic peridotites is considered to be a result of secular changes in the average degree of melting [*Griffin et al.*, 2003]. Broadly speaking, lithology fertility increases with depth and highly melt-depleted peridotites are found at depths shallower than ~ 150 km. As density decreases with increasing Mg#, cratonic mantle becomes compositionally buoyant [*Jordan*, 1979; *Lee*, 2003; *Schutt and Lesher*, 2006]. In perfect isopycnic conditions, this will be offset by its negative thermal buoyancy. Cratonic mantle is cooler than the ambient mantle ($\sim 1400\,°$C) by about 500-700$\,°$C and contracts thermally. Garnet-bearing pyroxenites (for example dense eclogite) with varying MgO content are the second most abundant minerals in SCLM [*Taylor and Neal*, 1989; *Beard et al.*, 1996; *Pyle and Haggerty*, 1998; *Barth et al.*, 2001, 2002; *Taylor et al.*, 2003; *Jacob*, 2004; *Horodyskyj et al.*, 2007; *Fung and Haggerty*, 2012]. The presence of water decreases the viscosity of olivine and has an influence on melting [*Hirth and Kohlstedt*, 1996]. Being incompatible with the solids, hydrogen partitions into the melt during partial melting, thereby leaving behind a dehydrated and intrinsically strong peridotite [*Pollack*, 1986; *Hirth et al.*, 2000; *Aubaud et al.*, 2008].

1.3.3 Composition of continental crust

The bulk continental crust is buoyant and is andesitic in composition, lying between basalt and rhyolite in terms of silica content. It is compositionally evolved with 60.6% SiO_2, 4.7% MgO [*Hawkesworth and Kemp*, 2006a] and has a high concentration of incompatible trace elements, thereby acting as a complimentary geochemical reservoir to the Earth's depleted mantle [*Hofmann*, 1988; *Rudnick*, 1995].

   After decades of research on identifying the processes instrumental in forming the continental crust, it has been widely accepted that two stages of differentiation are required to generate continental crust. First, the basaltic magma is extracted from the ambient mantle (pyrolytic). Second, it gets buried and partially melts to form continental crust with the possible help of sedimentary processes [e.g., *Taylor and McLennan*, 1985; *Rudnick*, 1995; *Albarède*, 1998; *Arculus*, 1999; *Rudnick and Gao*, 2003; *Kemp and Hawkesworth*, 2003; *Plank*, 2005; *Hawkesworth and Kemp*, 2006b].

   On modern Earth, one can find basalt along mid-ocean ridge systems, destructive plate margins at island or continental arcs, and in intra-plate settings owing to extensional tectonics, or to plume emplacement [*Rudnick*, 1995]. Out of these three, basaltic rocks from mid-ocean ridge settings are unlikely to contribute significantly to average present-day continental crust. Hence, they have to be sourced from either ocean island basalts (OIB: present-day representative of intra-plate magmas) or primitive island arc basalts (IAB: present-day representative of subduction magmas). Typically, subduction-related basalts have low Nb/La, high Sr/Nd ratios compared to intra-plate magmas. Based on major- and trace-element data (see Fig. 1.4), it is estimated that the composition of new continental crust must lie at the intersection of the differentiation trend between bulk continental crust, upper crust and the lower crust; and the array between basalts generated in intra-plate (OIB) and subduction-related (IAB) settings [*Taylor and McLennan*, 1985; *Sun and McDonough*, 1989; *Rudnick*, 1995; *Arculus*, 1999; *Barth et al.*, 2000; *Hawkesworth and Kemp*, 2006a,b]. It can be proposed that new continental crust is a simple mixture of ∼8% OIB and ∼92% IAB [*Rudnick*, 1995; *Barth et al.*, 2000] but it should be considered with caution. For example, significant crust production during the Archean times happened by the emplacement of tonalite-trondhjemite-granodiorite (TTG) suites. TTGs are thought to be generated by partial melting of hydrated basalts and usually in such processes, low Nb/La ratios are linked with low Ti/Zr ratios. In recent subduction settings, however, there is no Ti fractionation associated with low Nb/La. The important thing is that in the Archean, remelting of rocks generated in intra-plate settings could also have resulted in low Nb/La ratios. This poses a challenge while assessing the contribution of different

tectonic settings towards continental crust formation as they might have changed over time [*Condie*, 1994].
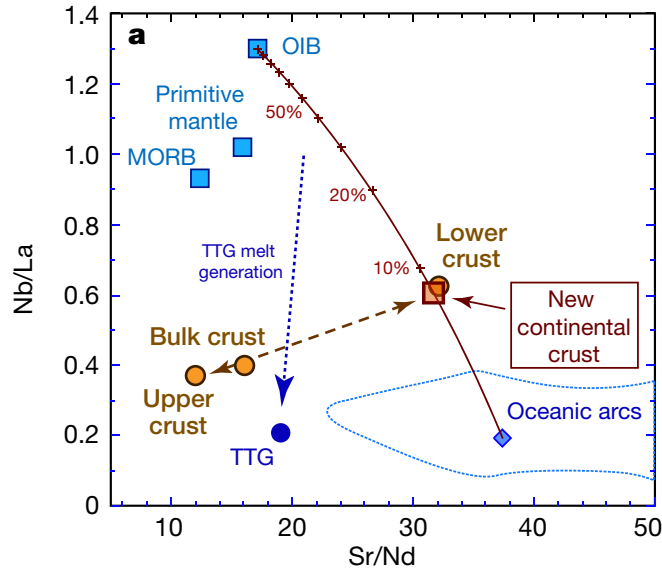
Fig. 1.4 A plot of the trace-element ratios Nb/La versus Sr/Nd, following *Rudnick* [1995] and *Hawkesworth and Kemp* [2006b]. MORB: mid-ocean ridge basalt; OIB: ocean island basalt; and TTG: tonalite-trondhjemite-granodiorite. The dotted blue line illustrates a general model for generating TTG from the remelting of hydrated basalt. From *Hawkesworth and Kemp* [2006a].

Igneous processes differentiate the continental crust resulting in depletion of certain elements. Using the compositions of the model new continental crust (see inset in Fig. 1.4) and the upper continental crust, *Hawkesworth and Kemp* [2006b] calculated this degree of differentiation to be 14%. Considering that the upper crust has an average thickness of 12.5 km [*Rudnick and Gao*, 2003], it would have generated a much thicker layer of residual mafic material underneath it. There is no geophysical evidence from the present day of this layer and therefore it is assumed that a large volume of residual crustal material has delaminated into the mantle [*Kay and Mahlburg-Kay*, 1991, 1993; *Plank and Langmuir*, 1998; *Jull and Kelemen*, 2001; *Kemp and Hawkesworth*, 2003]. The foundering of this residue, which has high Sr/Nd and low Rb/Sr, Sm/Nd, and Th/La ratios [*Kay and Mahlburg-Kay*, 1993; *Rudnick*, 1995; *Ellam and Hawkesworth*, 1988; *Arndt and Goldstein*, 1989; *Plank*, 2005] has made the average continental crust andesitic.

1.3.4 Formation of subcontinental lithospheric mantle

Continents are chemically insulated from the convecting mantle underneath by thick thermal boundary layers, which makes them stable over geological time scales. A decrease in the average degree of melting is observed in the cratonic peridotites with time from Archean to Phanerozoic. The positive compositional buoyancy works to offset the negative thermal buoyancy. Different possible mechanisms for forming SCLM described in *Lee et al.* [2011] with their strengths and weaknesses are outlined here (see Fig. 1.5).
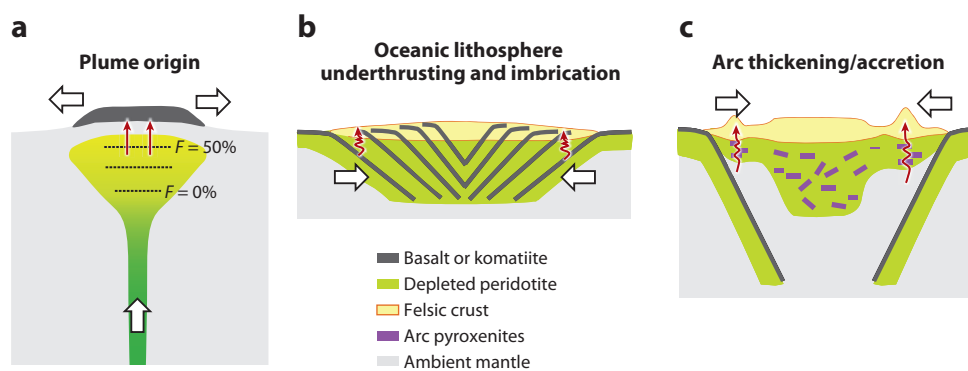
Fig. 1.5 Different mechanisms for making continents. *F* represents the average degree of melting; red and white arrows indicate partial melt extraction and direction of motion respectively. From *Lee et al.* [2011].

1.3.4.1 Plume Origin

High degrees of melting within a large thermal plume can create a melt-depleted, dehydrated, and low-density SCLM, associated with mantle-crustal differentiation processes at the same time [*Herzberg*, 1993; *Griffin et al.*, 2003; *Griffin and O'Reilly*, 2007; *Arndt et al.*, 2009]. A modern analogue to this mechanism is the Ontong Java oceanic plateau. Mantle upwellings during the hotter Archean conditions would be consistent with the inferred episodic age distribution of continents from geochemical data (see Section 1.3.8); however the lack of surviving cratons older than 3.5 Ga is puzzling. The expected secular increase in peridotite fertility with depth and high-degree of melting at a depth of $\sim 200\,\mathrm{km}$ expected from this mechanism is also not reflected in the xenoliths from cratons.

1.3.4.2   Underthrusting and Imbrication of Oceanic Lithosphere

Underthrusting coupled with imbrication of oceanic lithosphere can also create thick continents [e.g., *Helmstaedt and Schulze*, 1989; *Canil*, 2004; *Lee*, 2006; *Simon et al.*, 2007; *Canil*, 2008; *Pearson and Wittig*, 2008]. Although this mechanism can explain the formation of TTGs found in the Archean continental crust by the partial melting of underthrusting oceanic crust, it has its critics. *Arndt et al.* [2009] argued that the negatively buoyant oceanic lithosphere would subduct instead of subcrete. As a counter-argument, the process of plate capture is invoked. During the Cenozoic, the capture of the Farallon oceanic plate beneath western North America could be related to low-angle subduction or subduction of young lithosphere [*Dickinson and Snyder*, 1978; *Saleeby*, 2003; *Luffi et al.*, 2009]. And in the hotter Archean, plate capture might have been facilitated by thick and buoyant oceanic crust. For imbrication of oceanic lithosphere to work, the stable continental lithosphere has to accommodate large-scale weak zones or fault planes that must eventually strengthen with time [*Cooper et al.*, 2006a]. *Lee et al.* [2008] proposed that the serpentinised tops of oceanic mantle may have served as weak zones from mid-Archean to early Proterozoic, thereby providing the favourable conditions for craton formation.

1.3.4.3   Accretion and Orogenic Thickening of Arcs

Şengör et al. [1993] hypothesised that a significant amount of Eurasian continental crust was formed in subduction-accretion setting during the Phanerozoic Eon. First the basaltic island arcs form, and then they accrete and mature into continental arcs. Geological and geochemical evidence has shown the similarities between rocks from ancient continental lithosphere and modern continental arcs, thereby supporting this hypothesis for craton formation also during the Archean. For example, Archean TTGs are geochemically similar to calc-alkaline rocks from the continental arcs [*Chamberlain et al.*, 2003]. High MgO garnet pyroxenites in cratons have similar compositions as garnet bearing mafic residues from the lower crust and mantle of continental arcs [*Ducea and Saleeby*, 1998; *Kay et al.*, 2005; *Lee et al.*, 2006; *Jagoutz et al.*, 2009].

1.3.5   Destruction of subcontinental lithospheric mantle

As discussed in Section 1.3.1, continents do not subduct and survive longer than oceanic lithosphere, but they can also be destroyed and recycled into the convecting mantle. Geophysical evidence, combined with the geochemical studies of the xenoliths and magmas, suggest that continental lithosphere has undergone thinning and removal by

buoyancy forces. Different mechanisms for destroying continents reviewed by *Lee et al.* [2011] are described here (see Fig. 1.6):
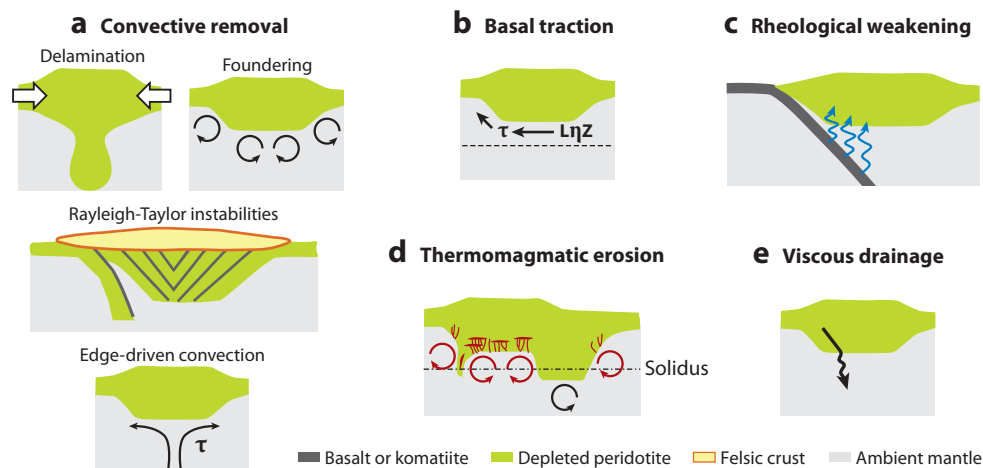
Fig. 1.6 Different mechanisms for destroying or recycling continents. Blue arrows indicate the release of hydrous fluids from a subducting oceanic plate and black-and red-arrowed circles represent small-scale convective overturns. τ represents shear stress. From *Lee et al.* [2011].

1.3.5.1 Convective removal

Convective removal is the removal of continental lithosphere by virtue of thermal or compositional buoyancy forces. Different processes capable of doing so are delamination, foundering, Rayleigh-Taylor instabilities, and edge-driven convection. Delamination (a form of small-scale convection) happens in the dense and cold subcontinental lithospheric mantle and the lower continental crust [*Bird*, 1978, 1979; *Bird and Baumgardner*, 1981; *Schubert et al.*, 2001]. It makes the average continental crust more silicic and also affects the isotopic balance of the mantle. Occurrences of delamination have been proposed in many different tectonic settings and locations around the world. Uplift of the Colorado Plateau [*Bird*, 1979]; collision zones like Wopmay orogen [*Hildebrand and Bowring*, 1999]; high-temperature metamorphism in the Himalayas [*Bird*, 1978; *Houseman et al.*, 1981]; island arcs [*McKenzie and O'nions*, 1983]; Archean North China craton [*Griffin et al.*, 1998; *Gao et al.*, 2002; *Rudnick et al.*, 2004; *Menzies et al.*, 2007] are a few examples. The flux of heat through the lithosphere can drive small-scale convective instabilities like Rayleigh-Taylor instabilities or edge-driven convection in the asthenospheric mantle. They can be instrumental in eroding the lithosphere from the bottom [*Huang et al.*, 2003; *Korenaga and Jordan*, 2003] or the sides [*King*, 2005] and are possibly operating on the edges of the Colorado Plateau.

1.3.5.2   Basal Traction

Basal shear stresses imposed by the mantle flow in the low-viscosity asthenosphere can also erode continental lithosphere. These shear tractions increase with lithospheric thickness and can be invoked for limiting the overall thickness of the craton but not for completely destroying it [*Cooper and Conrad*, 2009].

1.3.5.3   Rheological weakening

Melts or supercritical fluids released from the subducting slabs can rehydrate a lithosphere, thereby weakening it and facilitating its removal. For example, the subducting Farallon plate underneath western North America might have weakened the North American lithosphere [*Humphreys et al.*, 2003; *Lee*, 2005; *Li et al.*, 2008; *Rowe and Lassiter*, 2009; *Smith*, 2010].

1.3.5.4   Thermomagmatic erosion

Diking or porous flow can refertilise the SCLM with Fe or water, provided that enough silicate melts are produced. As a result, SCLM's density and temperature increase while the viscosity decreases, thereby promoting convective removal [*Foley*, 2008]. This mechanism is considered to be more effective underneath thin continents as more head space is available for decompression partial melting.

1.3.5.5   Viscous drainage

Another hypothetical scenario involves removing the inclined garnet pyroxenites from the continental lithosphere over geological time scales. As the garnet pyroxenites are denser and less viscous than the peridotite, *Lee et al.* [2011] suggested that their removal rate would be a function of density contrast, dip angle, and the thickness and viscosity of the pyroxenite layer.

1.3.6   Formation of continental crust

As mentioned in Section 1.3.3, continental crust formation is a two step differentiation process: extraction of basaltic magma from the ambient mantle followed by its partial melting. The bulk crust has an intermediate composition with 60.6% SiO_2, Mg# between 50-56 and is enriched in light rare-earth elements (REE). For the present day, the formation of new continental crust can be attributed to the basaltic magmas derived from convergent margins (IAB) and intra-plate (OIB) settings. However, during the

Archean, primordial continental crust was mostly generated by the emplacement of tonalite-trondhjemite-granodiorite (TTG) suites.

1.3.6.1   Convergent margins (Andesite model)

Taylor [1967, 1977] proposed following the theory of Uniformitarianism, that continents form by accretion of island arcs. This was based on the similarities observed between continental crust's andesitic composition and the andesitic volcanism occurring at convergent margins [*Rudnick*, 1995]. However, this andesite model could not account for the bulk crust Cr and Ni contents, and its Th/U ratio [*Taylor and McLennan*, 1985]. Furthermore, the analysis of zircons (more in Section 1.3.8) indicates that majority of continents probably formed during the Archean times but the andesites were not a common feature of Archean volcanic sequences. *Taylor and McLennan* [1985] revised the earlier proposal and suggested that this model might be valid for post-Archean crustal growth.

Another problem with the andesite model is the basaltic (and not andesitic) nature of magmas produced in intra-oceanic island arcs [*Arculus*, 1981; *Anderson*, 1982a; *Ellam and Hawkesworth*, 1988; *Pearcy et al.*, 1990]. This is consistent with high-pressure melting experiments on mantle peridotite that produced basaltic magmas. Andesitic magmas are more commonly produced in continental arc settings (such as Andes, Cascades).

Several variations of this andesite model have been proposed to overcome the aforementioned pitfalls. One of these suggested that high mantle potential temperature during the Archean might have generated intermediate to silicic melts. These mantle-derived intermediate melts then differentiated to form silicic TTGs that dominate the cratons from that eon [*Martin*, 1986; *Drummond and Defant*, 1990; *Hirose and Kushiro*, 1993]. Alternatively, direct melting of subducted oceanic crust can produce TTGs. The complimentary eclogitic residue would get recycled into the convecting mantle [*Martin*, 1986; *Drummond and Defant*, 1990]. Although with some discrepancies, there is experimental data that supports the formation of TTGs from altered Archean mafic basalts [e.g., *Stern and Wyllie*, 1978; *Rapp et al.*, 1991; *Winther and Newton*, 1991; *Sen and Dunn*, 1994; *Wolf and Wyllie*, 1994].

1.3.6.2   Intra-plate settings

The contribution of processes such as plume-related magmatism (in Archean greenstone belts), basaltic underplating (in flood basalt provinces) and accretion of oceanic plateaus (in Wrangellia terrain) to crustal production is also significant [*Ben-Avraham et al.*,

1981; *Richards et al.*, 1991; *Hill et al.*, 1992; *COX*, 1980; *Coffin and Eldholm*, 1994].
The trace-element characteristics for continental crust are similar to that of magmatic
rocks generated in convergent margin settings with a few exceptions. Continental crust
has lower Sr/Nd and La/Nb ratios than convergent margin magmas [*McDonough*, 1990].
Delamination of plagioclase-free eclogite mineralogy (or preferential Sr recycling) from
the lower crust can only account for the Sr/Nd ratio discrepancy [*Gao et al.*, 1992;
Rudnick and Fountain, 1995; *Hans Wedepohl*, 1995]. The deviation in La/Nb ratio of
continental crust may be solved if the crustal growth were to represent a mixture of
magmatism from convergent margins and intra-plate settings, with former being the
dominating setting.

1.3.6.3   Continental delamination

Though invoked initially to explain the uplift of the Colorado Plateau [*Bird*, 1979]
and the high-temperature metamorphism in the Himalayas [*Bird*, 1978; *Houseman
et al.*, 1981]; the process of delamination has also been shown to account for the
intermediate composition of the continental crust. The high-density lower continental
crust (mafic/ultramafic) delaminates as it is underlain by a less dense and depleted
peridotitic mantle. The lower crust's high density can be ascribed either to the
accumulation of iron-rich ultramafic crystals from fractionating basaltic magmas at
the base of the crust, or to the conversion of mafic lithologies to denser eclogite [*Arndt
and Goldstein*, 1989; *Kay and Mahlburg-Kay*, 1991; *Nelson*, 1991]. It is proposed that
lithospheric thickening (occurring at continental-scale collisions) plays an important role
in delamination [*Kay and Mahlburg-Kay*, 1991; *Houseman et al.*, 1981]. Lithosphere
thickening helps with eclogite formation and pushes the cold, dense lithospheric
mantle into the hot, buoyant asthenospheric mantle. It is worth noting that the
positive compositional buoyancy of fertile, asthenospheric peridotite may counteract this
negative thermal buoyancy. *Kay and Mahlburg-Kay* [1993] suggested that delamination
of the lower crust caused the temporal change in the composition of magmatism below
southern Puna plateau in Argentina.

1.3.6.4   Preferential Mg recycling

Preferential recycling of Mg from continents to mantle also helps in the composition
of continental crust to evolve from basaltic to andesitic, but it is not the primary
process behind it. Chemical weathering of igneous rocks results in the loss and eventual
precipitation of MgO and CaO as carbonates, and Na_2O as evaporites [*Garrels and
Mackenzie*, 1971; *Goldschmidt*, 1958]. Though a major portion of MgO is fixed in the

oceanic crust through hydrothermal exchange with Ca at mid-oceanic ridge spreading centres. The altered oceanic crust subducts, recycling the Mg back into the mantle [*Holland*, 1984].

1.3.7 Tonalite-Trondhjemite-Granodiorite (TTG)

A large portion of the Archean continental crust is made of grey gneiss complexes, among which a group of sodic granitoids collectively known as Tonalite-Trondhjemite-Granodiorite (TTG) is the main lithological component [*Jahn et al.*, 1981; *Drummond and Defant*, 1990; *Martin*, 1994]. There are also potassic granitoids with a higher concentration of large-ion lithophile elements (LILE) compared to the sodic ones. TTGs are silica-rich ($SiO_2 \sim 64\%$) and sodic ($3\,wt\% < Na_2O < 7\,wt\%$) and their trace element patterns are similar to calc-alkaline arc rocks. TTGs are formed when hydrated basalt melts at garnet-amphibolite, granulite or eclogite facies conditions [e.g., *Barker and Arth*, 1976; *Condie*, 1986; *Foley et al.*, 2002; *Jahn et al.*, 1981; *Martin*, 1986; *Moyen and Stevens*, 2006; *Rapp et al.*, 1991; *Springer and Seck*, 1997]. Sourced from a similar composition but melted over a range of pressures (different depths), Archean sodic TTGs have been classified by *Moyen* [2011] into three different types: low-pressure (10-12 kbar), medium-pressure (ca. 15 kbar), and high-pressure (20 kbar or higher) TTGs, which account for 20%, 60% and 20% of the sodic TTGs respectively.

TTGs form at very different geothermal gradients as the mafic lithologies melt between 700-1000 °C with little dependence on pressure. These geothermal gradients ascribe to different tectonic settings and their modern analogs on Earth as outlined by *Moyen* [2011] are shown in Fig. 1.7. The high-pressure group forms at cold geotherms ($< 10\,°C/km$) which is marginally hotter than the modern-day subduction zones (5-8 °C/km on average) [*Peacock and Wang*, 1999; *van Keken et al.*, 2002; *Peacock et al.*, 2005]. Archean mantle was hotter and hot subductions might have existed then; however it is also argued that the Archean TTGs did not form by subduction [*Johnson et al.*, 2017]. A hot geotherm (20-30 °C/km) for the low-pressure group is consistent with orogenic collapse, or intra-plate situations like plume magmatism below oceanic plateaus (e.g. Iceland) [*Willbold et al.*, 2009]. Geotherms associated with the medium-pressure group (12-20 °C/km) are consistent with either a hot subduction during the Archean, or continental collisions. Similar P-T conditions have been reported for Barberton Greenstone Belt of South Africa [*Moyen et al.*, 2006; *Stevens and Moyen*, 2007; *Lana et al.*, 2010], Bundelkhand craton of India [*Saha et al.*, 2010], and the Baltic shield [*Volodichev et al.*, 2004]. *Kisters et al.* [2003] proposed that thickening of crust

after an orogenic collapse and the subsequent delamination of the lower crust into the mantle could result in similar geotherms.
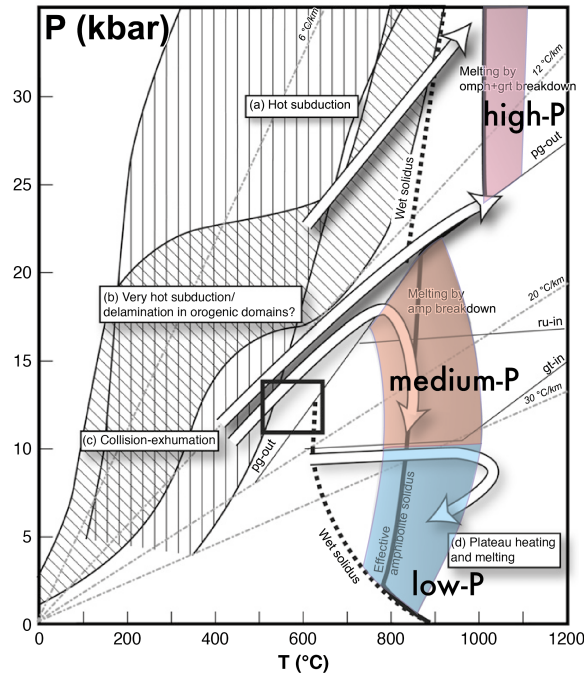
Fig. 1.7 P-T diagram showing the melting conditions of the three sodic TTG groups and their corresponding geotherms. Modified from *Moyen* [2011].

1.3.8 Age of the continents

Zircons are accessory minerals that are ubiquitous in the Earth's crust. They crystallise from medium- to high-silica magmas and their ability to survive intense metamorphism make them an ideal candidate to study the geological history of the continental crust [*Vervoort et al.*, 1996; *Amelin et al.*, 1999; *Bodet and Schärer*, 2000; *Valley et al.*, 2005]. They can be dated using the U-Pb isotopes [*Ireland and Williams*, 2003], and allow for the analyses of Hf- and O- isotopic systems [*Valley et al.*, 1994, 2005].

Hf isotopes give the model age of crust formation as they indicate the magma source (mantle or pre-existing crust) from which the zircon crystallised and also the time at which the source separated from the mantle [e.g., *DePaolo*, 1981; *Vervoort et al.*, 1996; *Amelin et al.*, 1999; *Bodet and Schärer*, 2000; *Knudsen et al.*, 2001; *Griffin et al.*, 2004; *Condie et al.*, 2005; *Hawkesworth and Kemp*, 2006c; *Kemp et al.*, 2006; *Dhuime et al.*, 2011, 2012]. However, if the crustal material contains older reworked material in addition to the juvenile material, then these crust formation ages may not

represent the actual crust forming event [*Arndt and Goldstein*, 1987]. The resulting uncertainties in continental growth curve can be avoided by combining stable O isotopes with radiogenic U-Pb and Lu-Hf isotopes [*Kemp et al.*, 2006; *Hawkesworth and Kemp*, 2006c]. Oxygen isotopes are helpful in identifying the individual contributions of igneous and sedimentary source rocks towards the magmas from which zircons are crystallised. Typically, zircons have a narrow range of $^{18}O/^{16}O$ ($\delta^{18}O = 5.3 \pm 0.6\%$ per mil) and when these $\delta^{18}O$ values are higher or lower than normal, it signals the presence of a sedimentary or hydrothermally altered parent magma [*Valley et al.*, 1994, 1998, 2005]. Such zircons yield hybrid ages and do not record the true period of crustal growth.

Analysis of U-Pb isotopic system in the zircons shows a multimodal age distribution for the continental crust with peaks around 3.0, 2.7, 2.1, 1.7-1.8, and 1.1 Ga as seen in Figure 1.8 [*Condie et al.*, 2009; *Hawkesworth and Kemp*, 2006a]. These peaks represent periods that span several hundred million years. These periods might have witnessed accelerated crustal production, hinting towards an episodicity in continent formation and destruction. Alternatively, these peaks could also be a reflection of the preservation history of the rocks.

Age distribution of the underlying mantle is inferred using Re-Os isotopic system with visible peaks at 2.7 ± 0.3 Ga, and between 1.0 and 2.0 Ga [*Carlson et al.*, 2005]. During melting, the parent isotope ^{187}Re prefers to partition into the melt while the daughter isotope ^{187}Os is compatible in the solid phase. A model age of separation from the convecting mantle can be inferred from the $^{187}Os/^{188}Os$ recorded in the residue [e.g., *Walker et al.*, 1989; *Pearson et al.*, 1995b,a; *Reisberg and Lorand*, 1995; *Handler et al.*, 1997; *Shirey and Walker*, 1998; *Chesley et al.*, 1999]. It appears that formation of continental crust and subcontinental lithospheric mantle was episodic, and they might have evolved simultaneously with some margin for error [*Lee et al.*, 2011].

1.3.9 Continental growth: continuous or episodic?

Continental crustal growth takes into account the new volume being created as well as the amount recycled into the mantle over time. In Fig. 1.9, *Cawood et al.* [2013] show a range of continental crustal growth models developed on the basis of age distribution and isotopic compositions of rocks. These models fall into two competing camps based on the nature of crustal growth: continuous growth with differing growth rates through Earth history [e.g., *Hurley and Rand*, 1969; *Armstrong*, 1981; *Allègre and Rousseau*, 1984; *Taylor and McLennan*, 1985; *Armstrong*, 1991; *Taylor and McLennan*, 1996; *Belousova et al.*, 2010; *Dhuime et al.*, 2012]; versus episodic growth corresponding to
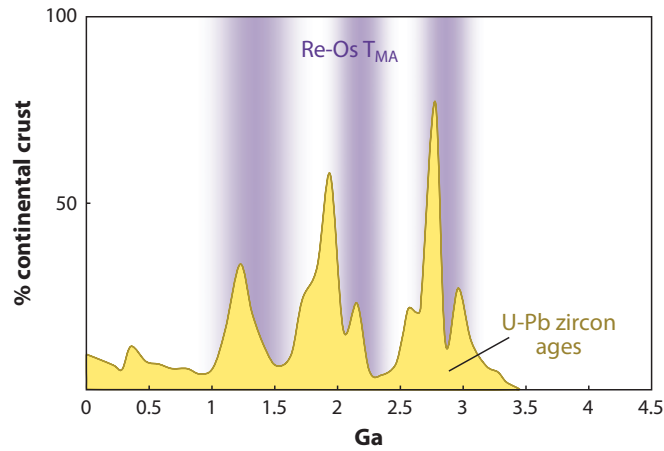
Fig. 1.8 Age distribution for the continental crust and subcontinental lithospheric mantle based on U-Pb [*Hawkesworth and Kemp*, 2006a] and Re-Os model [*Carlson et al.*, 2005] isotopic systems respectively. From *Lee et al.* [2011].

supercontinent cycles or mantle plume activity [e.g., *McCulloch and Bennett*, 1994; *Condie*, 1998, 2000, 2004a; *Rino et al.*, 2004; *Campbell and Allen*, 2008; *Voice et al.*, 2011]. However, some argued that these two groups of models may be reconciled. For example, *Gurnis and Davies* [1986] recognised that the preferential recycling of the elevated younger crust might lead to apparent peaks in continuous crustal growth curves around 2-3 Ga.
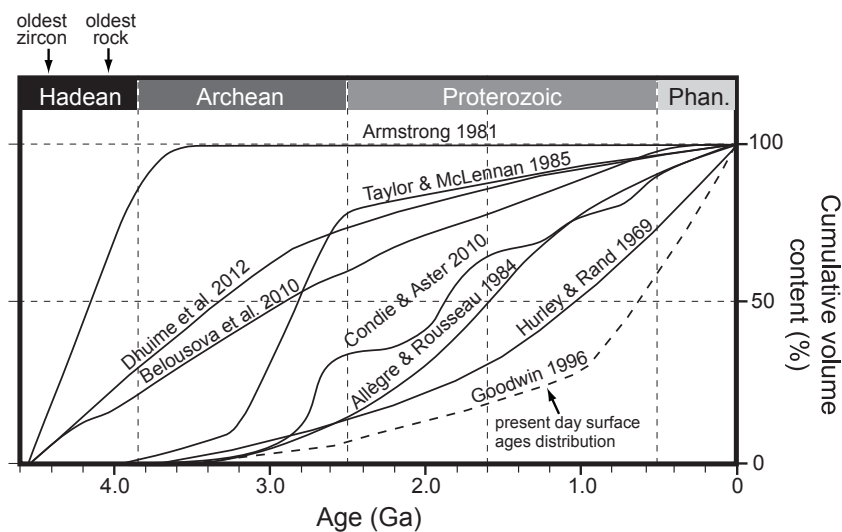
Fig. 1.9 Variety of continental crust growth models. Modified from *Cawood et al.* [2013].

In a recent review on continental growth, *Dhuime et al.* [2017] proposed that 65% of the present continental crust existed by 3 Ga as shown in Figure 1.10. They supported their proposal by presenting similar results from different continental growth models built on records of detrital zircons and sedimentary rocks. As discussed in Section 1.3.8, the authors have used the oxygen isotopes from zircons to adjust for uncertainties in their continental growth curve against the possible crustal reworking and the resulting hybrid ages. Moreover, they argued that there has been a continuous growth of continental crust throughout the evolution of the planet with a significant drop in average production rate from $2.9\text{-}3.4\,\text{km}^3\text{yr}^{-1}$ to $0.6\text{-}0.7\,\text{km}^3\text{yr}^{-1}$ around $\sim 3\,\text{Ga}$. This decrease in production rate has been attributed to higher crustal recycling and the onset of subduction-driven plate tectonics.
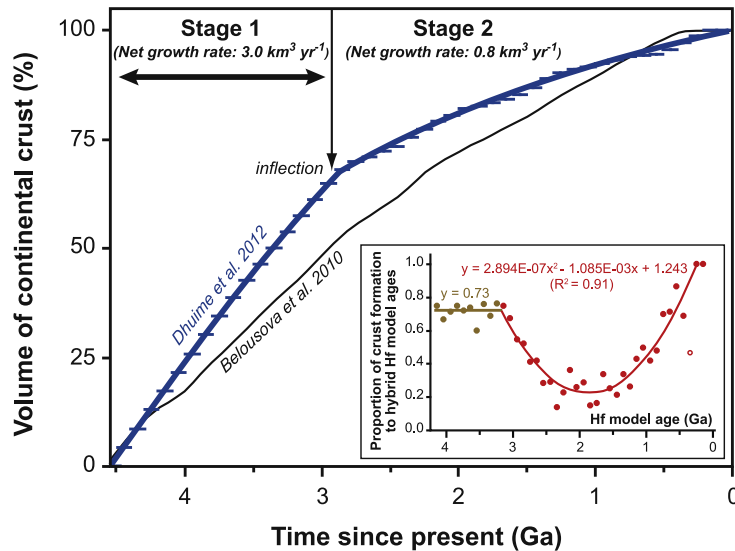
Fig. 1.10 Continental growth models based on the combination of Hf and U-Pb isotopic systems form worldwide zircon datasets. Calculated from a compilation of 6972 zircons from young sediments, the blue curve (*Dhuime et al.* [2012]) has been corrected for 'hybrid' ages using oxygen isotopes. From *Dhuime et al.* [2017].

This period is also marked with a major tectonic regime transition from "vertical tectonics" to "horizontal tectonics" (see Section 1.2.1). Based on the MgO content in the Archean rocks, *Tang et al.* [2016] suggested a gradual shift in the bulk composition of the Archean continental crust from mafic to felsic between 3-2.5 Ga. They hypothesised that this period witnessed an increased water availability from the subducting oceanic crust and might have been the onset of plate tectonics.

1.3.10 Role of continents in thermal insulation

The dynamic feedback between the continents and mantle convection has been well established. Continents influence the mantle's convective wavelength and the heat flow escaping from the planet's surface [e.g., *Gurnis*, 1988; *Zhong and Gurnis*, 1993; *Guillou and Jaupart*, 1995; *Lowman and Gable*, 1999; *Yoshida et al.*, 1999; *Phillips and Bunge*, 2005; *Grigné et al.*, 2007; *Zhong et al.*, 2007; *Zhong and Liu*, 2016]. Over the last decades, several numerical and analytical studies have contributed to the debate about whether the continents can warm up the underlying mantle or not and if they do, then to what extent [*Lenardic and Moresi*, 2001; *Lenardic et al.*, 2005; *Cooper et al.*, 2006b, 2013]? However, a consensus regarding the exact nature and extent of this insulation eludes the scientific community.

Anderson [1982b] proposed that the assembly of Pangea supercontinent during the Mesozoic warmed up the mantle. The resulting extensive volcanism was responsible for the Atlantic-African geoid high. Using convection modelling, *Coltice et al.* [2007, 2009] also argued in the favour of continental-aggregation induced elevated temperatures, producing large scale melting, leading to the emplacement of continental flood basalts of the Central Atlantic Magmatic Province following the breakup of Pangea.

Heron and Lowman [2010, 2011, 2014] highlighted the important role of continental width and convective vigour behind continental insulation in their simulations, albeit with a stationary supercontinent. *O'Neill et al.* [2009] also added to this discussion by considering a mix of basal (from the core) and internal (from the radioactive decay of heat-producing elements) heating in their models. They showed the tendency of cold slabs to subduct along continental margins, while hot plumes rise underneath the continents and warm the subcontinental mantle lithosphere. However, a drop in this warming is observed with strongly temperature-dependent viscosity or when small-scale convection cells develop under large continents. Their models with melting but no crustal production did not show any voluminous volcanism in the subcontinental mantle.

Phillips and Coltice [2010] simulated mobile continents in their models and observed an increase in subcontinental temperature as a function of both continental extent and convective wavelength. However, their study lacked oceanic plates and a temperature-dependent viscosity, which might result in overestimated temperature differences between suboceanic and subcontinental mantle. *Rolf et al.* [2012] showed temperature excesses of up to 140 K underneath the continents compared to the suboceanic mantle in their convection simulations. They considered internally heated 3D models with

different continental configuration and width but omitted basal heating and the effects of mantle plumes in their work.

1.4 Unresolved questions concerning the evolution of our planet

By studying the meteorites and the oldest rock samples from Earth and Moon, mankind has been able to construct a plausible model for Earth's origins and formation. Right after the planetary accretion, the Moon-forming impact around 4.53 Ga melted the Earth's rocky mantle into a global magma ocean [*Stevenson*, 1987; *Canup*, 2004]. Following that, the planet cooled off to become a rocky body while generating heat by radioactive decay of elements. This heat gets transported to the surface primarily by mantle convection and acts as a power source for the geological activity. At some point, the atmosphere and life developed and the Earth evolved to exhibit the plate tectonic regime with continents and oceans. Nevertheless, many fundamental questions driving Earth sciences remain unanswered [*Depaolo et al.*, 2008]. Some of the questions being tackled in this thesis are:

- **Earth's internal workings and continental insulation:** Do continents insulate the underlying mantle and if yes, to what extent? Many authors have presented arguments both in favour and against continental insulation. There is a lack of consensus on this topic (as discussed in Section 1.3.10). What is the heat flow coming from the core-mantle boundary (CMB) and what impact does it have on the insulation [e.g., *Lay et al.*, 2008; *Zhong*, 2006]?

- **Formation of continents:** How did the continents form and remain preserved for billions of years? Did the continental crust and subcontinental lithospheric mantle (SCLM) form around the same time [*Lee et al.*, 2011]? Was the growth of continents an episodic process related to thermal instabilities in the mantle [e.g., *Condie*, 1998, 2000, 2004a]? Or was it a continuous process with a significant drop in crustal growth rate around 3 Ga [*Dhuime et al.*, 2017]? How much of the continental crust has recycled into the mantle [*Spencer et al.*, 2017]?

- **Existence and onset of plate tectonics:** What makes Earth unique such that it is the only planet in the solar system to have plate tectonics? When did plate tectonics start? The proposed timings range from as late as Neoproterozoic Era to as early as the Hadean Eon [*Korenaga*, 2013]. Are continental growth and

plate tectonics related to each other? Did the continents play a role in a regime transition from vertical tectonics to horizontal tectonics around 3 Ga?

1.5   Goals of this thesis

Our comprehension of the inner workings and the surface aspects of Earth comes from tested theories, natural data, geophysical investigations, modelling and high-pressure experiments on materials. While the geophysical observations provide us with a snapshot of present-day Earth's structure, the preserved rocks (geological, geochemical, geochronological and petrological data) shed light on how the planet developed over time [*Gerya*, 2014]. Numerical and analogue modelling are instrumental in validating hypotheses and simulating planetary evolution for a broad range of spatial and time scales. Considering that natural observational constraints are scarce, geodynamical modelling efforts are becoming indispensable to progress our understanding of planetary evolution.

In this thesis, with the help of parameterised mantle convection simulations on a global scale, I have attempted to contribute on the following themes:

- the qualitative as well as quantitative relationship between continents at the surface and temperatures in the underlying subcontinental mantle.

- formation of continental crust in a self-consistent manner

These goals are achieved by conducting systematic studies in a parameter space relevant to the topic, e.g., core-mantle boundary temperature, size and distribution of continents, Rayleigh number, internal heating, eruption efficiency, friction coefficient.

1.6   Thesis structure

The content of this thesis is organised into 3 main chapters, an appendix, and concluding remarks.

Chapter 2.   Methodology. In this chapter, I introduce the computational and theoretical framework of the simulations presented in this thesis. I explain the state-of-the-art developments made to the code to create continents self-consistently. Furthermore, I describe the parameterisation of melt generation and melt extraction processes.

Chapter 3. Quantifying the correlation between mobile continents and elevated temperatures in the mantle. In this chapter, I systematically investigate the effect of continents on subcontinental warming. Results show that this correlation decreases with increasing core temperature, number of continents, internal heating, and Rayleigh numbers. When using more realistic compressible models, the results show that the melting and crustal production events resulting from this correlation tend to break the continents apart, thereby destroying the correlation and acting as a negative feedback. *This chapter has been submitted as: Jain, C., Rozel, A. B., and Tackley P. J. (2018), "Quantifying the correlation between mobile continents and elevated temperatures in the mantle" to Geochemistry, Geophysics, Geosystems.*

Chapter 4. Growing primordial continental crust self-consistently in global mantle convection models. In this chapter, I tackle the second goal of my thesis and present results of self-consistent continent generation by applying the parameterisation developed in Chapter 2. I systematically vary the ratio of intrusive (plutonic) and eruptive (volcanic) magmatism, and parameters such as initial core temperature and internal friction coefficient to investigate the global tectonic regime of early Earth. The results from my simulations and analytical scaling laws show two distinct stages of TTG production: a period of continuous linear growth with time and intense recycling similar to plutonic squishy lid tectonics that lasts until 1 billion years, followed by a stage with the TTG growth proportional to cubic root of time and moderate recycling. I observe this drop in TTG production in our simulations owing to mantle depletion around 3.5 Ga without a major shift in the global geodynamic regime towards subduction and plate tectonics. The crustal volumes obtained from my simulations are in agreement with many continental crust growth models based on geological proxies. This chapter is complemented by Appendix A, which contains solidus and liquidus functions, P-T conditions for TTG formation, and additional figures and tables. *This chapter is under preparation and is to be submitted as Jain, C., Rozel, A. B., Gerya, T., Sanan, P. and Tackley P. J. (2017), "Growing primordial continental crust self-consistently in global mantle convection models" to Gondwana Research.*

Chapter 5. Conclusions and perspectives. In this chapter, I briefly summarise the main findings of this thesis, and provide some future research directions.

Chapter 2

Methodology

The theoretical and computational framework of the simulations presented in this thesis are described in this chapter. The melting parameterisation is explained in detail along with the latest developments implemented to create continents self-consistently.

The thermo-chemical evolution of the compressible mantle is studied for the age of the Earth using the code StagYY [*Tackley*, 2008a]. The numerical model employed here incorporates pressure- and temperature- dependent viscosity, diffusion creep and plasticity, internal and basal heating, core cooling, phase transitions, melting, basaltic and TTG crust production.

2.1 Governing equations

As the solid rocks of the mantle deform as a fluid on geological time scales, the following equations of conservation of mass (continuity equation), momentum (Stokes equation), and energy for a fluid continuum are considered (see *Chandrasekhar* [1961]; *Schubert et al.* [2001] for details).

$$\frac{\partial}{\partial x_j} \left(\rho u_j \right) = 0, \tag{2.1}$$

$$0 = -\frac{\partial P}{\partial x_i} + \frac{\partial}{\partial x_j} \left\{ \eta \left(\frac{\partial u_i}{\partial x_j} + \frac{\partial u_j}{\partial x_i} - \frac{2}{3} \delta_{ij} \frac{\partial u_k}{\partial x_k} \right) \right\} + \rho g_i, \tag{2.2}$$

$$\rho C_P \left(\frac{\partial T}{\partial t} + \mathbf{u} \cdot \bigtriangledown T \right) - \alpha T \left(\mathbf{u} \cdot \bigtriangledown P \right) = \bigtriangledown \cdot \left(k \bigtriangledown T \right) + \frac{\partial u_i}{\partial x_j} \sigma_{ij} + \rho H, \tag{2.3}$$

with density ρ, time t, position x_j $(j = 1, 2, 3)$, viscosity η, velocity component u_j, Kronecker delta δ_{ij}, gravity g, specific heat capacity at constant pressure C_P, thermal expansivity α, pressure P, thermal conductivity k, stress tensor σ_{ij}, and internal heating rate H.

2.1.1 Compressibility and Boussinesq approximation

The increasing pressure with depth compresses the rocks significantly and increases their density by up to 60% at the core-mantle boundary. This can have important geometrical effects on the mantle flow. When considering a compressible fluid, an anelastic approximation is used, in which the density varies with position (usually depth) but not with time. Furthermore, the viscous dissipation (shear heating) and adiabatic heating/cooling terms are included in the energy equation. The depth-dependent physical properties such as thermal conductivity and thermal expansivity are also taken into account [*Ismail-Zadeh and Tackley*, 2009].

For an incompressible fluid, the Boussinesq approximation is used, in which the density is treated as a constant in the continuity and energy equations. And in the momentum equation, density is taken as a variable only in the gravitational (buoyancy) term. There is something analogous in the anelastic approximation - density varies laterally in the buoyancy term [*Ismail-Zadeh and Tackley*, 2009]. Usually, Boussinesq approximation refers to purely thermal convection. However, Boussinesq is extended here by using a composition-dependent density.

2.2 Rheology

Rheology is the study of deformation of a material. In nature, rocks deform by viscous, elastic, and plastic processes [*Gerya*, 2009]. The elastic processes operate on human timescale while the mantle behaves as a highly viscous fluid at geological timescales. Therefore, a visco-plastic rheology is widely used in numerical modelling of geodynamic problems [*Ismail-Zadeh and Tackley*, 2009]. The rocks behave viscously unless they fail in a brittle manner when the yield stress is reached.

At subsolidus temperatures, crystalline solids or rocks deform slowly when a stress is applied. This solid-state, viscous creep deformation occurs due to the motion of atoms and ions associated with crystalline defects such as atomic vacancies and dislocations [*Schubert et al.*, 2001]. The viscous deformation mechanisms can be diffusion creep, dislocation creep, grain boundary sliding, and Peierls creep. At very low stresses, the

solid behaves as a Newtonian fluid by diffusion creep processes. At higher stresses, the dislocations move, and the solid behaves as a non-Newtonian (or nonlinear) fluid. In both of these mechanisms, the viscosity has an exponential dependence on pressure and the inverse absolute temperature (see Eq. 2.4) [*Turcotte and Schubert*, 2014].

This temperature-dependent rheology acts as a regulator for mantle temperature, and it is important in understanding the role of convection in heat transport. An increase in mean mantle temperature reduces the mantle viscosity. As a result, the convective vigour increases and more heat is transported to the surface. Similarly, a decrease in mantle temperature would result in lower heat transport [*Turcotte and Schubert*, 2014]. The mantle viscosity can depend on temperature, pressure, grain size, water or melt content, stress, etc. and is the least well-known parameter used in geodynamic modelling [*Ismail-Zadeh and Tackley*, 2009].

For the simulations presented in this study, only the diffusion creep with homogenous grain size is taken into account and the viscosity η is given by Arrhenius law:

$$\eta(T, P) = \eta_0 \Delta\eta_i \exp\left(\frac{E_i + PV_i}{RT} - \frac{E_i}{RT_0}\right), \tag{2.4}$$

where η_0 is the reference viscosity at zero pressure and reference temperature T_0 (1600 K or 1900 K), $\Delta\eta_i$ is the viscosity jump between the layers i, E_i is the activation energy in the layer i, P is the pressure, V_i is the activation volume in layer i, R is the gas constant and T is the absolute temperature. The activation volume decreases with pressure according to the relation:

$$V(P) = V_i \exp\left(-\frac{P}{P_i}\right). \tag{2.5}$$

Following the viscosity profile expected by the inversion of post-glacial rebound [*Čížková et al.*, 2012], a viscosity jump of 30 is applied at the upper-lower mantle transition.

A strongly temperature-dependent viscosity naturally results in the formation of a stagnant lid [*Solomatov*, 1995]. To break this stagnant lid and obtain Earth-like plate tectonics, plastic yielding is assumed to be the weakening mechanism [*Moresi and Solomatov*, 1998a; *Tackley*, 2000]. The maximum stress that a material can sustain before deforming plastically is given by the yield stress σ_y having both brittle and ductile components:

$$\sigma_\mathrm{y} = \min\left(\sigma_\mathrm{y\_ductile}, \sigma_\mathrm{y\_brittle}\right). \tag{2.6}$$

The ductile yield stress increases linearly with depth d at a rate of $\acute{\sigma_{\mathrm{y}}}$ as:

$$\sigma_{\mathrm{y\_ductile}} = \sigma_{\mathrm{y}}^0 + d \cdot \acute{\sigma_{\mathrm{y}}}, \tag{2.7}$$

where σ_{y}^0 is the yield stress at the oceanic surface. Following *Byerlee* [1978], the brittle yield stress is calculated as:

$$\sigma_{\mathrm{y\_brittle}} = \mu P, \tag{2.8}$$

where μ is the friction coefficient. If the convective stresses exceed the yield stress, the viscosity is reduced to the yielding viscosity $\eta_{\mathrm{y}} = \sigma_{\mathrm{y}}/2\acute{\epsilon}$, where $\dot{\epsilon}$ is the second invariant of the strain-rate tensor. The effective viscosity η_{eff} is then given as:

$$\eta_{\mathrm{eff}} = \left(\frac{1}{\eta} + \frac{2\dot{\epsilon}}{\sigma_{\mathrm{y}}} \right)^{-1}. \tag{2.9}$$

The list of non-dimensional and dimensional parameters used in this thesis vary with the topic being studied, and is therefore presented in the subsequent chapters.

2.3   Computational framework

The equations described in Sections 2.1 and 2.2 are discretised using the code StagYY, which uses a finite difference approximation on a staggered grid [*Harlow and Welch*, 1965]. Pressure is defined at the cell-centre, and the velocities are defined at the centres of faces perpendicular to the relevant velocity components (see Fig. 2.1). A tracer field is advected through the mesh using a second-order spatial interpolation of the velocity field and a fourth-order Runge-Kutta scheme through time [*Rozel et al.*, 2017]. Each tracer carries many quantities such as temperature, composition, water content, concentration of heat-producing element, emplacement, depletion. Tracers can be of three different types: solid, molten, and transport (erupting and intruding). The tracer-to-cell interpolation is done following the tracer-ratio method as described by *Tackley and King* [2003].

A 2D spherical annulus geometry [*Hernlund and Tackley*, 2008] with a radially varying resolution is employed for all the simulations. The resolution is higher at the surface, around the 660 km phase transition, and the core-mantle boundary (CMB). Free-slip boundary conditions are used for the surface and CMB, with surface temperature fixed as 300 K. Based on the analytical models of *Buffett et al.* [1992, 1996] and the parameterisation by *Nakagawa and Tackley* [2004], core-cooling is also included. For an
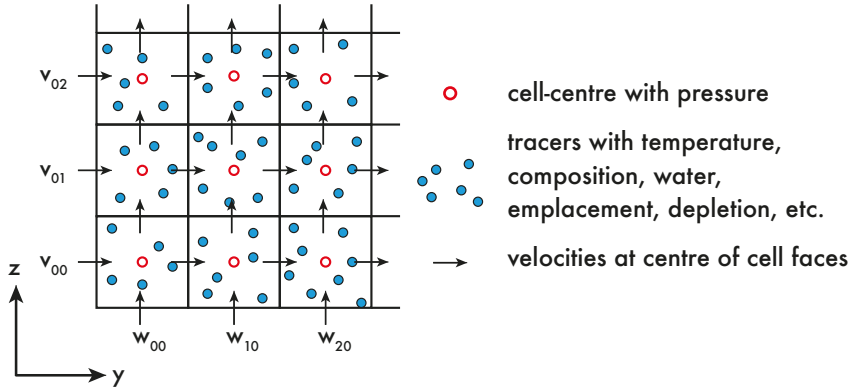
Fig. 2.1 A two-dimensional version of the staggered grid with cells and tracers.

incompressible model setup, a multigrid solver is used to obtain the velocity-pressure solution at each time-step. For the compressible setup, a parallel MUMPS solver available from the PETSc (Portable, Extensible Toolkit for Scientific Computation) package [*Amestoy et al.*, 2000] is used. All simulations were run on two high-performance clusters operated by ETH Zurich, namely BRUTUS (decommissioned in early 2017) and EULER.

2.4 Phase changes and composition

A parameterisation based on mineral physics data [*Irifune and Ringwood*, 1993; *Ono et al.*, 2001] is included in the model, in which the material is divided into olivine, pyroxene-garnet, TTG and melt phase systems. Solid rocks undergo phase transitions as previously considered in *Xie and Tackley* [2004b]; *Nakagawa and Tackley* [2012]. The mixture of minerals depends on the composition, which is mapped linearly into the fraction of different phase systems. Composition can either be in the continuum between *harzburgite (harz)* (75% olivine and 25% pyroxene-garnet) and *basalt (bas)* (100% pyroxene-garnet) or *TTG*. Harzburgite represents the ultramafic and depleted mantle material, basalt corresponds to the mafic igneous rocks, and TTG represents the felsic rocks, which are rich in silica content (Fig. 2.2). Additionally, residue from a global magma ocean can be initialised as *primordial* composition.

The physical properties of olivine and pyroxene-garnet phase systems change with temperature and pressure. Their density profiles are taken from *Nakagawa and Tackley* [2010]. Considering a reference olivine fraction of 0.6, the density profiles for harzburgite and basalt are computed. The mantle is initialised with a pyrolytic composition, which is taken as a petrological mixture of 80% harzburgite and 20% basalt (e.g. as in *Xu et al.*
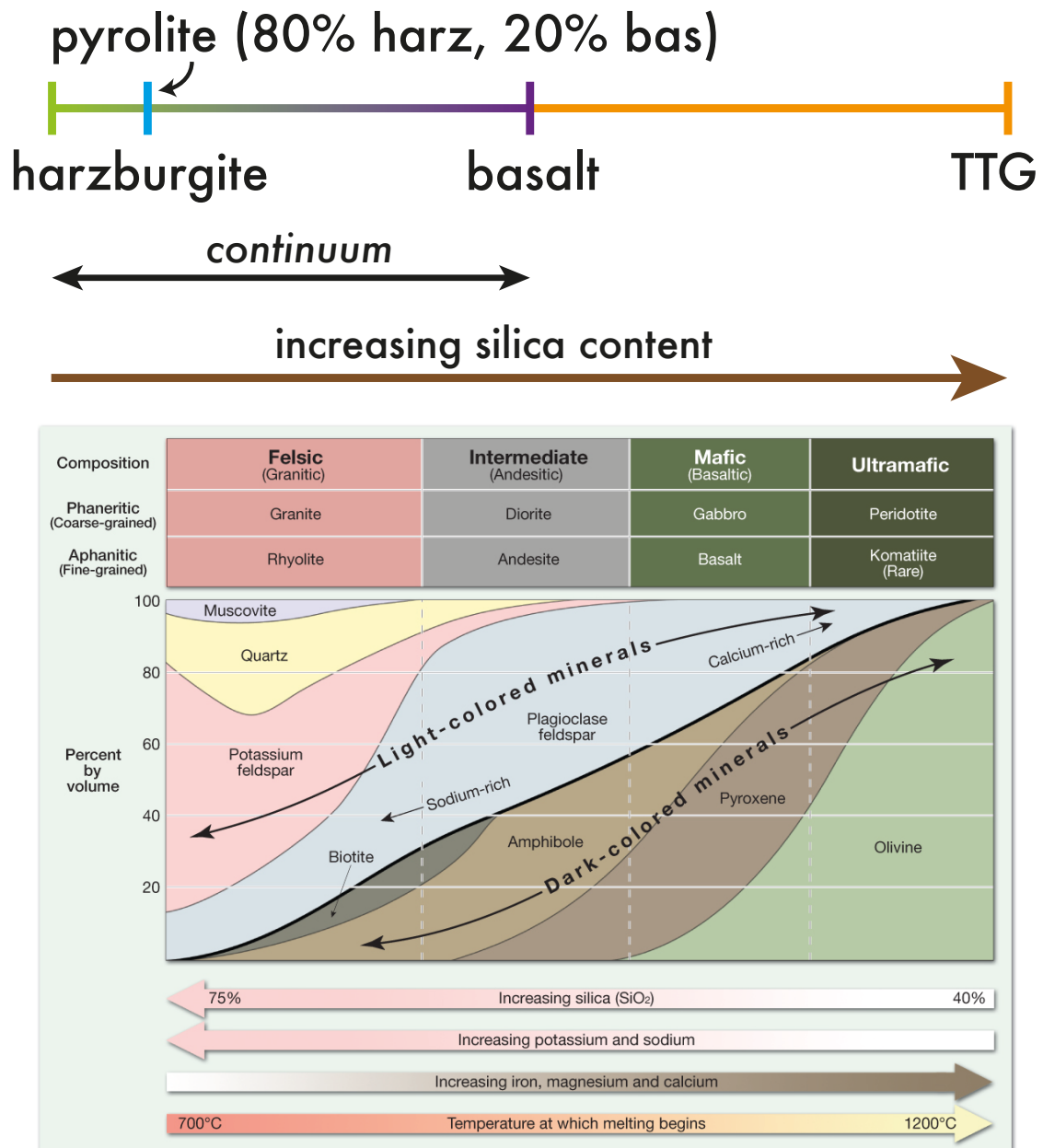
Fig. 2.2 A one-dimensional composition field in StagYY (top) representing the igneous rocks found in nature (bottom) (from *Lutgens and Tarbuck* [2003]).

Table 2.1 Phase change parameters for olivine, pyroxene-garnet, primordial, and TTG systems with surface density at zero pressure ρ_s, density jump across a phase transition $\Delta\rho$, and Clapeyron slope γ.

Depth (km)	Temperature (K)	$\Delta\rho$ (kg/m^3)	γ (MPa/K)
Olivine ($\rho_s = 3240\,\text{kg/m}^3$)			
410	1600	180	2.5
660	1900	400	-2.5
2740	2300	61.6	10
Pyroxene-Garnet ($\rho_s = 3080\,\text{kg/m}^3$) and Primordial ($\rho_s = 3140\,\text{kg/m}^3$)			
60[a]	1000	350	0
400	1600	150	1
720	1900	400	1
2740	2300	61.6	10
TTG ($\rho_s = 2700\,\text{kg/m}^3$)			
290[b]	1713	168	2.26

[a] Eclogite phase transition
[b] Stishovite phase transition

[2008]). For pyrolytic composition, a reference density profile $\rho_{\text{ref-pyr}}$ is calculated after taking the phase transitions into account (see Table 2.1). In addition, a tracer-based density $\rho_{\text{tracer-based}}$ can be computed in each cell by dividing the cumulative mass of tracers m_i present in a cell by its volume V_{cell} (see Eq. 2.10). Based on this density, tracers are vertically redistributed after melt emplacement (more in Section 2.5.6.3).

$$\rho_{\text{tracer-based}} = \frac{\sum_{i=1}^{n\,\text{tracers}} m_i}{V_{\text{cell}}} \tag{2.10}$$

At a depth of 60 km, basalt forms eclogite, which is around 190 kg/m^3 denser than olivine. At lowermost mantle depths, the phase transition to post-perovskite is also considered (e.g. *Tackley et al.* [2013]). Changes in composition arise from melt-induced differentiation and it is discussed in the next section.

2.5 Melting parameterisation

For creating basaltic (oceanic) and TTG (continental) crust, the processes of melt generation and melt extraction are parameterised. A comprehensive explanation of

Table 2.2 Required P (GPa) and T (°C) conditions for TTG formation taken from Figure 12 of *Moyen* [2011]. Low pressure TTGs form at $P < 1$ GPa, while medium pressure TTGs require higher pressures.

Low and medium pressure TTG		
$760 - 60\left(P - 1\right)^2$	$< T <$	$1000 - 150\left(\frac{P-1.2}{1.2}\right)^2$
$-0.5\left(\frac{T-870}{220}\right)$	$< P <$	$1.5 + 0.7\left(\frac{T-700}{200}\right)$
High pressure TTG		
1000	$< T <$	$1100 + 50\left(\frac{P-3.5}{3.5}\right)^2$
$2.35 + 0.15\left(\frac{T-1000}{100}\right)$	$< P <$	5

melting and crustal production is presented in this section. The model used in this study is an extension of the ones previously described by *Xie and Tackley* [2004b]; *Nakagawa et al.* [2010].

2.5.1 Terminology

The term *mixed-material* refers to the rocks lying in the one dimensional harzburgite-basalt continuum. *TTG* crust represents the felsic continental crust. The term *emplacement* means that the melt produced in the mantle has been either erupted at the surface (volcanism) or intruded at the base of the crust (plutonism). The terms *erupta* and *intruda* refer to the masses of molten material that will be erupted and intruded respectively. The term *TTG-formative conditions* refer to the combination of pressure-temperature conditions outlined by *Moyen* [2011] for TTG formation (see Table 2.2) and the availability of water in a cell. For simplicity, water is considered to penetrate fully into the top 10 km and is advected throughout the mantle on tracers.

2.5.2 Melting workflow

The parameterised melting happening at each time-step can be broadly divided into four main processes: determining the amount of melting and freezing (steps 1-3), melt generation (steps 4, 5), melt removal (steps 6, 7), and melt emplacement (steps 8, 9).

1. Solid composition C, melt fraction f and composition-fractions are computed on the mesh from tracers.

2. By comparing cell temperature T_cell to the solidus T_sol of each composition fraction, the cumulative amount of melting $(+\Delta f)$ or freezing $(-\Delta f)$ and the associated change in cell temperature ΔT_cell is calculated to bring the cell back to equilibrium conditions.

3. The total molten mass that is to be removed for subsequent eruption and intrusion is calculated using the current melt fraction and the required melting or freezing. The resulting decrease of rock volume in the cell $\boldsymbol{\Delta V_\text{compaction}}$ owing to melt loss is also computed.

4. Mass is exchanged between solid compositions and melt fractions by creating new molten or solid tracers.

5. The temperature on tracers is adjusted by interpolating the scalar field ΔT to tracer positions.

6. The molten mass that will be erupted and intruded is removed from the cells by creating transport tracers that carry the melt donated by the existing molten tracers.

7. Before any emplacement is done, trace elements are partitioned and outgassed between solid and melt.

8. For every column of the domain, the gaps in the lithosphere are identified where the removed melt will be erupted and intruded. As melt is intruded in the cells, their rock volume $\boldsymbol{\Delta V_\text{dilation}}$ increases. For eruption, a gap is created at the surface by transporting the tracers downwards with the displacement $\boldsymbol{z_\text{compaction}}$ and then transport tracers are placed in this gap as solid tracers. For intrusion, the tracers above the base of crust are moved upwards with displacement $\boldsymbol{z_\text{dilation}}$ to open a gap where the transport tracers are intruded as molten tracers.

9. While employing free-slip boundary condition, some tracers are transported outside the domain while the basaltic melt is removed from the mantle and erupted as less dense TTG crust. This is corrected by vertically redistributing tracers that lie in the top $300\,\text{km}$ and above the surface. Also the tracer-based cell densities are equilibrated by additional compaction or dilation of tracers.

A detailed explanation of these processes follows in the subsequent sections.

2.5.3   Amount of melting $(+\Delta f)$ or freezing $(-\Delta f)$ and composition-fractions in a cell

The solid composition C and melt fraction f are stored as solid and molten tracers respectively. As melting is calculated on a cell level to ensure numerical efficiency, the cell-based solid composition and melt fraction are computed at cell centres using mass averaging of the tracers. At each time-step, melting is done in an iterative manner where the required change in melt fraction Δf_{cell} for every cell is computed by comparing cell temperature T_{cell} with the pressure-dependent pyrolite solidus $T_{\text{sol,pyr}}$. In case the cell temperature exceeds or is lower than the solidus, then either more melt is generated or the existing melt is frozen in the cell to bring T_{cell} back to the solidus. Latent heat of melt is consumed during melting and released during freezing and the resulting change in temperature ΔT_{cell} is computed for each cell.

In the existing implementation, the pyrolite solidus is adapted by the average composition in the cell to give the instantaneous melting temperature T_{melting} as:

$$T_{\text{melting}} = T_{\text{bas-out}} + (T_{\text{sol,pyr}} - T_{\text{bas-out}}) \min\left(\frac{C_{\text{bas}}}{C_{\text{ref-bas}}}, 2\right) \tag{2.11}$$

$$+ \; (T_{\text{liq,pyr}} - T_{\text{bas-out}}) \left(\frac{f_{\text{harz}}}{1 - C_{\text{ref-bas}}}\right), \tag{2.12}$$

with pyrolite solidus $T_{\text{sol,pyr}}$, pyrolite liquidus $T_{\text{liq,pyr}}$, basalt fraction in the solid C_{bas}, reference basalt fraction in the solid $C_{\text{ref-bas}} = 0.2$, and fraction of harzburgite in the melt f_{harz}. $T_{\text{bas-out}}$ is calculated as:

$$T_{\text{bas-out}} = T_{\text{sol,pyr}} + C_{\text{ref-bas}} \left(T_{\text{liq,pyr}} - T_{\text{sol,pyr}}\right). \tag{2.13}$$

The instantaneous melting temperature T_{melting} increases linearly with melt fraction f from 0 to $T_{\text{basalt-out}}$. Once basalt is exhausted, T_{melting} increases linearly with harzburgite fraction in the melt f_{harz} up to $T_{\text{liq,pyr}}$. As shown above, the instantaneous melting temperature T_{melting} is composition-dependent, and therefore depends on the amount of melt being produced. Hence, computing the variation of melt fraction in a cell for mantle material in the harzburgite-basalt continuum is difficult. In this case, a first order extrapolation of the melting temperature in the melt fraction space is considered:

$$T_{\text{melting}}(f_0 + \Delta f) = T_{\text{melting}}(f_0) + \Delta f \left.\frac{\partial T_{\text{melting}}}{\partial f}\right|_{f_0}, \tag{2.14}$$

where f_0 is the initial (basaltic/harzburgitic) melt fraction in the cell. The composition-dependence of the instantaneous melting temperature $\partial T_{\text{melting}}/\partial f$ is estimated by imposing a very small Δf. Using Eq. 2.14, the variation of melt fraction is then computed implicitly and iteratively using:

$$\Delta f = \frac{T_{\text{cell}} - T_{\text{melting}}\left(f_0 + \Delta f\right)}{L_{\text{pyr}}} C_{P,\text{pyr}} = \frac{T_{\text{cell}} - \left(T_{\text{melting}} + \Delta f \frac{\partial T_{\text{melting}}}{\partial f}\right)}{L_{\text{pyr}}} C_{P,\text{pyr}}, \quad (2.15)$$

where L_{pyr} is the latent heat, and $C_{P,\text{pyr}}$ is the specific heat capacity of pyrolite.

This instantaneous melting temperature is adequate when treating igneous rocks lying within the harzburgite-basalt continuum. However, when basalt melts at temperatures much lower than that of pyrolite to create TTG rocks, it becomes necessary to consider melting on a scale finer than the cell level (see Fig. 2.3). Accordingly, a new mesh field called composition-fraction is calculated using mass averaging of the tracers. This field comprises of nine different components (Fig. 2.4), each having its own solidus function (see Fig. 2.5 and Section 2.5.3.3):
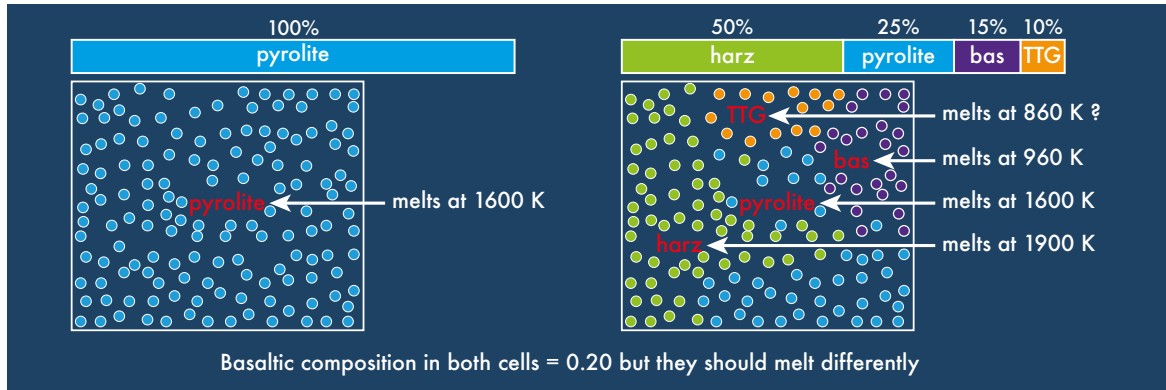
Fig. 2.3 Melting different parts of the cell at different temperatures by identifying composition-fractions.

1. **solid-mix-harzburgite-frac:** fraction of harzburgite in solid mixed-material. When there is no solid basalt in the cell, it melts to generate *molten-mix-harzburgite-frac*.

2. **solid-mix-basalt-frac:** fraction of basalt in solid mixed-material. Having a lower solidus temperature than harzburgite, basalt melts first to generate *molten-trapped-basalt*.

3. **molten-mix-harzburgite-frac:** fraction of harzburgite in molten mixed-material. It freezes before basalt as *solid-mix-harzburgite-frac*.
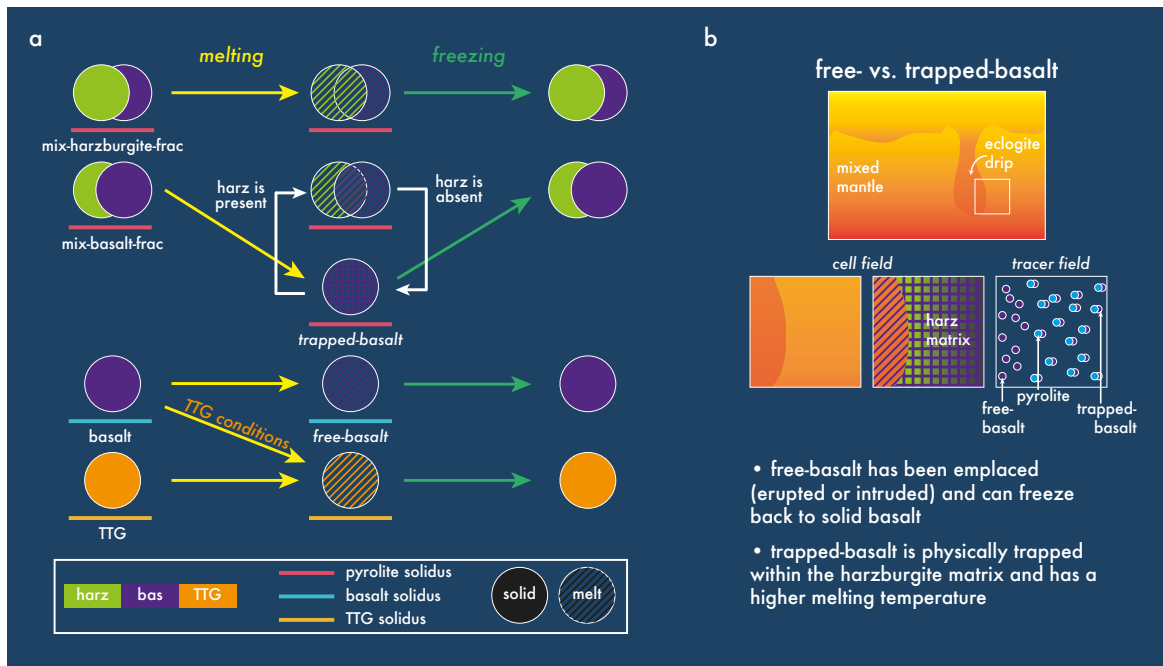
Fig. 2.4 **a,** Schematic showing 9 composition-fractions (4 solid, 5 melt) and indicating their solidus functions (given in Fig. 2.5). The arrows indicate the processes of melting (yellow), freezing (green), and transformation (white). **b,** The difference between free and trapped basalt is illustrated.

4. **molten-mix-basalt-frac:** fraction of basalt in molten mixed-material. It can neither be created by direct melting of solid mixed-material, nor it can solidify. It can only appear when the harzburgite matrix around trapped basalt melts. In the absence of *molten-mix-harzburgite-frac*, it changes into *molten-trapped-basalt*, which can solidify.

5. **solid-basalt:** solid basaltic rocks in the cell, which normally melt to generate *molten-free-basalt*. In case, the cell satisfies the TTG-formative conditions, these rocks melt to generate *molten-TTG*.

6. **molten-free-basalt:** molten basaltic rocks that have been emplaced (erupted or intruded) and can freeze back to *solid-basalt*.

7. **molten-trapped-basalt:** molten basaltic rocks that have not been emplaced and are physically trapped in the continuum matrix. They are below 300 km depth and cannot freeze back to *solid-basalt* to generate TTG. In the presence of *molten-mix-harzburgite-frac*, they change into *molten-mix-basalt-frac*.

8. **solid-TTG:** solid rocks with 100% TTG content. When above the TTG solidus, they can melt to generate *molten-TTG*

9. **molten-TTG:** molten rocks with 100% TTG content that can solidify back into *solid-TTG*.

With this new implementation, the cell temperature is compared to the solidus of each composition-fraction i (see Fig. 2.3) giving individual change in melt fraction Δf_i and Eq. 2.15 can be rewritten in the general form as:

$$\Delta f_i = \frac{T_{\text{cell}} - \left(T_{\text{sol},i} + \Delta f_i \frac{\partial T_{\text{sol},i}}{\partial f}\right)}{L_i} C_{P,i}. \tag{2.16}$$

Rearranging Eq. 2.16 (and neglecting the $\partial T_{\text{sol}}/\partial f$ term for basalt and TTG melting), we get:

$$\Delta f_i = \begin{cases} (T_{\text{cell}} - T_{\text{melting}}) / \left(\frac{L_{\text{pyr}}}{C_{P,\text{pyr}}} + \frac{\partial T_{\text{melting}}}{\partial f}\right), & \text{for } i = 1, 2, 3, 4, 7 \\ (T_{\text{cell}} - T_{\text{sol,bas}}) / \frac{L_{\text{bas}}}{C_{P,\text{bas}}}, & \text{for } i = 5, 6 \\ (T_{\text{cell}} - T_{\text{sol,TTG}}) / \frac{L_{\text{TTG}}}{C_{P,\text{TTG}}}, & \text{for } i = 8, 9 \end{cases} , \tag{2.17}$$

with basalt solidus $T_{\text{sol,bas}}$, latent heat of basalt L_{bas}, specific heat capacity of basalt $C_{P,\text{bas}}$, TTG solidus $T_{\text{sol,TTG}}$, latent heat of TTG L_{TTG}, and specific heat capacity of TTG $C_{P,\text{TTG}}$. TTG solidus is considered to be $100\,\text{K}$ lower than the basalt solidus. Accordingly, the corresponding melt is generated or frozen (if already present) from each component. Effectively, due to compositional heterogeneities, different parts of each cell melt at different temperatures. Fig. 2.4 shows how these components can change into each other. The amount of TTG melt to be generated by the melting of *solid-basalt* is given by $\mathbf{\Delta f_{\text{basalt-to-TTG}}}$. Once the $\mathbf{\Delta f_{\text{cell}}}$ is calculated, these composition fractions are updated and mapped back into the solid compositions and melt fractions. New melt fractions are obtained by adding the Δf_i of each composition fraction i to its initial melt fraction f_i. The cell temperature is adjusted using the latent heat consumed through the generation of Δf_i.

2.5.3.1   Mass of melt for emplacement

If the melt generated in the mantle is above $300\,\text{km}$ depth, then it is instantaneously transported to the surface, unless there is already some melt present at the top [*Christensen and Hofmann*, 1994; *Xie and Tackley*, 2004a]. This is equivalent to

considering a much shorter time-scale of melt migration than that of the mantle flow [*Kelemen et al.*, 1997]. This melt is placed both at the surface (volcanism) and at the *base of crust* (plutonism), and this ratio of erupta to intruda can be controlled by eruption efficiency. **Eruption efficiency** defines the percentage of mantle-derived melts (or basaltic-crust derived melts in case of TTG formation) that is erupted at the surface. In nature, the majority of mantle-derived melts intrude at a depth that corresponds to an eruption efficiency between 9% - 20%. It is one of the important parameters being tested in this study.

$\Delta f_{\mathbf{ei}}$ stores the change in melt fraction of each cell owing to possible eruption/intrusion of basaltic and TTG material and is used during melt removal. Erupta, intruda, and the decrease of rock volume in a cell $\Delta V_{\mathbf{compaction}}$ owing to melt removal are computed for every column of the domain while taking these considerations into account:

- Eruption is only possible if there is solid material (and no magma ocean) at the surface. In future work, the melt could be allowed to be added to the magma ocean.

- Mantle material and the existing basaltic crust can contribute to basalt-erupta, TTG-erupta, and TTG-intruda. Additionally, basalt-intruda can be sourced from the mantle material.

- The material in the basaltic crust that is older than 10 Myr is also allowed to melt and erupt again as basalt, however it can not be intruded.

- In the case where felsic crust already exists at the surface, the basaltic material is actually intruded below it.

2.5.3.2 Crustal thickness and detection

In addition to the already parameterised basaltic (oceanic) crustal formation by partial melting of the mantle rocks, the code now has the capability to create TTG (continental) crust by melting the basaltic rocks. As TTG rocks (surface density $\rho_{\mathrm{s}} = 2700 \, \mathrm{kg/m^3}$) are less dense compared to basalt (surface density $\rho_{\mathrm{s}} = 3080 \, \mathrm{kg/m^3}$), TTG crust stays above the basaltic crust. A portion of melt is intruded at the *base of crust* and for that purpose, the thicknesses of basaltic and TTG crust are required. It is possible that basaltic crust gets subducted or delaminated after transitioning into heavier eclogite [*Lourenco et al.*, 2016]. Such occurrences of the the crust at greater depths in the mantle are excluded and only the highest (from bottom) *base of crust* is considered.

2.5.3.3   Solidi and liquidi functions

The solidus functions used for basalt and TTG generation are given in Fig. 2.5. In all the functions, pressure P is in GPa and depth d is in km.
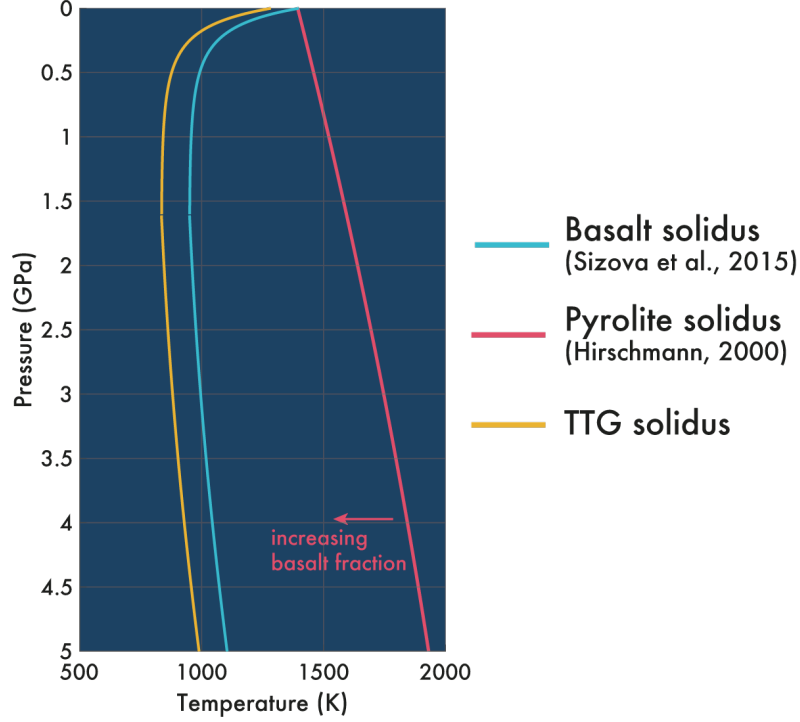
Fig. 2.5 Solidus functions for pyrolite, basalt, and TTG.

- **Pyrolite melting:** The solidus function for pyrolite has been taken from *Hirschmann* [2000] and it is given as:

$$T_{\text{sol,pyr}}(P)[K] = \begin{cases} 273.15 + 1120.661 + 132.899P - 5.104P^2, & \text{if } P < 10 \\ 273.15 + 1939.251 + 30.819\,(P - 10), & \text{if } P \geq 10 \end{cases}.$$

(2.18)

The liquidus for pyrolite is an ad hoc compromise between *Zerr et al.* [1998]; *Stixrude et al.* [2009]; *Andrault et al.* [2011] and it depends on depth as:

$$T_{\text{liq,pyr}}(d)[K] = \begin{cases} 5150 + 0.58d + 3750\left(\text{erf}\left(\frac{d}{8000}\right) - 1\right), & \text{for } d > 2900 \\ 2870 + 0.58d + 2800\left(\text{erf}\left(\frac{d}{800}\right) - 1\right), & \text{for } d > 660 \\ 2170 + 0.60d + 200\left(\text{erf}\left(\frac{d}{220}\right) - 1\right), & \text{for } d < 660 \end{cases}.$$

(2.19)

- **Basalt melting:** TTG formation by partial melting of basalt happens in the shallow mantle at low pressures. For pressures up to 5 GPa, the pressure-dependent solidus and liquidus functions for "hydrated basalt" (as defined in their paper) composition are taken from Table 1 of *Sizova et al.* [2015]:

$$T_{\text{sol,bas}}(P)[K] = \begin{cases} 973 - \frac{70,400}{1000P+354} + \frac{77,800,000}{(1000P+354)^2}, & \text{for } P < 1.6 \\ 935 + 3.5P + 6.2P^2, & \text{for } 1.6 \leq P < 5 \end{cases}, \quad (2.20)$$

$$T_{\text{liq,bas}}(P)[K] = 1423 + 105P. \quad (2.21)$$

For pressures between 5-135 GPa (up to core-mantle boundary), the pressure-dependent solidus and liquidus functions for "mid-oceanic ridge basalt" (as defined in their paper) composition are taken from Fig. 2 of *Andrault et al.* [2014]:

$$T_{\text{sol,bas}}(P)[K] = -\left(1.0116 \cdot 10^{-12}\right)P^7 + \left(8.9986 \cdot 10^{-10}\right)P^6 - \left(2.9466 \cdot 10^{-7}\right)P^5$$
$$+ \left(4.781 \cdot 10^{-5}\right)P^4 - 0.0039836P^3 + 0.0072596P^2 + 36.75P + 1257.9 \quad (2.22)$$

$$T_{\text{liq,bas}}(P)[K] = \left(1.3728 \cdot 10^{-10}\right)P^6 - \left(3.7739 \cdot 10^{-8}\right)P^5 - \left(5.0861 \cdot 10^{-7}\right)P^4$$
$$+ 0.0011277P^3 - 0.15346P^2 + 23.869P + 2854.0 \quad (2.23)$$

2.5.4 Melt generation

While the required melting or freezing is computed on the mesh, the mass is actually transferred between solid and melt by creating new tracers. Based on Δf_{cell}, new solid or molten tracers are created in every cell with their masses being proportional to the source tracers. Tracers carry properties such as position (x, y, z), mass, type, temperature, emplacement, depletion, water content, and the concentration of heat-producing element. Two of these fields are important for this mass exchange:

- **Emplacement:** It is an indicator of whether the tracer has previously been erupted/intruded or not. Using this, the mass of emplaced and non-emplaced solid/molten basalt in a cell is estimated. Initialised as 0 (non-emplaced) for all tracers, this field is set to 1 (for intrusion) or 2 (for eruption). It does not reset if the tracer gets recycled back into the mantle.

- **Depletion:** It gives the mass ratio of depleted basalt over total basalt (depleted and enriched) on a solid-basalt tracer. All tracers are initialised with a non-dimensional value of 0. This value is updated only for *solid-basalt* tracers (see Section 2.5.4.2 for details) with successive partial melting of basalt. The initial value of 0 implies that all the basalt on the *solid-basalt* tracer is enriched and can potentially partially melt to form TTG. With each subsequent melting event, the proportion of enriched basalt available on the tracer decreases. Conversely, there is an increase in the proportion of depleted basalt, or the basalt that can not melt to form TTG.

Following the melt generation, the temperature on tracers is updated by interpolating ΔT_{cell} from the mesh to tracer positions.

2.5.4.1 Melting and freezing of basalt

As discussed in Section 2.5.3, basalt can melt in two different ways depending on if the corresponding cell satisfies the TTG-formative conditions or not. When the cell undergoes melting but it does not have the TTG conditions, then *molten-basalt* tracers are generated. Compared to non-emplaced basalt, the emplaced basalt is considered as a separate rock type and has a lower melting temperature. While melting, emplaced basalt melts first and while freezing, non-emplaced basalt solidifies first. In the presence of harzburgite in the cell, molten basalt solidifies into the continuum.

Only when the cell has TTG-formative conditions and enriched basalt, molten TTG is generated. If erupted, this molten TTG solidifies to make felsic crust. However, not all the basalt available in the mantle (20% mass) can melt to generate TTG. A physical limit to this production of TTG is introduced and discussed in the following section.

2.5.4.2 Basalt depletion

A *solid-basalt* tracer can undergo partial melting multiple times and with each subsequent melting, the proportion of enriched basalt available on the tracer decreases. Conversely, the proportion of depleted basalt on a *solid-basalt* tracer increases with time. The production of TTG from basalt is limited by introducing a parameter called **depletion fraction $X_{\mathrm{depletion}}$**, which gives the allowable mass fraction of depleted basalt on a *solid-basalt* tracer. For example, using a value of $X_{\mathrm{depletion}} = 0.9$ would imply that 90% of basalt is depleted or not available for TTG production. Hence, only 10% of mass of *solid-basalt* will be used for TTG production whose mass is then limited

to 2% of mantle mass. This is an important parameter as it directly controls how much felsic crust can be produced in the code and it is used in the following equations.

Using $\Delta f_{\text{basalt-to-TTG}}$ calculated in Section 2.5.3, the ideal amount of TTG to be generated in a cell with mass M_{cell} is given as:

$$\Delta M_{\text{TTG}} = \Delta f_{\text{basalt-to-TTG}} M_{\text{cell}}. \tag{2.24}$$

This amount has to be sourced uniformly from the *solid-basalt* tracers present in the cell:

$$\Delta M_{\text{TTG}} = \sum_{i=1}^{n\,\text{tracers}} \Delta m_{\text{TTG},i}, \tag{2.25}$$

where Δm_{TTG} is the mass of TTG produced from the host tracer i.

Solid-basalt tracers are 100% enriched in basalt at time $t = 0$ and after a time step Δt, the new amount of enriched basalt on a tracer is:

$$m_{\text{enr},i}\left(t + \Delta t\right) = m_{\text{enr},i}\left(t\right) - \Delta m_{\text{dep},i} - \Delta m_{\text{TTG},i}, \tag{2.26}$$

where m_{enr} and m_{dep} denote the masses of enriched basalt and depleted basalt respectively on the tracer (see Fig. 2.6 for illustration).
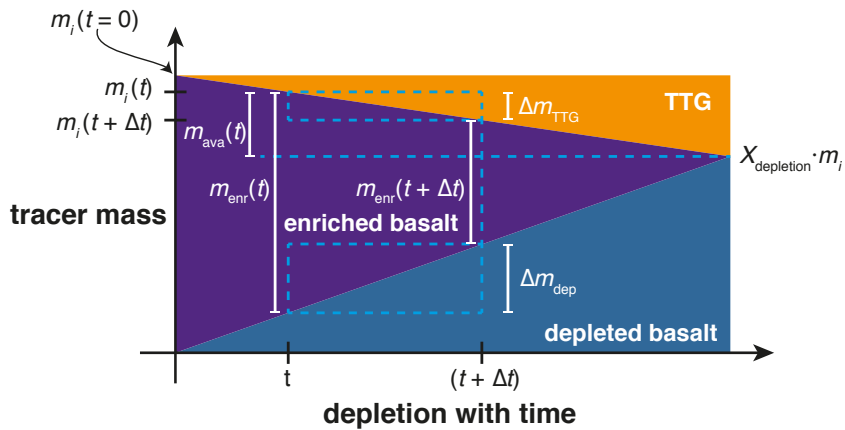
Fig. 2.6 Evolution of depletion on a *solid-basalt* tracer with time. The initial tracer mass m_i (in violet) decreases with time as some of it gets transferred to TTG (in orange).

The change in masses of depleted basalt Δm_{dep} and TTG Δm_{TTG} (produced from enriched basalt) are related using the **depletion fraction $X_{\mathbf{depletion}}$** as:

$$\Delta m_{\mathrm{dep},i} = \Delta m_{\mathrm{TTG},i} \left(\frac{X_{\mathrm{depletion}}}{1 - X_{\mathrm{depletion}}} \right). \tag{2.27}$$

Every *solid-basalt* tracer has an available mass m_{ava} for TTG production at a given time t:

$$m_{\mathrm{ava},i}(t) = m_{\mathrm{enr},i}(t)\left(1 - X_{\mathrm{depletion}}\right). \tag{2.28}$$

In order to uniformly source the mass of TTG from all the *solid-basalt* tracers present in the cell, a fraction χ of this available mass is taken as:

$$\Delta m_{\mathrm{TTG},i} = \chi m_{\mathrm{ava},i} = \chi m_{\mathrm{enr},i}\left(1 - X_{\mathrm{depletion}}\right). \tag{2.29}$$

Combining equations 2.25 and 2.29, we get:

$$\chi = \frac{\Delta M_{\mathrm{TTG}}}{\sum_{i=1}^{n\,\mathrm{tracers}} m_{\mathrm{enr},i}\left(1 - X_{\mathrm{depletion}}\right)}. \tag{2.30}$$

The mass of depleted basalt m_{dep} on each *solid-basalt* tracer changes with time according to this relation:

$$m_{\mathrm{dep},i}(t + \Delta t) = m_{\mathrm{dep},i}(t) + \Delta m_{\mathrm{dep},i} = m_{\mathrm{dep},i}(t) + \Delta m_{\mathrm{TTG},i}\left(\frac{X_{\mathrm{depletion}}}{1 - X_{\mathrm{depletion}}} \right), \tag{2.31}$$

and the dimensionless *depletion* value (< 1) on each *solid-basalt* tracer is updated as:

$$depletion_i(t + \Delta t) = \frac{m_{\mathrm{dep},i}(t + \Delta t)}{m_{\mathrm{dep},i}(t + \Delta t) + m_{\mathrm{enr},i}(t + \Delta t)}. \tag{2.32}$$

Next section explains how the melt is removed from the mantle.

2.5.5   Melt removal

$\Delta f_{\mathbf{ei}}$ from Section 2.5.3.1 gives the amount of melt that a cell has to donate. In the cells that undergo melting, the same fraction of mass is removed from all the *molten-mixed-material* tracers. Based on the **eruption efficiency**, this cumulative mass removed from the cell is divided among two new transport tracers, *intruding-mixed-material* and *erupting-mixed-material*. Similarly, mass is extracted from *molten-basalt* tracers to

generate *intruding-TTG* and *erupting-TTG* tracers per cell. These transport tracers are assigned mass-averaged properties of the donating molten tracers.

Before these tracers are transported, trace elements such as water and heat-producing element (HPE) are partitioned and outgassed (in case of eruption) between solid and melt. The concentration of heat-producing element is 100 times higher in the melt compared to the solid residue (partition coefficient $D_{\mathrm{part,HPE}} = 0.01$). Water has the same concentration in both the melt and the solid with $D_{\mathrm{part,H_2O}} = 1$.

2.5.6 Melt emplacement

The melt being removed from the mantle and the pre-existing basaltic crust is emplaced at different depths and at the surface using the transport tracers. The other tracers are transported downwards to make room for intrusion and eruption. Finally, if some tracers leave the model domain during the eruption process, they are brought back inside.

The variables defined in this section use the following naming convention. e: erupta, i: intruda, r: radius. When used as subscripts, e: eruption, i: intrusion, B: basalt, T: TTG, 1-2: source of melt as either basaltic crust (1) or mantle (2). For instance, $e_{\mathrm{B},2}$ refers to basaltic erupta sourced from the mantle. The full list of the variables used here is given in Table 2.3. A cartoon representation of the following calculations is given in Fig. 2.7.

2.5.6.1 Eruption and intrusion gaps

There are different possible locations to intrude the molten material: base of crust, middle of crust, surface, or at a specified depth. The gaps in the lithosphere (height windows) at which the molten material is emplaced are identified using the *base of crust* location. These gaps are calculated from the bottom of the domain in every column with the following steps:

- As the melt is removed from the mantle and transported above, the cells which lose mass are compacted and the volume of this compaction is given as:

$$V_{\mathrm{compaction}} = \frac{e_{\mathrm{B},2} + i_{\mathrm{B},2} + e_{\mathrm{T},2} + i_{\mathrm{T},2}}{\rho_{\mathrm{base}}}, \tag{2.33}$$

  with basalt erupta from the mantle $e_{\mathrm{B},2}$, basalt intruda from the mantle $i_{\mathrm{B},2}$, TTG erupta from the mantle $e_{\mathrm{T},2}$, and TTG intruda from the mantle $i_{\mathrm{T},2}$. ρ_{base}
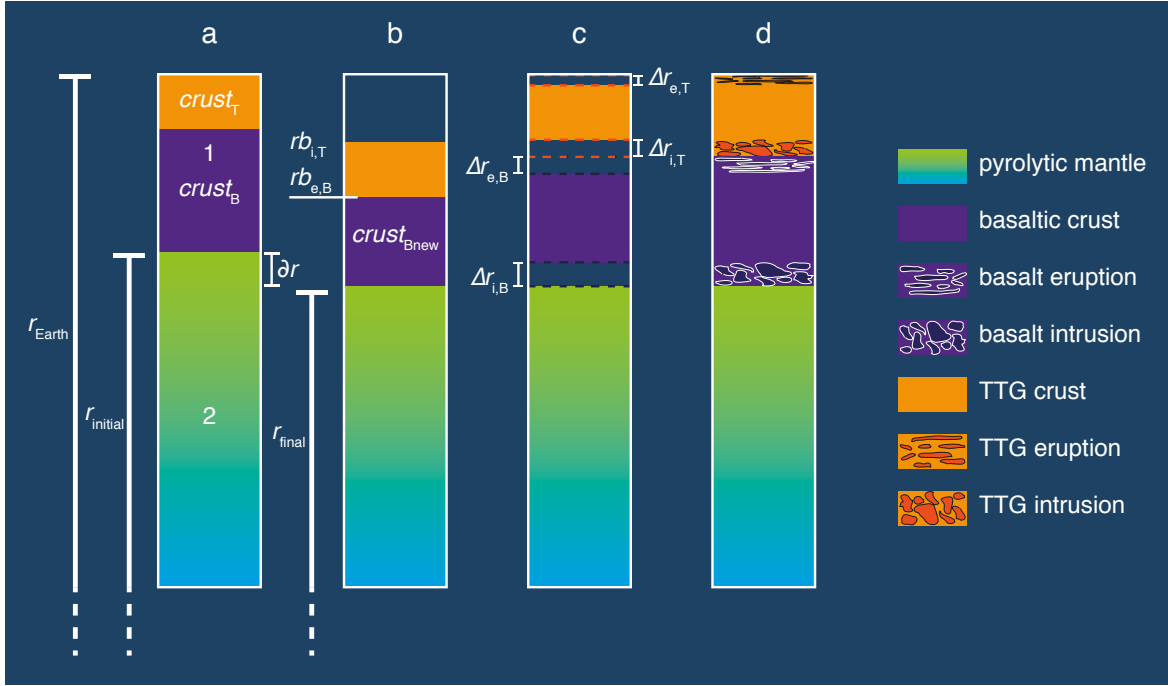
Fig. 2.7 Cartoon depicting a section of a domain column and stacking of different crusts in the lithosphere. **a,** Initial state with TTG crust, basaltic crust (1) and pyrolytic mantle (2). **b,** After melt removal and compaction with δr, but before opening gaps for emplacement. **c,** Opening gaps for eruption and intrusion. **d,** Final state with the placement of erupta and intruda in the gaps.

is the density of the cell where lies the base of the overall crust (basaltic and TTG combined).

- Excluding the thicknesses of basaltic ($crust_\mathrm{B}$) and TTG ($crust_\mathrm{T}$) crust, the radius of the domain before (r_initial) and after (r_final) mantle compaction are given as:

$$r_\mathrm{initial} = r_\mathrm{Earth} - crust_\mathrm{B} - crust_\mathrm{T}, \qquad (2.34)$$

$$r_\mathrm{final} = r_\mathrm{initial} - \delta r, \qquad (2.35)$$

with radius of Earth r_Earth and thickness of the mantle compaction δr corresponding to $V_\mathrm{compaction}$.

- The volume element δV in a spherical coordinate system (r, θ, ϕ) with radius r, co-latitude θ, and longitude ϕ (see Fig. 2.8) is given as:

$$\delta V = r^2 \sin\theta \delta r \delta\theta \delta\phi. \tag{2.36}$$

The model domain is spherical annulus, which is a 2D slice bisecting a spherical shell at the equator (see *Hernlund and Tackley* [2008] for details). Substituting $r = (r_{\text{initial}} + r_{\text{final}})/2$ gives the radius in the middle of the compacting volume. Combining this with Eq. 2.35 and 2.36 and using $\theta = 90°$, volume element δV is rewritten as:

$$\delta V = \left(r_{\text{initial}} - \frac{\delta r}{2}\right)^2 \delta r \delta\theta \delta\phi. \tag{2.37}$$

Considering $\delta r << r_{\text{initial}}$, Eq. 2.37 is rearranged as a quadratic expression and solved for δr to get:

$$\delta r = \frac{r_{\text{initial}} - \sqrt{r_{\text{initial}}^2 - \frac{4\delta V}{\delta\theta\delta\phi r_{\text{initial}}}}}{2}. \tag{2.38}$$
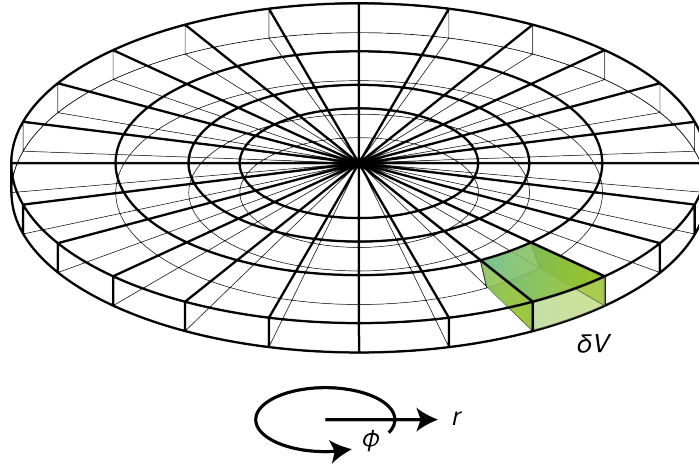
Fig. 2.8 Volume element in 2D spherical annulus geometry. Adapted from *Hernlund and Tackley* [2008].

- After considering the melt being removed from the basaltic crust itself, its thickness is updated as:

$$crust_{\text{Bnew}} = crust_{\text{B}} - \frac{e_{\text{B},1} + e_{\text{T},1} + i_{\text{T},1}}{\rho_{\text{B}} S_{\text{midB}}}, \tag{2.39}$$

with basaltic erupta from the crust itself $e_{B,1}$, TTG erupta from basaltic crust $e_{T,1}$, TTG intruda from basaltic crust $i_{T,1}$, and density in the middle of basaltic crust ρ_B. The area of the cell at a depth of mid-basaltic crust S_{midB} is given as:

$$S_{midB} = \delta\theta\delta\phi \left[r_{Earth} - \left(\frac{crust_B}{2} + crust_T + \left(\frac{e_{B,2} + e_{T,2} + i_{T,2}}{e_{B,2} + i_{B,2} + e_{T,2} + i_{T,2}} \right) \delta r \right) \right]^2. \tag{2.40}$$

It is assumed that the material is removed from below the pre-existing basaltic crust and will be deposited above it.

- Once the compaction has taken place, the molten basaltic material is intruded at the base of basaltic crust (with radius r_{final}) and the thickness of this intruda ($\Delta r_{i,B}$) is:

$$\Delta r_{i,B} = \frac{i_{B,2}}{\rho_{base}\delta\theta\delta\phi r_{final}^2}. \tag{2.41}$$

- The basaltic erupta is placed at the top of the basaltic crust (with radius $r_{final} + \Delta r_{i,B} + crust_{Bnew}$) and its thickness ($\Delta r_{e,B}$) is:

$$\Delta r_{e,B} = \frac{e_{B,1} + e_{B,2}}{\rho_B\delta\theta\delta\phi \left(r_{final} + \Delta r_{i,B} + crust_{Bnew} \right)^2}. \tag{2.42}$$

- It is assumed that TTG crust does not undergo compaction. TTG intruda is placed right above the basaltic erupta and its thickness ($\Delta r_{i,T}$) is:

$$\Delta r_{i,T} = \frac{i_{T,1} + i_{T,2}}{\rho_T\delta\theta\delta\phi \left(r_{final} + \Delta r_{i,B} + crust_{Bnew} + \Delta r_{e,B} \right)^2}. \tag{2.43}$$

- TTG erupta is placed at the surface within a gap whose thickness is calculated using the vertical displacements in the top cell:

$$\Delta r_{e,T} = - \left(z_{compaction,topcell} + z_{dilation,topcell} \right). \tag{2.44}$$

- Additionally, two more heights are recorded after the compaction has happened, but the gaps for eruption and intrusion have not been opened. The bottoms of the basaltic erupta layer ($rb_{e,B}$) and the TTG intruda layer ($rb_{i,T}$) are given as:

$$rb_{e,B} = rb_{i,T} = r_{final} + crust_{Bnew}. \tag{2.45}$$

These heights are the same because the *base of crust* intrusion location is employed here. They are used for moving up the non-transport tracers after compaction.

- The increase of rock volume in a cell $\boldsymbol{\Delta V_{\mathbf{dilation}}}$ owing to intrusion only is estimated by looking at the overlap between the cells and the intruda gaps for basalt ($\Delta r_{\mathrm{i,B}}$) and TTG ($\Delta r_{\mathrm{i,T}}$). If there is already a TTG crust at the surface, then molten basalt marked for eruption is also intruded. The vertical displacements $\boldsymbol{z_{\mathbf{compaction}}}$ (pointing radially inwards) and $\boldsymbol{z_{\mathbf{dilation}}}$ (pointing radially outwards) corresponding to compaction and gap opening are calculated and are used to transport tracers.

2.5.6.2 Tracer transport

In cells from which melt is removed, there will be radial compaction. But elsewhere, the material is simply moved down with no internal deformation creating a gap at the surface for eruption. Material that lies above the bottom of the basaltic erupta layer after compaction but before opening gaps (above $rb_{\mathrm{e,B}}$) is moved up without any deformation creating a gap for intrusion.

The compaction is effectively done by transporting the solid and molten tracers (excluding the transport ones) down with the displacement $\boldsymbol{z_{\mathbf{compaction}}}$ in every column. The erupting tracers are placed in the gap at the surface. They become solid and their temperature is set to the surface value (300 K).

For intrusion, another gap is created by moving up the solid and molten tracers lying above $rb_{\mathrm{e,B}}$ with the displacement $\boldsymbol{z_{\mathbf{dilation}}}$. These tracers had previously been moved downwards by compaction. This gap is filled by intruding tracers which remain molten.

- **Gap opening:** Tracers that are in the TTG crust (above $rb_{\mathrm{i,T}}$) are moved upwards to make a gap for intrusion because they have been previously moved downwards by compaction. This transport uses the displacement $\boldsymbol{z_{\mathbf{dilation}}}$ or $\Delta r_{\mathrm{i,T}}$ if the tracer lies in the same cell as the bottom of TTG intruda. Similarly, tracers that are in the basaltic crust (above $rb_{\mathrm{e,B}}$) are moved upwards with either the displacement $\boldsymbol{z_{\mathbf{dilation}}}$ or $\Delta r_{\mathrm{i,B}}$.

- **Melt intrusion:** *Intruding-mixed-material* tracers are placed in the gap $\Delta r_{\mathrm{i,B}}$ as *molten-mixed-material* tracers. *Intruding-TTG* tracers are placed in the gap $\Delta r_{\mathrm{i,T}}$ as *molten-TTG* tracers. The temperature of intruded tracers takes only adiabatic decompression into account, forming a warm lithosphere.

Table 2.3 Variables used in the calculations for eruption and intrusion gaps. e: erupta, i: intruda, r: radius. When used as subscripts, e: eruption, i: intrusion, B: basalt, T: TTG, 1-2: source of melt as either basaltic crust (1) or mantle (2). For instance, $e_{B,2}$ refers to basaltic erupta sourced from the mantle.

Symbol	Meaning
$e_{B,1}$	basaltic erupta from pre-existing basaltic crust
$e_{B,2}$	basaltic erupta from mantle
$i_{B,2}$	basaltic intruda from mantle
$e_{T,1}$	TTG erupta from pre-existing basaltic crust
$e_{T,2}$	TTG erupta from mantle
$i_{T,1}$	TTG intruda from pre-existing basaltic crust
$i_{T,2}$	TTG intruda from mantle
ρ_B	average density in the middle of basaltic crust
ρ_T	average density in the middle of TTG crust
ρ_{base}	reference density of cell with base of crust
$\rho_{topcell}$	reference density of top cell
$crust_B$	thickness of basaltic crust
$crust_{Bnew}$	thickness of basaltic crust after melt removal
$crust_T$	thickness of TTG crust
r_{Earth}	radius of Earth
$r_{initial}$	radius before mantle compaction
r_{final}	radius after mantle compaction
δr	thickness of mantle compaction
$\Delta r_{e,B}$	thickness of basaltic erupta layer
$\Delta r_{i,B}$	thickness of basaltic intruda layer
$\Delta r_{e,T}$	thickness of TTG erupta layer
$\Delta r_{i,T}$	thickness of TTG intruda layer
$rb_{e,B}$	bottom of basaltic erupta after compaction before opening gaps
$rb_{i,T}$	bottom of TTG intruda after compaction before opening gaps
z_e	top of erupted material
S_{midB}	area of cell at a depth of mid-basaltic crust
$V_{compaction}$	volume of compaction
δV	volume element in a spherical coordinate system (r, θ, ϕ)

- **Melt eruption:** In the presence of a TTG crust, *erupting-mixed-material* tracers
  are intruded below the TTG crust as *molten-mixed-material* tracers in the gap
  $\Delta r_{\mathrm{e,B}}$. When there is no TTG crust, these transport tracers are erupted as
  solid-mixed-material tracers in the same gap. Likewise, *erupting-TTG* tracers are
  placed in the gap $\Delta r_{\mathrm{e,T}}$ as *solid-TTG* tracers. The temperature of these tracers
  is set to the surface temperature, thereby allowing for a rapid formation of a cold
  lithosphere.

If the mass of the transport tracer exceeds ideal tracer mass, then multiple tracers
are inserted. Following this transport of tracers, the *emplacement* value (introduced in
Section 2.5.4) on the tracers is also updated.

2.5.6.3 Tracer redistribution and density homogenisation

As free-slip boundary condition is used at the surface, it is expected that some tracers
are transported outside the domain during eruption process. The basaltic melt is
removed from the mantle and placed at the surface as less dense TTG crust. Following
the conservation of mass, the less dense felsic material occupies a larger volume and this
can lead to overestimation of TTG eruption gap $\Delta r_{\mathrm{e,T}}$. This is corrected by vertically
redistributing tracers that lie in the top 300 km and above the surface.

If the model domain is vertically decomposed into different cores (CPUs), then
these calculations are considered only in the top cores. Depending on the presence of
the TTG crust, the top of the erupted material z_{e} is calculated as:

$$z_{\mathrm{e}} = \begin{cases} \Delta r_{\mathrm{e,T}} - \dfrac{e_{\mathrm{T,1}}+e_{\mathrm{T,2}}}{\rho_{\mathrm{topcell}}r_{\mathrm{Earth}}^2\delta\theta\delta\phi}, & \text{if } \dfrac{crust_{\mathrm{T}}}{D} > 1e-5 \\[2em] \Delta r_{\mathrm{e,T}} - \dfrac{e_{\mathrm{B,1}}+e_{\mathrm{B,2}}}{\rho_{\mathrm{topcell}}r_{\mathrm{Earth}}^2\delta\theta\delta\phi}, & \text{if } \dfrac{crust_{\mathrm{T}}}{D} < 1e-5 \end{cases}, \tag{2.46}$$

where ρ_{topcell} is the reference density of the top cell and D is the mantle thickness
(2890 km). A non-zero z_{e} means that the top of the erupted material does not coincide
with the top of the domain and the tracer positions need to be corrected in the
lithospheric column. With $z_{\mathrm{e}} > 0.$, the top of the erupted material lies below the
surface and the tracers are moved upwards. With $z_{\mathrm{e}} < 0.$, the top of the erupted
material lies above the surface and the tracers are compacted.

This vertical redistribution can result in anomalous variations in tracer-based
cell densities as some cells might get many heavy tracers. In case the tracer-based
density varies from reference density by more than 5% in a cell, then additional radial

compaction or dilation of tracers is carried out in those cells lying above 300 km of depth.

Chapter 3

Quantifying the correlation between mobile continents and elevated temperatures in the mantle

Abstract

The dynamic feedback between the continents and mantle convection has been well established. Continents influence the mantle's convective wavelength and the heat flow escaping from the planet's surface. Over the last decades, many numerical and analytical studies have contributed to the debate about whether the continents can warm up the underlying mantle or not and if they do, then to what extent? However, a consensus regarding the exact nature and magnitude of this correlation between continents and elevated temperatures in the mantle remains to be achieved. By conducting a systematic parameter study using 2D global mantle convection simulations with mobile continents, we provide qualitative and quantitative observations on the nature of this correlation. In our incompressible and compressible models, we observe the general processes of downwellings bringing cold material down into the mantle along continental margins and a buildup of thermal anomalies underneath the continents. We compute the amplitude and degree of this correlation using spectral decomposition of temperature and composition fields. The dominant degree of correlation evolves with

time and changes with continental configuration. Using scaling laws, we quantitatively argue that this correlation decreases with increasing core temperature, number of continents, internal heating, and Rayleigh number. Additionally, we show for the first time that the melting and crustal production events resulting from this correlation lead to voluminous volcanism. The emplacement of this basalt-eclogite material breaks the continents apart, thereby destroying the correlation and acting as a negative feedback.

3.1   Introduction

The existence of dynamic feedback between the convecting mantle and the drifting continents is evident from numerical simulations and laboratory experiments. It has been shown that continents exert a first-order influence on Earth's mantle flow by affecting convective wavelength and surface heat flow [e.g., *Gurnis*, 1988; *Zhong and Gurnis*, 1993; *Lowman and Jarvis*, 1993; *Guillou and Jaupart*, 1995; *Lowman and Jarvis*, 1996; *Lowman and Gable*, 1999; *Yoshida et al.*, 1999; *Phillips and Bunge*, 2005; *Grigné et al.*, 2007; *Zhong et al.*, 2007; *Zhong and Liu*, 2016]. The notion that continents can have an insulating effect on the mantle has received considerable attention over the last decades [*Lenardic and Moresi*, 2001; *Lenardic et al.*, 2005; *Cooper et al.*, 2006b, 2013]. *Anderson* [1982b] proposed that the geoid highs above Africa and Central Pacific were caused by elevated temperatures generated by the assembly of the Pangea supercontinent during the Mesozoic. *Coltice et al.* [2007, 2009] argued in favour of continental-aggregation induced elevated temperatures and thereby large-scale melting that caused the emplacement of continental flood basalts of the Central Atlantic Magmatic Province following the breakup of Pangea.

A diverse range of numerical studies with varying degrees of complexity have attempted to answer the question of whether continents elevate the temperature underneath them or not. Or in other words, whether continents at the surface and elevated temperatures in the mantle are correlated. Numerical simulations by *Gurnis* [1988]; *Zhong and Gurnis* [1993] showed the accumulation of heat underneath mechanically stiff, thick continental plates, and the development of long-wavelength thermal structures in the mantle. By using laboratory experiments, *Guillou and Jaupart* [1995] proposed that continents larger than the mantle depth are unstable as they generate large thermal anomalies below them. *Lowman and Gable* [1999] suggested that the inclusion of oceanic plates and internal heating in convection modelling reduces the thermal contrast between suboceanic and subcontinental mantle. By modelling mechanically and thermally distinct continental and oceanic plates, but with the same thickness and

a depth-dependent viscosity, *Heron and Lowman* [2010, 2011] argued that continental insulation plays a minor role in affecting the mantle's thermal field and did not report any elevated temperatures in the subcontinental mantle. *Heron and Lowman* [2014] further highlighted the decreasing role of continental insulation on subcontinental mantle temperatures with increasing Rayleigh number *Ra*, albeit with a stationary supercontinent and viscosity not being fully temperature-dependent in their models. In their mixed-heating (basal and internal) cartesian models, *O'Neill et al.* [2009] showed the propensity of plumes to rise underneath continents (∼3000 km in extent) and elevate temperatures away from the cold slabs subducting along continental margins. This temperature anomaly diminishes with strongly temperature dependent viscosity or when a cool thermal boundary layer and small-scale convection cells develop under large continents. They also explored the possible relation between melting and rifting and did not observe voluminous volcanism owing to hot upwelling subcontinental mantle in their steady-state simulations. By simulating mobile continents, *Phillips and Coltice* [2010] also observed an increase in subcontinental temperature as a function of both continental extent and convective wavelength, although their models lacked oceanic plates and a temperature-dependent viscosity, which might result in overestimation of the resulting temperature difference between suboceanic and subcontinental mantle. Based on their purely internally heated 3D models with various continental configurations and width, *Rolf et al.* [2012] showed temperature excess of up to 140 K underneath the continents compared to the suboceanic mantle. They showed that as opposed to a dispersed configuration, a cluster of continents results in higher insulation and provides a possible explanation for the episodic continental crustal growth [*Condie*, 2004b; *Hawkesworth and Kemp*, 2006a; *Pearson et al.*, 2007]. The absence of basal heating and plumes in their models is a huge simplification and demands further testing.

Melting-induced crustal production (hereby referred to as MCP) are considered as significant processes in planetary evolution and dynamics [e.g., *Stevenson*, 1990; *Xie and Tackley*, 2004b; *Davies*, 2007; *Nakagawa and Tackley*, 2012; *Ogawa*, 2014] and have also been shown to help plate tectonics [*Lourenco et al.*, 2016]. MCP has been mostly excluded from previous studies. In the present study, we include it to better understand the impact of continents on mantle convection. As pointed out in the previous studies, the correlation between continents and elevated temperatures in the subcontinental mantle seems to be elusive. In this paper, we study this correlation using a broad range of thermo-chemical mantle convection simulations by systematically varying parameters such as core-mantle boundary (CMB) temperature, continental configuration, mantle

heating modes (internal and basal heating), and Rayleigh number. We also investigate the effect of melting and crustal production on this correlation and observe how the mantle convective wavelength evolves with time. We introduce the methodology and the governing equations in section 3.2. We present the results of our simulations in section 3.3 and discuss their geophysical implications in section 3.4. Finally, we summarise the main findings of our study in section 3.5.

3.2   Physical Model and Numerical Model

We study the thermo-chemical evolution of the mantle coupled with mobile continents. Continents are simplified as homogeneous Archean cratons and represented by a continuous non-diffusive compositional field C ($0 \leq C \leq 1$) ($C = 1$ being pure continental and $C = 0$ being pure non-continental material). To ensure their long-term stability, continents are lighter and more viscous than the mantle. We use both incompressible (with non-dimensional units) and compressible (with dimensional units) setups for our models (see Table 3.1). The numerical model employed here incorporates pressure-temperature-dependence of viscosity, internal and basal heating, plasticity, phase transitions, diffusion creep, melting, and crustal production and is an extension of the ones described by [*Rolf and Tackley*, 2011; *Rolf et al.*, 2012].

3.2.1   Rheology

In our models, diffusion creep with homogenous grain size is the viscous deformation mechanism. Between continents and mantle material, the density contrast is specified by the buoyancy ratio B and the rheological contrast is controlled by viscosity contrast and yield stress ratio. The temperature- and pressure-dependent viscosity η is given by an Arrhenius law:

$$\eta(T, P, C) = \eta_0 \Delta \eta_i \Delta \eta^{\mathrm{C}} \exp \left(\frac{E_i + PV_i}{RT} - \frac{E_i}{RT_0} \right),   \tag{3.1}$$

where η_0 is the reference viscosity (which changes with Rayleigh number Ra) at zero pressure and reference temperature T_0 (1600 K), $\Delta \eta_i$ is the viscosity jump between the layers i, $\Delta \eta^{\mathrm{C}}$ is the composition-dependent viscosity factor, E_i is the activation energy in the layer i, P is the pressure, V_i is the activation volume in layer i, R is the gas constant and T is the absolute temperature. See Table 3.2 for a list of the

rheological properties used in the study. The activation volume decreases with pressure according to the relation:

$$V(P) = V_i \exp\left(-\frac{P}{P_i}\right). \tag{3.2}$$

In simulations with an incompressible setup (non-dimensional units), the viscosity takes the form:

$$\eta(T,C) = \Delta\eta^C \exp\left(\frac{\tilde{E}_A}{T+1} - \frac{\tilde{E}_A}{2}\right), \tag{3.3}$$

where $\Delta\eta^C = \eta\left(T, C=1\right)/\eta\left(T, C=0\right)$ accounts for the compositional dependence, and $\tilde{E}_A = \eta\left(T=1, C\right)/\eta\left(T=0, C\right)$ is the activation energy, which accounts for the temperature-dependence of the viscosity. A constant value of 23.03 for $\tilde{E}_A$ gives five orders of magnitude viscosity variation in the interval $0 \leq T \leq 1$. Following the viscosity profile expected by the inversion of postglacial rebound data [*Čížková et al.*, 2012], and geoid inversion studies [e.g., *Ricard et al.*, 1989], a viscosity jump of 30 is applied at the upper-lower mantle transition.

To break the stagnant lid and obtain Earth-like plate tectonics, plastic yielding is assumed to be the weakening mechanism [*Moresi and Solomatov*, 1998b; *Tackley*, 2008b]. The maximum stress that a material can sustain before deforming plastically is given by the yield stress τ_Y and it increases linearly with depth d at a rate of τ_Y',

$$\tau_Y(d, C) = \Delta\tau_Y^C \left(\tau_Y^0 + d\tau_Y'\right), \tag{3.4}$$

where $\Delta\tau_Y^C = \tau_Y\left(d, C=1\right)/\tau_Y\left(d, C=0\right)$ accounts for the different yield stresses of continental and oceanic lithosphere. $\tau_Y^0 = \tau_Y\left(d=0, C=0\right)$ is the yield stress at the oceanic surface. If the convective stresses exceed the yield stress, the viscosity is reduced to the yielding viscosity $\eta_Y = \tau_Y/2\dot{\epsilon}$, where $\dot{\epsilon}$ is the 2nd invariant of the strain-rate tensor. The effective viscosity is then given by:

$$\eta_{\text{eff}} = \left(\frac{1}{\eta} + \frac{2\dot{\varepsilon}}{\tau_Y}\right)^{-1}. \tag{3.5}$$

Continents are less dense by $100\,\text{kg/m}^3$ compared to the mantle. A viscosity contrast $\Delta\eta^C = 100$ and yield stress contrast $\Delta\tau_Y^C = 10$ are used to ensure cratonic lithosphere's stability and longevity. When considering non-dimensional units, yield stresses τ_Y are non-dimensionalised with the factor $\eta_0\kappa/D^2$. The dimensional time t is obtained from

the dimensionless time t^* using $t = t^* D^2 / \kappa$. Similarly, velocities v given in Table. 3.4 are obtained from dimensionless velocities v^* using $v = v^* \kappa / D$.

The potential correlation between continents and temperature in the subcontinental mantle are strongly related to mantle stirring. However, as we use various Rayleigh numbers, the average number of overturns occurring in the mantle decreases for cases with increasing viscosity (decreasing Ra) for a given amount of dimensional time. To overcome this issue, we use a renormalised time t_r based on the average dimensional velocity of our simulations. The renormalised time is given by:

$$t_\mathrm{r} = \frac{v_\mathrm{E}}{<v>_t} t, \tag{3.6}$$

with

$$<v>_t = \frac{1}{t_\mathrm{max}} \int_{t^*=0}^{t^*=t_\mathrm{max}} v_\mathrm{RMS} \, dt^*, \tag{3.7}$$

where v_RMS is the dimensional root-mean-square (RMS) velocity in the whole domain and v_E is the average plate velocity for present-day Earth ($3.4\,\mathrm{cm/yr}$ as used in *Rolf et al.* [2012]). t_max is the final dimensionless time in our simulations. We thus force a sufficiently large number of overturns in all cases, which leads to comparable evolution states.

3.2.2 Conservation Equations, Boundary Conditions and Solution Method

Using the code StagYY [*Tackley*, 2008a], we solve the equations for both incompressible (Boussinesq approximation) and compressible (anelastic approximation with infinite Prandtl number) Stokes flow. The equations of conservation of mass, momentum, and energy governing compressible flow are (see [*Chandrasekhar*, 1961; *Schubert et al.*, 2001] for details):

$$\frac{\partial}{\partial x_j} \left(\rho v_j \right) = 0, \tag{3.8}$$

$$0 = -\frac{\partial P}{\partial x_i} + \frac{\partial}{\partial x_j} \left\{ \eta \left(\frac{\partial v_i}{\partial x_j} + \frac{\partial v_j}{\partial x_i} - \frac{2}{3} \delta_{ij} \frac{\partial v_k}{\partial x_k} \right) \right\} + \rho g_i, \tag{3.9}$$

$$\rho C_P \left(\frac{\partial T}{\partial t} + \mathbf{v} \cdot \bigtriangledown T \right) - \alpha T \left(v_r \cdot \bigtriangledown_r P \right) = \bigtriangledown \cdot \left(k \bigtriangledown T \right) + \frac{\partial v_i}{\partial x_j} \sigma_{ij} + \rho H, \tag{3.10}$$

Table 3.1 Non-dimensional and dimensional parameters used in this study. Parameters that vary with simulations are given in Table 3.4.

Property	Symbol	Value	Units
Comp. yield stress contrast	$\Delta\tau_Y^C$	10	-
Comp. viscosity contrast	$\Delta\eta^C$	100	-
Buoyancy ratio	B	-0.4	-
Surface temperature	T_{surf}	300	K
Specific heat capacity	C_P	1200	J/kg/K
Gas constant	R	8.3145	J/K/mol
Gravity	g	9.81	m/s^2
Mantle thickness	D	2890	km
Surface thermal expansivity[s]	α	$3 \cdot 10^{-5}$	K^{-1}
Surface thermal diffusivity[s]	κ	$7.57 \cdot 10^{-7}$	m^2/s
Incompressible setup			
Surface yield stress	τ_Y^0	37	MPa
Initial potential temperature	T_{P0}	1600	K
Surface thermal conductivity[s]	k	3.0	W/m/K
Compressible setup with MCP			
Surface yield stress	τ_Y^0	40	MPa
Yield stress gradient	τ_Y'	0.005	-
Initial potential temperature	T_{P0}	1900	K
Surface thermal conductivity[s]	k	3.5	W/m/K
Initial internal heating rate	H	$18.77 \cdot 10^{-12}$	W/kg
Half-life	t_{half}	2.43	Gyr
Reference viscosity	η_0	$1 \cdot 10^{20}$	Pa·s
Latent heat of melting	L	600	kJ/kg

[s] valid at the surface for olivine phase system.

Table 3.2 Rheological properties used for the compressible setup.

Property	Symbol	Value	Units
- Upper Mantle			
Activation energy	E_1	300	kJ/mol
Activation volume	V_1	5.00	cm^3/mol
Pressure scale	P_1	∞	GPa
Viscosity multiplier	$\Delta\eta_1$	1.0	-
- Lower Mantle			
Activation energy	E_2	370	kJ/mol
Activation volume	V_2	3.65	cm^3/mol
Pressure scale	P_2	200	GPa
Viscosity multiplier	$\Delta\eta_2$	30.0	-
- Post-perovskite layer			
Activation energy	E_3	162	kJ/mol
Activation volume	V_3	1.40	cm^3/mol
Pressure scale	P_3	1610	GPa
Viscosity multiplier	$\Delta\eta_3$	0.1	-

with density ρ, position x_j (j = 1,2,3 hereinafter), velocity component v_j, Kronecker delta δ_{ij}, gravity g, specific heat capacity C_P, thermal expansivity α, thermal conductivity k, stress tensor σ_{ij} and internal heating rate H (when specified). The values of the parameters used in this study are listed in Table 3.1. The reader is referred to *Rolf et al.* [2012] for equations describing incompressible flow.

We use 2D spherical annulus geometry [*Hernlund and Tackley*, 2008] with a varying radial resolution and the domain is discretised by 768 (lateral) times 64 (radial) cells. Around 5 million tracers are advected through the domain using a 4th-order Runge-Kutta method, and converted to a continuum compositional field using the tracer-ratio method [*Tackley and King*, 2003] (around 1 million tracers in compressible cases). We employ free-slip boundary conditions for the surface and the core-mantle boundary with the surface temperature fixed as 300 K. In the compressible models, core cooling is included with a parameterisation based on [*Buffett et al.*, 1992, 1996] and for the parameterisation details, the reader is referred to [*Nakagawa and Tackley*, 2004]. The code uses a finite volume discretisation, with velocity and pressure defined on a staggered grid. For incompressible cases a multigrid solver is used. For compressible calculations, a parallel MUMPS solver from the PETSc package is used [*Amestoy et al.*, 2000].

Table 3.3 Phase change parameters for Olivine and Pyroxene-Garnet phase systems. ρ_s is the surface density at zero pressure, $\Delta\rho$ is the density jump across a phase transition, and γ is the Clapeyron slope.

Depth (km)	Temperature (K)	$\Delta\rho$ (kg/m^3)	γ (MPa/K)
Olivine ($\rho_s = 3240\,\mathrm{kg/m^3}$)			
410	1600	180	2.5
660	1900	400	-2.5
2740	2300	61.6	10
Pyroxene-Garnet ($\rho_s = 3080\,\mathrm{kg/m^3}$)			
60	1000	350	0
400	1600	150	1
720	1900	400	1
2740	2300	61.6	10

3.2.3 Phase Changes and Composition

The model includes a parameterisation based on mineral physics data [*Irifune and Ringwood*, 1993; *Ono et al.*, 2001] in which minerals are divided into olivine and pyroxene-garnet systems that undergo solid-solid phase transitions, as used in previous studies [*Xie and Tackley*, 2004b; *Nakagawa and Tackley*, 2012]. Their mixture depends on the chemical composition, which varies between basalt (100% pyroxene-garnet) and harzburgite (75% olivine and 25% pyroxene-garnet). The phase change parameters are given in Table 3.3. At a depth of 60 km, basalt forms eclogite, which is around 190 kg/m^3 denser than olivine. At lowermost mantle depths, the phase transition from perovskite to post-perovskite is also considered [e.g., *Tackley et al.*, 2013].

3.2.4 Melting and Crustal Production

When melting is considered, melt-induced differentiation changes the composition. The reader is referred to other publications [e.g., *Xie and Tackley*, 2004b; *Nakagawa et al.*, 2010; *Lourenco et al.*, 2016] for more details. The composition field is stored and advected on tracers. At each time step, a cell-based composition is computed by mass averaging the tracers. To obtain the change in melt fraction in each cell, we compare the cell temperature to the solidus temperature (as used by [*Nakagawa and Tackley*, 2004]). In case the cell temperature exceeds the solidus, enough melt is generated in the cell to bring its temperature back to solidus leaving behind a solid depleted residue. Accordingly, molten basaltic tracers are created in each cell. If the melt generated is at

less than $300 \, \text{km}$ depth, it is removed and erupted at the surface to generate oceanic crust with the surface temperature.

3.2.5 Criterion for Correlation

To investigate whether there is a correlation between continents and elevated temperatures in the subcontinental mantle, we perform Fourier decompositions of both temperature T and composition C fields. The Fourier coefficients $a_{i,\text{f}}, b_{i,\text{f}}$ of field f for harmonic degree i are given by:

$$a_{i,\text{f}} = \frac{1}{\pi (d_2 - d_1)} \int_{\theta=0}^{2\pi} \int_{d_1}^{d_2} f(\theta, R) \cos (i\theta) \, dR \, d\theta, \tag{3.11}$$

$$b_{i,\text{f}} = \frac{1}{\pi (d_2 - d_1)} \int_{\theta=0}^{2\pi} \int_{d_1}^{d_2} f(\theta, R) \sin (i\theta) \, dR \, d\theta, \tag{3.12}$$

where d_1 and d_2 are the depths between which the temperature and composition fields are averaged. For the composition field, the coefficients are averaged over the top $100 \, \text{km}$: $d_2 - d_1 = 100 \, \text{km}$. For the temperature field, the averaging of coefficients is done starting from $70 \, \text{km}$ beneath the continents: $d_1 = d_{\text{craton}} + 70$ where d_{craton} is given in Table 3.4. Two different depth windows are used: $w_{\text{T1}} = 2890 - d_1$ for the whole mantle and $w_{\text{T2}} = 1000 - d_1$ for the upper part of the mantle. See Fig. 3.1 for a schematic representation of the model setup.

Using Fourier coefficients, we calculate the correlation function between the temperature T and composition C fields using the relation:

$$\text{corr}_{i,\text{C,T}} = (a_{i,\text{C}} a_{i,\text{T}} + b_{i,\text{C}} b_{i,\text{T}}) \frac{\pi \Delta T}{\sum_{j=1}^{i} 2/j}, \tag{3.13}$$

where $\Delta T = 2500 \, \text{K}$ is a constant used to dimensionalise temperature. The second term on the right hand side of Eq. 3.13 is used to obtain the amplitude of the temperature anomalies assuming discontinuous continents. This formulation helps in detecting the amplitude of a degree i sinusoidal thermal anomaly below a Heaviside shaped continent of identical degree.

3.3 Results

In order to investigate both the magnitude of temperature anomalies appearing below continents and their effects on mantle convection, we performed two sets of simulations.
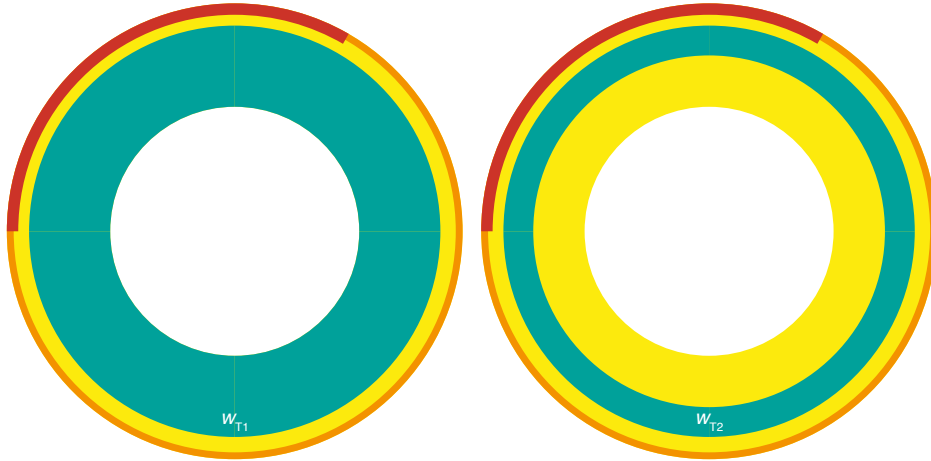
Fig. 3.1 Schematic representation of the model with continent (red), composition correlation window (orange), and temperature correlation windows w_T (teal) as defined in Section 3.2.5.

First, we ran 33 cases considering incompressible convection with constant basal and internal heating (Table 3.4). Second, we performed 18 simulations considering compressible convection with core cooling, time-dependent internal heating, melting and crustal production (Table 3.5).

The absence of melting, and thereby the lack of consumption of latent heat in the first set of simulations allows the mantle temperatures to rise. Thus, we were able to study the effect of core temperature T_{cmb}, number of continents n_{craton}, radiogenic heating H, and convective vigour Ra on the amplitude of these thermal anomalies. In cases with melting and crustal production, we also observed the development of these thermal anomalies below the continents, which often caused their breakup.

3.3.1 First set of simulations: Incompressible convection without MCP

In this set of simulations, we systematically varied the following parameters (see Table 3.4):

- Constant internal heating: $H = 0$, $3 \cdot 10^{-12}$ and $6 \cdot 10^{-12}$ W/kg,

- Constant core temperature: $T_{cmb} = 2000$, 3000 and 4000 K,

- Initial number of continents: 1, 2 and 6, where the sum of the continents' length is always 30% of the surface length,

- Position of continents: poles and equator,

Table 3.4 Incompressible simulations with core temperature T_{cmb} (K), radiogenic heating H (W/kg), Rayleigh number Ra, cratonic thickness d_{craton} (km), reference viscosity η_0 (Pa·s), number of continents n_{craton}, final model runtime t_r (Gyr), average velocity v_{RMS} (cm/yr), mean surface heat flow Q_{surf} (TW), mean CMB heat flow Q_{cmb} (TW), dominant degree of correlation deg and its amplitude $corr$ (K). For correlation, temperature field was averaged in the depth window w_{T1} for all simulations.

T_{cmb}	H	Ra	η_0	n_{craton}	d_{craton}	t_r	v_{RMS}	Q_{surf}	Q_{cmb}	deg	$corr$
2000^x	0	$1 \cdot 10^6$	$7.88 \cdot 10^{22}$	1	570	4.50	0.06	2.17	2.01	-	-
2000^x	0	$1 \cdot 10^6$	$7.88 \cdot 10^{22}$	2	570	4.14	0.05	2.14	1.96	-	-
2000^x	0	$1 \cdot 10^6$	$7.88 \cdot 10^{22}$	6	570	3.84	0.04	1.96	1.80	-	-
3000	0	$1 \cdot 10^6$	$7.88 \cdot 10^{22}$	1	570	4.50	0.46	12.57	11.78	1	231.24
3000	0	$1 \cdot 10^6$	$7.88 \cdot 10^{22}$	2	570	3.60	0.40	12.67	11.55	2	55.89
3000	0	$1 \cdot 10^6$	$7.88 \cdot 10^{22}$	3	570	4.50	0.39	13.74	12.08	3	3.57
3000	0	$1 \cdot 10^6$	$7.88 \cdot 10^{22}$	4	570	4.50	0.35	14.10	12.66	1	17.38
3000^x	0	$1 \cdot 10^6$	$7.88 \cdot 10^{22}$	5	570	4.50	0.33	14.14	12.86	-	-
3000^x	0	$1 \cdot 10^6$	$7.88 \cdot 10^{22}$	6	570	4.50	0.26	13.72	12.91	-	-
4000	0	$1 \cdot 10^6$	$7.88 \cdot 10^{22}$	1	570	4.50	1.81	31.67	34.61	2	10.02
4000	0	$1 \cdot 10^6$	$7.88 \cdot 10^{22}$	2	570	4.50	1.50	33.26	35.34	2	9.78
4000	0	$1 \cdot 10^6$	$7.88 \cdot 10^{22}$	6	570	2.69	1.29	31.06	36.19	1	7.29
$2000^{i,x}$	0	$1 \cdot 10^6$	$7.88 \cdot 10^{22}$	2	570	2.23	0.05	2.62	2.22	-	-
3000^i	0	$1 \cdot 10^6$	$7.88 \cdot 10^{22}$	2	570	2.93	0.36	13.22	11.63	1	65.81
$4000^{i,x}$	0	$1 \cdot 10^6$	$7.88 \cdot 10^{22}$	2	570	0.89	1.03	31.57	32.88	-	-
3000	$3 \cdot 10^{-12}$	$1 \cdot 10^6$	$7.88 \cdot 10^{22}$	1	570	4.50	1.08	20.25	12.40	1	75.71
3000	$3 \cdot 10^{-12}$	$1 \cdot 10^6$	$7.88 \cdot 10^{22}$	2	570	4.50	0.78	21.25	13.09	2	20.84
3000	$3 \cdot 10^{-12}$	$1 \cdot 10^6$	$7.88 \cdot 10^{22}$	6	570	4.50	0.74	21.64	13.75	1	14.47
3000^x	$3 \cdot 10^{-12}$	$5 \cdot 10^6$	$1.57 \cdot 10^{22}$	1	335	1.60	1.57	24.79	19.39	-	-
3000	$3 \cdot 10^{-12}$	$5 \cdot 10^6$	$1.57 \cdot 10^{22}$	2	335	4.50	1.67	28.23	20.61	2	14.98
3000	$3 \cdot 10^{-12}$	$5 \cdot 10^6$	$1.57 \cdot 10^{22}$	6	335	4.50	1.77	27.75	20.97	2	3.84
3000	$3 \cdot 10^{-12}$	$1 \cdot 10^7$	$7.88 \cdot 10^{21}$	1	263	4.50	2.35	29.83	23.12	1	18.34
3000	$3 \cdot 10^{-12}$	$1 \cdot 10^7$	$7.88 \cdot 10^{21}$	2	263	4.50	2.24	29.16	23.38	2	6.40
3000	$3 \cdot 10^{-12}$	$1 \cdot 10^7$	$7.88 \cdot 10^{21}$	6	263	4.50	2.49	29.09	24.08	1	5.67
3000	$6 \cdot 10^{-12}$	$1 \cdot 10^6$	$7.88 \cdot 10^{22}$	1	570	4.50	1.88	26.52	13.20	1	54.78
3000	$6 \cdot 10^{-12}$	$1 \cdot 10^6$	$7.88 \cdot 10^{22}$	2	570	4.50	1.13	29.55	14.01	2	28.24
3000	$6 \cdot 10^{-12}$	$1 \cdot 10^6$	$7.88 \cdot 10^{22}$	6	570	4.50	1.29	29.49	14.71	6	-3.76
3000	$6 \cdot 10^{-12}$	$5 \cdot 10^6$	$1.57 \cdot 10^{22}$	1	335	4.50	2.42	33.56	20.32	1	20.70
3000	$6 \cdot 10^{-12}$	$5 \cdot 10^6$	$1.57 \cdot 10^{22}$	2	335	4.50	2.39	34.53	21.19	2	9.33
3000	$6 \cdot 10^{-12}$	$5 \cdot 10^6$	$1.57 \cdot 10^{22}$	6	335	4.50	2.80	31.67	21.21	2	2.41
3000	$6 \cdot 10^{-12}$	$1 \cdot 10^7$	$7.88 \cdot 10^{21}$	1	263	4.50	3.05	35.74	23.70	1	17.79
3000	$6 \cdot 10^{-12}$	$1 \cdot 10^7$	$7.88 \cdot 10^{21}$	2	263	4.50	2.99	36.73	24.30	2	5.64
3000	$6 \cdot 10^{-12}$	$1 \cdot 10^7$	$7.88 \cdot 10^{21}$	6	263	4.50	3.44	35.82	24.83	1	6.29

[x] unrealistic cases excluded from scaling laws.

[i] continents in the same hemisphere.

Table 3.5 Compressible simulations with melting and crustal production. Initial core temperature T_{cmb} (K), number of continents n_{craton}, depth window for averaging temperature field w_T, average velocity v_{RMS} (cm/yr), mean surface heat flow Q_{surf} (TW), mean CMB heat flow Q_{cmb} (TW), dominant degree of correlation deg and its amplitude $corr$ (K). Reference viscosity $\eta_0 = 1 \cdot 10^{20}$ Pa·s, radiogenic heating H = $1.8 \cdot 10^{-11}$ W/kg, cratonic thickness $d_{craton} = 231$ km, and final model runtime t_r = 4.5 Gyr for all simulations.

T_{cmb}	n_{craton}	w_T	v_{RMS}	Q_{surf}	Q_{cmb}	deg	$corr$
3500	1	1	1.19	16.35	5.85	1	38.86
3500	1	2	0.91	13.12	5.45	1	17.32
3500	2	1	0.89	12.63	5.68	1	56.06
3500	2	2	0.94	13.04	5.92	2	20.30
4000	1	1	2.03	18.40	12.59	1	19.62
4000	1	2	1.74	17.48	13.17	1	28.08
4000	2	1	1.52	17.77	13.31	2	13.26
4000	2	2	2.01	16.68	12.03	2	0.07
4500	1	1	1.48	18.58	13.23	7	-3.05
4500	1	2	1.50	19.02	13.33	1	23.52
4500	2	1	1.50	16.97	13.30	9	-5.47
4500	2	2	1.49	19.31	12.95	2	5.95

- Rayleigh number: $Ra = 10^6$, $5 \cdot 10^6$ and 10^7, with $Ra = (\alpha \rho g \Delta T D^3)/(\kappa \eta)$ (see Table 3.1 for all parameters).

To obtain a realistic thickness ratio of continental to oceanic lithosphere [*Rolf and Tackley*, 2011], the initial thickness of continental material is scaled using the Rayleigh number, as the equilibrium lithosphere thickness depends on Ra [*Solomatov*, 1995]. The spectral decomposition of the temperature field is computed from 70 km below the continent to the core-mantle boundary: $d_1 = d_{craton} + 70$. The Fourier coefficients of the composition field are computed in the top 100 km of the mantle. A small thermal perturbation of 125 K is introduced in the mid-mantle on the polar opposite side of the supercontinent to help initiate the first upwellings.

3.3.1.1 Qualitative observations

Fig. 3.2 and 3.3 depict the temporal evolution of 4 cases to help understand why and how temperature rises below continents. Fig. 3.2 shows the evolution of the temperature fields and Fig. 3.3 represents the evolution of the correlation between temperature and composition field (cratons) for harmonic degrees 1 to 20. The rows of both figures are organised as follows:

- a: one supercontinent, no internal heating,

- b: two continents initially at poles, no internal heating,

- c: two continents initially in the same hemisphere, no internal heating,

- d: one supercontinent, strong internal heating ($H = 6 \cdot 10^{-12}\,\mathrm{W/kg}$).

These four cases employ a Rayleigh number of 10^6 and a core temperature of $3000\,\mathrm{K}$.

Fig. 3.2 shows that the initial plumes rising from the core-mantle boundary are slower below the continents in all cases. Away from the continents, the oceanic lithosphere is weak enough to subduct and it brings cold material down into the lower mantle, thus providing additional buoyancy to the plumes. As the continents are 100 times more viscous and have 10 times the yield stress compared to the oceanic lithosphere, they do not break. A higher heat flux is generated around the continents and the downwellings along continental margins start to cool the mantle. The mantle exhibits a degree-1 thermal structure with a hotter region underneath the supercontinent and a colder region on the polar opposite side of the mantle ($450\,\mathrm{Myr}$ onwards in Fig. 3.2a, 3.3a). The correlation between continent and temperature field arises as soon as convection cells form due to the strength of the cratonic material and this correlation is maintained throughout the simulation with a maximum amplitude of $237\,\mathrm{K}$.

Additionally, cases with 2 continents (each covering $15\,\%$ of surface area) initialised at the poles and in the same hemisphere are also presented. When the 2 continents are on the polar opposites, a degree-2 thermal structure is dominant in the mantle (Fig. 3.2b, 3.3b) with a brief episode of anti-correlation in degree-2 between 1 and $1.5\,\mathrm{Gyr}$ of evolution. This anti-correlation can be understood by looking at the last column of Fig. 3.2b, which shows that downwellings can be pushed to the edges of the continents and produce cold anomalies below the continents. In Fig. 3.2c, 3.3c, continents are first grouped until $500\,\mathrm{Myr}$, which generates a degree-1 correlation. They separate and form a degree-2 correlation until $1.3\,\mathrm{Gyr}$ and then come close again, which brings the correlation back to degree-1. These cases show that thermal structure of the mantle and the degree of the continent-temperature correlation follows the geometrical configuration of the cratons.

Finally, Fig. 3.2d, 3.3d show that a degree-1 correlation below a supercontinent can survive strong internal heating but is lower in amplitude.
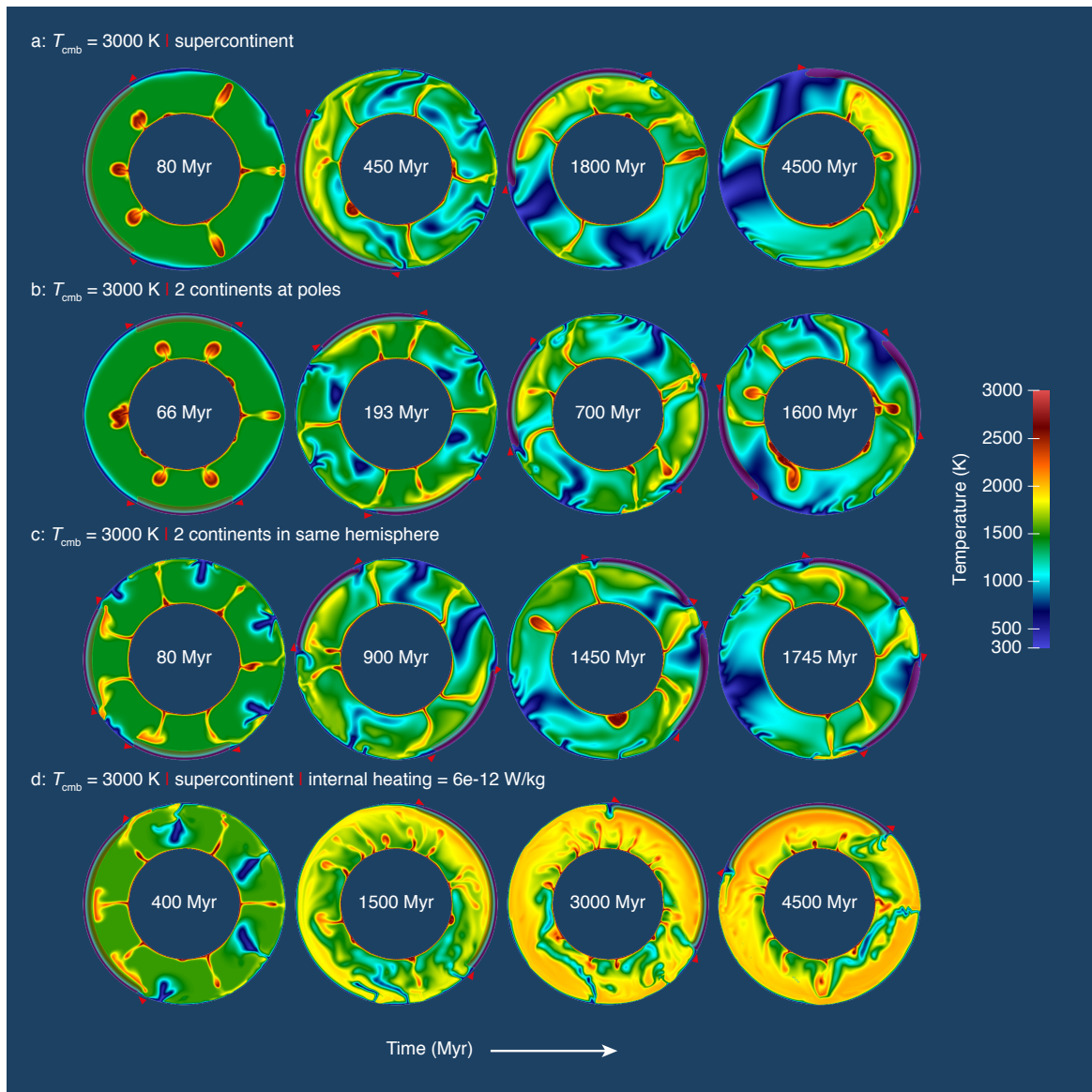
Fig. 3.2 Thermal evolution of the incompressible models without MCP. Red triangles demarcate the continents, which are represented by composition field (violet) superimposed over the temperature field.

Effect of the core temperature

Cases with $T_{\mathrm{cmb}} = 2000\,\mathrm{K}$ (not shown) show similar processes of rising mantle plumes, subduction and entrenchment of cold slabs in the convecting mantle and a buildup of elevated temperatures in the subcontinental mantle. Yet, the low core temperature does not allow the mantle to maintain a reasonable internal temperature. Large downwellings strongly decrease the ambient temperature, which leads to an unrealistic situation in
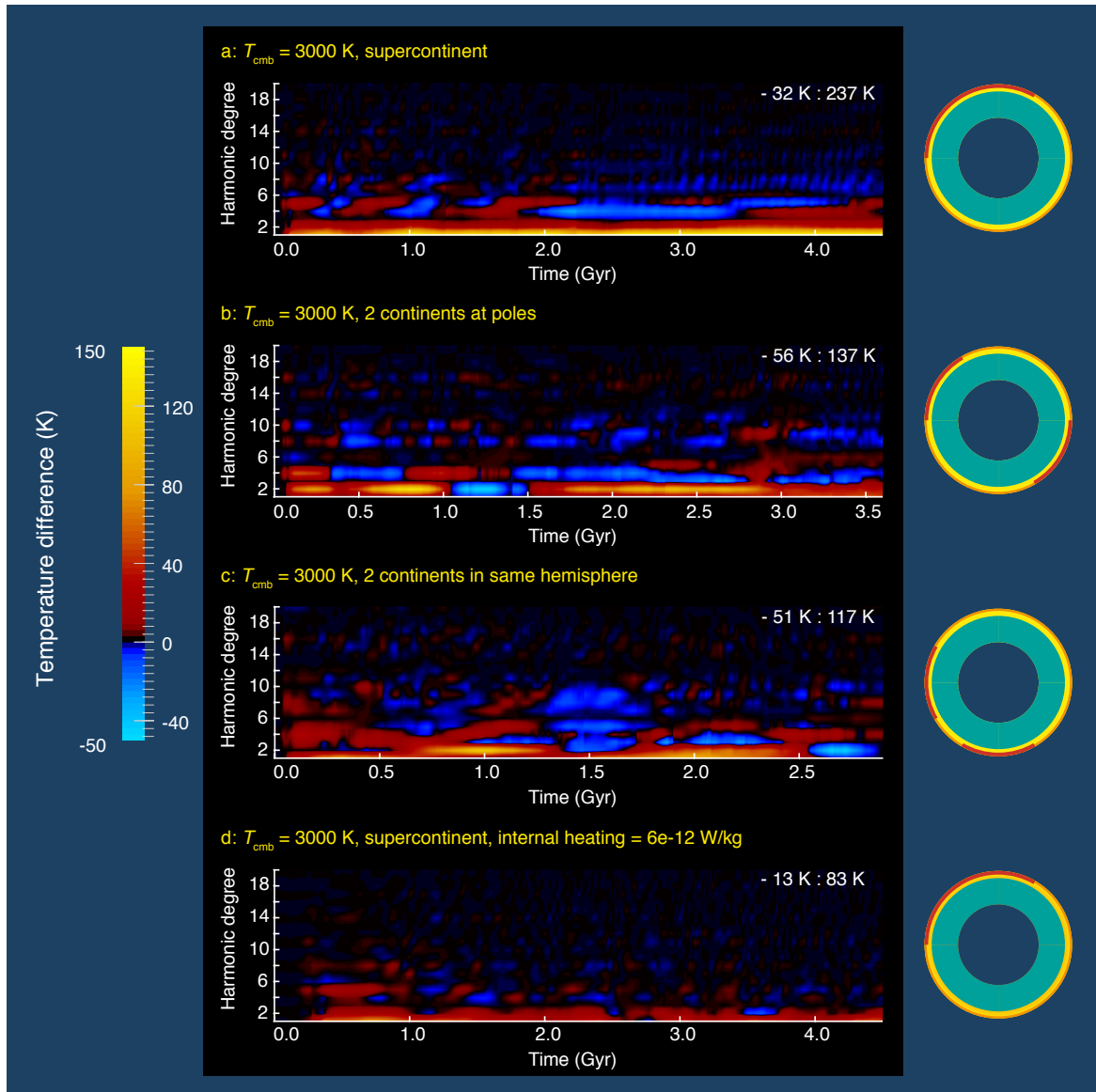
Fig. 3.3 (left) Spectrogram where positive (red to yellow) and negative (shades of blue) values indicate correlation and anti-correlation between continental material at the surface and elevated temperatures underneath it respectively. Also shown are the minimum and maximum temperature contrasts obtained from the models. (right) Schematic representation of the model with the initial position of the continents and the temperature correlation window w_{T1}

which the lithosphere propagates in the entire mantle away from plumes. We do not use these cases for our scaling laws of correlation amplitude (see below). In cases with $T_{\mathrm{cmb}} = 4000\,\mathrm{K}$ (not shown), there are many more thermal instabilities at the bottom,

which is expected with a hotter core. Again, the region of subcontinental warming develops but this thermal contrast is diffused over time with the strong convective flow.

Effects of the Rayleigh number and internal heating rate

We observe that an increase in Rayleigh number or internal heating rate both tend to decrease the magnitude of the correlation between continents and mantle temperature. In both cases, convective stirring tends to make the correlation fade away, even though it still spontaneously appears due to the downwellings. This naturally happens when the Rayleigh number is high as the flow is fast and small wavelengths form. When strong radiogenic heating is considered, strong stirring takes some time to appear as it arises from the decrease of viscosity with time.

3.3.2 Second set of simulations: Compressible convection with MCP

In this second set of simulations, we used a more realistic setup in which the core cools with time, radiogenic heating decays and more importantly, melting and crustal production are considered. As these features result in much higher computational costs, a smaller number of simulations were run in the selected parameter space.

The primary distinguishing aspect of these models is the inclusion of melting of pyrolytic mantle and the subsequent basaltic crustal production. Two different correlation windows w_T define the depth range over which the temperature field is averaged with $w_\text{T1} = 300 - 2890\,\text{km}$ and $w_\text{T2} = 300 - 1000\,\text{km}$. Continental thickness is initialised as $230\,\text{km}$ and all the cases have mixed heating with a reference viscosity $\eta_0 = 10^{20}\,\text{Pa·s}$ (the viscosity now also depends on pressure). The concentration of heat-producing trace elements is initially $H = 18 \cdot 10^{-22}\,\text{W/kg}$, decreasing with time with a half-life of $2.43\,\text{Gyr}$. Unlike the incompressible cases, no thermal anomaly is introduced in the models because it might lead to an artificial melting event.

CMB Temperature, Continental Configuration and Correlation Windows

In this set of simulations, the mechanical behaviour leading to cooling around the continents is also observed. The main difference with the first set of simulations is that a continent-temperature correlation now leads to melting and crustal production events, which tend to break continents apart and therefore destroy the correlation. Fig. 3.4 shows the time-dependence of the correlation for each degree (panel a) and

illustrates a breakup event resulting from melting and crustal production (panel b) for a simulation starting with one supercontinent.

Fig. 3.4a shows that the temperatures in the subcontinental mantle get elevated owing to the supercontinent above and a degree-1 correlation quickly develops and grows until ∼1.3 Gyr. Afterwards, correlations in degree 2 and 4 appear in the spectrogram until ∼2.2 Gyr, when a degree 6 correlation and a degree 2 anti-correlation become dominant. The strong anti-correlation demonstrates that continental insulation is a transient phenomenon and can be explained as follows.

These elevated temperatures exceed the pyrolytic mantle solidus and result in the partial melting and production of basaltic melt (1333 Myr in Fig. 3.4b). This melt is instantaneously removed from the depth and placed at the surface above the continents to simulate volcanic eruption. With time, this basaltic material gets buried and transforms into eclogite at a depth of 60 km. Eclogite is around 190 kg/m^3 denser than olivine and it becomes gravitationally unstable in the lithosphere [*Lourenco et al.*, 2016]. A combination of this dense eclogitic material and the high stresses imposed by the mantle plumes break the supercontinent apart into several fragments.

Fig. 3.4b shows that the breakup of a supercontinent does not happen instantly. A first crustal production event initiates the breakup around 1333 Myr, but the plume providing the basaltic melt does not fully break the continent. The breakup fully happens only 300 Myr later above another plume cluster. The timing of this breakup might strongly depend on the Rayleigh number, which was not tested in this set of simulations. Following the breakup, these smaller continents drift apart with the convecting mantle and the continent-temperature correlation slowly fades away. The buildup of a new correlation requires large-scale mantle flow reorganisation, which might never happen if the continents are too small or too mobile.
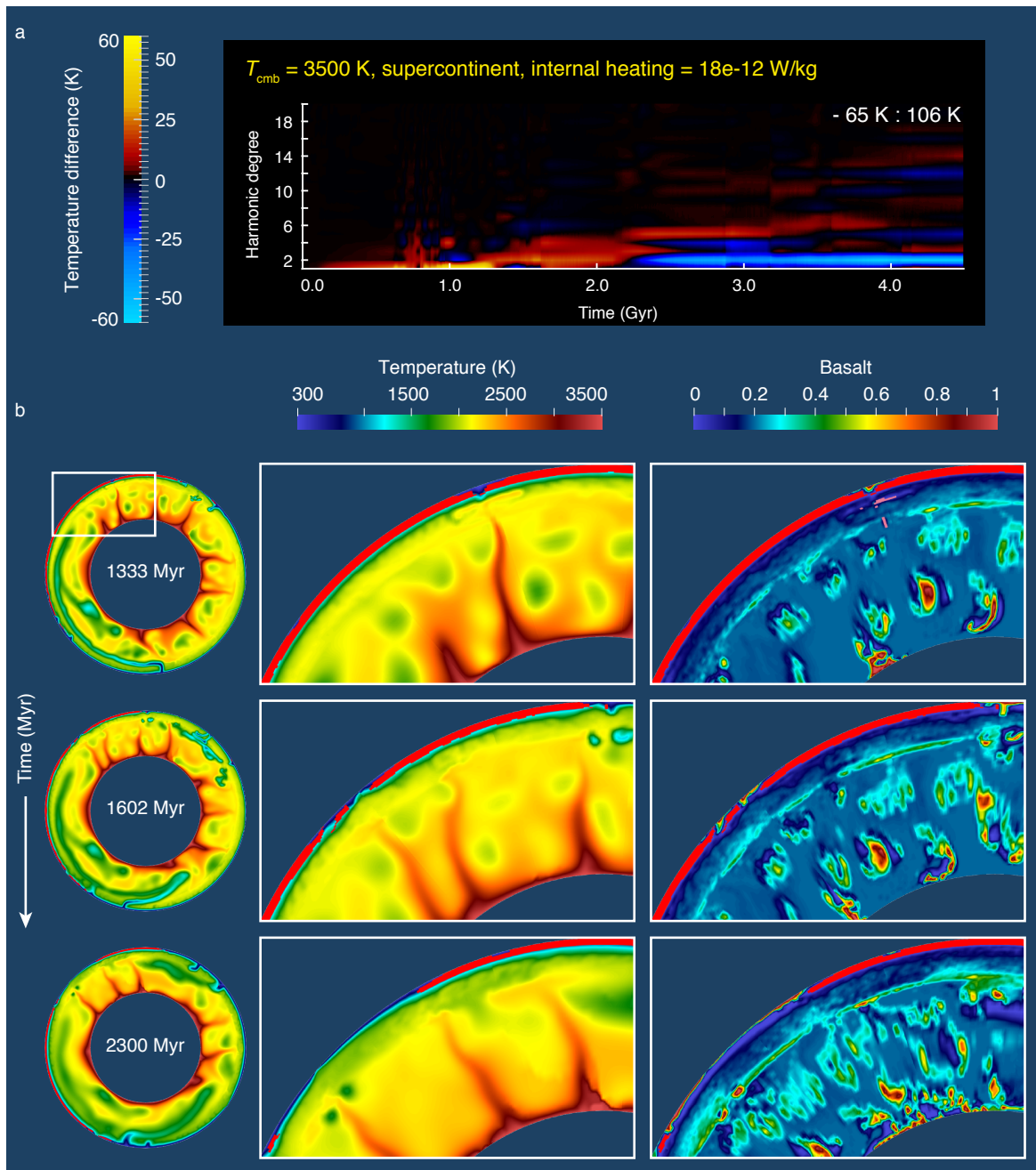
Fig. 3.4 Continental breakup in a compressible simulation with MCP, 3500 K CMB temperature, supercontinent, internal heating, and correlation temperature window w_{T2}. **a,** spectrogram showing how the dominant harmonic degrees changes with time. **b,** thermal evolution of the simulation with time on global scale (left) and local scale (middle). Also shown is the basalt content (right) with pockets of mantle melt (pink). Continents are represented by composition field (red) superimposed over temperature and basalt fields.

3.4   Discussion

3.4.1   Scaling laws for continent-temperature correlation

Our spectral decomposition of temperature and composition fields allows us to quantify the correlation between continents and mantle temperature. Using most of the cases depicted in Table 3.4 (see superscripts in the table for details), we were able to find a first order empirical equation to quantify the magnitude of the correlation. Table 3.6 shows the scaling laws for the first and second sets of simulations. For the first set of simulations, 4 parameters have been used to perform the regression of the correlation: T_{cmb}, n_{craton}, H and Ra. For the second set, H and Ra were identical in all simulations and are therefore absent from the scaling laws. Two scalings are provided for the second set of simulations as we perform correlations in the entire mantle (300-2890 km) and upper part of mantle (300-1000 km).

In all cases, we observe that the correlations scale exponentially with all parameters. We therefore investigate the linear effect of each parameter on the logarithm of the correlation. We observe that an increase in T_{cmb}, n_{craton}, H or Ra all lead to a decrease in correlation. The dominant degree was used to scale the second sets of simulations instead of the initial number of continents as the continents are split in several parts and therefore their number varies. Looking at the entire mantle, we find that the core temperature plays a negligible role in forming a correlation. Yet, the third equation in Table 3.6 shows that the correlation between the upper part of the mantle and the continents strongly depends on the core temperature. This shows that the plumes provide large temperature anomalies in the upper part of the mantle but contribute less to the formation of low degree patterns in the lower mantle. Moreover, broad downwellings tend to gather in the lower mantle disregarding the continental configuration at the surface due to the spherical geometry.

Fig. 3.5 represents the correlations used to perform the scaling laws (on the y-axis) versus the results of the scalings (x-axis). Globally, correlation amplitudes are between 0 and 40 K but also reach up to 100 to 200 K. Amplitudes of correlations in simulations considering melting and crustal production reach a maximum of 30 to 60 K (red squares and purple diamonds respectively). Overall, regressions are of good quality as the standard deviations are of the order of 5-7 K (see Table 3.6).

Table 3.6 Scaling laws for the continent-temperature correlation (K). $\text{corr}_{i,\text{C,T}}$ is the correlation of the degree that shows the highest value.

Incompressible convection - No melting	Stand. Dev.

$$\begin{aligned} \ln\left(\text{corr}_{i,\text{C,T}} - 6.944\right) \quad = \quad & 0.732 - 12.422\left(\tfrac{T_{\text{cmb}}}{3000} - 1\right) - 4.416\left(\tfrac{n_{\text{craton}}}{3} - 1\right) \\ - \quad & 0.893\left(\tfrac{H}{2.72\cdot 10^{-12}} - 1\right) - 1.043\left(\tfrac{Ra}{5\cdot 10^6} - 1\right) \end{aligned}$$

7.31 (K)

Compressible convection - Melting - whole mantle	Stand. Dev.

$$\ln\left(\text{corr}_{i,\text{C,T}} - 1.148\right) \quad = \quad 0.980 - 3.154\left(\tfrac{\text{degree}}{3} - 1\right)$$

6.77 (K)

Compressible convection - Melting - upper part of mantle	Stand. Dev.

$$\ln\left(\text{corr}_{i,\text{C,T}} + 6.254\right) \quad = \quad 2.711 - 0.810\left(\tfrac{\text{degree}}{3} - 1\right) - 5.863\left(\tfrac{T_{\text{cmb}}}{4000} - 1\right)$$
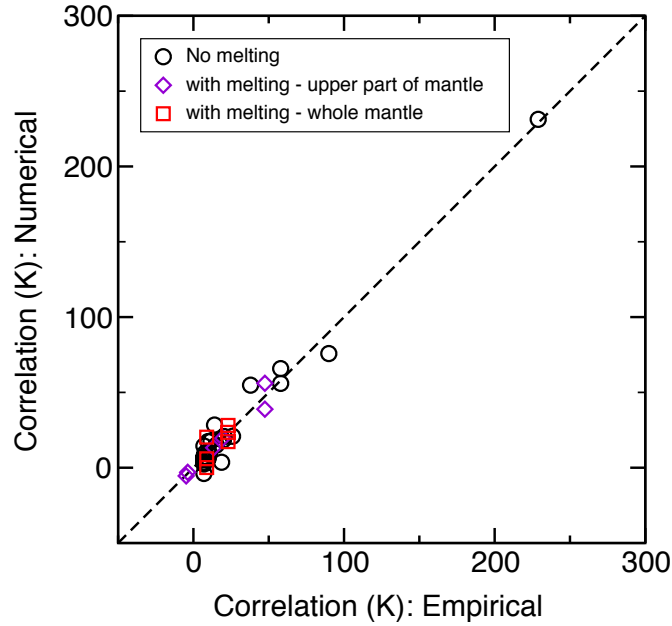
4.98 (K)

Fig. 3.5 Numerical continent-temperature correlations (K) (y-axis) versus their scaling laws as defined in Table 3.6 (x-axis) for all cases. Black circles represent the first set of simulations with no melting and crustal production, diamonds and squares depict the results of the second set of simulations. Correlations are of the order of tens to hundreds of K.

3.4.2   Implications of our results

We have tested the impact of basal heating on correlation by initialising our models with different CMB temperature at the bottom boundary. The need to test this arises due to the uncertain nature and contribution of CMB heat flow towards mantle dynamics. Continental motion is attributed to the viscous stresses imparted by the convecting mantle and the extent of this motion depends on the heat budget of the mantle. CMB heat flow, internal heating from decay of radioactive elements in the mantle, and secular mantle cooling contribute to this heat budget. Recent indications that the core's thermal conductivity may be three times higher than previous mineral physics estimates [*de Koker et al.*, 2012; *Pozzo et al.*, 2013; *Gomi et al.*, 2013] and the inclusion of the post-perovskite phase change in the lower mantle [*Hernlund et al.*, 2005] constrain the heat flow from the core to be in the range of 10-16 TW [*Lay et al.*, 2006; *van der Hilst et al.*, 2007; *Lay et al.*, 2008; *Hernlund*, 2010], although a lower core thermal conductivity has been advocated by [*Zhang et al.*, 2015]. Some mantle convection models [*Zhong*, 2006; *Leng and Zhong*, 2008] have shown that heat flow from plumes can account for a significant fraction of the CMB heat flow, implying that mantle plumes should be considered when studying mantle dynamics coupled with continents. Table 3 gives the CMB heat flow and v_{RMS} of the whole mantle for all the cases averaged over their simulation time. Cases with $T_{\mathrm{cmb}} = 3000\,K$ give CMB heat flow and v_{RMS} of the order of 11-13 TW and 0.25-0.45 cm/yr respectively. The heat flow values obtained from these models are in agreement with the recent heat flow estimates as discussed above and the low root-mean-square velocity of the whole mantle can be attributed to the lack of internal heating. Our models show a general trend of decreasing correlation with increasing T_{cmb} but this could be misleading. Using the CMB heat flow from these models as a metric to check how close they are to the actual Earth, we argue that CMB temperatures of 2000 K or 4000 K are not realistic values in an incompressible setup. It should be noted that in an incompressible model with $T_{\mathrm{surf}} = 300\,\mathrm{K}$ and $T_{\mathrm{cmb}} = 3000\,\mathrm{K}$, the entire 2700 K will drive convection whereas in a compressible model, around 1000-1200 K of it will be taken up by an adiabatic temperature increase and only the remaining 1500-1700 K will drive convection. This implies that a given T_{cmb} in an incompressible model will give similar behaviour (e.g. in terms of plumes excess temperature) to one about 1000-1200 K higher in a compressible model.

To validate our numerical models by comparing them with present-day seismic observations and long-term observations such as plate-tectonic reconstructions is a good idea [e.g., *Engebretson et al.*, 1984; *Scotese*, 1991; *Deparis et al.*, 1995; *Lithgow-*

Bertelloni and Richards, 1998; *Torsvik et al.*, 2010]. Numerous seismic tomographic studies [e.g., *Su et al.*, 1994; *Li and Romanowicz*, 1996; *Su and Dziewonski*, 1997; *van der Hilst et al.*, 1997; *Ritsema et al.*, 1999; *Masters et al.*, 2000; *Grand*, 2002; *Zhao*, 2004; *Panning and Romanowicz*, 2006; *Houser et al.*, 2008; *Ritsema et al.*, 2011] have unanimously observed slow S-wave velocity anomalies beneath Africa and the Pacific, indicating a degree-2 structure for the Earth's mantle. Though our models only show a dominant degree-1 structure with a supercontinent (Fig. 3.2a & 3.3a) and degree-2 with 2 continents (Fig. 3.2b & 3.3b), these observations might have been relevant in early geological history.

The latest plate-tectonic reconstruction models have gone back as far as 500 Ma. *Torsvik et al.* [2014] found a correlation between the edges of large low shear-wave velocity provinces (LLSVPs) and the reconstructed positions of large igneous provinces (LIPs) and kimberlites. They proposed that the African and Pacific LLSVPs have been mostly stable and stationary, giving the mantle its degree-2 structure through the entire Phanerozoic Eon (∼500 Ma). This proposal has been challenged by *Zhong et al.* [2007]; *Zhong and Liu* [2016] who concluded from their models that the formation of African LLSVP occurred around 330 Ma following the supercontinent Pangea assembly. They proposed that an intrinsic degree-1 mantle structure may force the smaller continents to aggregate over the antipodal downwelling hemisphere [*Monin*, 1991; *Evans*, 2003] and form a supercontinent over a time scale of 300 Myr. The following circum-supercontinent subduction would create upwellings and elevate the temperature in the subcontinental mantle, thereby turning a degree-1 pattern into degree-2. Eventually, the supercontinent may break apart. However, this result was obtained by placing a fixed continent above the centre of the downwelling region.

Although our models do not allow the continents to merge, they do show continents moving over downwelling regions (Fig. 3.2b, 1600 Myr), which also occurs with the continents in the same hemisphere (Fig. 3.2c, 1450 Myr). Our models show that continents focus heat underneath them causing subcontinental mantle warming. The amplitude of this warming changes with continental extent, CMB temperature, Rayleigh number and internal heating. A higher amplitude is observed with a supercontinent (up to 237 K) and it decreases with smaller extent of the continents. This is in agreement with previous results of *Coltice et al.* [2007]; *O'Neill et al.* [2009]; *Phillips and Coltice* [2010]; *Lenardic et al.* [2011]; *Rolf et al.* [2012] who also reported elevated temperatures below continents. This is in contrast with the findings of *Heron and Lowman* [2010, 2011] where they did not observe any thermal contrast between subcontinental and suboceanic mantle. However, they prescribed the same thickness for continental and

oceanic plates in their models, which is not representative of Earth. We see the tendency of slabs to subduct along continental margins in all our models, which helps in creating subcontinental mantle upwellings. Previous work by *O'Neill et al.* [2009]; *Heron et al.* [2015] has shown similar results.

When included, internal heating increases the effective convective vigor of the mantle and makes for a drastic change in the style of mantle dynamics. The internal temperature is higher and a decrease in the number of slabs stagnating at the lower boundary is observed. The more effective mantle mixing lowers the thermal isolation between the subcontinental and suboceanic mantle. Compared to the models with only basal heating, the amplitude of degree-1 decreases (Fig. 3.3d) and for cases with effective $Ra_H > 2e7$, no correlation is observed. This is in agreement with the main findings of *Heron and Lowman* [2014] who also report a decreasing effect of continental insulation with increasing Ra.

Anderson [1982b] proposed that a supercontinent can insulate the underlying mantle and the subsequent build-up of this heat can cause a large-scale melting event. Previous work by *Coltice et al.* [2007, 2009] has supported this proposal. Alternatively, it has been suggested that mantle plumes can cause intense magmatic activity while emplacing continental flood basalts followed by continental rifting [e.g., *Morgan*, 1983; *Richards et al.*, 1989; *Condie*, 2004b]. Studies have also shown the propensity of plumes to rise and concentrate under the relatively hotter subcontinental mantle [e.g., *Gurnis*, 1988; *Zhong and Gurnis*, 1993; *Guillou and Jaupart*, 1995; *Phillips and Bunge*, 2005]. Our compressible models with melting and crustal production are somewhat a mix of both the scenarios mentioned above. The plumes that rise up to the surface result in large-scale magmatism, producing a basaltic crust. This basaltic material changes into denser eclogite at a depth of 60 km and helps in rifting the continents. These voluminous basalt generating events in our models can be likened to the emplacement of continental flood basalts of the Central Atlantic Magmatic Province following the breakup of Pangea. In general, a supercontinent or 2 large continents are still able to focus heat underneath them and the continental breakup is reflected in the changing dominant degree of correlation. This correlation is elusive when the continents are broken apart into smaller fragments due to MCP and are not effective in warming the subcontinental mantle.

3.5   Conclusions

In the past, many numerical studies of varying complexity have tried to answer the question of whether continents warm up the underlying mantle. We contribute to this discussion by offering qualitative observations from 2D mantle convection simulations with mobile continents. Furthermore, we provide numbers quantifying the extent of this continent-temperature correlation by analytical scaling laws. Starting with simple incompressible models, we show that the dominant degree of correlation changes with continental distribution and its amplitude can reach up to 200 K, depending on the extent of the continents. We also show that this correlation decreases with increasing core temperature, number of continents, radiogenic heat production, and Rayleigh number. These results reaffirm the previous findings of *O'Neill et al.* [2009]; *Phillips and Coltice* [2010]; *Rolf et al.* [2012]; *Heron and Lowman* [2014]. When using a more realistic compressible setup with core cooling and MCP, our models tell a different story not seen before. We observe that melting and crustal production caused by the correlation helps to break the continents apart, thereby drastically reducing this correlation (amplitude of tens of K). Further modelling efforts should include real continental growth by differentiation of the mantle, instead of using prescribed continents. In this study, we considered fully eruptive magmatism. In the future, the influence of plutonism on this correlation should be explored as it has been to shown to play an important role in shaping the Earth's lithosphere [*Crisp*, 1984; *Cawood et al.*, 2013; *Rozel et al.*, 2017].

Chapter 4

Growing primordial continental crust self-consistently in global mantle convection models

This chapter is under preparation and is to be submitted as Jain, C., Rozel A. B., Tackley, P. J., Sanan, P., and Gerya, T. (2017), Growing primordial continental crust self-consistently in global mantle convection models. *Gondwana Research*

Abstract

It is widely accepted that the majority of continental crust formed during the hotter Archean was composed of Tonalite-Trondhjemite-Granodiorite (TTG) rocks. In contrast to the present-day loci of crust formation around subduction zones and intra-plate tectonic settings, TTGs are formed when hydrated basalt melts at garnet-amphibolite, granulite or eclogite facies conditions. Generating continental crust requires a two step differentiation process. The basaltic magma is extracted from the pyrolytic mantle, it gets hydrated, and then partially melts to form continental crust. Here we parameterise the melt production and melt extraction processes and show the self-consistent generation of primordial continental crust using evolutionary thermochemical mantle convection models, which to our knowledge is the first time it has been done on a global scale. To study the growth of TTG and the geodynamic regime of early Earth, we systematically vary the ratio of intrusive (plutonic) and eruptive (volcanic) magmatism, initial core temperature, and internal friction coefficient. Corroborated by scaling laws, our simulations show two distinct stages of TTG production: a period of

continuous linear growth with time and intense recycling similar to plutonic squishy lid tectonics that lasts until 1 billion years, followed by a stage with the TTG growth proportional to cubic root of time and moderate recycling. We observe this drop in TTG production owing to mantle depletion around 3.5 Ga and without a major shift in the global geodynamic regime towards subduction and plate tectonics. The crustal volumes obtained from our simulations are in agreement with many continental crust growth models based on geological proxies. The resolution of our simulations allows us to see lower crustal delamination and dripping, formation of stacked continental-like terranes, and recycling of continental crust. Future improvements will include magmatic weakening and the coeval formation of strong, depleted, and viscous cratonic roots.

4.1   Introduction

Floating at the top of the mantle and helping to sustain life, continents cover about a third of the Earth's surface area. They have cores of Archean and Proterozoic cratonic basements [*Goodwin*, 1991; *Hoffmann*, 1989] underlying a chemically evolved continental crust. Continental crust has an average thickness of 40 km [*Rudnick and Gao*, 2003] and is separated from the ultramafic rocks of the mantle by the Mohorovičić discontinuity. Compared to the thin (7 km on average) and ephemeral oceanic crust with a maximum life span of ~ 200 Myr, continental crust is much older [*Rudnick and Gao*, 2003]. The crust is andesitic in composition, which lies between basalt and rhyolite with 60.6% SiO_2 and 4.7% MgO [*Hawkesworth and Kemp*, 2006a]. Though accounting for only 0.57% of the mass of the Earth's mantle, continental crust is significantly richer in incompatible trace elements and acts as a geochemical repository [*Hofmann*, 1988].

After decades of research on identifying the processes instrumental in forming the continental crust, it has been widely accepted that at least two stages of differentiation are required to generate continental crust. First, basaltic magma is extracted from the mantle. Second, it gets buried and partially melts to form more silicic continental crust with the possible help of sedimentary processes [e.g., *Rudnick*, 1995; *Rudnick and Gao*, 2003; *Taylor and McLennan*, 1985; *Albarède*, 1998; *Arculus*, 1999; *Kemp and Hawkesworth*, 2003; *Plank*, 2005; *Hawkesworth and Kemp*, 2006b]. Considering that a basaltic precursor is needed for its generation, continental crust has long been assumed to form in only two distinct plate tectonic settings [*Rudnick*, 1995]. Either the basaltic protolith is sourced from convergent plate margins at island or continental arcs where oceanic crust subducts, or it originates from an intra-plate tectonic setting as a result

of plume-associated magmatism or extensional tectonics. For present day continental crust, the dominant role of island arc basalts (IAB: present-day representative of subduction magmas) over ocean island basalts (OIB: present-day representative of intra-plate magmas) has been highlighted [*Taylor and McLennan*, 1985; *Sun and McDonough*, 1989; *Rudnick*, 1995; *Arculus*, 1999; *Barth et al.*, 2000; *Hawkesworth and Kemp*, 2006b].

However, during the Archean Eon (4.0-2.5 Ga), the upper mantle potential temperature is estimated to be ∼250 K higher than its present-day value [*Labrosse and Jaupart*, 2007; *Herzberg and Gazel*, 2009; *Herzberg et al.*, 2010; *Condie et al.*, 2016]. A large proportion of Archean continental crust is made of grey gneiss complexes, among which a group of sodic granitoids collectively known as Tonalite-Trondhjemite-Granodiorite (TTG) is the main lithological component [*Jahn et al.*, 1981; *Drummond and Defant*, 1990; *Martin*, 1994]. Based on experimental data, it is suggested that Archean TTGs are formed when hydrated basalt melts at garnet-amphibolite, granulite or eclogite facies conditions [e.g., *Barker and Arth*, 1976; *Condie*, 1986; *Foley et al.*, 2002; *Jahn et al.*, 1981; *Martin*, 1986; *Moyen and Stevens*, 2006; *Rapp et al.*, 1991; *Springer and Seck*, 1997]. Sourced from similar compositions but melted over a range of pressures, Archean TTGs have been classified by *Moyen* [2011] into three different types: low, medium, and high pressure TTGs. Furthermore, the low-pressure (10-12 kbar), medium-pressure (ca. 15 kbar) and high-pressure (20 kbar or higher) groups account for 20%, 60% and 20% of the sodic TTGs respectively. Specific pressure-temperature conditions corresponding to different tectonic settings for these TTG types have been proposed by *Moyen* [2011] and we use them as a criterion for generating Archean TTG in our geodynamic models.

In a recent review on continental growth, *Dhuime et al.* [2017] proposed that 65% of the present continental crust existed before 3 Ga. They supported their proposal by presenting similar results from different continental growth models built on records of detrital zircons and sedimentary rocks. Moreover, they argued that there has been a continuous growth of continental crust over the evolution of the planet with a significant drop in average production rate from 2.9 - 3.4 km^{3}yr^{-1} to 0.6 - 0.7 km^{3}yr^{-1} around ∼3 Ga. Interestingly, it has been suggested that Earth might have undergone a major tectonic regime transition around the same time owing to secular cooling and the resulting evolution of mantle viscosity [e.g., *van Hunen et al.*, 2008; *Sizova et al.*, 2010; *Van Kranendonk*, 2010; *Korenaga*, 2011, 2013; *van Hunen and Moyen*, 2012; *Debaille et al.*, 2013; *Gerya*, 2014; *Johnson et al.*, 2013a, 2017; *Gerya et al.*, 2015; *Condie et al.*, 2016; *Fischer and Gerya*, 2016; *Van Kranendonk and Kirkland*, 2016; *Rozel et al.*, 2017]. Based on geochemical data, it is also suggested that this global

geodynamic transition marks the period of significant silicification of the continental crust [*Tang et al.*, 2016], which could be explained by the peeling off and recycling of the mafic lower continental crust after the onset of Archean-style plate tectonics [*Chowdhury et al.*, 2017].

The answer to the question of when plate tectonics commenced on Earth remains hotly debated, with a multitude of studies proposing its inception anytime between the Hadean Eon (4.5-4.0 Ga) and the Neoproterozoic Era (1.0-0.54 Ga) (see *Korenaga* [2013]; *Dhuime et al.* [2017] and the references within). The igneous zircons from Jack Hills, Western Australia that formed > 4 billion years ago make up for a sparse geological record of the early Earth [*Wilde et al.*, 2001]. Based on their geochemical investigations, *Hopkins et al.* [2008, 2010] proposed that these zircons formed in environments that are similar to modern convergent margins. They therefore argued that plate tectonics might have been active during the Hadean Eon (4.5-4.0 Ga). Many authors preferred the Archean Eon (4.0-2.5 Ga) for the onset of plate tectonics because relevant indicators, such as orogens, accretionary prisms, and paired metamorphic belts became more prevalent in the late Archean [e.g., *Komiya et al.*, 1999; *Brown*, 2006; *Van Kranendonk et al.*, 2007; *Shirey et al.*, 2008; *Condie and Kröner*, 2008]. Citing the lack of ultrahigh-pressure metamorphism and ophiolites before the Neoproterozoic Era (1.0-0.54 Ga), *Stern* [2005] argued that plate tectonics could not have been operational before 1 Ga. Some studies have attributed the aforementioned decline in growth of continental crust to higher crustal recycling and the onset of subduction-driven plate tectonics around ∼ 3 Ga [e.g., *Cawood et al.*, 2006; *Shirey and Richardson*, 2011; *Dhuime et al.*, 2012; *Hawkesworth et al.*, 2016a,b].

The formation of Archean TTGs and the enigma behind the origin of plate tectonics have piqued the interest of the geodynamics community over the years. About a decade ago, based on their thermo-chemical mantle convection models, *van Thienen et al.* [2004] proposed that the transition of basalt into denser eclogite at a depth of 30 km creates a gravitational instability. This might trigger a resurfacing event in which a major portion of the crust sinks into the mantle and the resulting pressure release melting produces new replacement crust. In their models, the felsic melts are generated by partial melting either at the base of this new crust or when the dense crust sinks into the mantle. *Moore and Webb* [2014] offered an alternative scenario for early Earth, in which volcanism dominates the surface heat transport (heat-pipe Earth). Erupting all the mafic melt at the surface creates a cold and thick lithosphere [*O'Reilly and Davies*, 1981]. This thickened lithosphere is advected downward and may melt to generate felsic volcanics and TTG plutons.

However, neither of these models considered generating and emplacing the felsic melts within or beneath the crust. Geological field data suggests that the majority of mantle-derived melts intrude at depth, with the ratio of intrusive (plutonic) to eruptive (volcanic) melt volumes ranging between 4:1 and 10:1 [*Crisp*, 1984]. This would correspond to an eruption efficiency between 9% and 20%. Using sophisticated coupled petrological-thermomechanical regional-scale numerical experiments, *Sizova et al.* [2015] identified three distinct tectono-magmatic settings in which felsic melts can be generated from hydrated basaltic crust in the hotter Archean conditions. Lower crustal delamination and the subsequent dripping or small-scale overturns could generate Archean TTGs while the rest of the Archean granitoids could come from local thickening of primitive basaltic crust.

Rozel et al. [2017] have recently demonstrated the possibility of tracking formation conditions for Archean TTGs in numerical simulations on a global scale, which motivated our numerical modelling study. They showed that a plutonism-dominated plutonic squishy lid tectonic regime results in hotter crustal geotherms and is able to reproduce the observed proportions of various TTG rocks, as reported by *Moyen* [2011]. Here, we present global mantle convection simulations in which continental crust is generated self-consistently, which to our knowledge is the first time. Based on the melting conditions proposed by *Moyen* [2011], we parameterise TTG formation and investigate continental growth and recycling by systematically varying parameters such as eruption efficiency, core temperature, and friction coefficient. We introduce the methodology with a focus on melting parameterisation in the section 4.2. We present the results of our simulations in section 4.3 and discuss their geophysical implications in section 4.4. Finally, we summarise the main findings of our study in section 4.5.

4.2 Physical Model and Numerical Model

We model the thermo-chemical evolution of the compressible mantle using the code StagYY [*Tackley*, 2008a], which has been extended by implementing new two-stage crustal growth algorithm needed for our study. The models incorporate pressure- and temperature-dependence of viscosity, plasticity, internal and basal heating, core cooling, phase transitions, and melting leading to both basaltic and TTG crust production. The values used for the parameters are given in Table 4.1.

Table 4.1 Non-dimensional and dimensional parameters used in this study (UM = Upper Mantle (dry olivine); PV = Perovskite; PPV = Post-Perovskite)

Property	Symbol	Value	Units
Rayleigh number	Ra	$7.73 \cdot 10^7$	-
Initial internal heating rate	H	$18.77 \cdot 10^{-12}$	W/kg
Half-life	t_{half}	2.43	Gyr
Surface yield stress	σ_Y^0	40	MPa
Yield stress gradient	σ_Y'	0.01	MPa/km
Reference viscosity	η_0	$1 \cdot 10^{21}$	Pa·s
Surface temperature	T_{surf}	300	K
Initial potential temperature	T_{P0}	1900	K
Gas constant	R	8.3145	J/K/mol
Gravity	g	9.81	m/s^2
Mantle thickness	D	2890	km
Specific heat capacity of pyrolite	$C_{P,\text{pyr}}$	1200	J/kg/K
Specific heat capacity of basalt	$C_{P,\text{bas}}$	1000	J/kg/K
Specific heat capacity of TTG[c]	$C_{P,\text{TTG}}$	1000	J/kg/K
Latent heat of pyrolite	L_{pyr}	600	kJ/kg
Latent heat of basalt	L_{bas}	380	kJ/kg
Latent heat of TTG[l]	L_{TTG}	300	kJ/kg
Surface thermal expansivity[s]	α	$3 \cdot 10^{-5}$	K^{-1}
Surface thermal conductivity[s]	k	3.5	W/m/K
Activation energy - UM	E_1	300	kJ/mol
Activation volume - UM	V_1	5.00	cm^3/mol
Pressure scale - UM	P_1	∞	GPa
Viscosity multiplier - UM	$\Delta\eta_1$	1.0	-
Activation energy - PV	E_2	370	kJ/mol
Activation volume - PV	V_2	3.65	cm^3/mol
Pressure scale - PV	P_2	200	GPa
Viscosity multiplier - PV	$\Delta\eta_2$	30.0	-
Activation energy - PPV	E_3	162	kJ/mol
Activation volume - PPV	V_3	1.40	cm^3/mol
Pressure scale - PPV	P_3	1610	GPa
Viscosity multiplier - PPV	$\Delta\eta_3$	0.1	-

[c] 1200 J/kg/K for simulations with $X_{\text{depletion}} = 0.5$.
[l] 600 kJ/kg for simulations with $X_{\text{depletion}} = 0.5$.
[s] valid at the surface for olivine phase system.

4.2.1   Rheology

Diffusion creep with homogenous grain size is considered as the viscous deformation mechanism. The temperature- and pressure-dependent viscosity η follows the Arrhenius formulation:

$$\eta(T, P) = \eta_0 \Delta\eta_i \exp\left(\frac{E_i + PV_i}{RT} - \frac{E_i}{RT_0}\right), \tag{4.1}$$

where η_0 is the reference viscosity at zero pressure and reference temperature T_0 (1600 K), $\Delta\eta_i$ is the viscosity jump between the layers i, E_i is the activation energy in the layer i, P is the pressure, V_i is the activation volume in layer i (corresponding to material between the phase transitions, see Section 4.2.3), R is the gas constant and T is the absolute temperature. The activation volume decreases with pressure according to the relation:

$$V(P) = V_i \exp\left(-\frac{P}{P_i}\right). \tag{4.2}$$

A viscosity jump of 30 is applied at the upper-lower mantle transition in accordance with the viscosity profile expected by the inversion of postglacial rebound data [*Čížková et al.*, 2012] and geoid inversion studies [e.g., *Ricard et al.*, 1989].

To allow for lithospheric deformation, plastic yielding is assumed to be the weakening mechanism [*Moresi and Solomatov*, 1998a; *Tackley*, 2000]. The maximum stress that a material can sustain before deforming plastically is given by the yield stress σ_Y, which has both brittle and ductile components

$$\sigma_Y = \min\left(\sigma_{Y\_ductile}, \sigma_{Y\_brittle}\right). \tag{4.3}$$

The ductile yield stress $\sigma_{Y\_ductile}$ increases linearly with depth d at a rate of σ'_Y as:

$$\sigma_{Y\_ductile} = \sigma_Y^0 + d \cdot \sigma'_Y, \tag{4.4}$$

where σ_Y^0 is the yield stress at the surface. Following *Byerlee* [1978], the brittle yield stress $\sigma_{Y\_brittle}$ is calculated as

$$\sigma_{Y\_brittle} = \mu P, \tag{4.5}$$

where μ is the friction coefficient. Different values of the friction coefficient for the lithosphere that are consistent with experimentally-measured values are used in this

study. If the convective stresses exceed the yield stress, the viscosity is reduced to the yielding viscosity $\eta_Y = \sigma_Y/2\dot{\epsilon}$, where $\dot{\epsilon}$ is the 2nd invariant of the strain-rate tensor. The effective viscosity is then given by

$$\eta_{\text{eff}} = \left(\frac{1}{\eta} + \frac{2\dot{\varepsilon}}{\sigma_Y}\right)^{-1}. \tag{4.6}$$

Viscosity limiters (10^{18} and 10^{28} Pa·s) are then used to prevent too large viscosity variations, which would decrease the stability of the code.

4.2.2 Boundary Conditions and Solution Method

We solve the following equations for compressible anelastic Stokes flow with infinite Prandtl number:

$$\nabla \cdot (\rho \mathbf{u}) = 0, \tag{4.7}$$

$$0 = -\nabla P + \nabla \cdot \tau + \rho \mathbf{g}, \tag{4.8}$$

$$\rho C_P \left(\frac{\partial T}{\partial t} + \mathbf{u} \cdot \nabla T\right) - \alpha T \left(u_r \cdot \nabla_r P\right) = \nabla \cdot (k \nabla T) + \tau : \nabla \mathbf{u} + \rho H, \tag{4.9}$$

with density ρ, time t, velocity $\mathbf{u}$, gravity $\mathbf{g}$, heat capacity C_P, thermal expansivity α, thermal conductivity k, deviatoric stress tensor τ, and H is the internal heating rate. $\tau : \nabla \mathbf{u}$ denotes tensor contraction, such that: $\tau : \nabla \mathbf{u} = \sum_{ij} \tau_{ij} \partial v_i / \partial x_j$, where x_j is the position. The values of the parameters used in this study are listed in Table 4.1.

We use 2D spherical annulus geometry [*Hernlund and Tackley*, 2008] with a resolution that varies radially and is higher at the surface, around the 660 km phase transition, and the core-mantle boundary. The computational domain consists of 1024 (laterally) times 128 (radially) cells. ~ 4 million tracers are advected through the mesh using a fourth-order Runge-Kutta scheme with a second-order spatial interpolation of the velocity field. Each tracer carries several quantities such as temperature, composition, water content, concentration of heat-producing element, emplacement, and depletion. The tracer-to-cell interpolation is done following the tracer-ratio method as described by *Tackley and King* [2003], adapted to do mass averaging of tracer quantities. We employ free-slip boundary conditions at the surface and the core-mantle boundary, which are also isothermal. The surface temperature is fixed at 300 K, while the core temperature decreases with time due to heat lost, using a parameterisation based on

Buffett et al. [1992, 1996], for details of which the reader is referred to *Nakagawa and Tackley* [2004]. A parallel MUMPS solver from the PETSc package is used to obtain a velocity-pressure solution at each time-step on a staggered grid [*Amestoy et al.*, 2000].

4.2.3 Phase Changes and Composition

The model includes a parameterisation based on mineral physics data [*Irifune and Ringwood*, 1993; *Ono et al.*, 2001], in which the minerals are divided into olivine, pyroxene-garnet, TTG and melt phase systems. Within the olivine and pyroxene-garnet phase systems we assume the solid-solid phase transitions as considered previously in *Xie and Tackley* [2004b]; *Nakagawa and Tackley* [2012]. The mixture of minerals depends on the composition, which is mapped linearly into the fraction of different phase systems. Composition can either be in the continuum between *harzburgite* (ultramafic and depleted material) and *basalt* (mafic igneous rocks), or *TTG* (felsic rocks). Harzburgite is considered to be a mixture of 75% olivine and 25% pyroxene-garnet and basalt is made of pure pyroxene-garnet. The mantle is initialised with a pyrolytic composition: 80% harzburgite and 20% basalt [*Xu et al.*, 2008]. At a depth of 60 km, basalt transforms to eclogite, which is around $190 \, \mathrm{kg/m^3}$ denser than olivine. At lowermost mantle depths, the phase transition to post-perovskite is also considered (e.g. *Tackley et al.* [2013]). The phase change parameters are given in Table 4.2. Changes in composition arise from melt-induced differentiation, which is described in the next section.

4.2.4 Melting and Crustal Production

For self-consistent creation of basaltic (mafic, oceanic-like) and TTG (felsic, continental-like) crust, we parameterise the processes of melt generation and melt extraction. For the sake of numerical efficiency, we compute the melt production at the cell level. Molten tracers are then generated accordingly and transported upwards to erupt on or intrude into the pre-existing crust (mimicking large-scale eruptive and intrusive magmatism) if appropriate conditions are met. The model developed in this study is an extension of the ones previously described by *Xie and Tackley* [2004b]; *Nakagawa et al.* [2010]. Water is considered to penetrate fully into the top 10 km and is advected throughout the mantle on tracers. The non-dimensional water concentration is the same both in solid and melt phases (using partition coefficient $D_{\mathrm{part,H_2O}} = 1$), which varies between 1 implying fully hydrated and 0 meaning no water (see Fig. A.1 in Appendix). Heat-producing elements (HPE) are partitioned during melting and their

Table 4.2 Phase change parameters for olivine, pyroxene-garnet, and TTG systems with surface density at zero pressure ρ_s, density jump across a phase transition $\Delta\rho$, and Clapeyron slope γ.

Depth (km)	Temperature (K)	$\Delta\rho$ (kg/m^3)	γ (MPa/K)
Olivine ($\rho_s = 3240\,\text{kg/m}^3$)			
410	1600	180	2.5
660	1900	400	-2.5
2740	2300	61.6	10
Pyroxene-Garnet ($\rho_s = 3080\,\text{kg/m}^3$)			
60	1000	350	0
400	1600	150	1
720	1900	400	1
2740	2300	61.6	10
TTG ($\rho_s = 2700\,\text{kg/m}^3$)			
290[a]	1713	168	2.26

[a] Stishovite phase transition considered for simulations given in Table 4.4.

non-dimensional concentration Rh^* is 100 times higher in the melt compared to the solid residue (using partition coefficient $D_{\text{part,HPE}} = 0.01$; see Fig. A.2 in Appendix). A detailed description of our new melting-induced crustal production (MCP) procedure is given in the next sections.

4.2.4.1   Melt generation

Amount of melt produced

As melting is calculated at the cell level, the cell-based solid composition C and melt fraction f have to be computed at cell centres using mass averaging of the tracers. At each time-step, the amount of melt Δf appearing in each cell is computed iteratively. More precisely, the cell temperature T is compared to the solidus $T_{\text{sol},i}$ of each composition i giving individual changes in melt fraction Δf_i. In case the cell temperature exceeds or is lower than a composition's solidus, then melt is respectively generated or frozen (if already present) from that composition, with the goal of bringing the temperature back to the solidus. Latent heat L (see Table 4.1) of melt is consumed during melting and released during freezing and the resulting change in temperature

ΔT is computed for each cell. This is compared to the change in temperature DT needed to return the cell temperature to the solidus, and if not close enough, the procedure is iterated on. In principle, melting or solidification should occur at constant temperature. But as latent heat is absent from the heat equation, the process of latent heat related heating or cooling has to be done during the melting treatment as a sort of correction. Effectively, due to compositional heterogeneities, different materials within each cell melt at different temperatures.

For simplicity, we consider 3 solidus temperatures (given in Appendix A.2):

- $T_{\mathrm{sol,bas}}$ for pure basalt that has already been erupted or intruded,

- $T_{\mathrm{sol,TTG}}$ for pure TTG,

- T_{melting} for a harzburgite-basalt mixture or pure basalt that has never been erupted or intruded (see next section for details).

Computing the variation of melt fraction in a cell for mantle material in the harzburgite-basalt continuum is difficult, as the instantaneous melting temperature T_{melting} is composition-dependent, and therefore depends on the amount of melt being produced. In this case, a first order extrapolation of this melting temperature in the melt fraction space is considered:

$$T_{\mathrm{melting}}\left(f_0 + \Delta f\right) = T_{\mathrm{melting}}\left(f_0\right) + \Delta f \frac{\partial T_{\mathrm{melting}}}{\partial f}\bigg|_{f_0}, \qquad (4.10)$$

where f_0 is the initial (basaltic/harzburgitic) melt fraction in the cell. The composition-dependence of the melting temperature $\partial T_{\mathrm{melting}}/\partial f$ is estimated by imposing a very small Δf. Using Eq. 4.10, the variation of melt fraction is then computed implicitly and iteratively using:

$$\Delta f = \frac{T - T_{\mathrm{melting}}\left(f_0 + \Delta f\right)}{L} C_{P,\mathrm{pyr}} = \frac{T - \left(T_{\mathrm{melting}} + \Delta f \frac{\partial T_{\mathrm{melting}}}{\partial f}\right)}{L} C_{P,\mathrm{pyr}}, \quad (4.11)$$

where $C_{P,\mathrm{pyr}}$ is the specific heat capacity. Rearranging Eq. 4.11 (and neglecting the $\partial T_{\mathrm{sol}}/\partial f$ term for basalt and TTG melting), we get:

$$\Delta f = \begin{cases} \left(T - T_{\mathrm{melting}}\right) / \left(\frac{L_{\mathrm{pyr}}}{C_{P,\mathrm{pyr}}} + \frac{\partial T_{\mathrm{melting}}}{\partial f}\right), & \text{for the mantle} \\ \left(T - T_{\mathrm{sol,bas}}\right) C_{P,\mathrm{bas}}/L_{\mathrm{bas}}, & \text{for basalt} \\ \left(T - T_{\mathrm{sol,TTG}}\right) C_{P,\mathrm{TTG}}/L_{\mathrm{TTG}}, & \text{for TTG} \end{cases} \qquad (4.12)$$

with latent heat of pyrolite L_{pyr}, specific heat capacity of pyrolite $C_{P,\mathrm{pyr}}$, latent heat of basalt L_{bas}, specific heat capacity of basalt $C_{P,\mathrm{bas}}$, latent heat of TTG L_{TTG}, and specific heat capacity of TTG $C_{P,\mathrm{TTG}}$. TTG solidus is considered to be $100\,\mathrm{K}$ lower than the basalt solidus.

New melt fractions are obtained by adding the Δf_i of each composition i to its initial melt fraction f_i. New tracers of composition corresponding to Δf_i appear. The cell temperature is adjusted using the latent heat consumed through the generation of Δf_i.

Type of melt produced

The composition of the melts produced are obtained using the following procedure:

- Basaltic melt is produced using the instantaneous melting temperature T_{melting} when melting occurs on solid tracers with a mixed harzburgite-basalt composition (like in the beginning of the simulations). Pure basaltic solid tracers that have never been erupted or intruded before also produce molten basalt using T_{melting}. We made this choice as non-erupted-intruded basaltic tracers represent basalt that is not a separate rock type, but rather a chemical component of rocks that are a chemical mixture of basaltic and harzburgitic end-member components.

- When melting happens on a basaltic solid tracer that has been erupted or intruded in the past (hereby referred to as *solid-basalt* tracer), we consider it as a separate rock type. We therefore use the solidus temperature for pure basalt $T_{\mathrm{sol,bas}}$. Depending on whether the cell satisfies the specific P-T conditions for TTG formation outlined by *Moyen* [2011] or not (see Appendix A.1), solid basalt can melt in two different ways. When the cell undergoes melting but it does not have TTG formation conditions, then basaltic melt is generated. Only when the cell has water (50% or more of the imposed surface hydration conditions) and *enriched basalt* (see section 4.2.4.2 for explanation), and it meets the TTG formation conditions, is TTG melt generated.

- For simplicity, molten TTG is always produced when solid TTG melts, using the solidus temperature $T_{\mathrm{sol,TTG}}$.

- Molten harzburgite (i.e., ultramafic melt) is produced in extreme cases (at the beginning of the simulations) when all the basaltic mantle component is already molten and the cell temperature still exceeds the T_{melting} for harzburgite (see Appendix A.2).

The mantle is initially pyrolytic, with a composition corresponding to 20% basalt and 80% harzburgite end-member components. For partially-melting pyrolite to generate basalt, a solidus function fitting experimental data by *Hirschmann* [2000] is used (see Appendix A.2.2). For partially-melting basalt to generate TTG, the pressure-dependent solidus and liquidus functions are taken from Table 1 of *Sizova et al.* [2015] for "hydrated basalt" composition (as defined in their paper, see also Appendix A.2.1.1). To simulate melt extraction from partially molten lithologies [*Nikolaeva et al.*, 2008; *Sizova et al.*, 2015], we do not allow the melting of all the basalt available in the mantle to generate TTG.

4.2.4.2   Depletion fraction

When initialised, the entire mass of basalt on the *solid-basalt* tracer can potentially partially melt to form TTG (or *enriched basalt*) With each subsequent melting event, the proportion of *enriched basalt* available on the tracer decreases. Conversely, there is an increase in the proportion of *depleted basalt*, or the basalt that can not melt to form TTG. The production of TTG from basalt is limited by introducing a parameter called depletion fraction $X_{\text{depletion}}$, which gives the allowable mass fraction of depleted basalt on a *solid-basalt* tracer. For example, using a value of $X_{\text{depletion}} = 0.9$ would imply that 90% of basalt is depleted or not available for TTG production. Hence, only 10% of mass of *solid-basalt* will be used for TTG production. This is an important parameter as it directly controls how much felsic crust can be produced in the code and it is used in the following equations.

The amount of TTG melt to be generated by the melting of *solid-basalt* is given by $\Delta f_{\text{basalt-to-TTG}}$. Using this, the ideal amount of TTG to be generated in a cell with mass M_{cell} is given as:

$$\Delta M_{\text{TTG}} = \Delta f_{\text{basalt-to-TTG}} M_{\text{cell}}. \tag{4.13}$$

This amount has to be sourced uniformly from the *solid-basalt* tracers present in the cell:

$$\Delta M_{\text{TTG}} = \sum_{i=1}^{n\,\text{tracers}} \Delta m_{\text{TTG},i}, \tag{4.14}$$

where Δm_{TTG} is the mass of TTG produced from the host tracer i. *Solid-basalt* tracers are 100% enriched in basalt at time $t = 0$ and after a time step Δt, the new amount of

enriched basalt on a tracer is:

$$m_{\text{enr},i}\left(t + \Delta t\right) = m_{\text{enr},i}\left(t\right) - \Delta m_{\text{dep},i} - \Delta m_{\text{TTG},i}, \tag{4.15}$$

where m_{enr} and m_{dep} denote the masses of *enriched basalt* and *depleted basalt* on the tracer, respectively (see Fig. 4.1 for illustration). The change in masses of *depleted basalt* Δm_{dep} and TTG Δm_{TTG} (produced from *enriched basalt*) are related using the depletion fraction $X_{\text{depletion}}$ as:

$$\Delta m_{\text{dep},i} = \Delta m_{\text{TTG},i}\left(\frac{X_{\text{depletion}}}{1 - X_{\text{depletion}}}\right). \tag{4.16}$$
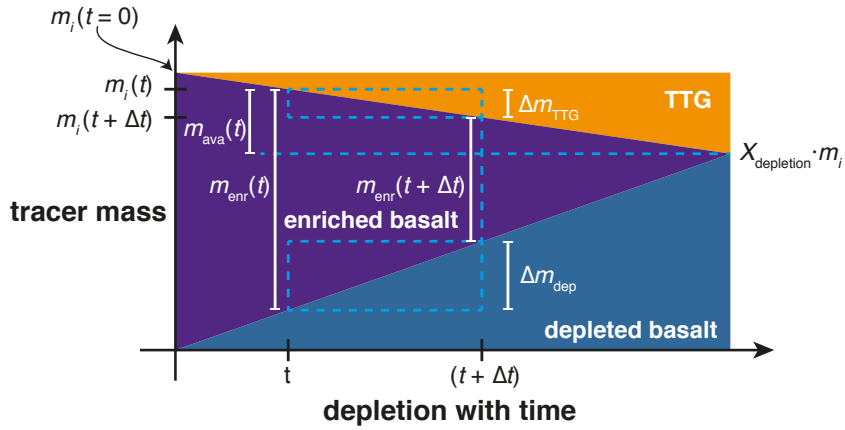
Fig. 4.1 Evolution of depletion on a *solid-basalt* tracer with time. The initial tracer mass m_i (in violet) decreases with time as some of it gets transferred to TTG (in orange).

Every *solid-basalt* tracer has an available mass m_{ava} for TTG production at a given time t:

$$m_{\text{ava},i}\left(t\right) = m_{\text{enr},i}\left(t\right)\left(1 - X_{\text{depletion}}\right). \tag{4.17}$$

In order to uniformly source the mass of TTG from all the *solid-basalt* tracers present in the cell, a fraction χ of this available mass is taken as:

$$\Delta m_{\text{TTG},i} = \chi m_{\text{ava},i} = \chi m_{\text{enr},i}\left(1 - X_{\text{depletion}}\right). \tag{4.18}$$

Combining equations 4.14 and 4.18, we get:

$$\chi = \frac{\Delta M_{\text{TTG}}}{\sum_{i=1}^{n\,\text{tracers}} m_{\text{enr},i}\left(1 - X_{\text{depletion}}\right)}. \tag{4.19}$$

The mass of depleted basalt m_{dep} on each *solid-basalt* tracer changes with time according to this relation:

$$m_{\mathrm{dep},i}\left(t + \Delta t\right) = m_{\mathrm{dep},i}\left(t\right) + \Delta m_{\mathrm{dep},i} = m_{\mathrm{dep},i}\left(t\right) + \Delta m_{\mathrm{TTG},i}\left(\frac{X_{\mathrm{depletion}}}{1 - X_{\mathrm{depletion}}}\right), \quad (4.20)$$

and the dimensionless *depletion* value (< 1) on each *solid-basalt* tracer is updated as:

$$\mathrm{depletion}_i\left(t + \Delta t\right) = \frac{m_{\mathrm{dep},i}\left(t + \Delta t\right)}{m_{\mathrm{dep},i}\left(t + \Delta t\right) + m_{\mathrm{enr},i}\left(t + \Delta t\right)}. \quad (4.21)$$

This *depletion* gives the amount of depleted and enriched basalt in a cell.

4.2.4.3   Melt extraction

Fig. 4.2 illustrates our melt extraction treatment. As we are interested in long-term planetary evolution, we simplify the crust production process as was first done for basaltic crust in *Xie and Tackley* [2004a] and used since then [*Nakagawa et al.*, 2010; *Lourenco et al.*, 2016]. At each time step, we assume instantaneous radial transport of melt, which is calculated separately in each vertical column of our mesh.

If the melt generated is above 300 km depth, then it is instantaneously removed for emplacement [*Christensen and Hofmann*, 1994; *Xie and Tackley*, 2004a]. As described in the previous sections, molten tracers of various compositions appear in each cell (Fig. 4.2B). The thicknesses of both pre-existing TTG and basaltic crusts are then computed (Fig. 4.2A1). Molten tracers that have to be transported are removed from the cells and their masses are computed (Fig. 4.2A2). Non-transport tracers in the entire column are then compacted downwards to account for the mass loss by removal of molten tracers. Gaps are created at both the bottom and top of existing TTG and basaltic crusts. The melt is transported both to the bottom of the crust (*plutonism* or *intrusion*) and to the top of the domain (*volcanism* or *eruption*), unless there is already some melt present at the surface (Fig. 4.2A3). The intruded melt stays molten while taking adiabatic decompression into account and forming a weak and warm lithosphere. The erupted melt is rapidly solidified by setting its temperature to the surface temperature (300 K), resulting in a strong and cold lithosphere [*Rozel et al.*, 2017]. The mass ratio of erupted to intruded melts can be controlled by the eruption efficiency. Eruption efficiency defines the percentage of mantle-derived melts (or basaltic-crust derived melts in the case of TTG formation) that is erupted at the surface. In nature, the majority of mantle-derived melts intrude at a depth, corresponding to an eruption efficiency between 9% and 20%. It is one of the important
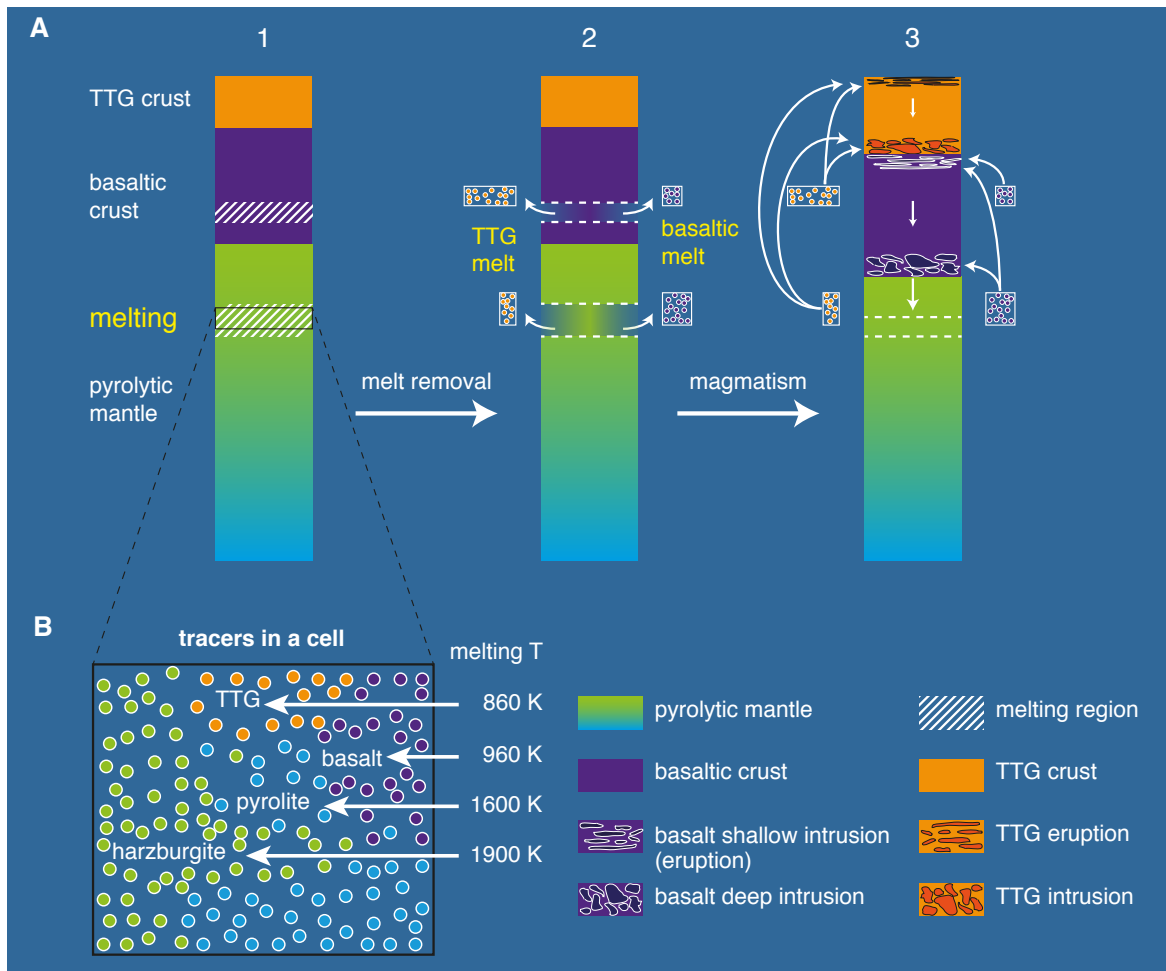
Fig. 4.2 Cartoon depicting a section of a mesh column. **A1,** Initial state with TTG crust, basaltic crust, pyrolytic mantle, and the region undergoing melting. **A2,** After melt removal but before compaction or opening gaps in lithosphere for magmatism. **A3,** Final state with the eruption and intrusion of the melt. **B,** Different melting temperatures for different compositions.

parameters being tested in this study. Geological evidence suggests that komatiites have erupted above Archean continental crust in the past [*Nisbet*, 1982] and basalt frequently erupts above TTG in nature. However, the low resolution in our global models would not allow us to resolve such geological features, and therefore our melt extraction treatment does not allow for basalt to erupt above TTG. This should be improved in the future versions of the code.

4.3   Results

We ran 21 simulations of compressible convection with core cooling, time-dependent internal heating, melting and crust production with depletion fraction $X_{\text{depletion}} = 0.5$, reference viscosity $\eta_0 = 10^{21}$ Pa·s and initial mantle potential temperature $T_{\text{P0}} = 1900$ K. The heat production from radioactive elements H is initially $18.77 \cdot 10^{-22}$ W/kg and decreases with time with a half-life of 2.43 Gyr. Additionally, we ran another 14 simulations with different depletion fraction values and a lower solidus temperature (see Appendix A.2 for details). We systematically varied the following parameters (see Table 4.3 and 4.4):

- Eruption efficiency: $e = 10, 20, 30, 40, 60, 80$, and 100%

- Initial core temperature: $T_{\text{cmb}} = 5000$ and 6000 K

- Friction coefficient: $\mu = 0.2, 0.4$

- Depletion fraction $X_{\text{depletion}} = 0.5, 0.9$

4.3.1   Volume and Crustal Recycling Rate

At any given time t, the volume of total TTG produced $V_{\text{TTG,total}}$ and crustal TTG remaining at the surface $V_{\text{TTG,crustal}}$ are given by:

$$V_{\text{TTG,total}}\left(t\right) = \frac{n_y}{\pi}\left(\frac{M_{\text{TTG}}\left(t\right)}{\rho_{\text{s,TTG}}}\right), \tag{4.22}$$

$$V_{\text{TTG,crustal}}\left(t\right) = 4\pi d_{\text{TTG}}\left(t\right)\left(r_{\text{Earth}} - \frac{d_{\text{TTG}}\left(t\right)}{2}\right)^2, \tag{4.23}$$

with number of cells in lateral direction n_y, mass of TTG produced M_{TTG} and mean global TTG crustal thickness d_{TTG} at that time, and radius of Earth r_{Earth}. The volume of basaltic crust that remains at the surface or underlies the TTG crust is given by:

$$V_{\text{bas,crustal}}\left(t\right) = 4\pi d_{\text{bas}}\left(t\right)\left(r_{\text{Earth}} - \frac{d_{\text{bas}}\left(t\right)}{2}\right)^2, \tag{4.24}$$

with mean global basaltic crustal thickness d_{bas} at that time. The difference between total and crustal volumes gives the amount of TTG that has been recycled back into the mantle. The rate of recycling of continental crust at time t_i with timestep $i = 1, 2, 3..$

Table 4.3 Simulations with depletion fraction $X_{\text{depletion}} = 0.5$, initial core temperature T_{cmb} (K), friction coefficient μ, eruption efficiency e (%), final model runtime t_{r} (Gyr), volume of total TTG produced $V_{\text{TTG,total}}$, volume of crustal TTG $V_{\text{TTG,crustal}}$, and volume of basaltic crust $V_{\text{bas,crustal}}$. All volumes reported here are in km^3 after 1 Gyr of evolution.

T_{cmb}	μ	e	t_{r}	$V_{\text{TTG,total}}$	$V_{\text{TTG,crustal}}$	$V_{\text{bas,crustal}}$
5000	0.2	10	1.82	$7.74 \cdot 10^{10}$	$2.75 \cdot 10^{10}$	$8.59 \cdot 10^9$
5000[a]	0.2	20	0.88	$6.37 \cdot 10^{10}$	$1.23 \cdot 10^{10}$	$5.94 \cdot 10^9$
5000	0.2	30	3.81	$6.80 \cdot 10^{10}$	$1.36 \cdot 10^{10}$	$7.99 \cdot 10^9$
5000	0.2	40	2.28	$6.44 \cdot 10^{10}$	$1.09 \cdot 10^{10}$	$7.43 \cdot 10^9$
5000[x]	0.2	60	2.74	$6.12 \cdot 10^{10}$	$7.15 \cdot 10^9$	$6.39 \cdot 10^9$
5000[a]	0.2	80	0.43	$3.01 \cdot 10^{10}$	$1.92 \cdot 10^9$	$4.37 \cdot 10^9$
5000	0.2	100	4.28	$5.36 \cdot 10^{10}$	$5.06 \cdot 10^9$	$5.43 \cdot 10^9$
6000	0.2	10	2.78	$9.42 \cdot 10^{10}$	$2.92 \cdot 10^{10}$	$8.13 \cdot 10^9$
6000	0.2	20	2.60	$9.38 \cdot 10^{10}$	$2.53 \cdot 10^{10}$	$8.39 \cdot 10^9$
6000[b]	0.2	30	4.31	$9.22 \cdot 10^{10}$	$2.16 \cdot 10^{10}$	$8.21 \cdot 10^9$
6000	0.2	40	3.11	$8.46 \cdot 10^{10}$	$1.32 \cdot 10^{10}$	$6.35 \cdot 10^9$
6000	0.2	60	2.70	$7.96 \cdot 10^{10}$	$1.00 \cdot 10^{10}$	$6.62 \cdot 10^9$
6000	0.2	80	4.50	$7.62 \cdot 10^{10}$	$8.45 \cdot 10^9$	$6.62 \cdot 10^9$
6000	0.2	100	4.50	$7.08 \cdot 10^{10}$	$9.48 \cdot 10^9$	$6.16 \cdot 10^9$
6000	0.4	10	2.50	$9.74 \cdot 10^{10}$	$3.69 \cdot 10^{10}$	$9.86 \cdot 10^9$
6000[x]	0.4	20	1.70	$9.32 \cdot 10^{10}$	$3.79 \cdot 10^{10}$	$1.10 \cdot 10^{10}$
6000	0.4	30	1.29	$8.69 \cdot 10^{10}$	$2.09 \cdot 10^{10}$	$8.56 \cdot 10^9$
6000	0.4	40	2.47	$8.34 \cdot 10^{10}$	$1.46 \cdot 10^{10}$	$7.62 \cdot 10^9$
6000	0.4	60	1.58	$7.92 \cdot 10^{10}$	$1.01 \cdot 10^{10}$	$7.06 \cdot 10^9$
6000	0.4	80	4.39	$7.51 \cdot 10^{10}$	$7.90 \cdot 10^9$	$6.18 \cdot 10^9$
6000	0.4	100	4.50	$7.20 \cdot 10^{10}$	$9.64 \cdot 10^9$	$6.19 \cdot 10^9$

[a] volumes reported after final model runtime t_{r}

[b] simulation *e30x5* presented in Fig. 4.3, 4.4, 4.5, and 4.6

[x] excluded from scaling laws owing to data corruption

Table 4.4 Simulations with a lower solidus temperature, Stishovite phase transition, initial core temperature $T_{cmb} = 6000\,K$, friction coefficient $\mu = 0.2$, depletion fraction $X_{depletion}$, eruption efficiency e (%), final model runtime t_r (Gyr), volume of total TTG produced $V_{TTG,total}$, volume of crustal TTG $V_{TTG,crustal}$, and volume of basaltic crust $V_{bas,crustal}$. All volumes reported here are in km^3 after 1 Gyr of evolution.

$X_{depletion}$	e	t_r	$V_{TTG,total}$	$V_{TTG,crustal}$	$V_{bas,crustal}$
0.5	10	2.01	$9.89 \cdot 10^{10}$	$4.37 \cdot 10^{10}$	$9.98 \cdot 10^{9}$
0.5^a	20	0.46	$6.02 \cdot 10^{10}$	$5.95 \cdot 10^{9}$	$5.72 \cdot 10^{9}$
0.5	30	2.04	$9.03 \cdot 10^{10}$	$1.79 \cdot 10^{10}$	$8.55 \cdot 10^{9}$
0.5^a	40	0.38	$4.30 \cdot 10^{10}$	$3.27 \cdot 10^{9}$	$5.29 \cdot 10^{9}$
0.5	60	3.46	$9.09 \cdot 10^{10}$	$1.05 \cdot 10^{10}$	$7.08 \cdot 10^{9}$
0.5	80	1.01	$8.62 \cdot 10^{10}$	$1.04 \cdot 10^{10}$	$7.45 \cdot 10^{9}$
0.5	100	1.94	$8.01 \cdot 10^{10}$	$9.70 \cdot 10^{9}$	$6.14 \cdot 10^{9}$
0.9	10	1.43	$2.25 \cdot 10^{10}$	$4.20 \cdot 10^{9}$	$6.86 \cdot 10^{9}$
0.9	20	2.35	$2.26 \cdot 10^{10}$	$2.31 \cdot 10^{9}$	$7.33 \cdot 10^{9}$
0.9^a	30	0.23	$9.50 \cdot 10^{9}$	$1.45 \cdot 10^{9}$	$5.81 \cdot 10^{9}$
0.9^b	40	3.45	$2.23 \cdot 10^{10}$	$2.47 \cdot 10^{9}$	$4.70 \cdot 10^{9}$
0.9^a	60	0.35	$1.69 \cdot 10^{10}$	$1.08 \cdot 10^{9}$	$4.56 \cdot 10^{9}$
0.9	80	3.06	$2.23 \cdot 10^{10}$	$1.59 \cdot 10^{9}$	$5.32 \cdot 10^{9}$
0.9	100	1.25	$2.14 \cdot 10^{10}$	$1.73 \cdot 10^{9}$	$4.67 \cdot 10^{9}$

[a] volumes reported after final model runtime t_r
[b] simulation *e40x9* presented in Fig. 4.8

is given by:

$$\text{recycling}(t_i) = \frac{(V_{\text{TTG,total}} - V_{\text{TTG,crustal}})_{t_{i+1}} - (V_{\text{TTG,total}} - V_{\text{TTG,crustal}})_{t_{i-1}}}{t_{i+1} - t_{i-1}} \quad (4.25)$$

As not all simulations reached 4.5 Gyr of evolution, the final global volumes are not comparable to each other. Therefore, the global volumes for all simulations after 1 Gyr of runtime are given in Table 4.3. For volumes generated by all simulations at their final runtime, see Table A.1 in Appendix.

4.3.2   Observations

The thermal and compositional evolution with time of a simulation with $X_{\text{depletion}} = 0.5$, $e = 30\%$, $T_{\text{cmb}} = 6000\,\text{K}$, and $\mu = 0.2$ (hereby referred to as *e30x5*) is depicted in Fig. 4.3, 4.4, 4.5 and 4.6. The cell-based composition field represents the following different material: *TTG* ($\geq 60\%$ in pink), *basalt* ($\geq 60\%$ in blue), *harzburgite* ($\geq 40\%$ in teal, lighter shades represent higher harzburgite content and mantle depletion), *TTG-melt* ($\geq 50\%$ in yellow), *basaltic-melt* ($\geq 50\%$ in sky blue), *harzburgitic-melt* ($\geq 50\%$ in mint green), and *TTG-basalt-mix* ($\geq 40\%$ *TTG* and $\geq 40\%$ *basalt* in purple). The empty cells in black represent mixes of different materials with very low concentration that do not fit either of the above criteria.

Fig. 4.3, 4.4, 4.5 and 4.6 show the general processes of TTG formation, crustal recycling, delamination and density-driven dripping, which happen in all simulations. Fig. 4.7 shows the influence of different parameters, such as eruption efficiency and initial core temperature on crustal volume and recycling. The formation of TTG can be divided into two distinct stages: continuous linear growth with time and intense recycling from 0-1 Gyr, and a growth proportional to cubic root of time and moderate recycling afterwards.

Around 127 Myr (Fig. 4.3), the first strong plumes arrive at the surface resulting in partial melting of the pyrolytic mantle. Basaltic melt is generated, leaving behind a depleted mantle residue. The basaltic melt is both erupted at the surface to form oceanic crust, and intruded at a depth as molten material. The intense plume activity melts the basaltic crust to generate TTG melt and also delaminates the lower basaltic crust (eclogite), which drips down into the mantle. TTG melt is also both erupted at the surface to make TTG crust, and intruded at the base of the crust as molten material. The total TTG volume produced increases linearly (see Eq. 4.22 and Fig. 4.7a) and at the same time, the intense plumes recycle a lot of TTG and basaltic material back into the mantle during this period of vigorous mantle convection lasting until about

223 Myr. The upper mantle becomes depleted with increasing harzburgite content. Looking at the zoom-in in Fig. 4.3, a lot of harzburgitic melt (mint green) can be seen at the core-mantle boundary and in the upper mantle. These regions also have molten basalt (sky blue), however owing to its low concentration (less then 50%) in the cells, it is not visualised.

Around 506 Myr (Fig. 4.4), this intense deformation phase has subsided and the crustal volume of TTG (see Eq. 4.23 and Fig. 4.7a) increases while the recycling rate decreases (see Eq. 4.25 and Fig. 4.7c). Around this time, a lot of "jelly-fish" shaped structures can be seen in the upper and mid-mantle, which are a mix of TTG and basalt-eclogite material. Owing to the density contrast between TTG and basalt-eclogite, this mix material is neutrally buoyant and does not subduct to the bottom of the mantle. Around 993 Myr, TTG crust has covered a large portion of the surface. The core temperature has cooled to about 5000 K and the plumes have become weaker. A drop in the crustal production and recycling rate is also observed (Fig. 4.7c). The total TTG growth, which was so far linear with time, has reached a plateau and now the growth curve follows the cubic root of time (Fig. 4.7a). By 1504 Myr (Fig. 4.5), TTG crust covers most of the surface and is underlain by basaltic crust. There are chunks of basaltic material dripping down into the mantle and many "jelly-fish" shaped structures exist. By 4300 Myr, most of these structures have been destroyed by mantle mixing and the entire surface is covered by a very thick TTG crust.

Fig. 4.6 shows the compositional and thermal evolution of the same simulation for a period of 20 Myr. Around 1107 Myr, a plume reaches the surface, resulting in a large scale melting event. The pre-existing basaltic and TTG crust are pushed aside and compressed together to form structures that are perhaps similar to stacked terranes found in the Eoarchean Era [*Bédard*, 2006]. It has been suggested that such granite-greenstone terranes form in convergent margins and account for the stable cratonic interiors of continents [*Kusky and Polat*, 1999]. However, our models produce these terranes without the need for subduction and do not provide any stability to the overlying TTG crust.

Fig. 4.3 Thermal (*top*) and compositional (*middle* and zoom-in at *bottom*) evolution with time for simulation *e30x5*. The lighter shades of teal in composition field represent progressive mantle depletion (higher harzburgite content) with time. Continued on Fig. 4.4.

Fig. 4.4 Continued from Fig. 4.3. Thermal (*top*) and compositional (*middle* and zoom-in at *bottom*) evolution with time for simulation *e30x5*. The lighter shades of teal in composition field represent progressive mantle depletion (higher harzburgite content) with time. Continued on Fig. 4.5.
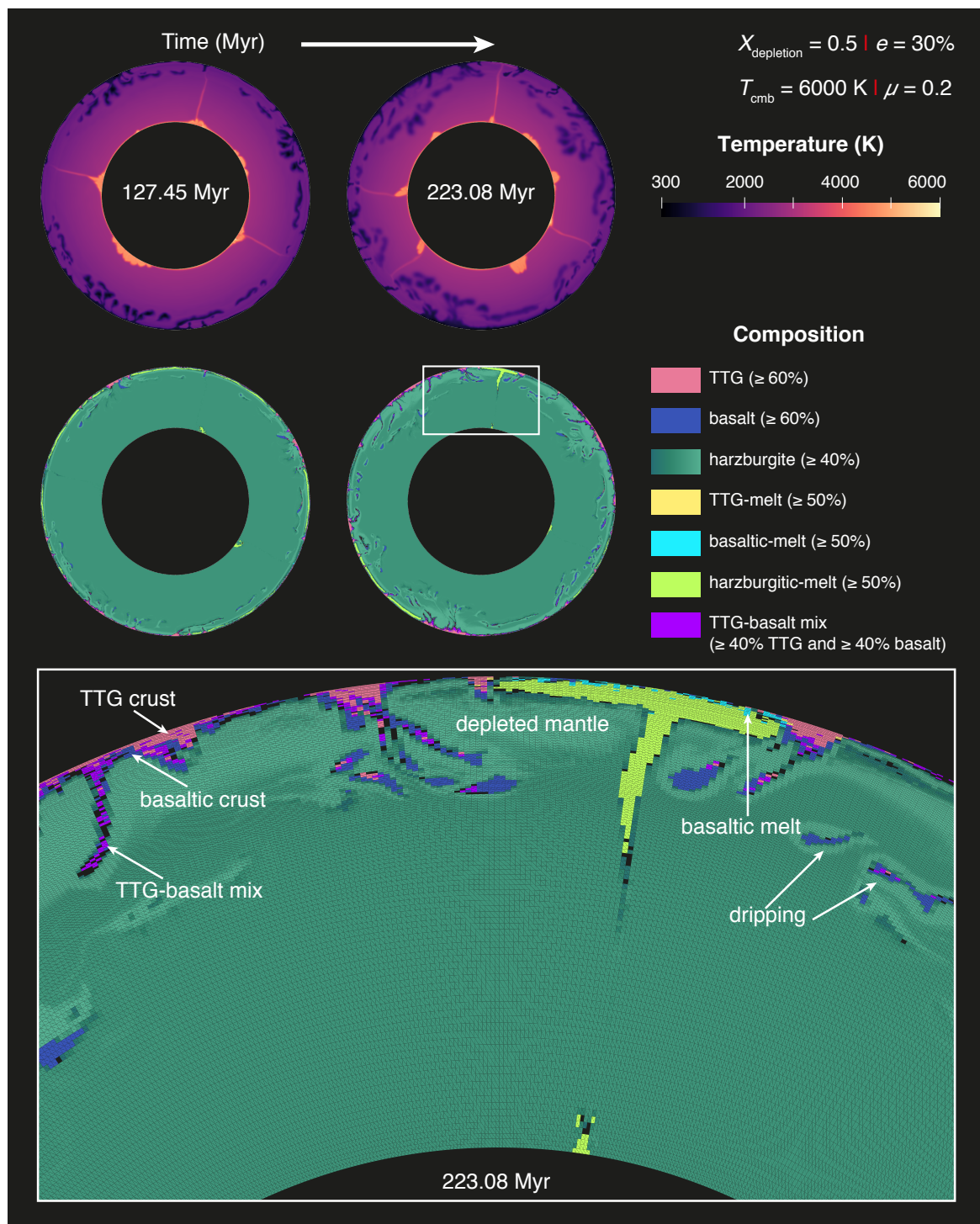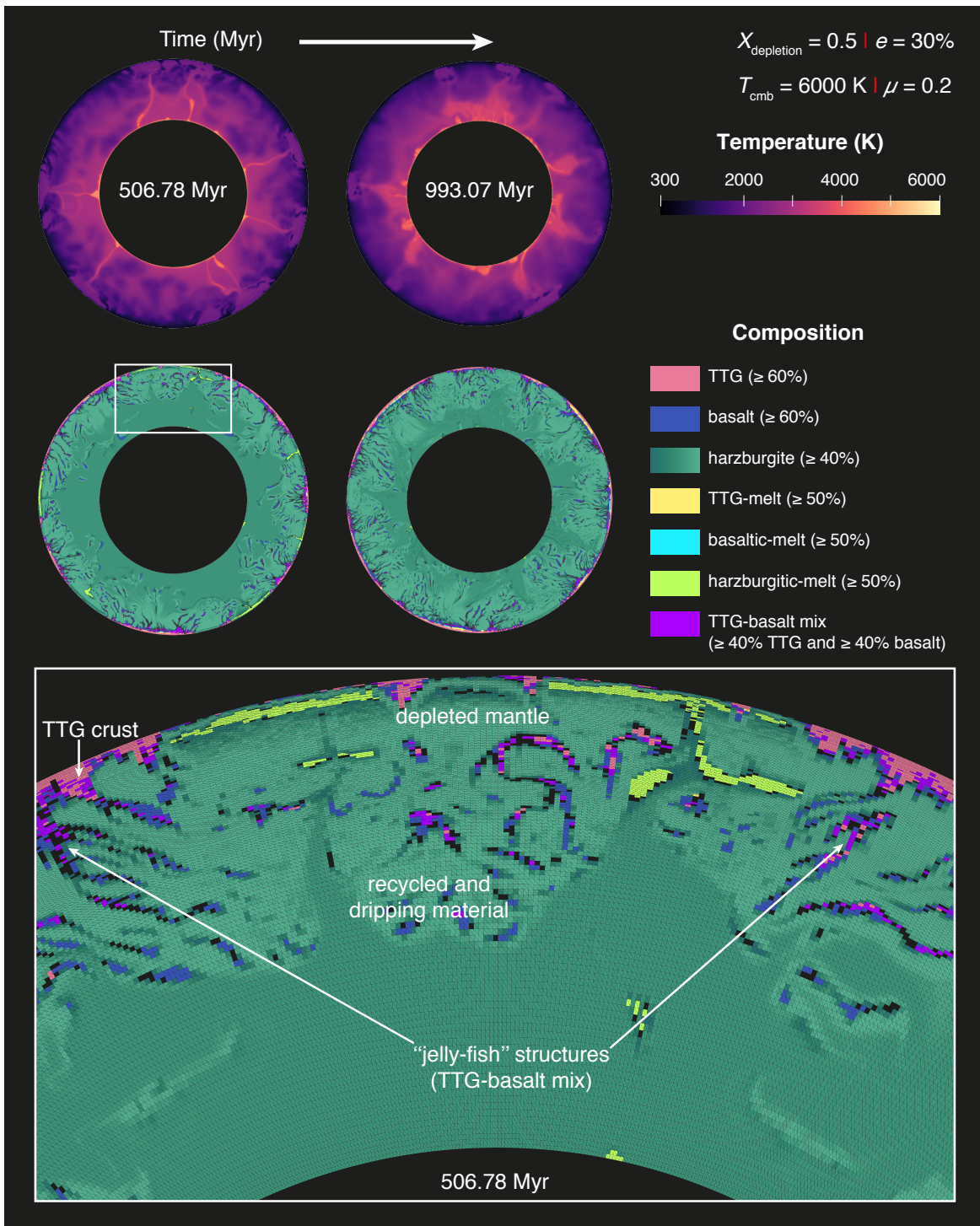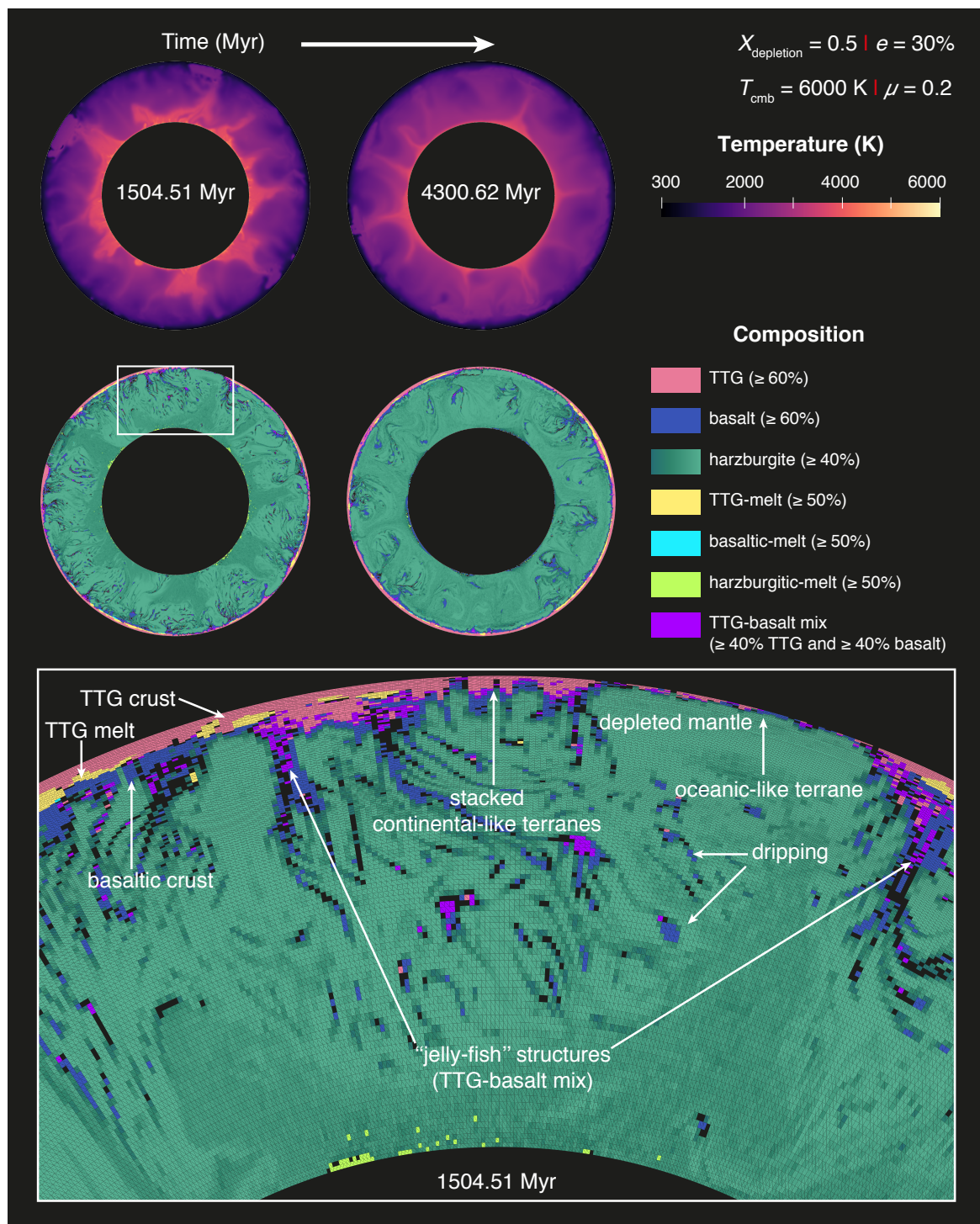
Fig. 4.5 Continued from Fig. 4.4. Thermal (*top*) and compositional (*middle* and zoom-in at *bottom*) evolution with time for simulation *e30x5*. The lighter shades of teal in composition field represent progressive mantle depletion (higher harzburgite content) with time.
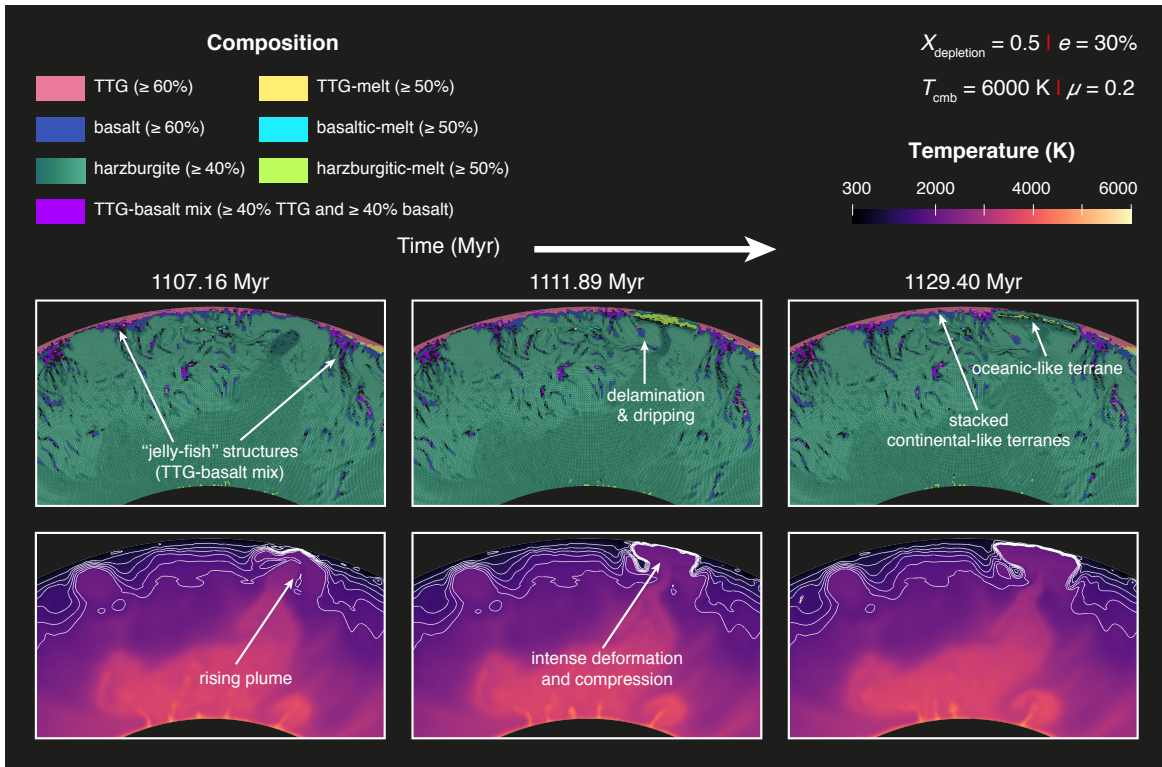
Fig. 4.6 Formation of stacked continental-like terranes over a period of 20 Myr for simulation *e30x5*. The lighter shades of teal in the composition field represent progressive mantle depletion (higher harzburgite content) with time. White lines are isotherms shown from 900-1900 K with increments of 200 K.

4.3.2.1   Influence of eruption efficiency

The volumetric percentage of mantle-derived melt erupted as surface volcanism is given by the eruption efficiency. It has previously been shown in numerical simulations that eruption efficiency has an influence on the pressure-temperature conditions of TTG melt formation [*Sizova et al.*, 2015; *Fischer and Gerya*, 2016]. Fig. 4.7a shows that total and crustal volume of TTG in simulations depend on the eruption efficiency only in the "early stages" (between 250 Myr and 750 Myr). The cold and thick basaltic crust created as a result of volcanism by high eruption efficiency [*Moore and Webb*, 2014; *Lourenco et al.*, 2016; *Rozel et al.*, 2017] is not warm enough to coincide with TTG formation conditions. With low eruption efficiency, more melt is intruded at depths, creating a warmer basaltic crust. This crust melts to form TTG in the presence of water and *enriched basalt*.

4.3.2.2 Influence of lower initial core temperature

Compared to the simulations with an initial core temperature of 6000 K, a value of 5000 K results in lower production of basaltic and TTG material (Fig. 4.7b). A lower core temperature makes the initial plumes less strong and the recycling rates are slightly lower (Fig. 4.7d). The crustal growth follows a parabolic curve representing the intense deformation phase until 1 Gyr.
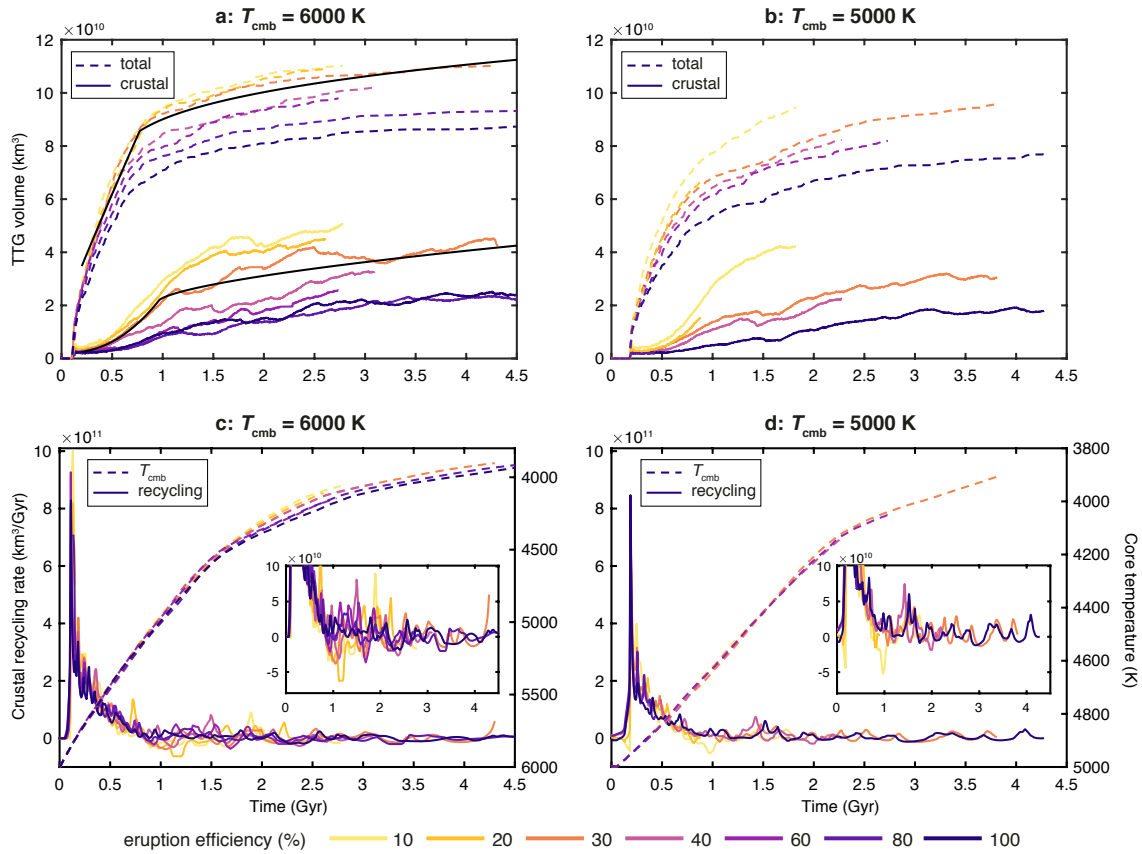
Fig. 4.7 **a, b:** Growth curves for total and crustal volume of TTG with time for initial core temperature of 6000 K and 5000 K. Scaling laws for the simulation presented in the Section 4.3 are represented in black. **c, d:** Crustal recycling rate and evolution of core temperature with time. The insets show a close up of recycling rates with oscillations. All plots are shown for different eruption efficiency.

4.3.2.3 Influence of higher friction coefficient

The internal friction coefficient μ of the lithosphere has been shown to influence the global and regional lithospheric dynamics [e.g., *Tackley*, 2000; *Gerya et al.*, 2015]. We used a higher value of 0.4 in some of our simulations (see Table 4.3) and it showed

negligible differences. The crustal growth followed the same two stages (not shown here) as with a value of 0.2 (discussed in Section 4.3.2 and shown in Fig. 4.7a) and the total volume of TTG produced is comparable to the volumes given by simulations with a lower friction coefficient.

4.3.2.4 Influence of higher depletion fraction

As introduced in Section 4.2.4.2, with a value of depletion fraction $X_{\mathrm{depletion}} = 0.5$, our simulations can generate a mass of TTG reaching up to 10% of the mantle mass. Present-day continental crust only accounts for 0.57% of the Earth's mantle mass, and there is no evidence of widespread Archean crust in the sparse geological record. It is hypothesised that a major portion of the continental crust has recycled back into the mantle. We tested here the influence of a higher value of 0.9 on the crustal growth of TTG, thereby limiting the mass of TTG that can be produced to 2% of the mantle mass.

The thermal and compositional evolution with time for a simulation with $X_{\mathrm{depletion}}$ = 0.9, $e = 40\%$, $T_{\mathrm{cmb}} = 6000\,\mathrm{K}$, and $\mu = 0.2$ (hereby referred to as *e40x9*) is depicted in Fig. 4.8. The first plumes arriving at the surface raise the temperatures in the upper mantle to generate basaltic crust, which subsequently melts to generate TTG material. The less dense TTG material is both intruded and erupted on top of the existing basaltic crust. Owing to this vigorous plume activity, a lot of non-depleted mantle material (represented as darker shades of teal in the compositional field) reaches the surface and propagates laterally, thereby pushing the existing crust (TTG + basaltic) towards the sides and compressing it. Over time, the underlying basaltic crust thickens and gets buried, transforming into denser eclogite. This denser material gets delaminated and starts dripping into the lower mantle. Some of the TTG crust also gets recycled due to entrainment by the convecting mantle. Even after 2552 Myr of evolution (Fig. 4.8), TTG crust covers only a small fraction of the global surface area, which is a more realistic scenario compared to the previous simulations, which produced a lot of TTG crust (Fig. 4.5). Fig. 4.9 shows a decrease in the total and crustal volume of TTG for simulations with a higher depletion fraction (0.9 versus 0.5). Fig. 4.12 compares the volume of basaltic and TTG crust obtained from these simulations to some continental crust growth models built on geological proxies and this is discussed further in Section 4.4.2.

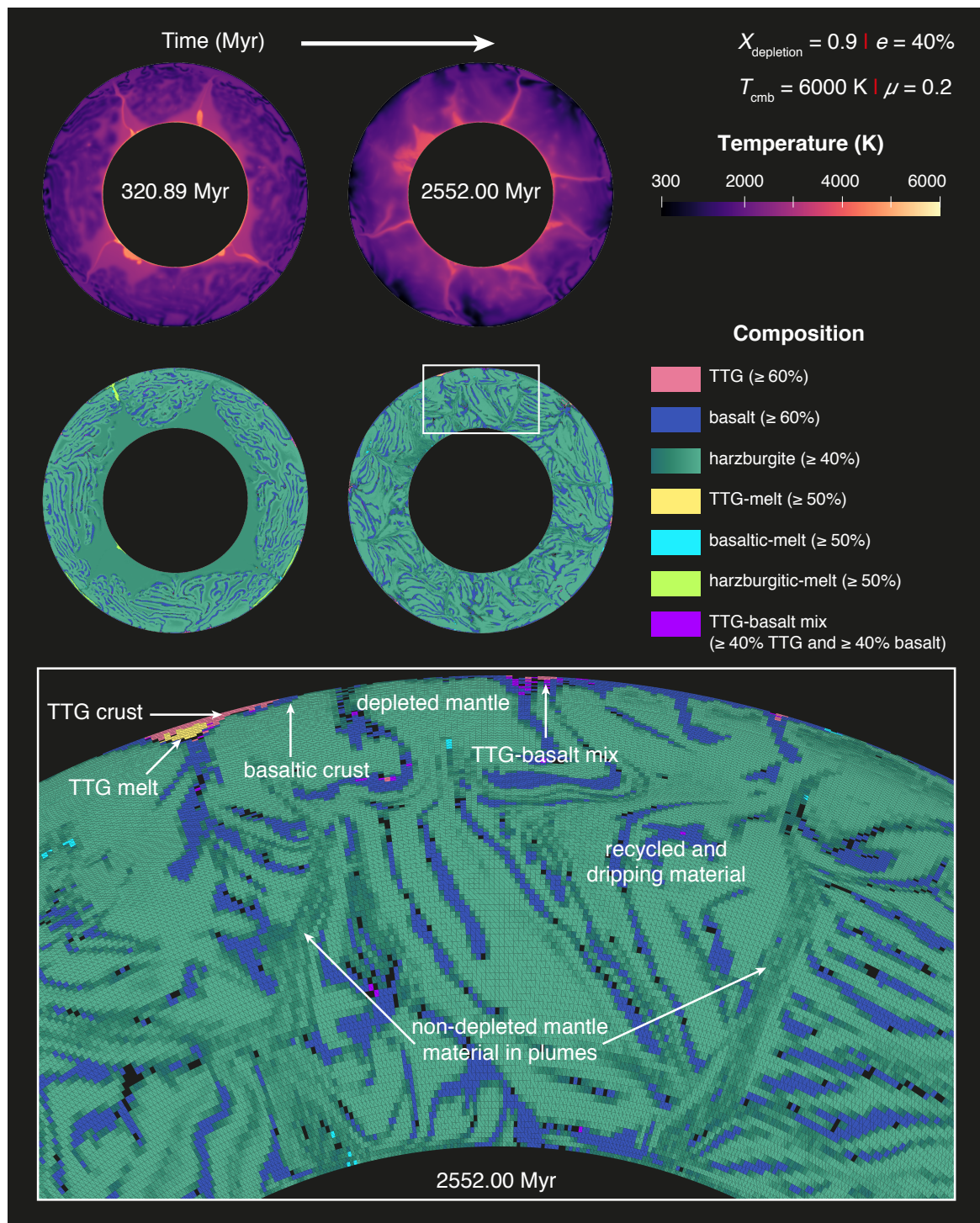Fig. 4.8 Thermal (*top*) and compositional (*middle* and zoom-in at *bottom*) evolution with time for simulation *e40x9*. The lighter shades of teal in composition field represent progressive mantle depletion (higher harzburgite content) with time.
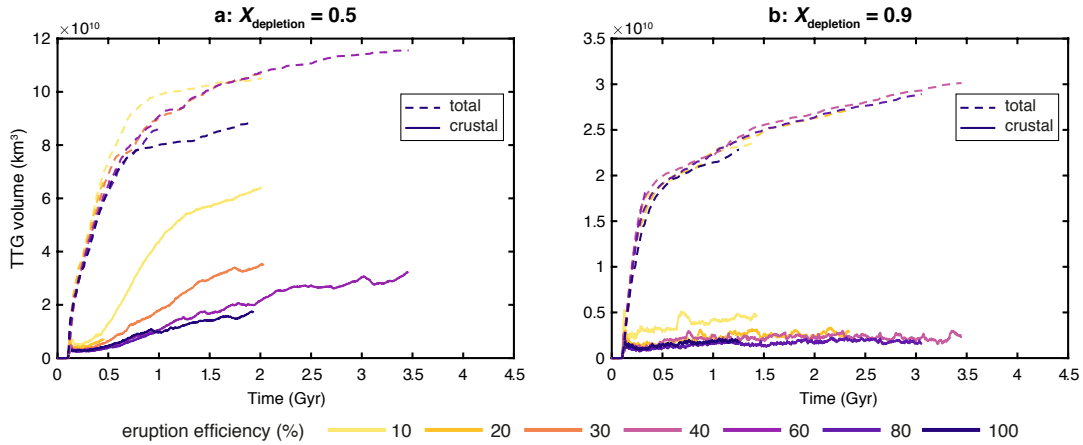
Fig. 4.9 Growth curves for total and crustal volume of TTG with time for simulations with $T_{cmb} = 6000\,\mathrm{K}$ and $\mu = 0.2$ for **a:** $X_{depletion} = 0.5$ and **b:** $X_{depletion} = 0.9$. Both plots are shown for different eruption efficiency.

4.4 Discussion

4.4.1 Scaling laws for TTG generation

Table 4.5 shows the scaling laws for volumes of total TTG produced $V_{TTG,total}$ and crustal TTG remaining at the surface $V_{TTG,crustal}$. Since in both cases we observe a two-stage growth, we performed scalings for "early stages", between 250 Myr and 750 Myr, and "late stages" after 1 Gyr. Fig. 4.10 represents the TTG volume generated in all our simulations (y-axis) as a function of our scaling laws (x-axis). All numbers presented in Table 4.5 have been obtained by automated search of the possible combinations giving the lowest misfit.

4.4.1.1 Volume of total TTG produced

TTG production only starts when the first plumes arrive at the surface. Yet, we did not attempt to perform an estimation of the plume arrival time as our initial state might be unrealistic. The arrival time of plumes depends on the time of growth of thermal boundary layer at the core-mantle boundary and the transit time of Earth's mantle (time taken by a plume to reach the surface). In the Earth, very vigorous solid-state convection probably started during crystallisation of the magma ocean, which is unfortunately very hard to simulate numerically. Starting from a very smooth

Table 4.5 Scaling laws for the volume of TTG rocks as a function of time. Two stages are observed for both cases: total TTG production and crustal TTG.

A - Total TTG volume produced, early stages	Stand. Dev.

$$V_{\text{TTG,total}} = 10^{10}\, A_0\, (t - t_0)^{0.929}$$

$$A_0 = 10.047 - 1.339\tfrac{e}{50}$$

$$t_0 = 1.076 - 1.227\tfrac{T_{\text{cmb}}}{6000}$$

Stand. Dev. $2.43 \cdot 10^9$

B - Total TTG volume produced, late stages	Stand. Dev.

$$V_{\text{TTG,total}} = 10^{10}\, \left(A_0(t_1 - t_0)^{0.929} + 3.432\,(t - t_1)^{0.281}\right)$$

$$t_1 = 0.552 - 0.0884\tfrac{e}{50}$$

Stand. Dev. $2.38 \cdot 10^9$

C - Crustal TTG volume, early stages	Stand. Dev.

$$V_{\text{TTG,crustal}} = 10^{10}\, \left(0.213 + A_1 t^{2.319}\right)$$

$$A_1 = \max\!\left(-7.320 + 4.839 \exp\left(-1.512\tfrac{e}{50}\right) + 7.536\tfrac{T_{\text{cmb}}}{6000}\,,\; 0\right)$$

Stand. Dev. $6.86 \cdot 10^8$

D - Crustal TTG volume, late stages	Stand. Dev.

$$V_{\text{TTG,crustal}} = 10^{10}\, \left(0.213 + A_1 t_2^{2.319} + 0.934\,(t - t_2)^{0.639}\right)$$

$$t_2 = 1.021 - 0.108\tfrac{e}{50}$$
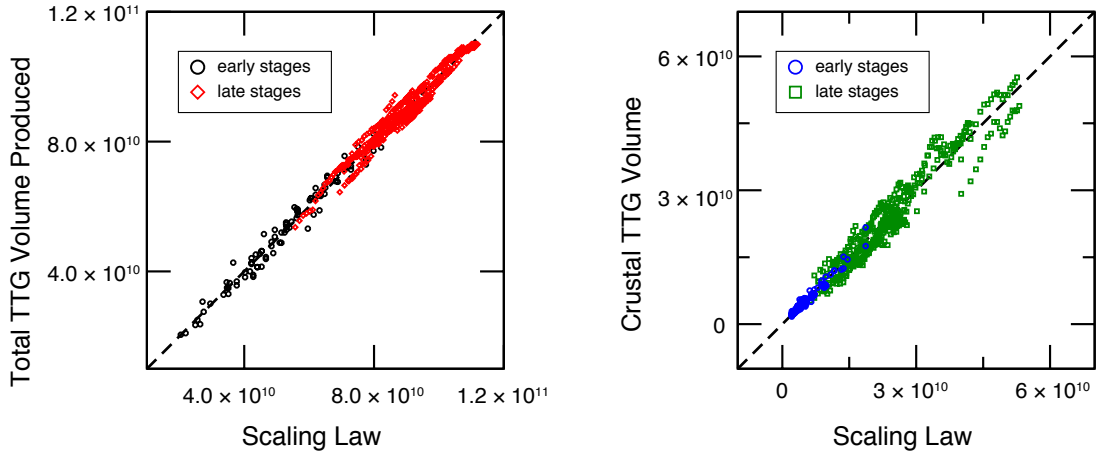
Stand. Dev. $2.97 \cdot 10^9$

Fig. 4.10 Total TTG production (left) and crustal TTG volume (right). One point per hundred million years have been extracted from the curves represented in Figure 4.7 for all simulations. Numerical results are presented in the y-axis, scaling laws are shown on the x-axis. Scaling laws for early stages (black and blue circles) and late stages (red diamonds and green squares) are represented separately (see Table 4.5 for their expressions).

state (boundary layers superimposed on an adiabatic temperature profile), we know that the timing of plume arrival has very little physical meaning.

When the plumes arrive at the surface, we observe a very strong TTG production rate. Table 4.5A shows that the growth is almost linear with time (exponent 0.929). The growth prefactor depends on the eruption efficiency: high eruption efficiency can decrease the TTG production by up to 25%. An origin time t_0 is found that depends on the initial core temperature, with higher temperature resulting in smaller origin time. Although this makes sense from a dynamical point of view, we believe that this observation might be strongly based on our over-simplified initial condition. Interestingly, we found that the core temperature has a negligible effect on the growth rate of TTG. This makes sense as plumes are not controlling the vertical temperature gradient responsible for TTG formation conditions, whereas the eruption efficiency strongly impacts the geotherm.

From Table 4.5B and Fig. 4.7, we can see that TTG production decreases drastically around 0.7-0.9 Gyr. The growth curve suddenly follows a cubic root of time (exponent 0.281) and has not been found to depend on initial core temperature or eruption

efficiency. The inflection time t_i at which growth slows down is different from the time t_1 presented in Table 4.5: t_1 represents the origin of the time-root. Yet, we can see on Fig. 4.7 that the inflection time depends on the eruption efficiency: TTG production slows down quickly for simulations with high eruption efficiency than for the ones with intrusive magmatism. After the inflection, the simplicity of the TTG production rate is remarkable and surprising. No matter what happened in the first billion years of evolution, TTG production slows down and proceeds at the exact same rate for all simulations. Such a drop in crust production rate is usually interpreted as the onset of subduction-driven plate tectonics [e.g., *Cawood et al.*, 2006; *Shirey and Richardson*, 2011; *Dhuime et al.*, 2012; *Hawkesworth et al.*, 2016a,b]. However, we find here that TTG production can suddenly decrease without a significant change in the convection regime and this can be explained as follows. The production of TTG happens as a result of the plumes, which are fed by material with a pyrolytic composition (non-depleted mantle material) at the start of our simulations. Over 1 billion years of evolution, the mantle material becomes depleted (represented as lighter shades of teal in compositional field in Fig. 4.3, 4.4, 4.5 and 4.6) and thus the basalt available in the upper mantle is not enriched enough to produce a lot of TTG.

4.4.1.2 Volume of crustal TTG

The volume of crustal TTG remaining at the surface in our simulations follows a very different trend than the total TTG production itself. Fig. 4.7 shows that a volume of TTG appears with the arrival of the first plumes. This initial volume seems to not depend on the eruption efficiency, except for the extremely low values of e (see yellow curves). Table 4.5C shows that a quasi-parabolic growth follows for about 1 Gyr (exponent 2.319). Both initial core temperature and eruption efficiency have an influence on this growth rate. In particular, cases with low eruption efficiency generate up to 3 times more TTG rocks compared to eruptive cases. TTG production is slightly smaller for cases with lower initial core temperature, but the governing parameter here seems to be the eruption efficiency.

A late growth phase of TTG crust starts after 1-1.4 Gyr. Table 4.5D shows that all curves then follow a simple trend following a quasi square root of time (exponent 0.639). Similar to the total TTG production, this shows that crustal growth does not depend on the initial core temperature or eruption efficiency in the "late stages". It seems that the most important contribution comes from the initial stages of production, and growth slows down at the inflection point, even though plate tectonics do not start.

4.4.2   Comparison with continental crust growth models

Comparing the volume of TTG produced in our global numerical simulations with continental crust growth models is important. However, one must consider that these results may vary with different initial conditions or a different choice of model parameters. Moreover, a major drawback in the continental crust growth models based on geological proxies is the preservation bias. Such models provide records of continents preserved today and do not record the crust that has been destroyed over the evolution of Earth [*Roberts and Spencer*, 2015; *Hawkesworth et al.*, 2016a; *Spencer et al.*, 2017]. A quick comparison between the continental crust volumes obtained from our simulations and growth models shows that they can both have the same order of magnitude, which is dependent on several model parameters. In this section, we comment on the robustness of these parameters and discuss how they might influence TTG production and/or recycling.

Continental crust growth should take into account the new volume being created by magmatic processes as well as the amount recycled back into the mantle by tectonic erosion and lower crustal delamination [*Cawood et al.*, 2013; *Spencer et al.*, 2017]. A range of continental crust growth models have been developed on the basis of age distribution and isotopic compositions of rocks. These models fall into two competing camps based on the nature of crustal growth: continuous growth with differing growth rates through Earth history [e.g., *Hurley and Rand*, 1969; *Armstrong*, 1981; *Allègre and Rousseau*, 1984; *Taylor and McLennan*, 1985; *Armstrong*, 1991; *Taylor and McLennan*, 1996; *Belousova et al.*, 2010; *Dhuime et al.*, 2012]; versus episodic growth corresponding to supercontinent cycles or mantle plume activity [e.g., *McCulloch and Bennett*, 1994; *Condie*, 1998, 2000, 2004a; *Rino et al.*, 2004; *Campbell and Allen*, 2008; *Voice et al.*, 2011]. Using growth models built on records of detrital zircons and sedimentary rocks, *Dhuime et al.* [2017] proposed that 65% of the present continental crust existed by 3 Ga. They argued that there has been a continuous growth of continental crust throughout the evolution of the planet with a significant drop in net production rate from 2.9 - 3.4 km^{3}yr^{-1} on average to 0.6 - 0.7 km^{3}yr^{-1} on average at around $\sim$3 Ga.

4.4.2.1   Crustal composition and production

In all our simulations, the TTG crustal growth (Fig. 4.7a,b) clearly shows two stages of formation (as described in Section 4.4.1.2). The first is a quasi-parabolic growth, which lasts until around 0.7-1.0 Gyr. Afterwards, the growth curve follows a quasi square root of time. This two-stage growth is akin to the proposal of *Dhuime et al.* [2017],

however the drop in TTG production happens about 500 Myr earlier in our simulations and interestingly, this happens without the initiation of subduction or plate tectonics.

Dhuime et al. [2017] considered two different types of continental crust in their crustal growth calculations: mafic, thin, and dense crust formed before 3 Ga, and thick, buoyant crust with intermediate composition formed after 3 Ga. In our simulations, we do not model the progressive evolution of the crust's composition from mafic to intermediate over time. Yet, we can distinguish between the basaltic oceanic crust and felsic TTG crust as they are being generated, and estimate the change in global average crustal composition with time as shown in Fig. 4.11. The very first plumes generate a crust which is entirely basaltic in nature around 100 Myr (for 6000 K) and 200 Myr (for 5000 K). Following their arrival, a growth in felsic crust is observed lasting about 1 billion years. This results in a linear shift in the average global crustal composition from basaltic to felsic. The final basaltic content of the crust (20-40%) changes with the volume of crustal TTG, which in turn is a function of the eruption efficiency. Using MgO content as a proxy for silicification of the bulk Archean crust, *Tang et al.* [2016] suggested a gradual shift in its average composition from mafic to felsic between 3-2.5 Ga. They hypothesised that this period witnessed an increased water availability from the subducting oceanic crust and might have been the onset of plate tectonics. Our simulations reproduce the similar trend of crustal silicification, however, for different reasons. As the core cools down, the plumes are less strong around 2.5 Ga and they generate less basaltic crust. The newly generated crust melts again to form TTG crust which is ubiquitous at the surface. Moreover, the underlying dense crust made of basaltic-eclogitic material delaminates and recycles more efficiently, thereby contributing towards increasing felsic crustal composition.

According to *Dhuime et al.* [2017], the volume of continental crust after the first 1.5 billion years (timing of inflection as defined in their paper) of Earth's evolution would be $\approx 4.5 \cdot 10^9 \, \text{km}^3$, or 65% of present-day volume estimate $\approx 6.9 \cdot 10^9 \, \text{km}^3$. After 1.0 Gyr (timing of inflection in our simulations), the overall volume of TTG and basaltic crust ($V_{\text{TTG,crustal}} + V_{\text{bas,crustal}}$ from Table 4.3) in our simulation *e30x5* is $2.98 \cdot 10^{10} \, \text{km}^3$, which is around 56% of the final overall crustal volume at 4.3 Gyr ($5.36 \cdot 10^{10} \, \text{km}^3$). On average, for simulations with $X_{\text{depletion}} = 0.5$, this overall crustal volume is 5-10 times higher (depending on eruption efficiency) than the estimates of *Dhuime et al.* [2017].

For simulations with $X_{\text{depletion}} = 0.9$, TTG production shows the same two-stage growth as before: a linear growth that plateaus after 0.7-0.9 Gyr of evolution. However, the volume of total TTG produced (Fig. 4.9) has dropped by about 75% when compared to simulations with $X_{\text{depletion}} = 0.5$. The volumes of both TTG and basaltic crust
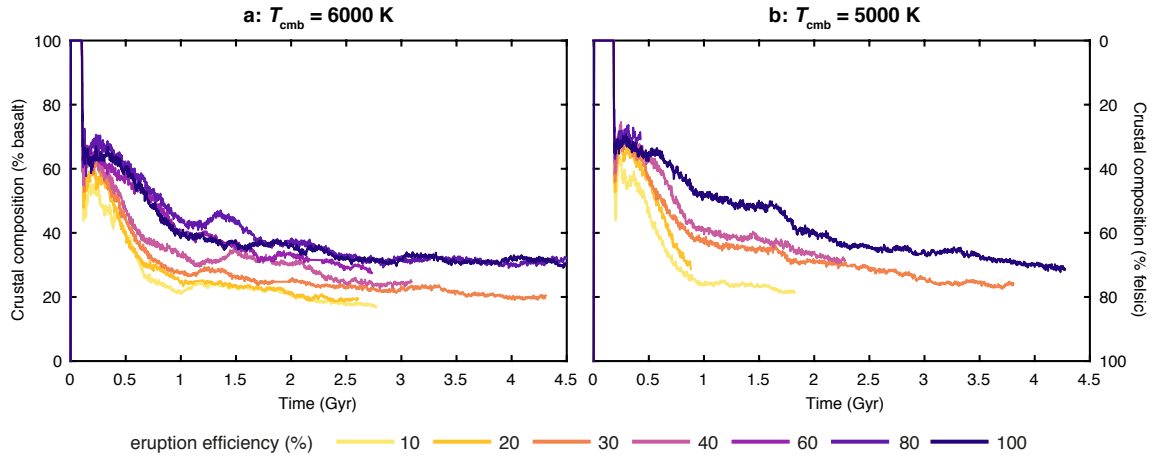
Fig. 4.11 Evolution of average global crustal composition from basaltic to felsic over time for simulations with $X_{\text{depletion}} = 0.5$ and $\mu = 0.2$ for **a:** $T_{\text{cmb}} = 6000\,\text{K}$ and **b:** $T_{\text{cmb}} = 5000\,\text{K}$. Both plots are shown for different eruption efficiency.

reach a peak in the first $150\,\text{Myr}$ before they get recycled owing to strong plume activity (Fig. 4.12). Following this, the crustal volumes remain roughly at the same level throughout the evolution, which is attributed to the episodic generation and recycling of the crust. Most importantly, the combined global crustal volume (TTG + basaltic) obtained from these simulations have the same order of magnitude as different crustal growth models [*Armstrong*, 1981; *Dhuime et al.*, 2017].

A factor that directly influences the production of TTG in our simulations is the availability of water in the mantle. For simplicity, the material within the top $10\,\text{km}$ of the mantle is considered to be fully hydrated at the time of initialisation, and this water is free to advect on tracers throughout the mantle (Fig. A.1 in Appendix). In the simulations presented here, the concentration of water is taken to be the same (with partition coefficient $D_{\text{part,H}_2\text{O}} = 1$) in both the solid and melt phases. In nature, water is incompatible in the solid phase and partitions into the melt during partial melting. For future work, lower values of $D_{\text{part,H}_2\text{O}}$: 0.01, 0.1 should be explored as this will substantially reduce the amount of water available in a cell for TTG production with subsequent partial melting events. Additionally, water-dependent basalt solidus should be used as the presence of water lowers the melting temperatures. Also, depth and temperature limits for water penetration could be applied, as previously done by *Gregg et al.* [2009] for hydrothermal fluid circulation in their melt migration study.

Simulations presented in this study can produce TTG whose mass can reach up to $\approx 4.04 \cdot 10^{23}\,\text{kg}$ (10% of mantle mass for $X_{\text{depletion}} = 0.5$) or $\approx 8.08 \cdot 10^{22}\,\text{kg}$ (2% of mantle
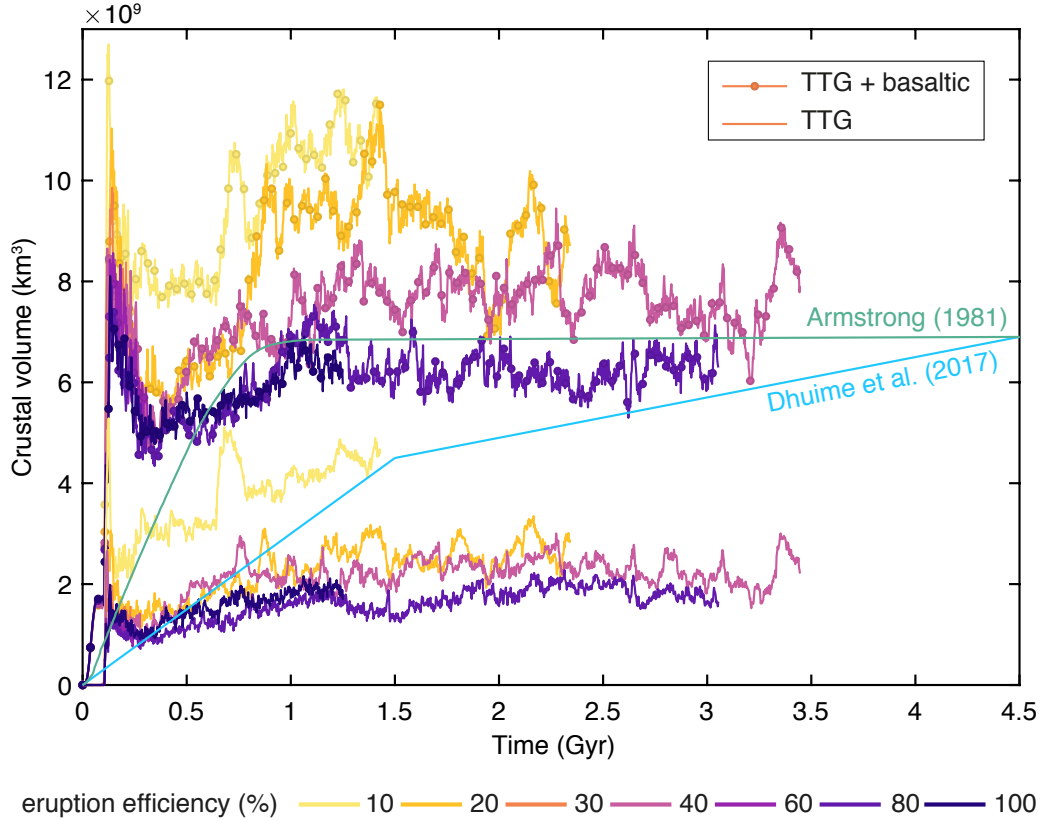
Fig. 4.12 Growth curves for crustal volume of TTG and basalt with time for simulations with $X_{\text{depletion}} = 0.9$, $T_{\text{cmb}} = 6000\,\text{K}$, and $\mu = 0.2$. All plots are shown for different eruption efficiency. Additionally, two different continental crust growth models based on geological proxies are shown here [*Armstrong*, 1981; *Dhuime et al.*, 2017].

mass for $X_{\text{depletion}} = 0.9$). Using a reference density of TTG as $2700\,\text{kg/m}^3$, these mass limits would correspond to volume limits of $1.49 \cdot 10^{11}\,\text{km}^3$ and $2.99 \cdot 10^{10}\,\text{km}^3$ respectively. However, this physical limit is not the reason for the drop in TTG production at the inflection point in our simulations as none of them produce this much TTG after $1.0\,\text{Gyr}$ of evolution (see $V_{\text{TTG,total}}$ in Table 4.3, 4.4 and Fig. 4.7, 4.9).

4.4.2.2 Crustal recycling and preservation

All our simulations show intense recycling of the TTG and basaltic crust with delamination and eclogitic dripping in the first $\sim 500\,\text{Myr}$ (Fig. 4.7c,d). This behaviour is similar to the 'plutonic squishy lid' or vertical-tectonics geodynamic regime that has been suggested for the early Earth [e.g., *Van Kranendonk et al.*, 2004; *Sizova et al.*, 2010; *Johnson et al.*, 2013b; *Gerya et al.*, 2015; *Condie*, 2016; *Fischer and Gerya*, 2016].

The rate of recycling keeps decreasing until 1 Gyr and becomes roughly constant with small oscillations. The positive fluctuations in recycling rate are attributed to the buoyant TTG material being brought back upwards by the convecting mantle and some of it getting relaminated to the base of the crust. The negative fluctuations correspond to the delamination and dripping of the lower crust owing to plume activity.

Convergent margins are considered to be the loci of continental crust destruction. It has been suggested that the growth of continental crust dropped around 3 Ga owing to higher crustal recycling and the onset of subduction-driven plate tectonics. However, none of our simulations exhibit subduction or modern-style plate tectonics, which would have increased the recycling rate of continental crust. Figure A.3 in the Appendix shows the age of the mantle based on the time since it melted last. The majority of TTG crust (black contour lines) is only 300-400 Myr old. This relatively young age of the continental material is because of the constant moderate recycling and its inability to form strong continents. Some of it has also melted again and solidified over time.

Another factor that might increase continental crust recycling in our simulations is the inclusion of phase transitions. For example, when TTG/felsic material is buried or subducted, its density increases by about $168 \, \text{kg/m}^3$ at a depth of 290 km (Stishovite phase transition given in [*Gerya et al.*, 2004]). A treatment of all the relevant phase transitions leads to an even higher density increase, with TTG likely becoming denser than basalt throughout most of the upper mantle, and having a density similar to pyrolite in the lower mantle [*Komabayashi et al.*, 2009; *Kawai et al.*, 2009]. When Stishovite phase transition is incorporated in the simulations given in Table 4.4, no more "jelly-fish" structures are observed in the mantle (Fig. 4.8). Using a reference viscosity one order of magnitude lower than the value used in the simulations here ($1 \cdot 10^{21} \, \text{Pa·s}$) would result in a higher convective vigour, which may also increase the recycling rate by thinning the lithosphere [*Rozel et al.*, 2017].

Forming a stiff subcontinental lithospheric mantle (SCLM) underlying the TTG crust can help in reducing its recycling and ensuring its preservation. It has been suggested that low density, viscous, and melt depleted SCLM might have co-evolved with the continental crust [*Herzberg*, 1993; *Griffin et al.*, 2003; *Griffin and O'Reilly*, 2007; *Arndt et al.*, 2009; *Lee et al.*, 2011]. Presently, we do not form such rheologically strong cratonic roots in our models, possibly because our rheology is not composition-dependent and therefore the depleted harzburgitic material has the same viscosity as the background mantle.

4.5   Conclusions

We have presented here a new numerical modelling approach allowing for the self-consistent creation of primordial continental crust (TTG) in global mantle convection models, which to our knowledge is the first time it has been done. This is achieved by parameterising the processes of melt generation and melt extraction. Two distinct stages of TTG production are observed in our simulations: a period of continuous linear growth with time and intense recycling that lasts for 1 Gyr, followed by a stage with the TTG growth proportional to cubic root of time and moderate recycling. Moreover, we show that a drop in TTG production happens as the mantle becomes depleted over time without needing subduction or plate tectonics. This has significant implications for comparative planetology and the ongoing debate about when plate tectonics started. Our simulations and scaling laws support the important role of intrusive magmatism in shaping the Earth's lithosphere [*Crisp*, 1984; *Cawood et al.*, 2013]. Most significantly, crustal volumes obtained from our simulations have the same order of magnitude as with many other continental crust growth models based on geological proxies. We show lower crustal delamination and dripping, formation of stacked continental-like terranes, and recycling of the continental crust. Yet, dome and keel structures, which are typical of some Archean cratons [*Van Kranendonk et al.*, 2004; *Hickman*, 2004; *Van Kranendonk*, 2011] are not resolvable in our global models. Moreover, our simple petrological model does not consider magmatic weakening or a density increase of the residue after melt extraction [e.g., *Sizova et al.*, 2010; *Vogt et al.*, 2012; *Sizova et al.*, 2015]. Future improvements should also allow us to reproduce and explain the coeval formation of strong, depleted, and viscous cratonic roots.

Chapter 5

Conclusions and perspectives

5.1 Thesis summary

In this thesis, numerical models were developed and used to: (i) investigate the qualitative as well as quantitative relationship between continents and elevated temperatures in the mantle, (ii) create primordial continental crust self-consistently and investigate the global geodynamic regime of early Earth. The main developments and findings of the previous chapters are briefly summarised here.

- **Chapter 2** details the theoretical and computational framework behind all the mantle convection simulations presented in this thesis. It introduces the governing equations, mantle rheology, and the phase changes considered. However, the main focus of this chapter is the melting parameterisation. The existing implementation of basaltic crust production has been extended to form continental crust (TTG) by two-step differentiation of the pyrolytic mantle. The chapter explains the iterative procedure of how change in melt fraction is calculated on the cell level. Once the melt is generated in the mantle, it is carried on tracers and transported above to the gaps that are created in the lithosphere for eruption (volcanism) and intrusion (plutonism). This extended melting treatment leading to the self-consistent generation of continents is the novelty of this thesis.

- **Chapter 3** contributes to the ongoing debate whether there is a correlation between continents and elevated temperatures in the mantle by offering qualitative and quantitative arguments. Using 2D global models (both incompressible and compressible) with prescribed, yet mobile continents, the evolution of this correlation is shown. The amplitude of this correlation is calculated by the spectral decomposition of temperature and composition fields. Starting with

simple incompressible models, I show that the dominant degree of correlation changes with continental distribution and its amplitude can reach up to $200\,\mathrm{K}$. A systematic parameter study and analytical scaling laws show a decrease in correlation with increasing core temperature, number of continents, internal heating, and Rayleigh number. These results are in agreement with previous findings of other authors. However, the results differ when a more realistic model setup is employed with core cooling and melting-induced crustal production (MCP). These simulations show that MCP events resulting from the correlation tend to break the continents apart, thereby destroying the correlation. This result is unique and has never been reported before in previous studies.

- **Chapter 4** investigates the global geodynamic regime in the hotter Archean Earth. The melting parameterisation developed in Chapter 2 is employed to create primordial continental crust (TTG rocks) in a self-consistent manner. I systematically vary the ratio of intrusive (plutonism) and eruptive (volcanism) magmatism, initial core temperature and internal friction coefficient to study TTG growth. Two distinct stages of TTG production are observed in my 2D simulations and analytical scaling laws: a period of continuous linear growth with time and intense recycling that lasts for 1 billion years, followed by a stage with the TTG growth proportional to cubic root of time and moderate recycling. The resolution of my simulations allow us to see lower crustal delamination and dripping, formation of stacked terranes, and recycling of the continental crust. However, dome and keel structures, which are typical of Archean cratons are not resolvable. The results of this chapter reaffirm the significant role of intrusive magmatism in shaping our planet's lithosphere. Most importantly, my results show that initiation of subduction and plate tectonics was not required during the Archean to force a drop in TTG production.

5.2   Future directions

Though we are still far from fully answering the unresolved questions raised in the introductory chapter, the results of my research have provided some useful insights. The generation of continents by the melting parameterisation extended in this thesis has brought the capabilities of the code StagYY one step further. A lot more modelling efforts are needed and some future improvements are suggested next.

Formation of cratonic roots

The next interesting and logical step would be to model the coupled formation of sub-continental lithospheric mantle (SLCM) with continental crust. It has been suggested that low density, viscous, and melt depleted SCLM might have co-evolved with the continental crust [*Herzberg*, 1993; *Griffin et al.*, 2003; *Griffin and O'Reilly*, 2007; *Arndt et al.*, 2009; *Lee et al.*, 2011]. The possibility to generate cratonic roots by using a composition-dependent rheology, where the depleted harzburgitic material has higher viscosity than the surrounding mantle should be explored.

Trace-element partitioning

Continental crust is andesitic in composition with 60.6% SiO_2 and 4.7% MgO [*Hawkesworth and Kemp*, 2006a] with a high concentration of incompatible trace elements, thereby acting as a complimentary geochemical reservoir to the Earth's depleted mantle [*Hofmann*, 1988; *Rudnick*, 1995]. At present, the partitioning of trace-elements into the crust is not implemented and it could be developed further.

Lithospheric weakening

Previous studies have shown that emplacement of sub-lithospheric melts and fluids into the lithosphere weakens it. This has important consequences for the strength of the plates and it changes the style of subduction [*Sizova et al.*, 2010; *Vogt et al.*, 2012; *Sizova et al.*, 2015]. Considering that plutonism has played a significant role in shaping the Earth's lithosphere, the effect of melt-induced weakening should be explored. Also, a decrease in the viscosity of olivine in the presence of water should be considered [*Hirth and Kohlstedt*, 1996]

Dimensionality and numerical resolution

All the results presented in this thesis were performed in a 2D spherical annulus geometry [*Hernlund and Tackley*, 2008], which has been shown to give similar results for thermo-chemical mantle convection and core evolution as in 3D spherical geometry [*Nakagawa and Tackley*, 2010]. As 3D simulations are computationally expensive, future studies could run cases with a higher dimensionality in a limited parameter space. The numerical resolution used in my simulations varies radially, with the highest vertical resolution of ~ 6-$7\,km$ at the surface. This could be improved in the future

studies to be able to resolve dome and keel structures, which are typical of Archean cratons [*Van Kranendonk et al.*, 2015].

References

Abe, Y. (1993a). Physical state of the very early Earth. *LITHOS*, 30(3-4):223–235.

Abe, Y. (1993b). Thermal Evolution and Chemical Differentiation of the Terrestrial Magma Ocean. In *Evolution of the Earth and Planets*, pages 41–54. American Geophysical Union, Washington, D. C.

Abe, Y. (1997). Thermal and chemical evolution of the terrestrial magma ocean. *Physics of the Earth and Planetary Interiors*, 100(1-4):27–39.

Albarède, F. (1998). The growth of continental crust. *Tectonophysics*, 296(1-2):1–14.

Allègre, C. J. and Rousseau, D. (1984). The growth of the continent through geological time studied by Nd isotope analysis of shales. *Earth and Planetary Science Letters*, 67(1):19–34.

Amelin, Y., Lee, D.-C., Halliday, A. N., and Pidgeon, R. T. (1999). Nature of the Earth's earliest crust from hafnium isotopes in single detrital zircons. *Nature*, 399(6733):252–255.

Amestoy, P. R., Duff, I. S., and L'Excellent, J. Y. (2000). Multifrontal parallel distributed symmetric and unsymmetric solvers. *Computer Methods in Applied Mechanics and Engineering*, 184(2-4):501–520.

Anderson, A. T. (1982a). Parental basalts in subduction zones: Implications for continental evolution. *Journal of Geophysical Research*, 87(B8):7047–7060.

Anderson, D. L. (1982b). Hotspots, Polar Wander, Mesozoic Convection and the Geoid. *Nature*, 297(5865):391–393.

Andrault, D., Bolfan-Casanova, N., Lo Nigro, G., Bouhifd, M. A., Garbarino, G., and Mezouar, M. (2011). Solidus and liquidus profiles of chondritic mantle: Implication for melting of the Earth across its history. *Earth and Planetary Science Letters*, 304(1-2):251–259.

Andrault, D., Pesce, G., Bouhifd, M. A., Bolfan-Casanova, N., Henot, J.-M., and Mezouar, M. (2014). Melting of subducted basalt at the core-mantle boundary. *Science*, 344(6186):892–895.

Arculus, R. J. (1981). Island arc magmatism in relation to the evolution of the crust and mantle. *Tectonophysics*, 75(1-2):113–133.

Arculus, R. J. (1999). Origins of the continental crust. *Journal and Proceedings of the Royal Society of New South Wales*, 132:83–110.

Armann, M. and Tackley, P. J. (2012). Simulating the thermochemical magmatic and tectonic evolution of Venus's mantle and lithosphere: Two-dimensional models. *Journal of Geophysical Research*, 117(E12).

Armstrong, R. L. (1981). Radiogenic Isotopes: The Case for Crustal Recycling on a Near-Steady-State No-Continental-Growth Earth. *Philosophical Transactions of the Royal Society of London Series A: Mathematical Physical and Engineering Sciences*, 301(1461):443–472.

Armstrong, R. L. (1991). The persistent myth of crustal growth. *Australian Journal of Earth Sciences*, 38(5):613–630.

Arndt, N. T., Coltice, N., Helmstaedt, H., and Gregoire, M. (2009). Origin of Archean subcontinental lithospheric mantle: Some petrological constraints. *LITHOS*, 109(1-2):61–71.

Arndt, N. T. and Goldstein, S. L. (1987). Use and abuse of crust-formation ages. *Geology*, 15(10):893.

Arndt, N. T. and Goldstein, S. L. (1989). An open boundary between lower continental crust and mantle: its role in crust formation and crustal recycling. *Tectonophysics*, 161(3-4):201–212.

Aubaud, C., Hirschmann, M. M., Withers, A. C., and Hervig, R. L. (2008). Hydrogen partitioning between melt, clinopyroxene, and garnet at 3 GPa in a hydrous MORB with 6 wt.% H_2O. *Contributions to Mineralogy and Petrology*, 156(5):607–625.

Barker, F. and Arth, J. G. (1976). Generation of trondhjemitic-tonalitic liquids and Archean bimodal trondhjemite-basalt suites. *Geology*, 4(10):596.

Barth, M. G., McDonough, W. F., and Rudnick, R. L. (2000). Tracking the budget of Nb and Ta in the continental crust. *Chemical geology*, 165(3-4):197–213.

Barth, M. G., Rudnick, R. L., Horn, I., McDonough, W. F., Spicuzza, M. J., Valley, J. W., and Haggerty, S. E. (2001). Geochemistry of xenolithic eclogites from West Africa, part I: A link between low MgO eclogites and archean crust formation. *GEOCHIMICA ET COSMOCHIMICA ACTA*, 65(9):1499–1527.

Barth, M. G., Rudnick, R. L., Horn, I., McDonough, W. F., Spicuzza, M. J., Valley, J. W., and Haggerty, S. E. (2002). Geochemistry of xenolithic eclogites from West Africa, part 2: origins of the high MgO eclogites. *GEOCHIMICA ET COSMOCHIMICA ACTA*, 66(24):4325–4345.

Beard, B. L., Fraracci, K. N., Clayton, R. A., Mayeda, T. K., Snyder, G. A., Sobolev, N. V., and Taylor, L. A. (1996). Petrography and geochemistry of eclogites from the Mir kimberlite, Yakutia, Russia. *Contributions to Mineralogy and Petrology*, 125(4):293–310.

Bédard, J. H. (2006). A catalytic delamination-driven model for coupled genesis of Archaean crust and sub-continental lithospheric mantle. *GEOCHIMICA ET COSMOCHIMICA ACTA*, 70(5):1188–1214.

Belousova, E. A., Kostitsyn, Y. A., Griffin, W. L., Begg, G. C., O'Reilly, S. Y., and Pearson, N. J. (2010). The growth of the continental crust: Constraints from zircon Hf-isotope data. *LITHOS*, 119(3-4):457–466.

Ben-Avraham, Z., Nur, A., Jones, D., and COX, A. (1981). Continental Accretion: From Oceanic Plateaus to Allochthonous Terranes. *Science*, 213(4503):47–54.

Bénard, H. (1900). Les tourbillons cellulaires dans une nappe liquide. *Revue Generale des Sciences Pures et Appliquees*, 11:1261–1271, 1309–1328.

Bénard, H. (1901). Les tourbillons cellulaires dans une nappe liquide tranportant de la chaleur par convection en régime permanent. *Annales de Chimie et de Physique*, 23:62–144.

Bird, P. (1978). Initiation of intracontinental subduction in the Himalaya. *Journal of Geophysical Research*, 83(B10):4975–4987.

Bird, P. (1979). Continental delamination and the Colorado Plateau. *Journal of Geophysical Research*, 84(B13):7561–7571.

Bird, P. and Baumgardner, J. (1981). Steady propagation of delamination events. *Journal of Geophysical Research*, 86(B6):4891–4903.

Bodet, F. and Schärer, U. (2000). Evolution of the SE-Asian continent from U-Pb and Hf isotopes in single grains of zircon and baddeleyite from large rivers. *GEOCHIMICA ET COSMOCHIMICA ACTA*, 64(12):2067–2091.

Borucki, W. J., Koch, D. G., Basri, G., Batalha, N., Brown, T. M., Bryson, S. T., Caldwell, D., Christensen-Dalsgaard, J., Cochran, W. D., DeVore, E., Dunham, E. W., Gautier, T. N., Geary, J. C., Gilliland, R., Gould, A., Howell, S. B., Jenkins, J. M., Latham, D. W., Lissauer, J. J., Marcy, G. W., Rowe, J., Sasselov, D., Boss, A., Charbonneau, D., Ciardi, D., Doyle, L., Dupree, A. K., Ford, E. B., Fortney, J., Holman, M. J., Seager, S., Steffen, J. H., Tarter, J., Welsh, W. F., Allen, C., Buchhave, L. A., Christiansen, J. L., Clarke, B. D., Das, S., Désert, J.-M., Endl, M., Fabrycky, D., Fressin, F., Haas, M., Horch, E., Howard, A., Isaacson, H., Kjeldsen, H., Kolodziejczak, J., Kulesa, C., Li, J., Lucas, P. W., Machalek, P., McCarthy, D., MacQueen, P., Meibom, S., Miquel, T., Prsa, A., Quinn, S. N., Quintana, E. V., Ragozzine, D., Sherry, W., Shporer, A., Tenenbaum, P., Torres, G., Twicken, J. D., Van Cleve, J., Walkowicz, L., Witteborn, F. C., and Still, M. (2011). Characteristics of planetary candidates observed by Kepler. II. Analysis of the first four months of data. *Astrophysical Journal*, 736(1):19.

Boyd, F. R. (1987). High-and low-temperature garnet peridotite xenoliths and their possible relation to the lithosphere-asthenosphere boundary beneath Africa. In Nixon, P. H., editor, *Mantle Xenolith*, pages 403–412. John Wiley & Sons Ltd.

Boyd, F. R. (1989). Compositional distinction between oceanic and cratonic lithosphere. *Earth and Planetary Science Letters*, 96(1-2):15–26.

Brown, M. (2006). Duality of thermal regimes is the distinctive characteristic of plate tectonics since the Neoarchean. *Geology*, 34(11):961.

Brown, S. C. (1957). Count Rumford Discovers Thermal Convection. *Daedalus*, 86(4):340–343.

Buffett, B. A., Huppert, H. E., Lister, J. R., and Woods, A. W. (1992). Analytical Model for Solidification of the Earths Core. *Nature*, 356(6367):329–331.

Buffett, B. A., Huppert, H. E., Lister, J. R., and Woods, A. W. (1996). On the thermal evolution of the Earth's core. *Journal of Geophysical Research*, 101(B4):7989–8006.

Byerlee, J. (1978). Friction of rocks. *Pure and Applied Geophysics*, 116(4-5):615–626.

Campbell, I. H. and Allen, C. M. (2008). Formation of supercontinents linked to increases in atmospheric oxygen. *Nature Geoscience*, 1(8):554–558.

Canil, D. (2004). Mildly incompatible elements in peridotites and the origins of mantle lithosphere. *LITHOS*, 77(1-4):375–393.

Canil, D. (2008). Canada's craton: A bottoms-up view. *GSA Today*, 18(6):4.

Canup, R. M. (2004). Dynamics of Lunar Formation. *Annual Review of Astronomy and Astrophysics*, 42(1):441–475.

Carlson, R. W., Pearson, D. G., and James, D. E. (2005). Physical, chemical, and chronological characteristics of continental mantle. *Reviews of Geophysics*, 43(1):1.

Cawood, P. A., Hawkesworth, C. J., and Dhuime, B. (2013). The continental record and the generation of continental crust. *Geological Society of America Bulletin*, 125(1-2):14–32.

Cawood, P. A., Kröner, A., and Pisarevsky, S. (2006). Precambrian plate tectonics: Criteria and evidence. *GSA Today*, 16(7):4.

Chamberlain, K. R., Frost, C. D., and Frost, B. R. (2003). Early Archean to Mesoproterozoic evolution of the Wyoming Province: Archean origins to modern lithospheric architecture. *Canadian Journal of Earth Sciences*, 40(10):1357–1374.

Chandrasekhar, S. (1961). *Hydrodynamic and Hydromagnetic Stability*. Oxford University Press, New York.

Chesley, J. T., Rudnick, R. L., and Lee, C.-T. (1999). Re-Os systematics of mantle xenoliths from the East African Rift: age, structure, and history of the Tanzanian craton. *GEOCHIMICA ET COSMOCHIMICA ACTA*, 63(7-8):1203–1217.

Chowdhury, P., Gerya, T., and Chakraborty, S. (2017). Emergence of silicic continents as the lower crust peels off on a hot plate-tectonic Earth. *Nature Geoscience*, 10(9):698–703.

Christensen, U. R. and Hofmann, A. W. (1994). Segregation of subducted oceanic crust in the convecting mantle. *Journal of Geophysical Research*, 99(B10):19867–19884.

Čížková, H., van den Berg, A. P., Spakman, W., and Matyska, C. (2012). The viscosity of Earth's lower mantle inferred from sinking speed of subducted lithosphere. *Physics of the Earth and Planetary Interiors*, 200-201:56–62.

Coffin, M. F. and Eldholm, O. (1994). Large igneous provinces: Crustal structure, dimensions, and external consequences. *Reviews of Geophysics*, 32(1):1–36.

Coltice, N., Bertrand, H., Rey, P., Jourdan, F., Phillips, B. R., and Ricard, Y. (2009). Global warming of the mantle beneath continents back to the Archaean. *Gondwana Research*, 15(3-4):254–266.

Coltice, N., Phillips, B. R., Bertrand, H., Ricard, Y., and Rey, P. (2007). Global warming of the mantle at the origin of flood basalts over supercontinents. *Geology*, 35(5):391.

Condie, K. C. (1986). Origin and Early Growth-Rate of Continents. *Precambrian research*, 32(4):261–278.

Condie, K. C. (1994). Chapter 3 Greenstones Through Time. In *Archean Crustal Evolution*, pages 85–120. Elsevier.

Condie, K. C. (1998). Episodic continental growth and supercontinents: a mantle avalanche connection? *Earth and Planetary Science Letters*, 163(1-4):97–108.

Condie, K. C. (2000). Episodic continental growth models: afterthoughts and extensions. *Tectonophysics*, 322(1-2):153–162.

Condie, K. C. (2004a). Supercontinents and superplume events: distinguishing signals in the geologic record. *Physics of the Earth and Planetary Interiors*, 146(1-2):319–332.

Condie, K. C. (2004b). Supercontinents and superplume events: distinguishing signals in the geologic record. *Physics of the Earth and Planetary Interiors*, 146(1-2):319–332.

Condie, K. C. (2016). A planet in transition: The onset of plate tectonics on Earth between 3 and 2 Ga? *Geoscience Frontiers*.

Condie, K. C., Aster, R. C., and van Hunen, J. (2016). A great thermal divergence in the mantle beginning 2.5 Ga: Geochemical constraints from greenstone basalts and komatiites. *Geoscience Frontiers*, 7(4):543–553.

Condie, K. C., Belousova, E., Griffin, W. L., and Sircombe, K. N. (2009). Granitoid events in space and time: Constraints from igneous and detrital zircon age spectra. *Gondwana Research*, 15(3-4):228–242.

Condie, K. C., Beyer, E., Belousova, E., Griffin, W. L., and O'Reilly, S. Y. (2005). U–Pb isotopic ages and Hf isotopic composition of single zircons: The search for juvenile Precambrian continental crust. *Precambrian Research*, 139(1-2):42–100.

Condie, K. C. and Kröner, A. (2008). When did plate tectonics begin? Evidence from the geologic record. In *Special Paper 440: When Did Plate Tectonics Begin on Planet Earth?*, pages 281–294. Geological Society of America.

Cooper, C. M. and Conrad, C. P. (2009). Does the mantle control the maximum thickness of cratons? *Lithosphere*, 1(2):67–72.

Cooper, C. M., Lenardic, A., Levander, A., and Moresi, L. (2006a). Creation and preservation of cratonic lithosphere: Seismic constraints and geodynamic models. In *Archean Geodynamics and Environments*, pages 75–88. American Geophysical Union, Washington, D. C.

Cooper, C. M., Lenardic, A., and Moresi, L. (2004). The thermal structure of stable continental lithosphere within a dynamic mantle. *Earth and Planetary Science Letters*, 222(3-4):807–817.

Cooper, C. M., Lenardic, A., and Moresi, L. (2006b). Effects of continental insulation and the partitioning of heat producing elements on the Earth's heat loss. *Geophysical Research Letters*, 33(13):4741.

Cooper, C. M., Moresi, L. N., and Lenardic, A. (2013). Effects of continental configuration on mantle heat loss. *Geophysical Research Letters*, 40(11):2647–2651.

COX, K. G. (1980). A Model for Flood Basalt Vulcanism. *Journal of Petrology*, 21(4):629–650.

Crisp, J. A. (1984). Rates of Magma Emplacement and Volcanic Output. *Journal of Volcanology and Geothermal Research*, 20(3-4):177–211.

Davies, G. (2007). Thermal Evolution of the Mantle. In *Volume 9: Evolution of the Earth*, pages 197–216. Elsevier.

de Koker, N., Steinle-Neumann, G., and Vlcek, V. (2012). Electrical resistivity and thermal conductivity of liquid Fe alloys at high P and T, and heat flux in Earth's core. *Proceedings of the National Academy of Sciences*, 109(11):4070–4073.

Debaille, V., O'Neill, C., Brandon, A. D., Haenecour, P., Yin, Q.-Z., Mattielli, N., and Treiman, A. H. (2013). Stagnant-lid tectonics in early Earth revealed by 142Nd variations in late Archean rocks. *Earth and Planetary Science Letters*, 373:83–92.

DePaolo, D. J. (1981). Neodymium isotopes in the Colorado Front Range and crust–mantle evolution in the Proterozoic. *Nature*, 291(5812):193–196.

Depaolo, D. J., Cerling, T. E., Hemming, S. R., Knoll, A. H., Richter, F. M., Royden, L. H., Rudnick, R. L., Stixrude, L., and Trefil, J. S. (2008). *Origin and Evolution of Earth: Research Questions for a Changing Planet*. The National Academies Press, Washington, DC.

Deparis, V., Legros, H., and Ricard, Y. (1995). Mass anomalies due to subducted slabs and simulations of plate motion since 200 My. *Physics of the Earth and Planetary Interiors*, 89(3-4):271–280.

Dhuime, B., Hawkesworth, C., and Cawood, P. (2011). When Continents Formed. *Science*, 331(6014):154–155.

Dhuime, B., Hawkesworth, C. J., Cawood, P. A., and Storey, C. D. (2012). A Change in the Geodynamics of Continental Growth 3 Billion Years Ago. *Science*, 335(6074):1334–1336.

Dhuime, B., Hawkesworth, C. J., Delavault, H., and Cawood, P. A. (2017). Continental growth seen through the sedimentary record. *Sedimentary Geology*, 357:16–32.

Dickinson, W. R. and Snyder, W. S. (1978). Plate tectonics of the Laramide orogeny. In *Laramide Folding Associated with Basement Block Faulting in the Western United States*, pages 355–366. Geological Society of America.

Dietz, R. S. (1961). Continent and Ocean Basin Evolution by Spreading of the Sea Floor. *Nature*, 190(4779):854–857.

Drummond, M. S. and Defant, M. J. (1990). A model for Trondhjemite-Tonalite-Dacite Genesis and crustal growth via slab melting: Archean to modern comparisons. *Journal of Geophysical Research*, 95(B13):21503–21521.

Ducea, M. N. and Saleeby, J. B. (1998). The age and origin of a thick mafic–ultramafic keel from beneath the Sierra Nevada batholith. *Contributions to Mineralogy and Petrology*, 133(1-2):169–185.

Elkins-Tanton, L. T. (2012). Magma Oceans in the Inner Solar System. *Annual Review of Earth and Planetary Sciences*, 40(1):113–139.

Ellam, R. M. and Hawkesworth, C. J. (1988). Is average continental crust generated at subduction zones? *Geology*, 16(4):314.

Engebretson, D. C., Cox, A., and Gordon, R. G. (1984). Relative Motions Between Oceanic Plates of the Pacific Basin. *Journal of Geophysical Research*, 89(NB12):291–310.

Evans, D. A. D. (2003). True polar wander and supercontinents. *Tectonophysics*, 362(1-4):303–320.

Fischer, R. and Gerya, T. (2016). Early Earth plume-lid tectonics: A high-resolution 3D numerical modelling approach. *Journal of Geodynamics*, 100:198–214.

Fisher, O. (1881). *Physics of the Earth's Crust*. Macmillan, London.

Foley, S., Tiepolo, M., and Vannucci, R. (2002). Growth of early continental crust controlled by melting of amphibolite in subduction zones. *Nature*, 417(6891):837–840.

Foley, S. F. (2008). Rejuvenation and erosion of the cratonic lithosphere. *Nature Geoscience*, 1(8):503–510.

Forsyth, D. and Uyeda, S. (1975). On the Relative Importance of the Driving Forces of Plate Motion. *Geophysical Journal International*, 43(1):163–200.

Fung, A. T. and Haggerty, S. E. (2012). Petrography and mineral compositions of eclogites from the Koidu Kimberlite Complex, Sierra Leone. *Journal of Geophysical Research*, 100(B10):20451–20473.

Gao, S., Rudnick, R. L., Carlson, R. W., McDonough, W. F., and Liu, Y.-S. (2002). Re–Os evidence for replacement of ancient mantle lithosphere beneath the North China craton. *Earth and Planetary Science Letters*, 198(3-4):307–322.

Gao, S., Zhang, B. R., Luo, T. C., Li, Z. J., Xie, Q. L., Gu, X. M., Zhang, H. F., Ouyang, J. P., Wang, D. P., and Gao, C. L. (1992). Chemical composition of the continental crust in the Qinling Orogenic Belt and its adjacent North China and Yangtze cratons. *GEOCHIMICA ET COSMOCHIMICA ACTA*, 56(11):3933–3950.

Garrels, R. M. and Mackenzie, F. T. (1971). *Evolution of Sedimentary Rocks*. Norton, New York, 1st edition.

Gerya, T. (2009). *Introduction to Numerical Geodynamic Modelling*. Cambridge University Press, Cambridge.

Gerya, T. (2014). Precambrian geodynamics: Concepts and models. *Gondwana Research*, 25(2):442–463.

Gerya, T. V., Maresch, W. V., Podlesskii, K. K., and Perchuk, L. L. (2004). Semi-empirical Gibbs free energy formulations for minerals and fluids for use in thermodynamic databases of petrological interest. *Physics and Chemistry of Minerals*, 31(7):429–455.

Gerya, T. V., Stern, R. J., Baes, M., Sobolev, S. V., and Whattam, S. A. (2015). Plate tectonics on the Earth triggered by plume-induced subduction initiation. *Nature*, 527(7577):221–225.

Gillon, M., Triaud, A. H. M. J., Demory, B.-O., Jehin, E., Agol, E., Deck, K. M., Lederer, S. M., de Wit, J., Burdanov, A., Ingalls, J. G., Bolmont, E., Leconte, J., Raymond, S. N., Selsis, F., Turbet, M., Barkaoui, K., Burgasser, A., Burleigh, M. R., Carey, S. J., Chaushev, A., Copperwheat, C. M., Delrez, L., Fernandes, C. S., Holdsworth, D. L., Kotze, E. J., Van Grootel, V., Almleaky, Y., Benkhaldoun, Z., Magain, P., and Queloz, D. (2017). Seven temperate terrestrial planets around the nearby ultracool dwarf star TRAPPIST-1. *Nature*, 542(7642):456–460.

Goldschmidt, V. M. (1958). *Geodynamics*. Oxford University Press.

Gomi, H., Ohta, K., Hirose, K., Labrosse, S., Caracas, R., Verstraete, M. J., and Hernlund, J. W. (2013). Physics of the Earth and Planetary Interiors. *Physics of the Earth and Planetary Interiors*, 224(C):88–103.

Goodwin, A. M. (1991). *Precambrian geology: the dynamic evolution of the continental crust*. Academic Press, London.

Gordon, R. B. (1965). Diffusion creep in the Earth's mantle. *Journal of Geophysical Research*, 70(10):2413–2418.

Grand, S. P. (2002). Mantle shear-wave tomography and the fate of subducted slabs. *Philosophical Transactions of the Royal Society of London Series a-Mathematical Physical and Engineering Sciences*, 360(1800):2475–2491.

Gregg, P. M., Behn, M. D., Lin, J., and Grove, T. L. (2009). Melt generation, crystallization, and extraction beneath segmented oceanic transform faults. *Journal of Geophysical Research*, 114(B11):115.

Griffin, W. L., Andi, Z., O'Reilly, S. Y., and Ryan, C. G. (1998). Phanerozoic evolution of the lithosphere beneath the Sino-Korean craton. In *Mantle Dynamics and Plate Interactions in East Asia*, pages 107–126. American Geophysical Union, Washington, D. C.

Griffin, W. L., Belousova, E. A., Shee, S. R., Pearson, N. J., and O'Reilly, S. Y. (2004). Archean crustal evolution in the northern Yilgarn Craton: U–Pb and Hf-isotope evidence from detrital zircons. *Precambrian Research*, 131(3-4):231–282.

Griffin, W. L. and O'Reilly, S. Y. (2007). Cratonic lithospheric mantle: Is anything subducted? *Episodes*, 30(1):43–53.

Griffin, W. L., O'Reilly, S. Y., Abe, N., Aulbach, S., Davies, R. M., Pearson, N. J., Doyle, B. J., and Kivi, K. (2003). The origin and evolution of Archean lithospheric mantle. *Precambrian Research*, 127(1-3):19–41.

Griffin, W. L., O'Reilly, S. Y., Afonso, J. C., and Begg, G. C. (2009). The Composition and Evolution of Lithospheric Mantle: a Re-evaluation and its Tectonic Implications. *Journal of Petrology*, 50(7):1185–1204.

Grigné, C., Labrosse, S., and Tackley, P. J. (2007). Convection under a lid of finite conductivity in wide aspect ratio models: Effect of continents on the wavelength of mantle flow. *Journal of Geophysical Research*, 112(B8):139.

Guillou, L. and Jaupart, C. (1995). On the effect of continents on mantle convection. *Journal of Geophysical Research*, 100(B12):24217–24238.

Gurnis, M. (1988). Large-scale mantle convection and the aggregation and dispersal of supercontinents. *Nature*, 332(6166):695–699.

Gurnis, M. and Davies, G. F. (1986). Apparent episodic crustal growth arising from a smoothly evolving mantle. *Geology*, 14(5):396.

Handler, M. R., Bennett, V. C., and Esat, T. M. (1997). The persistence of off-cratonic lithospheric mantle: Os isotopic systematics of variably metasomatised southeast Australian xenoliths. *Earth and Planetary Science Letters*, 151(1-2):61–75.

Hans Wedepohl, K. (1995). The composition of the continental crust. *GEOCHIMICA ET COSMOCHIMICA ACTA*, 59(7):1217–1232.

Harlow, F. H. and Welch, J. E. (1965). Numerical Calculation of Time-Dependent Viscous Incompressible Flow of Fluid with Free Surface. *Physics of Fluids*, 8(12):2182.

Hawkesworth, C. J., Cawood, P. A., and Dhuime, B. (2016a). Tectonics and crustal evolution. *GSA Today*, 26(09):4–11.

Hawkesworth, C. J., Cawood, P. A., Dhuime, B., and Kemp, T. I. S. (2016b). Earth's Continental Lithosphere Through Time. *Annual Review of Earth and Planetary Sciences*, 45(1):annurev–earth–063016–020525.

Hawkesworth, C. J. and Kemp, A. I. S. (2006a). Evolution of the continental crust. *Nature*, 443(7113):811–817.

Hawkesworth, C. J. and Kemp, A. I. S. (2006b). The differentiation and rates of generation of the continental crust. *Chemical Geology*, 226(3-4):134–143.

Hawkesworth, C. J. and Kemp, A. I. S. (2006c). Using hafnium and oxygen isotopes in zircons to unravel the record of crustal evolution. *Chemical Geology*, 226(3-4):144–162.

Helmstaedt, H. and Schulze, D. J. (1989). Southern African kimberlites and their mantle sample: Implications for Archean tectonics and lithosphere evolution. *Journal of the Geological Society of Australia*, 14:358–368.

Hernlund, J. W. (2010). On the interaction of the geotherm with a post-perovskite phase transition in the deep mantle. *Physics of the Earth and Planetary Interiors*, 180(3-4):222–234.

Hernlund, J. W. and Tackley, P. J. (2008). Modeling mantle convection in the spherical annulus. *Physics of the Earth and Planetary Interiors*, 171(1-4):48–54.

Hernlund, J. W., Thomas, C., and Tackley, P. J. (2005). A doubling of the post-perovskite phase boundary and structure of the Earth's lowermost mantle. *Nature*, 434(7035):882–886.

Heron, P. J. and Lowman, J. P. (2010). Thermal response of the mantle following the formation of a "super-plate". *Geophysical Research Letters*, 37(22).

Heron, P. J. and Lowman, J. P. (2011). Tectonophysics. *Tectonophysics*, 510(1-2):28–38.

Heron, P. J. and Lowman, J. P. (2014). The impact of Rayleigh number on assessing the significance of supercontinent insulation. *Journal of Geophysical Research: Solid Earth*, 119(1):711–733.

Heron, P. J., Lowman, J. P., and Stein, C. (2015). Influences on the positioning of mantle plumes following supercontinent formation. *Journal of Geophysical Research: Solid Earth*, 120(5):3628–3648.

Herzberg, C., Condie, K., and Korenaga, J. (2010). Thermal history of the Earth and its petrological expression. *Earth and Planetary Science Letters*, 292(1-2):79–88.

Herzberg, C. and Gazel, E. (2009). Petrological evidence for secular cooling in mantle plumes. *Nature*, 458(7238):619–622.

Herzberg, C. T. (1993). Lithosphere peridotites of the Kaapvaal craton. *Earth and Planetary Science Letters*, 120(1-2):13–29.

Hess, H. H. (1962). History of Ocean Basins. In Engel, A. E. J., James, H. L., and Leonard, B. F., editors, *Petrologic Studies*, pages 599–620. Geological Society of America, New York.

Hess, H. H. (1965). Mid-oceanic ridges and tectonics of the sea-floor. In Bradshaw, R. and Whittard, W. F., editors, *Submarine Geology and Geophysics*, pages 317–322. 7th Symposium of the Colston Research Society, London. Butterworths.

Hickman, A. H. (2004). Two contrasting granite-greenstone terranes in the Pilbara Craton, Australia: evidence for vertical and horizontal tectonic regimes prior to 2900Ma. *Precambrian research*, 131(3-4):153–172.

Hildebrand, R. S. and Bowring, S. A. (1999). Crustal recycling by slab failure. *Geology*, 27(1):11.

Hill, R. I., Campbell, I. H., Davies, G. F., and Griffiths, R. W. (1992). Mantle Plumes and Continental Tectonics. *Science*, 256(5054):186–193.

Hirose, K. and Kushiro, I. (1993). Partial melting of dry peridotites at high pressures: Determination of compositions of melts segregated from peridotite using aggregates of diamond. *Earth and Planetary Science Letters*, 114(4):477–489.

Hirschmann, M. M. (2000). Mantle solidus: Experimental constraints and the effects of peridotite composition. *Geochemistry, Geophysics, Geosystems*, 1(10).

Hirth, G., Evans, R. L., and Chave, A. D. (2000). Comparison of continental and oceanic mantle electrical conductivity: Is the Archean lithosphere dry? *Geochemistry, Geophysics, Geosystems*, 1(12).

Hirth, G. and Kohlstedt, D. L. (1996). Water in the oceanic upper mantle: implications for rheology, melt extraction and the evolution of the lithosphere. *Earth and Planetary Science Letters*, 144(1-2):93–108.

Hoffmann, P. F. (1989). *Precambrian geology and tectonic history of North America.* Geology of North America—An Overview. Geological Society of America.

Hofmann, A. W. (1988). Chemical Differentiation of the Earth - the Relationship Between Mantle, Continental-Crust, and Oceanic-Crust. *Earth and Planetary Science Letters*, 90(3):297–314.

Holland, H. D. (1984). *The Chemical Evolution of the Atmosphere and Oceans.* Princeton Univ. Press, Princeton, NJ.

Holmes, A. (1931). XVIII. Radioactivity and Earth Movements. *Transactions of the Geological Society of Glasgow*, 18(3):559–606.

Holmes, A. (1933). The thermal history of the earth. *Journal of the Washington Academy of Sciences*, 23(4):169–195.

Hopkins, M., Harrison, T. M., and Manning, C. E. (2008). Low heat flow inferred from >4 Gyr zircons suggests Hadean plate boundary interactions. *Nature*, 456(7221):493–496.

Hopkins, M. D., Harrison, T. M., and Manning, C. E. (2010). Constraints on Hadean geodynamics from mineral inclusions in >4Ga zircons. *Earth and Planetary Science Letters*, 298(3-4):367–376.

Horodyskyj, U. N., Lee, C.-T. A., and Ducea, M. N. (2007). Similarities between Archean high MgO eclogites and Phanerozoic arc-eclogite cumulates and the role of arcs in Archean continent formation. *Earth and Planetary Science Letters*, 256(3-4):510–520.

Houseman, G. A., McKenzie, D. P., and Molnar, P. (1981). Convective instability of a thickened boundary layer and its relevance for the thermal evolution of continental convergent belts. *Journal of Geophysical Research*, 86(B7):6115–6132.

Houser, C., Masters, G., Shearer, P., and Laske, G. (2008). Shear and compressional velocity models of the mantle from cluster analysis of long-period waveforms. *Geophysical Journal International*, 174(1):195–212.

Huang, J., Zhong, S., and van Hunen, J. (2003). Controls on sublithospheric small-scale convection. *Journal of Geophysical Research: Solid Earth (1978–2012)*, 108(B8).

Huang, S.-S. (1959). The Problem of Life in the Universe and the Mode of Star Formation. *Publications of the Astronomical Society of the Pacific*, 71(422):421.

Humphreys, E., Hessler, E., Dueker, K., Farmer, G. L., Erslev, E., and Atwater, T. (2003). How Laramide-Age Hydration of North American Lithosphere by the Farallon Slab Controlled Subsequent Activity in the Western United States. *International Geology Review*, 45(7):575–595.

Hurley, P. M. and Rand, J. R. (1969). Pre-Drift Continental Nuclei. *Science*, 164(3885):1229–1242.

Ireland, T. R. and Williams, I. S. (2003). Considerations in Zircon Geochronology by SIMS. *Reviews in Mineralogy and Geochemistry*, 53(1):215–241.

Irifune, T. and Ringwood, A. E. (1993). Phase-Transformations in Subducted Oceanic-Crust and Buoyancy Relationships at Depths of 600-800 Km in the Mantle. *Earth and Planetary Science Letters*, 117(1-2):101–110.

Ismail-Zadeh, A. and Tackley, P. (2009). *Computational Methods for Geodynamics*. Cambridge University Press, Cambridge.

Jacob, D. E. (2004). Nature and origin of eclogite xenoliths from kimberlites. *LITHOS*, 77(1-4):295–316.

Jagoutz, O. E., Burg, J. P., Hussain, S., Dawood, H., Pettke, T., Iizuka, T., and Maruyama, S. (2009). Construction of the granitoid crust of an island arc part I: geochronological and geochemical constraints from the plutonic Kohistan (NW Pakistan). *Contributions to Mineralogy and Petrology*, 158(6):739–755.

Jahn, B.-M., Glikson, A. Y., Peucat, J. J., and Hickman, A. H. (1981). REE geochemistry and isotopic data of Archean silicic volcanics and granitoids from the Pilbara Block, Western Australia: implications for the early crustal evolution. *GEOCHIMICA ET COSMOCHIMICA ACTA*, 45(9):1633–1652.

Jaupart, C., Labrosse, S., and Mareschal, J. C. (2007). Temperatures, Heat and Energy in the Mantle of the Earth. In *Treatise on Geophysics*, pages 253–303. Elsevier.

Johnson, T. E., Brown, M., Gardiner, N. J., Kirkland, C. L., and Smithies, R. H. (2017). Earth's first stable continents did not form by subduction. *Nature*, 543(7644):239–242.

Johnson, T. E., Brown, M., Kaus, B. J. P., and VanTongeren, J. A. (2013a). Delamination and recycling of Archaean crust caused by gravitational instabilities. *Nature Geoscience*, 7(1):47–52.

Johnson, T. E., Fischer, S., and White, R. W. (2013b). Field and petrographic evidence for partial melting of TTG gneisses from the central region of the mainland Lewisian complex, NW Scotland. *Journal of the Geological Society*, 170(2):319–326.

Jordan, T. H. (1978). Composition and development of the continental tectosphere. *Nature*, 274(5671):544–548.

Jordan, T. H. (1979). Mineralogies, densities and seismic velocities of garnet lherzolites and their geophysical implications. In *The Mantle Sample: Inclusion in Kimberlites and Other Volcanics*, pages 1–14. American Geophysical Union, Washington, D. C.

Jordan, T. H. (1988). Structure and Formation of the Continental Tectosphere. *Journal of Petrology*, Special Volume(1):11–37.

Jull, M. and Kelemen, P. B. (2001). On the conditions for lower crustal convective instability. *Journal of Geophysical Research*, 106(B4):6423–6446.

Kasting, J. F., Toon, O. B., and Pollack, J. B. (1988). How Climate Evolved on the Terrestrial Planets. *Scientific American*, 258(2):90–97.

Kawai, K., Tsuchiya, T., Tsuchiya, J., and Maruyama, S. (2009). Lost primordial continents. *Gondwana Research*, 16(3-4):581–586.

Kay, R. W. and Mahlburg-Kay, S. (1991). Creation and destruction of lower continental crust. *Geologische Rundschau*, 80(2):259–278.

Kay, R. W. and Mahlburg-Kay, S. (1993). Delamination and delamination magmatism. *Tectonophysics*, 219(1-3):177–189.

Kay, S. M., Godoy, E., and Kurtz, A. (2005). Episodic arc migration, crustal thickening, subduction erosion, and magmatism in the south-central Andes. *Geological Society of America Bulletin*, 117(1):67.

Kelemen, P. B., Hirth, G., Shimizu, N., Spiegelman, M., and Dick, H. J. (1997). A review of melt migration processes in the adiabatically upwelling mantle beneath oceanic spreading ridges. *Philosophical Transactions of the Royal Society of London Series a-Mathematical Physical and Engineering Sciences*, 355(1723):283–318.

Kelly, R. K., Kelemen, P. B., and Jull, M. (2003). Buoyancy of the continental upper mantle. *Geochemistry, Geophysics, Geosystems*, 4(2):45.

Kemp, A. I. S. and Hawkesworth, C. J. (2003). Granitic Perspectives on the Generation and Secular Evolution of the Continental Crust. In *Treatise on Geochemistry*, pages 349–410. Elsevier.

Kemp, A. I. S., Hawkesworth, C. J., Paterson, B. A., and Kinny, P. D. (2006). Episodic growth of the Gondwana supercontinent from hafnium and oxygen isotopes in zircon. *Nature*, 439(7076):580–583.

King, S. (2005). Archean cratons and mantle dynamics. *Earth and Planetary Science Letters*, 234(1-2):1–14.

Kisters, A. F. M., Stevens, G., Dziggel, A., and Armstrong, R. A. (2003). Extensional detachment faulting and core-complex formation in the southern Barberton granite–greenstone terrain, South Africa: evidence for a 3.2 Ga orogenic collapse. *Precambrian research*, 127(4):355–378.

Knudsen, T. L., Griffin, W., Hartz, E., Andresen, A., and Jackson, S. (2001). In-situ hafnium and lead isotope analyses of detrital zircons from the Devonian sedimentary basin of NE Greenland: a record of repeated crustal reworking. *Contributions to Mineralogy and Petrology*, 141(1):83–94.

Komabayashi, T., Maruyama, S., and Rino, S. (2009). A speculation on the structure of the D″ layer: The growth of anti-crust at the core–mantle boundary through the subduction history of the Earth. *Gondwana Research*, 15(3-4):342–353.

Komiya, T., Maruyama, S., Masuda, T., Nohda, S., Hayashi, M., and Okamoto, K. (1999). Plate tectonics at 3.8-3.7 Ga: Field evidence from the Isua Accretionary Complex, southern West Greenland. *Journal of Geology*, 107(5):515–554.

Korenaga, J. (2011). Thermal evolution with a hydrating mantle and the initiation of plate tectonics in the early Earth. *Journal of Geophysical Research: Solid Earth*, 116(B12).

Korenaga, J. (2012). Plate tectonics and planetary habitability: current status and future challenges. *Annals of the New York Academy of Sciences*, 1260(1):87–94.

Korenaga, J. (2013). Initiation and Evolution of Plate Tectonics on Earth: Theories and Observations. *Annual Review of Earth and Planetary Sciences*, 41(1):117–151.

Korenaga, J. and Jordan, T. H. (2003). Physics of multiscale convection in Earth's mantle: Onset of sublithospheric convection. *Journal of Geophysical Research*, 108(B7):385.

Kusky, T. M. and Polat, A. (1999). Growth of granite–greenstone terranes at convergent margins, and stabilization of Archean cratons. *Tectonophysics*, 305(1-3):43–73.

Labrosse, S., Hernlund, J. W., and Hirose, K. (2015). Fractional Melting and Freezing in the Deep Mantle and Implications for the Formation of a Basal Magma Ocean. In *The Early Earth*, pages 123–142. John Wiley & Sons, Inc, Hoboken, NJ.

Labrosse, S. and Jaupart, C. (2007). Thermal evolution of the Earth: Secular changes and fluctuations of plate characteristics. *Earth and Planetary Science Letters*, 260(3-4):465–481.

Lana, C., Kisters, A., and Stevens, G. (2010). Exhumation of Mesoarchean TTG gneisses from the middle crust: Insights from the Steynsdorp core complex, Barberton granitoid-greenstone terrain, South Africa. *Geological Society of America Bulletin*, 122(1-2):183–197.

Lay, T., Hernlund, J., and Buffett, B. A. (2008). Core–mantle boundary heat flow. *Nature Geoscience*, 1(1):25–32.

Lay, T., Hernlund, J., Garnero, E. J., and Thorne, M. S. (2006). A post-perovskite lens and D ” heat flux beneath the central Pacific. *Science*, 314(5803):1272–1276.

Lee, C.-T. A. (2003). Compositional variation of density and seismic velocities in natural peridotites at STP conditions: Implications for seismic imaging of compositional heterogeneities in the upper mantle. *Journal of Geophysical Research*, 108(B9):589.

Lee, C.-T. A. (2005). Trace Element Evidence for Hydrous Metasomatism at the Base of the North American Lithosphere and Possible Association with Laramide Low-Angle Subduction. *Journal of Geology*, 113(6):673–685.

Lee, C.-T. A. (2006). Geochemical/petrologic constraints on the origin of cratonic mantle. In *Archean Geodynamics and Environments*, pages 89–114. American Geophysical Union, Washington, D. C.

Lee, C.-T. A., Cheng, X., and Horodyskyj, U. (2006). The development and refinement of continental arcs by primary basaltic magmatism, garnet pyroxenite accumulation, basaltic recharge and delamination: insights from the Sierra Nevada, California. *Contributions to Mineralogy and Petrology*, 151(2):222–242.

Lee, C.-T. A., Luffi, P., and Chin, E. J. (2011). Building and Destroying Continental Mantle. *Annual Review of Earth and Planetary Sciences*, 39(1):59–90.

Lee, C.-T. A., Luffi, P., Höink, T., Li, Z.-X. A., and Lenardic, A. (2008). The role of serpentine in preferential craton formation in the late Archean by lithosphere underthrusting. *Earth and Planetary Science Letters*, 269(1-2):96–104.

Lenardic, A. and Moresi, L. (2001). Heat flow scaling for mantle convection below a conducting lid: Resolving seemingly inconsistent modeling results regarding continental heat flow. *Geophysical Research Letters*, 28(7):1311–1314.

Lenardic, A., Moresi, L., Jellinek, A., and Manga, M. (2005). Continental insulation, mantle cooling, and the surface area of oceans and continents. *Earth and Planetary Science Letters*, 234(3-4):317–333.

Lenardic, A., Moresi, L., Jellinek, A. M., O'Neill, C. J., Cooper, C. M., and Lee, C. T. (2011). Continents, supercontinents, mantle thermal mixing, and mantle thermal isolation: Theory, numerical simulations, and laboratory experiments. *Geochemistry, Geophysics, Geosystems*, 12(10).

Lenardic, A. and Moresi, L. N. (1999). Some thoughts on the stability of cratonic lithosphere: Effects of buoyancy and viscosity. *Journal of Geophysical Research*, 104(B6):12747–12758.

Lenardic, A., Moresi, L. N., and Muhlhaus, H. (2003). Longevity and stability of cratonic lithosphere: Insights from numerical simulations of coupled mantle convection and continental tectonics. *Journal of Geophysical Research: Solid Earth*, 108(B6).

Leng, W. and Zhong, S. (2008). Controls on plume heat flux and plume excess temperature. *Journal of Geophysical Research: Solid Earth*, 113(B4).

Li, X. D. and Romanowicz, B. (1996). Global mantle shear velocity model developed using nonlinear asymptotic coupling theory. *Journal of Geophysical Research: Solid Earth*, 101(B10):22245–22272.

Li, Z.-X. A., Lee, C.-T. A., Peslier, A. H., Lenardic, A., and Mackwell, S. J. (2008). Water contents in mantle xenoliths from the Colorado Plateau and vicinity: Implications for the mantle rheology and hydration-induced thinning of continental lithosphere. *Journal of Geophysical Research*, 113(B9):963.

Lithgow-Bertelloni, C. and Richards, M. A. (1998). The dynamics of Cenozoic and Mesozoic plate motions. *Reviews of Geophysics*, 36(1):27–78.

Lourenco, D. L., Rozel, A., and Tackley, P. J. (2016). Melting-induced crustal production helps plate tectonics on Earth-like planets. *Earth and Planetary Science Letters*, 439:18–28.

Lowman, J. P. and Gable, C. W. (1999). Thermal evolution of the mantle following continental aggregation in 3D convection models. *Geophysical Research Letters*, 26(17):2649–2652.

Lowman, J. P. and Jarvis, G. T. (1993). Mantle convection flow reversals due to continental collisions. *Geophysical Research Letters*, 20(19):2087–2090.

Lowman, J. P. and Jarvis, G. T. (1996). Continental collisions in wide aspect ratio and high Rayleigh number two-dimensional mantle convection models. *Journal of Geophysical Research*, 101(B11):25485–25497.

Luffi, P., Saleeby, J. B., Lee, C.-T. A., and Ducea, M. N. (2009). Lithospheric mantle duplex beneath the central Mojave Desert revealed by xenoliths from Dish Hill, California. *Journal of Geophysical Research*, 114(B3):375.

Lutgens, F. K. and Tarbuck, E. J. (2003). *Essentials of Geology.* Prentice Hall, 8th edition.

Martin, H. (1986). Effect of steeper Archean geothermal gradient on geochemistry of subduction-zone magmas. *Geology*, 14(9):753.

Martin, H. (1994). Chapter 6 The Archean Grey Gneisses and the Genesis of Continental Crust. In *Archean Crustal Evolution*, pages 205–259. Elsevier.

Masters, G., Laske, G., Bolton, H., and Dziewonski, A. (2000). *The Relative Behavior of Shear Velocity, Bulk Sound Speed, and Compressional Velocity in the Mantle: Implications for Chemical and Thermal Structure*, volume 117 of *Geophysical Monograph Series.* American Geophysical Union, Washington, D. C.

McCulloch, M. T. and Bennett, V. C. (1994). Progressive growth of the Earth's continental crust and depleted mantle: Geochemical constraints. *GEOCHIMICA ET COSMOCHIMICA ACTA*, 58(21):4717–4738.

McDonough, W. F. (1990). Constraints on the composition of the continental lithospheric mantle. *Earth and Planetary Science Letters*, 101(1):1–18.

McKenzie, D. and O'nions, R. K. (1983). Mantle reservoirs and ocean island basalts. *Nature*, 301(5897):229–231.

Menzies, M., Xu, Y., Zhang, H., and Fan, W. (2007). Integration of geology, geophysics and geochemistry: A key to understanding the North China Craton. *LITHOS*, 96(1-2):1–21.

Monin, A. S. (1991). Planetary Evolution and Global Tectonics. *Tectonophysics*, 199(2-4):149–164.

Moore, W. B. and Webb, A. A. G. (2014). Heat-pipe Earth. *Nature*, 501(7468):501–505.

Moresi, L. and Solomatov, V. (1998a). Mantle convection with a brittle lithosphere: thoughts on the global tectonic styles of the Earth and Venus. *Geophysical Journal International*, 133(3):669–682.

Moresi, L. and Solomatov, V. (1998b). Mantle convection with a brittle lithosphere: thoughts on the global tectonic styles of the earth and venus. *Geophysical Journal International*, 133(3).

Morgan, J. W. (1983). Hotspot tracks and the early rifting of the Atlantic. *Tectonophysics*, 94(1-4):123–139.

Moyen, J.-F. (2011). The composite Archaean grey gneisses: Petrological significance, and evidence for a non-unique tectonic setting for Archaean crustal growth. *LITHOS*, 123(1-4):21–36.

Moyen, J.-F. and Stevens, G. (2006). Experimental constraints on TTG petrogenesis: Implications for Archean geodynamics. In *Archean Geodynamics and Environments*, pages 149–175. American Geophysical Union, Washington, D. C.

Moyen, J.-F., Stevens, G., and Kisters, A. (2006). Record of mid-Archaean subduction from metamorphism in the Barberton terrain, South Africa. *Nature*, 442(7102):559–562.

Nakagawa, T. and Tackley, P. J. (2004). Effects of thermo-chemical mantle convection on the thermal evolution of the Earth's core. *Earth and Planetary Science Letters*, 220(1-2):107–119.

Nakagawa, T. and Tackley, P. J. (2010). Influence of initial CMB temperature and other parameters on the thermal evolution of Earth's core resulting from thermochemical spherical mantle convection. *Geochemistry, Geophysics, Geosystems*, 11(6).

Nakagawa, T. and Tackley, P. J. (2012). Influence of magmatism on mantle cooling, surface heat flow and Urey ratio. *Earth and Planetary Science Letters*, 329:1–10.

Nakagawa, T., Tackley, P. J., Deschamps, F., and Connolly, J. A. D. (2010). The influence of MORB and harzburgite composition on thermo-chemical mantle convection in a 3-D spherical shell with self-consistently calculated mineral physics. *Earth and Planetary Science Letters*, 296(3-4):403–412.

Nelson, K. D. (1991). A unified view of craton evolution motivated by recent deep seismic reflection and refraction results. *Geophysical Journal International*, 105(1):25–35.

Nikolaeva, K., Gerya, T. V., and Connolly, J. A. D. (2008). Numerical modelling of crustal growth in intraoceanic volcanic arcs. *Physics of the Earth and Planetary Interiors*, 171(1-4):336–356.

Nisbet, E. G. (1982). The tectonic setting and petrogenesis of komatiites. In Arndt, N. T. and Nisbet, E. G., editors, *Komatiites*, pages 501–520. George Allen & Unwin.

Ogawa, M. (2014). Two-stage evolution of the Earth's mantle inferred from numerical simulation of coupled magmatism-mantle convection system with tectonic plates. *Journal of Geophysical Research: Solid Earth*, 119(3):2462–2486.

O'Neill, C., Lenardic, A., Jellinek, A. M., and Moresi, L. (2009). Gondwana Research. *Gondwana Research*, 15(3-4):276–287.

Ono, S., Ito, E., and Katsura, T. (2001). Mineralogy of subducted basaltic crust (MORB) from 25 to 37 GPa, and chemical heterogeneity of the lower mantle. *Earth and Planetary Science Letters*, 190(1-2):57–63.

O'Reilly, T. C. and Davies, G. F. (1981). Magma transport of heat on Io: A mechanism allowing a thick lithosphere. *Geophysical Research Letters*, 8(4):313–316.

Panning, M. and Romanowicz, B. (2006). A three-dimensional radially anisotropic model of shear velocity in the whole mantle. *Geophysical Journal International*, 167(1):361–379.

Patterson, C. (1956). Age of meteorites and the earth. *GEOCHIMICA ET COS-MOCHIMICA ACTA*, 10(4):230–237.

Peacock, S. M., Keken, P. E. v., Holloway, S. D., Hacker, B. R., Abers, G. A., and Fergason, R. L. (2005). Thermal structure of the Costa Rica – Nicaragua subduction zone. *Physics of the Earth and Planetary Interiors*, 149(1-2):187–200.

Peacock, S. M. and Wang, K. (1999). Seismic Consequences of Warm Versus Cool Subduction Metamorphism: Examples from Southwest and Northeast Japan. *Science*, 286(5441):937–939.

Peale, S. J., Cassen, P., and Reynolds, R. T. (1979). Melting of Io by Tidal Dissipation. *Science*, 203(4383):892–894.

Pearcy, L. G., DeBari, S. M., and Sleep, N. H. (1990). Mass balance calculations for two sections of island arc crust and implications for the formation of continents. *Earth and Planetary Science Letters*, 96(3-4):427–442.

Pearson, D. G., Carlson, R. W., Shirey, S. B., Boyd, F. R., and Nixon, P. H. (1995a). Stabilisation of Archaean lithospheric mantle: A ReOs isotope study of peridotite xenoliths from the Kaapvaal craton. *Earth and Planetary Science Letters*, 134(3-4):341–357.

Pearson, D. G., Parman, S. W., and Nowell, G. M. (2007). A link between large mantle melting events and continent growth seen in osmium isotopes. *Nature*, 449(7159):202–205.

Pearson, D. G., Shirey, S. B., Carlson, R. W., Boyd, F. R., Pokhilenko, N. P., and Shimizu, N. (1995b). Re-Os, Sm-Nd, and Rb-Sr isotope evidence for thick Archaean lithospheric mantle beneath the Siberian craton modified by multistage metasomatism. *GEOCHIMICA ET COSMOCHIMICA ACTA*, 59(5):959–977.

Pearson, D. G. and Wittig, N. (2008). Formation of Archaean continental lithosphere and its diamonds: the root of the problem. *Journal of the Geological Society*, 165(5):895–914.

Phillips, B. and Bunge, H. (2005). Heterogeneity and time dependence in 3D spherical mantle convection models with continental drift. *Earth and Planetary Science Letters*, 233(1-2):121–135.

Phillips, B. R. and Coltice, N. (2010). Temperature beneath continents as a function of continental cover and convective wavelength. *Journal of Geophysical Research*, 115(B4).

Plank, T. (2005). Constraints from thoriumlanthanum on sediment recycling at subduction zones and the evolution of the continents. *Journal of Petrology*, 46(5):921–944.

Plank, T. and Langmuir, C. H. (1998). The chemical composition of subducting sediment and its consequences for the crust and mantle. *Chemical geology*, 145(3-4):325–394.

Pollack, H. N. (1986). Cratonization and thermal evolution of the mantle. *Earth and Planetary Science Letters*, 80(1-2):175–182.

Pozzo, M., Davies, C., Gubbins, D., and Alfè, D. (2013). Thermal and electrical conductivity of iron at Earth's core conditions. *Nature*, 485(7398):355–358.

Prout, W. (1834). *Bridgewater Treatises, volume 8*. W. Pickering, London.

Pyle, J. M. and Haggerty, S. E. (1998). Eclogites and the Metasomatism of Eclogites from the Jagersfontein Kimberlite: Punctuated Transport and Implications for Alkali Magmatism. *GEOCHIMICA ET COSMOCHIMICA ACTA*, 62(7):1207–1231.

Rapp, R. P., Watson, E. B., and Miller, C. F. (1991). Partial Melting of Amphibolite Eclogite and the Origin of Archean Trondhjemites and Tonalites. *Precambrian Research*, 51(1-4):1–25.

Rasool, S. I. and de Bergh, C. (1970). The runaway Greenhouse and the accumulation of CO_2 in the Venus atmosphere. *Nature*, 226(5250):1037–1039.

Rayleigh, L. (1916). LIX. On convection currents in a horizontal layer of fluid, when the higher temperature is on the under side. *Philosophical Magazine Series 6*, 32(192):529–546.

Reisberg, L. and Lorand, J. P. (1995). Longevity of sub-continental mantle lithosphere from osmium isotope systematics in orogenic peridotite massifs. *Nature*, 376(6536):159–162.

Ricard, Y., Vigny, C., and Froidevaux, C. (1989). Mantle heterogeneities, geoid, and plate motion: A Monte Carlo inversion. *Journal of Geophysical Research*, 94(B10):13739–13754.

Richards, M. A., DUNCAN, R. A., and COURTILLOT, V. E. (1989). Flood Basalts and Hot-Spot Tracks: Plume Heads and Tails. *Science*, 246(4926):103–107.

Richards, M. A., Jones, D. L., Duncan, R. A., and Depaolo, D. J. (1991). A Mantle Plume Initiation Model for the Wrangellia Flood Basalt and Other Oceanic Plateaus. *Science*, 254(5029):263–267.

Rino, S., Komiya, T., Windley, B. F., Katayama, I., Motoki, A., and Hirata, T. (2004). Major episodic increases of continental crustal growth determined from zircon ages of river sands; implications for mantle overturns in the Early Precambrian. *Physics of the Earth and Planetary Interiors*, 146(1-2):369–394.

Ritsema, J., Deuss, A., van Heijst, H. J., and Woodhouse, J. H. (2011). S40RTS: a degree-40 shear-velocity model for the mantle from new Rayleigh wave dispersion, teleseismic traveltime and normal-mode splitting function measurements. *Geophysical Journal International*, 184(3):1223–1236.

Ritsema, J., van Heijst, H. J., and Woodhouse, J. H. (1999). Complex shear wave velocity structure imaged beneath Africa and Iceland. *Science*, 286(5446):1925–1928.

Rivera, E. J., Lissauer, J. J., Butler, R. P., Marcy, G. W., Vogt, S. S., Fischer, D. A., Brown, T. M., Laughlin, G., and Henry, G. W. (2005). A ~ 7.5 Earth-Mass Planet Orbiting the Nearby Star, GJ 876. *arXiv.org*, (1):625–640.

Roberts, N. M. W. and Spencer, C. J. (2015). The zircon archive of continent formation through time. *Geological Society, London, Special Publications*, 389(1):197–225.

Rolf, T., Coltice, N., and Tackley, P. J. (2012). Earth and Planetary Science Letters. *Earth and Planetary Science Letters*, 351-352(C):134–146.

Rolf, T. and Tackley, P. J. (2011). Focussing of stress by continents in 3D spherical mantle convection with self-consistent plate tectonics. *Geophysical Research Letters*, 38(18).

Rowe, M. C. and Lassiter, J. C. (2009). Chlorine enrichment in central Rio Grande Rift basaltic melt inclusions: Evidence for subduction modification of the lithospheric mantle. *Geology*, 37(5):439–442.

Rozel, A. (2012). Impact of grain size on the convection of terrestrial planets. *Geochemistry, Geophysics, Geosystems*, 13(10).

Rozel, A. B., Golabek, G. J., Jain, C., Tackley, P. J., and Gerya, T. (2017). Continental crust formation on early Earth controlled by intrusive magmatism. *Nature*, 545(7654):332–335.

Rudnick, R. L. (1995). Making Continental-Crust. *Nature*, 378(6557):571–578.

Rudnick, R. L. and Fountain, D. M. (1995). Nature and composition of the continental crust: A lower crustal perspective. *Reviews of Geophysics*, 33(3):267–309.

Rudnick, R. L. and Gao, S. (2003). Composition of the Continental Crust. In *Treatise on Geochemistry*, pages 1–64. Elsevier.

Rudnick, R. L., Gao, S., Ling, W.-l., Liu, Y.-s., and McDonough, W. F. (2004). Petrology and geochemistry of spinel peridotite xenoliths from Hannuoba and Qixia, North China craton. *LITHOS*, 77(1-4):609–637.

Saha, L., Pant, N. C., Pati, J. K., Upadhyay, D., Berndt, J., Bhattacharya, A., and Satynarayanan, M. (2010). Neoarchean high-pressure margarite–phengitic muscovite–chlorite corona mantled corundum in quartz-free high-Mg, Al phlogopite–chlorite schists from the Bundelkhand craton, north central India. *Contributions to Mineralogy and Petrology*, 161(4):511–530.

Saleeby, J. (2003). Segmentation of the Laramide Slab—evidence from the southern Sierra Nevada region. *Geological Society of America Bulletin*, 115:655–668.

Schubert, G., Turcotte, D. L., and Olson, P. (2001). *Mantle Convection in the Earth and Planets*. Cambridge University Press, Cambridge.

Schutt, D. L. and Lesher, C. E. (2006). Effects of melt depletion on the density and seismic velocity of garnet and spinel lherzolite. *Journal of Geophysical Research*, 111(B5).

Scotese, C. R. (1991). Jurassic and Cretaceous Plate Tectonic Reconstructions. *Palaeogeography Palaeoclimatology Palaeoecology*, 87(1-4):493–501.

Sen, C. and Dunn, T. (1994). Dehydration melting of a basaltic composition amphibolite at 1.5 and 2.0 GPa: implications for the origin of adakites. *Contributions to Mineralogy and Petrology*, 117(4):394–409.

Şengör, A. M. C., Natal'in, B. A., and Burtman, V. S. (1993). Evolution of the Altaid tectonic collage and Palaeozoic crustal growth in Eurasia. *Nature*, 364(6435):299–307.

Shirey, S. B., Kamber, B. S., Whitehouse, M. J., Mueller, P. A., and Basu, A. R. (2008). A review of the isotopic and trace element evidence for mantle and crustal processes in the Hadean and Archean: Implications for the onset of plate tectonic subduction. In *Special Paper 440: When Did Plate Tectonics Begin on Planet Earth?*, pages 1–29. Geological Society of America.

Shirey, S. B. and Richardson, S. H. (2011). Start of the Wilson cycle at 3 Ga shown by diamonds from subcontinental mantle. *Science*, 333(6041):434–436.

Shirey, S. B. and Walker, R. J. (1998). The Re-Os Isotope System in Cosmochemistry and High-Temperature Geochemistry. *Annual Review of Earth and Planetary Sciences*, 26(1):423–500.

Simon, N. S. C., Carlson, R. W., Pearson, D. G., and Davies, G. R. (2007). The Origin and Evolution of the Kaapvaal Cratonic Lithospheric Mantle. *Journal of Petrology*, 48(3):589–625.

Sizova, E., Gerya, T., Brown, M., and Perchuk, L. L. (2010). Subduction styles in the Precambrian: Insight from numerical experiments. *LITHOS*, 116(3-4):209–229.

Sizova, E., Gerya, T., Stuewe, K., and Brown, M. (2015). Generation of felsic crust in the Archean: A geodynamic modeling perspective. *Precambrian Research*, 271:198–224.

Sleep, N. H. (2003). Survival of Archean cratonal lithosphere. *Journal of Geophysical Research*, 108(B6).

Smith, D. (2010). Antigorite Peridotite, Metaserpentinite, and other Inclusions within Diatremes on the Colorado Plateau, SW USA: Implications for the Mantle Wedge during Low-angle Subduction. *Journal of Petrology*, 51(6):1355–1379.

Solomatov, V. S. (1995). Scaling of Temperature-Dependent and Stress-Dependent Viscosity Convection. *Physics of Fluids*, 7(2):266–274.

Spencer, C. J., Roberts, N. M. W., and Santosh, M. (2017). Growth, destruction, and preservation of Earth's continental crust. *Earth Science Reviews*, 172:87–106.

Springer, W. and Seck, H. A. (1997). Partial fusion of basic granulites at 5 to 15 kbar: Implications for the origin of TTG magmas. *Contributions to Mineralogy and Petrology*, 127(1-2):30–45.

Stern, C. R. and Wyllie, P. J. (1978). Phase compositions through crystallization intervals in basalt-andesite-H2O at 30 kbar with implications for subduction zone magmas. *American Mineralogist*, 63(7-8):641–663.

Stern, R. J. (2005). Evidence from ophiolites, blueschists, and ultrahigh-pressure metamorphic terranes that the modern episode of subduction tectonics began in Neoproterozoic time. *Geology*, 33(7):557.

Stevens, G. and Moyen, J.-F. (2007). Chapter 5.7 Metamorphism in the Barberton Granite Greenstone Terrain: A Record of Paleoarchean Accretion. In *Earth's Oldest Rocks*, pages 669–698. Elsevier.

Stevenson, D. J. (1987). Origin of the Moon-The Collision Hypothesis. *Annual Review of Earth and Planetary Sciences*, 15(1):271–315.

Stevenson, D. J. (1990). Fluid dynamics of core formation. In *Origin of the earth*, pages 231–249. Oxford University Press, New York.

Stixrude, L., de Koker, N., Sun, N., Mookherjee, M., and Karki, B. B. (2009). Thermodynamics of silicate liquids in the deep Earth. *Earth and Planetary Science Letters*, 278(3-4):226–232.

Su, W.-j. and Dziewonski, A. M. (1997). Simultaneous inversion for 3-D variations in shear and bulk velocity in the mantle. *Physics of the Earth and Planetary Interiors*, 100(1-4):135–156.

Su, W. J., Woodward, R. L., and Dziewonski, A. M. (1994). Degree-12 Model of Shear Velocity Heterogeneity in the Mantle. *Journal of Geophysical Research: Solid Earth*, 99(B4):6945–6980.

Sun, S. S. and McDonough, W. F. (1989). Chemical and isotopic systematics of oceanic basalts: implications for mantle composition and processes. *Geological Society, London, Special Publications*, 42(1):313–345.

Tackley, P. J. (2000). Self-consistent generation of tectonic plates in time-dependent, three-dimensional mantle convection simulations. *Geochemistry, Geophysics, Geosystems*, 1(8).

Tackley, P. J. (2008a). Modelling compressible mantle convection with large viscosity contrasts in a three-dimensional spherical shell using the yin-yang grid. *Physics of the Earth and Planetary Interiors*, 171(1-4):7–18.

Tackley, P. J. (2008b). Self-consistent generation of tectonic plates in time-dependent, three-dimensional mantle convection simulations. *Geochemistry, Geophysics, Geosystems*, 1(8).

Tackley, P. J., Ammann, M., Brodholt, J. P., Dobson, D. P., and Valencia, D. (2013). Mantle dynamics in super-Earths: Post-perovskite rheology and self-regulation of viscosity. *Icarus*, 225(1):50–61.

Tackley, P. J. and King, S. D. (2003). Testing the tracer ratio method for modeling active compositional fields in mantle convection simulations. *Geochemistry, Geophysics, Geosystems*, 4(4).

Tang, M., Chen, K., and Rudnick, R. L. (2016). Archean upper crust transition from mafic to felsic marks the onset of plate tectonics. *Science*, 351(6271):372–375.

Taylor, F. B. (1910). Bearing of the tertiary mountain belt on the origin of the earth's plan. *Geological Society of America Bulletin*, 21(1):179–226.

Taylor, L. A. and Neal, C. R. (1989). Eclogites with Oceanic Crustal and Mantle Signatures from the Bellsbank Kimberlite, South Africa, Part I: Mineralogy, Petrography, and Whole Rock Chemistry. *Journal of Geology*, 97(5):551–567.

Taylor, L. A., Snyder, G. A., Keller, R., Remley, D. A., Anand, M., Wiesli, R., Valley, J., and Sobolev, N. V. (2003). Petrogenesis of group?A eclogites and websterites: evidence from the Obnazhennaya kimberlite, Yakutia. *Contributions to Mineralogy and Petrology*, 145(4):424–443.

Taylor, S. R. (1967). The origin and growth of continents. *Tectonophysics*, 4(1):17–34.

Taylor, S. R. (1977). Island arc models and the composition of the continental crust. In *Island Arcs, Deep Sea Trenches and Back-Arc Basins*, pages 325–335. American Geophysical Union, Washington, D. C.

Taylor, S. R. and McLennan, S. M. (1985). *The continental crust: Its composition and evolution*. Blackwell Scientific Pub., Palo Alto, CA.

Taylor, S. R. and McLennan, S. M. (1996). The Evolution of Continental Crust. *Scientific American*, 274(1):76–81.

Torsvik, T. H., Steinberger, B., Gurnis, M., and Gaina, C. (2010). Plate tectonics and net lithosphere rotation over the past 150My. *Earth and Planetary Science Letters*, 291(1-4):106–112.

Torsvik, T. H., van der Voo, R., Doubrovine, P. V., Burke, K., Steinberger, B., Ashwal, L. D., Tronnes, R. G., Webb, S. J., and Bull, A. L. (2014). Deep mantle structure as a reference frame for movements in and on the Earth. *Proceedings of the National Academy of Sciences of the United States of America*, 111(24):8735–8740.

Turcotte, D. L. (1989). A heat pipe mechanism for volcanism and tectonics on Venus. *Journal of Geophysical Research*, 94(B3):2779–2785.

Turcotte, D. L. and Schubert, G. (2014). *Geodynamics*. Cambridge University Press.

Valley, J. W., Chiarenzelli, J. R., and McLelland, J. M. (1994). Oxygen isotope geochemistry of zircon. *Earth and Planetary Science Letters*, 126(4):187–206.

Valley, J. W., Kinny, P. D., Schulze, D. J., and Spicuzza, M. J. (1998). Zircon megacrysts from kimberlite: oxygen isotope variability among mantle melts. *Contributions to Mineralogy and Petrology*, 133(1-2):1–11.

Valley, J. W., Lackey, J. S., Cavosie, A. J., Clechenko, C. C., Spicuzza, M. J., Basei, M. A. S., Bindeman, I. N., Ferreira, V. P., Sial, A. N., King, E. M., Peck, W. H., Sinha, A. K., and Wei, C. S. (2005). 4.4 billion years of crustal maturation: oxygen isotope ratios of magmatic zircon. *Contributions to Mineralogy and Petrology*, 150(6):561–580.

van der Hilst, R. D., de Hoop, M. V., Wang, P., Shim, S. H., Ma, P., and Tenorio, L. (2007). Seismostratigraphy and Thermal Structure of Earth9s Core-Mantle Boundary Region. *Science*, 315(5820):1813–1817.

van der Hilst, R. D., Widiyantoro, S., and Engdahl, E. R. (1997). Evidence for deep mantle circulation from global tomography. *Nature*, 386(6625):578–584.

van Hunen, J. and Moyen, J.-F. (2012). Archean Subduction: Fact or Fiction? *Annual Review of Earth and Planetary Sciences*, 40(1):195–219.

van Hunen, J. and van den Berg, A. P. (2008). Plate tectonics on the early Earth: Limitations imposed by strength and buoyancy of subducted lithosphere. *LITHOS*, 103(1-2):217–235.

van Hunen, J., van Keken, P. E., Hynes, A., and Davies, G. F. (2008). Tectonics of early Earth: Some geodynamic considerations. In *Special Paper 440: When Did Plate Tectonics Begin on Planet Earth?*, pages 157–171. Geological Society of America.

van Keken, P. E., Kiefer, B., and Peacock, S. M. (2002). High-resolution models of subduction zones: Implications for mineral dehydration reactions and the transport of water into the deep mantle. *Geochemistry, Geophysics, Geosystems*, 3(10):1–20.

Van Kranendonk, M. J. (2010). Two types of Archean continental crust: Plume and plate tectonics on early Earth. *American Journal of Science.*

Van Kranendonk, M. J. (2011). Cool greenstone drips and the role of partial convective overturn in Barberton greenstone belt evolution. *Journal of African Earth Sciences*, 60(5):346–352.

Van Kranendonk, M. J., Collins, W. J., Hickman, A., and Pawley, M. J. (2004). Critical tests of vertical vs. horizontal tectonic models for the Archaean East Pilbara Granite–Greenstone Terrane, Pilbara Craton, Western Australia. *Precambrian research*, 131(3-4):173–211.

Van Kranendonk, M. J., Hugh Smithies, R., Hickman, A. H., and Champion, D. C. (2007). Review: secular tectonic evolution of Archean continental crust: interplay between horizontal and vertical processes in the formation of the Pilbara Craton, Australia. *Terra Nova*, 19(1):1–38.

Van Kranendonk, M. J. and Kirkland, C. L. (2016). Conditioned duality of the Earth system: Geochemical tracing of the supercontinent cycle through Earth history. *Earth Science Reviews*, 160:171–187.

Van Kranendonk, M. J., Smithies, R. H., Griffin, W. L., Huston, D. L., Hickman, A. H., Champion, D. C., Anhaeusser, C. R., and Pirajno, F. (2015). Making it thick: a volcanic plateau origin of Palaeoarchean continental lithosphere of the Pilbara and Kaapvaal cratons. *Geological Society, London, Special Publications*, 389(1):83–111.

van Thienen, P., van den Berg, A. P., and Vlaar, N. J. (2004). On the formation of continental silicic melts in thermochemical mantle convection models: implications for early Earth. *Tectonophysics*, 394(1-2):111–124.

Vervoort, J. D., Patchett, P. J., Gehrels, G. E., and Nutman, A. P. (1996). Constraints on early Earth differentiation from hafnium and neodymium isotopes. *Nature*, 379(6566):624–627.

Vine, F. J. and Matthews, D. H. (1963). Magnetic Anomalies Over Oceanic Ridges. *Nature*, 199(4897):947–949.

Vogt, K., Gerya, T. V., and Castro, A. (2012). Crustal growth at active continental margins: Numerical modeling. *Physics of the Earth and Planetary Interiors*, 192-193:1–20.

Voice, P. J., Kowalewski, M., and Eriksson, K. A. (2011). Quantifying the Timing and Rate of Crustal Evolution: Global Compilation of Radiometrically Dated Detrital Zircon Grains. *Journal of Geology*, 119(2):109–126.

Volodichev, O. I., Slabunov, A. I., Bibikova, E., Konilov, A. N., and Kuzenko, T. I. (2004). Archean eclogites in the Belomorian Mobile Belt, Baltic Shield. 12:540–560.

Walker, R. J., Carlson, R. W., Shirey, S. B., and F R, B. (1989). Os, Sr, Nd, and Pb isotope systematics of southern African peridotite xenoliths: Implications for the chemical evolution of subcontinental mantle. *GEOCHIMICA ET COSMOCHIMICA ACTA*, 53(7):1583–1595.

Wegener, A. (1915). *Die Enstehung der Kontinente und Ozeane*. Vieweg, Braunschweig.

Wilde, S. A., Valley, J. W., Peck, W. H., and Graham, C. M. (2001). Evidence from detrital zircons for the existence of continental crust and oceans on the Earth 4.4 Gyr ago. *Nature*, 409(6817):175–178.

Willbold, M., Hegner, E., Stracke, A., and Rocholl, A. (2009). Continental geochemical signatures in dacites from Iceland and implications for models of early Archaean crust formation. *Earth and Planetary Science Letters*, 279(1-2):44–52.

Winther, K. T. and Newton, R. C. (1991). Experimental melting of hydrous low-potassium tholeiite: evidence on the origin of Archean cratons. *Bulletin of the Geological Society of Denmark*, 39(3-4):213–228.

Wolf, M. B. and Wyllie, P. J. (1994). Dehydration-melting of amphibolite at 10 kbar: the effects of temperature and time. *Contributions to Mineralogy and Petrology*, 115(4):369–383.

Xie, S. and Tackley, P. J. (2004a). Evolution of helium and argon isotopes in a convecting mantle. *Physics of the Earth and Planetary Interiors*, 146(3-4):417–439.

Xie, S. and Tackley, P. J. (2004b). Evolution of U-Pb and Sm-Nd systems in numerical models of mantle convection and plate tectonics. *Journal of Geophysical Research*, 109(B11).

Xu, W., Lithgow-Bertelloni, C., Stixrude, L., and Ritsema, J. (2008). The effect of bulk composition and temperature on mantle seismic structure. *Earth and Planetary Science Letters*, 275(1-2):70–79.

Yoshida, M., Iwase, Y., and Honda, S. (1999). Generation of plumes under a localized high viscosity lid in 3-D spherical shell convection. *Geophysical Research Letters*, 26(7):947–950.

Zerr, A., Diegeler, A., and Boehler, R. (1998). Solidus of Earth's deep mantle. *Science*, 281(5374):243–246.

Zhang, P., Cohen, R. E., and Haule, K. (2015). Effects of electron correlations on transport properties of iron at Earth's core conditions. *Nature*, 517(7536):605–607.

Zhao, D. P. (2004). Global tomographic images of mantle plumes and subducting slabs: insight into deep Earth dynamics. *Physics of the Earth and Planetary Interiors*, 146(1-2):3–34.

Zhong, S. and Gurnis, M. (1993). Dynamic feedback between a continentlike raft and thermal convection. *Journal of Geophysical Research*, 98(B7):12219–12232.

Zhong, S. and Liu, X. (2016). The long-wavelength mantle structure and dynamics and implications for large-scale tectonics and volcanism in the Phanerozoic. *Gondwana Research*, 29(1):83–104.

Zhong, S., Zhang, N., Li, Z.-X., and Roberts, J. H. (2007). Supercontinent cycles, true polar wander, and very long-wavelength mantle convection. *Earth and Planetary Science Letters*, 261(3-4):551–564.

Zhong, S. J. (2006). Constraints on thermochemical convection of the mantle from plume heat flux, plume excess temperature, and upper mantle temperature. *Journal of Geophysical Research: Solid Earth*, 111(B4).

Appendix A

Supplementary Materials to "Growing primordial continental crust self-consistently in global mantle convection models"

A.1   P-T conditions for TTG formation

The amount of TTG produced by partially melting hydrated basalt is computed using the solidus and liquidus temperatures presented in Appendix A.2. Yet, TTG melts are only formed in the pressure-temperature range presented in this Appendix. In the present study, we consider that basalt simply forms molten basalt if the P-T conditions for TTG formation are not met.

Following the parameterisation of *Rozel et al.* [2017] (based on *Moyen* [2011]), low and medium pressure TTGs form from hydrated basalt in the following conditions (T is in °C and P is in GPa):

$$760 - 60\left(P - 1\right)^2 \quad < T < \quad 1000 - 150\left(\frac{P - 1.2}{1.2}\right)^2 \tag{A.1}$$

$$-0.5\left(\frac{T - 870}{220}\right) \quad < P < \quad 1.5 + 0.7\left(\frac{T - 700}{200}\right), \tag{A.2}$$

where low pressure TTGs form at pressures lower than $1\,\text{GPa}$ and medium pressure form above $1\,\text{GPa}$. Additionally, high pressure TTG rocks form under these conditions:

$$1000 \quad < T < \quad 1100 + 50 \left(\frac{P - 3.5}{3.5} \right)^2 \tag{A.3}$$

$$2.35 + 0.15 \left(\frac{T - 1000}{100} \right) \quad < P < \quad 5. \tag{A.4}$$

A.2 Solidus and liquidus temperatures

We detail here the various solidus and liquidus functions used in the present study. In all the functions, pressure P is in GPa, depth d is in km, and T is in K.

A.2.1 Basalt melting

A.2.1.1 Below $5\,\text{GPa}$

For pressures up to $5\,\text{GPa}$, the pressure-dependent solidus and liquidus functions for "hydrated basalt" (as defined in their paper) composition are taken from Table 1 of *Sizova et al.* [2015]:

$$T_{\text{sol,bas}}(P)[K] \;\;=\;\; \begin{cases} 973 - \frac{70{,}400}{1000P + 354} + \frac{77{,}800{,}000}{(1000P + 354)^2}, & \text{for } P < 1.6 \\ 935 + 3.5P + 6.2P^2, & \text{for } 1.6 \le P < 5 \end{cases}, \tag{A.5}$$

$$T_{\text{liq,bas}}(P)[K] \;\;=\;\; 1423 + 105P. \tag{A.6}$$

While analysing the results, we realised that we used a basalt solidus that was shifted towards higher temperatures by 100-200 K (for pressures up to $1.6\,\text{GPa}$). This happened due to a publication error of Eq. A.5 in *Sizova et al.* [2015] and such a shift in the solidus temperature can be considered as having a lower water content in the mantle (or dry basalt solidus), which remains a big unknown. We made the necessary corrections in order to lower the solidus temperature and ran additional simulations (presented in Table 4.4), whose results showed that this small error had a minimal impact on the overall TTG produced and its crustal growth (compare Fig. 4.7a and 4.9a).

A.2.1.2 Above $5\,\text{GPa}$

For pressures between 5-135 GPa (up to core-mantle boundary), the pressure-dependent solidus and liquidus functions for "mid-oceanic ridge basalt" (as defined in their paper)

composition are taken from Fig. 2 of *Andrault et al.* [2014]:

$$
\begin{aligned}
T_{\text{sol,bas}}(P)[K] &= \left(-1.0116 \cdot 10^{-12}\right) P^7 + \left(8.9986 \cdot 10^{-10}\right) P^6 \\
&\quad - \left(2.9466 \cdot 10^{-7}\right) P^5 + \left(4.781 \cdot 10^{-5}\right) P^4 \\
&\quad - 0.0039836 P^3 + 0.0072596 P^2 + 36.75 P + 1257.9 \quad \text{(A.7)} \\
T_{\text{liq,bas}}(P)[K] &= \left(1.3728 \cdot 10^{-10}\right) P^6 - \left(3.7739 \cdot 10^{-8}\right) P^5 \\
&\quad - \left(5.0861 \cdot 10^{-7}\right) P^4 + 0.0011277 P^3 \\
&\quad - 0.15346 P^2 + 23.869 P + 2854.0 \quad \text{(A.8)}
\end{aligned}
$$

A.2.2 Pyrolite melting

The solidus function for pyrolite has been taken from *Hirschmann* [2000] and it is given as:

$$
T_{\text{sol,pyr}}(P)[K] = \begin{cases} 273.15 + 1120.661 + 132.899 P - 5.104 P^2, & \text{if } P < 10 \\ 273.15 + 1939.251 + 30.819 \left(P - 10\right), & \text{if } P \geq 10 \end{cases}. \quad \text{(A.9)}
$$

The liquidus for pyrolite is an ad hoc compromise between *Zerr et al.* [1998]; *Stixrude et al.* [2009]; *Andrault et al.* [2011] and it depends on depth as:

$$
T_{\text{liq,pyr}}(d)[K] = \begin{cases} 5150 + 0.58d + 3750 \left(\text{erf}\left(\frac{d}{8000}\right) - 1\right), & \text{for } d > 2900 \\ 2870 + 0.58d + 2800 \left(\text{erf}\left(\frac{d}{800}\right) - 1\right), & \text{for } d > 660 \\ 2170 + 0.60d + 200 \left(\text{erf}\left(\frac{d}{220}\right) - 1\right), & \text{for } d < 660 \end{cases}. \quad \text{(A.10)}
$$

Table A.1 Simulations with depletion fraction $X_{\text{depletion}} = 0.5$, core temperature T_{cmb} (K), friction coefficient μ, eruption efficiency e (%), final model runtime t_{r} (Gyr), volume of total TTG produced $V_{\text{TTG,total}}$, volume of crustal TTG $V_{\text{TTG,crustal}}$, and volume of basaltic crust $V_{\text{bas,crustal}}$. All volumes reported here are in km^3 and at final model runtime.

T_{cmb}	μ	e	t_{r}	$V_{\text{TTG,total}}$	$V_{\text{TTG,crustal}}$	$V_{\text{bas,crustal}}$
5000	0.2	10	1.82	$9.43 \cdot 10^{10}$	$4.19 \cdot 10^{10}$	$1.16 \cdot 10^{10}$
5000	0.2	20	0.88	$6.37 \cdot 10^{10}$	$1.23 \cdot 10^{10}$	$5.94 \cdot 10^{9}$
5000	0.2	30	3.81	$9.57 \cdot 10^{10}$	$3.04 \cdot 10^{10}$	$9.40 \cdot 10^{9}$
5000	0.2	40	2.28	$8.17 \cdot 10^{10}$	$2.20 \cdot 10^{10}$	$9.86 \cdot 10^{9}$
5000^{x}	0.2	60	2.74	$8.16 \cdot 10^{10}$	$1.78 \cdot 10^{10}$	$1.05 \cdot 10^{10}$
5000	0.2	80	0.43	$3.01 \cdot 10^{10}$	$1.92 \cdot 10^{9}$	$4.37 \cdot 10^{9}$
5000	0.2	100	4.28	$7.68 \cdot 10^{10}$	$1.77 \cdot 10^{10}$	$7.17 \cdot 10^{9}$
6000	0.2	10	2.78	$1.10 \cdot 10^{11}$	$4.89 \cdot 10^{10}$	$1.04 \cdot 10^{10}$
6000	0.2	20	2.60	$1.09 \cdot 10^{11}$	$4.49 \cdot 10^{10}$	$1.06 \cdot 10^{10}$
6000^{b}	0.2	30	4.31	$1.10 \cdot 10^{11}$	$4.30 \cdot 10^{10}$	$1.06 \cdot 10^{10}$
6000	0.2	40	3.11	$1.02 \cdot 10^{11}$	$3.24 \cdot 10^{10}$	$1.06 \cdot 10^{10}$
6000	0.2	60	2.70	$9.77 \cdot 10^{10}$	$2.54 \cdot 10^{10}$	$9.89 \cdot 10^{9}$
6000	0.2	80	4.50	$9.32 \cdot 10^{10}$	$2.22 \cdot 10^{10}$	$1.04 \cdot 10^{10}$
6000	0.2	100	4.50	$8.73 \cdot 10^{10}$	$2.41 \cdot 10^{10}$	$1.09 \cdot 10^{10}$
6000	0.4	10	2.50	$1.09 \cdot 10^{11}$	$5.53 \cdot 10^{10}$	$1.30 \cdot 10^{10}$
6000^{x}	0.4	20	1.70	$1.03 \cdot 10^{11}$	$3.21 \cdot 10^{10}$	$1.09 \cdot 10^{10}$
6000	0.4	30	1.29	$8.96 \cdot 10^{10}$	$2.57 \cdot 10^{10}$	$1.01 \cdot 10^{10}$
6000	0.4	40	2.47	$1.00 \cdot 10^{11}$	$2.96 \cdot 10^{10}$	$1.04 \cdot 10^{10}$
6000	0.4	60	1.58	$8.46 \cdot 10^{10}$	$1.63 \cdot 10^{10}$	$1.02 \cdot 10^{10}$
6000	0.4	80	4.39	$9.20 \cdot 10^{10}$	$2.39 \cdot 10^{10}$	$1.06 \cdot 10^{10}$
6000	0.4	100	4.50	$9.01 \cdot 10^{10}$	$2.83 \cdot 10^{10}$	$1.17 \cdot 10^{10}$

[b] simulation *e30x5* presented in Fig. 4.3, 4.4 and 4.6
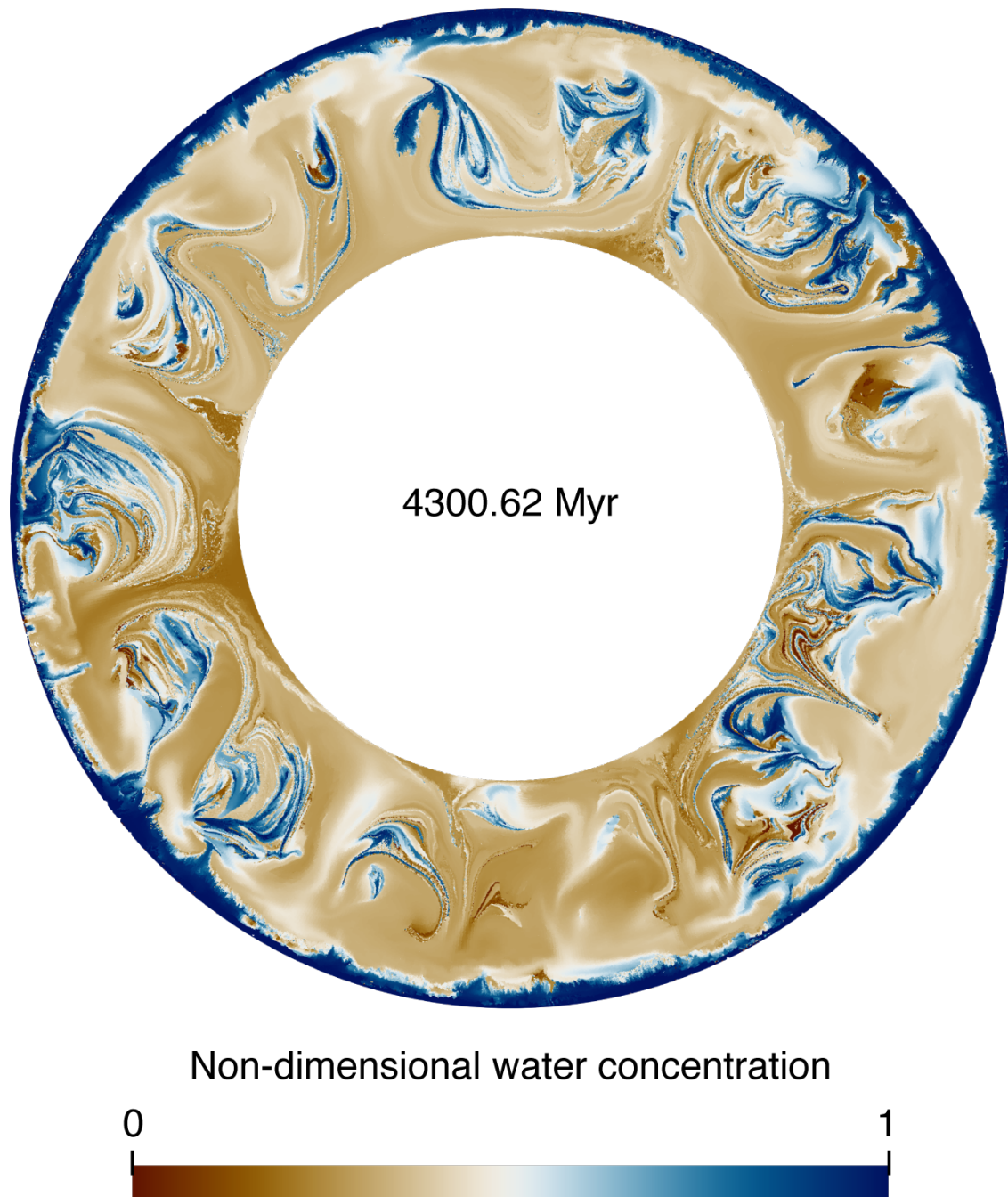[x] excluded from scaling laws owing to data corruption

Fig. A.1 Tracer-based field of simulation *e30x5* showing the amount of water in the mantle. The non-dimensional concentration is relative with 1 implying fully hydrated and 0 meaning no water.
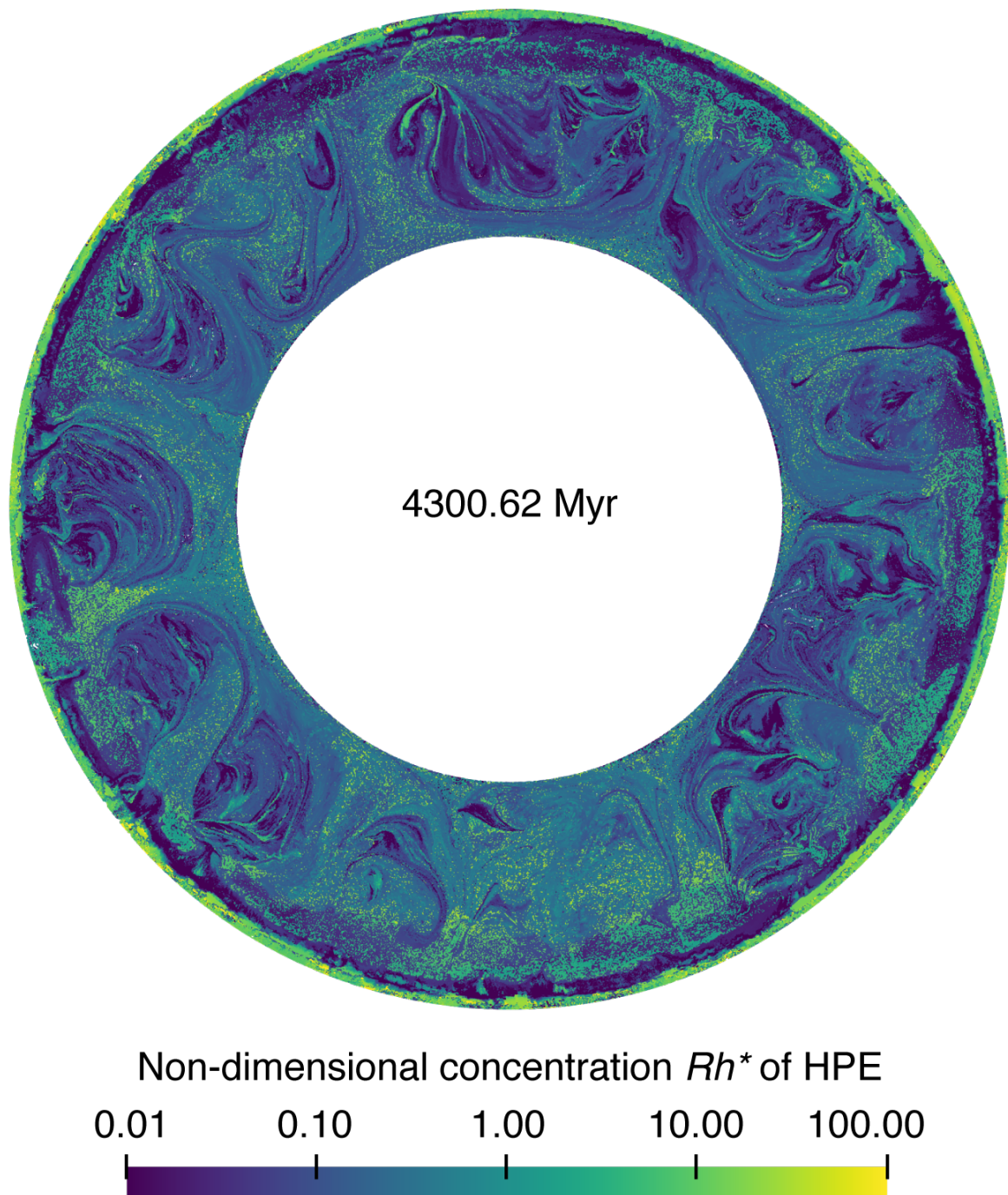
Fig. A.2 Tracer-based field of simulation *e30x5* showing the non-dimensional concentration of heat-producing element Rh^* with higher values in the crust at the surface. The dimensional concentration Rh can be computed as $Rh = Rh^* H e^{-\lambda t}$ with initial internal heating rate H, time t and decay constant $\lambda = 1/t_{\text{half}}$.
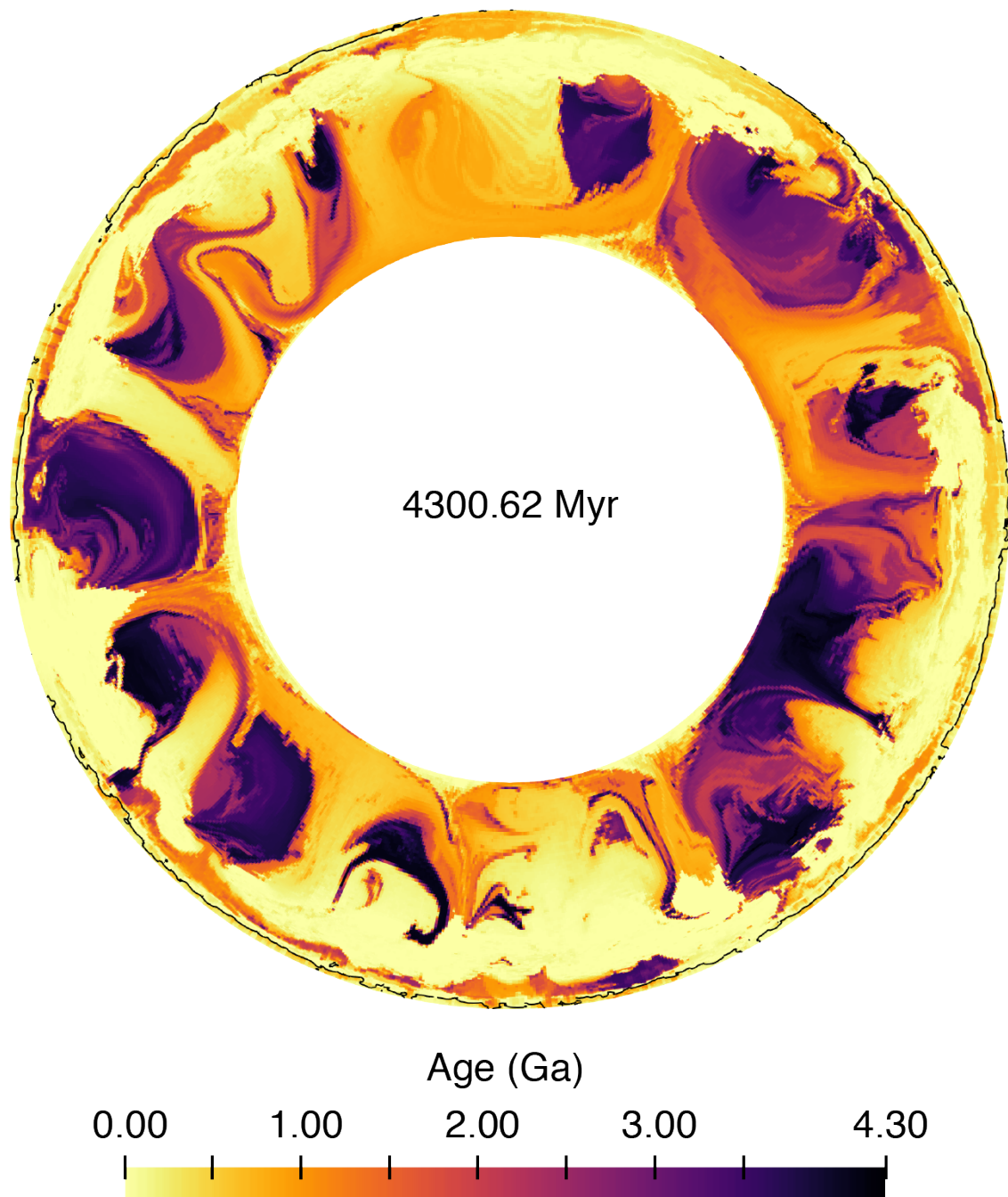
Fig. A.3 Cell-based field of simulation *e30x5* showing the age of the mantle based on the time since it melted last. The black contours highlight TTG crust ($\geq 99\%$ in a cell) and its relatively young age.

Acknowledgements

I would like to take this opportunity to thank a lot of wonderful people whom I have had the pleasure of knowing and working with. Some of you raised me, some of you influenced me, and some of you accompanied me on this long journey. I am here today because of you all. Thank you all for that!

To Paul Tackley, for giving me this opportunity to work with him knowing that I didn't have much experience with coding before. For giving me the independence to carry out my research but at the same time being available to guide me whenever required. Thank you for bringing me closer to Japanese culture, especially karaoke. You are the coolest supervisor ever!

To Taras Gerya, for motivating me and inspiring me to dream a little bigger. Your grasp of petrology and geology never ceases to amaze me. Thank you for the many insightful comments regarding my research.

To Antoine without whom this thesis would not have materialised. Thank you for being so patient with me all this time. You played all different characters from the *Fellowship* while I brought this adventure to completion. Thank you for all the fun times while conferencing, traveling, singing karaoke, watching Ghibli and Monty Python movies, and coding with you.

To the present and former members of GFD group: Antoine, Antonio, Casper, Caro, Claudio, Dan, Daniela, Dave, David, Diogo, Frank, Gregor, Ilya, Jana, Jessica, Jie, Jun, Kosuke, Luca, Maxim, Nicole, Patrick, Paul, Robert, Ria, Simon, Stefan, Suzanne, Taras, Tim, Vojta, Xiaogang, Xin. I could not have asked for a better place and group of wonderful people to work with.

To Elisabeth and Monika, for helping me navigate the administrative stuff and making sure that I got reimbursed for conferences in time.

To friends from other groups: Barbara, Brandi, Christoph, Emily, Fabian, Fede, Iris, Krisztina, Leo, Lisa, Martina, Mike, Moritz, Nele, Nienke, Nicolo, Saulé, Stefano, Yoann. You all made my time in Zurich worth remembering.

To Jana for tolerating my presence in "her" office, especially in the last months of writing. Thank you for the cakes, cookies, and clementines. To Dan and Maxim for

the many fruitful scientific discussions. To Silke for hosting us on many occasions for dinner and board-games. To Jana and Tim for translating my abstract into German.

To Caro, Lisbeth, Tim and Ulli for helping me with so many things over the last years. You were there for me especially when the times were tough. To Diogo, for welcoming me in the group on the first day and always recommending some good music. To Suzanne for approaching me 3 years ago at a conference in Japan. There hasn't been a dull moment while having you around since then. Thank you for reading parts of my thesis and improving them. So long, and thanks for all the coffee!

To Nico Coltice for always being enthusiastic about my research and giving me the opportunity to meet the amazing people working in Lyon: Léa, Claire, Marie, Martina, Mélanie and Maelis. Those AUGURY workshops in Valflaunès were some of the best times I ever had while working.

To Tobias for interesting conversations regarding continents. Your continents broke apart, so I made new ones. Hope you like them! To Fabio, for inspiring me to do something different visually every time I made a poster. Special thanks to Patrick and Adrien for making my life easier with code compilation.

To my flatmates: Christos, Colin, Pinar, Vito for all the evening discussions, fun times and making my stay comfortable in Zurich.

To my friends from the master's, especially Marlies, Melchior, Rita, Shankar, Sebs and Vero who made hopping between 3 countries worth the effort. To Annika and Deepu for looking after me during my stay in Aachen.

To my friends from my time in Bremen: Suna, Sammy, Hozefa, Jensen, Katsia, Max, Aska for exploring the diversity in the bubble together. To Niky and Vikram for providing a homey and stimulating environment at Mercator for the young minds.

To Christine and Bernhard, for receiving me at Bremen airport 10 years ago and welcoming me in their home ever since then. I am extremely lucky to have you as my family in Germany.

To Carin and Roy for accepting me as one of your own. You broadened my horizons and I learned a lot from you concerning music, photography, design, origami, life, the universe and everything.

To my cousin Rahul and Prerna for their amazing cooking skills and for being my little India here in Switzerland. To my brother Bhavuk and Kanika, for always believing in me and motivating me to excel at everything I do.

To my parents for their unconditional love and patience all these years I spent away from home. Without your constant support and understanding, I would not be here today.

Curriculum Vitae

Charitra Jain

Indian · 11 Jan 1989

ETH Zurich, Institute of Geophysics
Sonneggstrasse 5, 8092 Zurich, Switzerland
☎ *+41 44 633 3248*
✉ *charitra.jain@erdw.ethz.ch*
🖳 *charitrajain.net*
in *charitrajain*

Education

Oct 2013 – Feb 2018
PhD in Computational Geodynamics, *ETH Zurich*, Zurich, Switzerland.
Thesis: Self-Consistent Generation of Continents and Their Influence on Global Mantle Dynamics
Advisors: Paul Tackley, Taras Gerya, Antoine Rozel, Jeroen van Hunen

Sep 2010 – Aug 2012
M.Sc. in Applied Geophysics (graduated cum laude), *TU Delft, ETH Zurich, RWTH Aachen*, Delft, Netherlands.
Thesis: Optimized Layout of Engineered Geothermal Systems and Potential in Germany
Advisor: Christoph Clauser

Sep 2007 – Jun 2010
B.Sc. in Earth & Space Sciences, *Jacobs University*, Bremen, Germany.
Thesis: Hydrological and Morphological Analysis of the Okavango Delta, Botswana
Advisor: Vikram Unnithan

Apr 1995 – Apr 2007
Secondary School Diploma, *St. Mary's Sr. Sec. School*, Haridwar, India.
Subjects: Physics, Chemistry, Mathematics, Computer Science

Experience

Research & Work

Oct 2013 – Feb 2018
Graduate Research Assistant, *Institute of Geophysics, ETH Zurich*, Zurich, Switzerland.
- Designed and developed a numerical model for continent formation using Fortran
- Conducted parameterised studies to understand the evolution and internal dynamics of Earth
- Analysed and visualised data using Bash, MATLAB and ParaView
- Published results in scientific journals and presented them at international conferences
- Coordinated logistical and technical aspects of the scientific workshop organised by the group

Oct 2012 – Dec 2012
Junior Researcher, *E.ON Energy Research Center*, Aachen, Germany.
- Published a research paper on the potential of geothermal energy in Germany

Feb 2012 – Jul 2012
Undergraduate Research Assistant, *RWTH Aachen University*, Aachen, Germany.
- Modelled and optimised the energy output of Engineered Geothermal Systems (EGS) reservoirs
- Analysed data and visualised results using MATLAB

Jan 2010 – May 2010
Undergraduate Research Assistant, *Jacobs University*, Bremen, Germany.
- Investigated the hydrological features of the Okavanga Delta, Botswana
- Integrated satellite imagery and geospatial datasets using ArcGIS
- Prepared teaching material (GIS data, maps) for use in Helgoland field excursion and GIS course

Jul 2009 – Aug 2009
Summer Intern, *Wildlife and Community Development Fund*, Katima Mulilo, Namibia.
- Mapped and visualised GIS data acquired in the field
- Carried out community building work with the locals
- Raised awareness about wildlife protection and human-predator conflict (HPC)

Extracurricular

May 2015
Co-Organiser, *ERDW Doctoral Retreat 2015, ETH Zurich*, Bernau, Germany.
- Organised the departmental social event facilitating knowledge exchange among PhD students

Aug 2008
Intercultural Trainer, *Orientation Week, Jacobs University*, Bremen, Germany.
- Conducted workshops for undergraduate students to acclimatise them to the culturally diverse environment

Publications

Published:

○ A. B. Rozel, G. J. Golabek, <u>C. Jain</u>, P. J. Tackley, T. Gerya, "Continental crust formation on early Earth controlled by intrusive magmatism", *Nature* **2017**, *545, 332-335*

○ <u>C. Jain</u>, C. Vogt, and C. Clauser, "Maximum potential for geothermal power in Germany based on engineered geothermal systems", *Geothermal Energy* **2015**, *3:15*

Under review:

○ <u>C. Jain</u>, A. B. Rozel, P. J. Tackley, "Quantifying the correlation between mobile continents and elevated temperatures in the mantle", *Geochemistry, Geophysics, Geosystems* **2018**

In preparation:

○ <u>C. Jain</u>, A. B. Rozel, P. J. Tackley, P. Sanan, T. Gerya, "Growing primordial continents self-consistently in global mantle convection models", *Gondwana Research* **2018**

Honours & Awards

○ 2017 recipient of **Outstanding Student Poster (OSP) award** at XV International Workshop on Modelling of Mantle and Lithosphere Dynamics.

○ 2013 recipient of **Prof. Karl-Heinrich Heitfeld Foundation award** for excellent M.Sc. thesis at RWTH Aachen University.

○ 2010 recipient of **Mercatorian of the Year award** for active involvement and commitment in the cultural events happening in Mercator College at Jacobs University.

Major Scientific Achievements

1. Developed a petrological model for two-stage melting that can self-consistently generate Archean continental crust (TTG rocks) in global mantle convection code. Demonstrated a two-stage crustal growth without the initiation of subduction-driven plate tectonics and compared the modelling results with geological and geochemical data (Jain et al. 2018, in preparation)
   ⇒ Lead author, contributed to study design, performed all calculations, designed all figures, wrote the manuscript

2. Quantified the effect of initial core temperature, continental size, internal heating, and Rayleigh number on subcontinental mantle warming using convection models. Demonstrated continental breakup as a result of decompression melting and magmatism (Jain et al. 2018, under review)
   ⇒ Lead author, contributed to study design, performed all calculations, designed all figures, wrote the manuscript

3. Demonstrated the dominating role of intrusive magmatism compared to extrusive magmatism towards generating primordial continental crust (Rozel et al., 2017)
   ⇒ Contributed in comparing the modelling results to geological data and writing the manuscript

Skills

Languages

Hindi (mother tongue), **English** (proficient), **German** (basic knowledge)

Software

OS	Windows, MacOS and Linux	**Languages**	C, C++, Fortran, Bash, HTML, CSS
Publishing	LaTeX, MS Office (Word, Powerpoint & Excel), GitHub, Papers, EndNote, Illustrator, Lightroom	**Scientific**	Matlab, StagYY, ParaView, ArcGIS, SHEMAT, ProMAX Seismic, GRASS, GMT, IDL

Interests & Hobbies

Landscape and candid photography, modular origami, graphic design, DJing

Conferences & Workshops

18. <u>C. Jain</u>, A. B. Rozel, and P. J. Tackley, "Self-consistent generation of primordial continental crust in global mantle convection models" (Poster), *AGU Fall Meeting*, December **2017**, New Orleans, USA.

17. <u>C. Jain</u>, A. B. Rozel, and P. J. Tackley, "Self-consistent generation of primordial continental crust in global mantle convection models" (Poster), *XV International Workshop on Modelling of Mantle and Lithosphere Dynamics*, August **2017**, Putten, Netherlands.

16. <u>C. Jain</u>, A. B. Rozel, and P. J. Tackley, "Self-consistent generation of primordial continental crust in global mantle convection models" (Presentation), *Goldschmidt Conference*, August **2017**, Paris, France.

15. <u>C. Jain</u>, A. B. Rozel, and P. J. Tackley, "Self-consistent generation of continental crust in global mantle convection models" (Poster), *EGU General Assembly*, April **2017**, Vienna, Austria.

14. <u>C. Jain</u>, A. B. Rozel, and P. J. Tackley, "Self-consistent generation of continental crust in global mantle convection models" (Poster), *AGU Fall Meeting*, December **2016**, San Francisco, USA.

13. <u>C. Jain</u>, A. B. Rozel, and P. J. Tackley, "Self-consistent generation of continental crust in global mantle convection models" (Poster), *German-Swiss Geodynamics Workshop*, September **2016**, Lichtenfels, Germany.

12. <u>C. Jain</u>, A. B. Rozel, and P. J. Tackley, "Self-consistent generation of continental crust in global mantle convection models" (Poster), *Workshop on the Origin and Evolution of Plate Tectonics*, July **2016**, Locarno, Switzerland.

11. <u>C. Jain</u>, A. B. Rozel, and P. J. Tackley, "Self-consistent generation of continental crust in global mantle convection models" (Poster), *Goldschmidt Conference*, June **2016**, Yokohama, Japan.

10. <u>C. Jain</u>, A. Rozel, and P. Tackley, "Correlation between mobile continents and elevated temperatures in the subcontinental mantle" (PICO Presentation), *EGU General Assembly*, April **2016**, Vienna, Austria.

9. <u>C. Jain</u>, A. Rozel, and P. Tackley, "Correlation between mobile continents and elevated temperatures in the subcontinental mantle" (Presentation), *AUGURY Workshop*, February **2016**, Valflaunès, France.

8. <u>C. Jain</u>, A. Rozel, and P. Tackley, "Correlation between mobile continents and elevated temperatures in the subcontinental mantle" (Poster), *AGU Fall Meeting*, December **2015**, San Francisco, USA.

7. <u>C. Jain</u>, A. Rozel, and P. Tackley, "Is there any correlation between continents and elevated temperatures in the subcontinental mantle?" (Poster), *XIV International Workshop on Modelling of Mantle and Lithosphere Dynamics*, August **2015**, Oléron, France.

6. <u>C. Jain</u>, A. Rozel, and P. Tackley, "Is there any correlation between continents and elevated temperatures in the subcontinental mantle?" (PICO Presentation), *EGU General Assembly*, April **2015**, Vienna, Austria.

5. <u>C. Jain</u>, A. Rozel, and P. Tackley, "The effect of plumes on the dynamics of supercontinents in a self- consistent plate tectonics setting" (Poster), *AGU Fall Meeting*, December **2014**, San Francisco, USA.

4. <u>C. Jain</u>, A. Rozel, and P. Tackley, "The effect of plumes and a free surface on mantle dynamics with continents and self-consistent plate tectonics" (Presentation), *AUGURY Workshop*, November **2014**, Valflaunès, France.

3. <u>C. Jain</u>, A. Rozel, and P. Tackley, "The effect of plumes and a free surface on mantle dynamics with continents and self-consistent plate tectonics" (Presentation), *German-Swiss Geodynamics Workshop*, October **2014**, Bad Münster am Stein-Ebernburg, Germany.

2. <u>C. Jain</u>, A. Rozel, and P. Tackley, "The effect of plumes and a free surface on mantle dynamics with continents and self-consistent plate tectonics" (Poster), *14th International Symposium on SEDI*, August **2014**, Kanagawa, Japan.

1. <u>C. Jain</u>, A. Rozel, and P. Tackley, "The effect of plumes and a free surface on mantle dynamics with continents and self-consistent plate tectonics" (PICO Presentation), *EGU General Assembly*, April **2014**, Vienna, Austria.